Molecular absorption in variable brightest cluster galaxies

ROSE, THOMAS,DAVID

Molecular absorption in variable brightest cluster galaxies

Tom Rose

A thesis presented for the degree of
Doctor of Philosophy

Centre for Extragalactic Astronomy
Department of Physics
University of Durham
United Kingdom

August 2021

Molecular absorption in variable brightest cluster galaxies

Tom Rose

Submitted for the degree of Doctor of Philosophy
August 2021

Abstract

Supermassive black holes devour immense quantities of mass from their surroundings, and in doing so have a profound effect upon the galaxy they reside in. Most of the mass they consume is thought to be in the form of cold molecular gas clouds, but the ways in which these form and migrate to the supermassive black hole are still uncertain. This thesis aims to reveal the properties of molecular clouds in the cores of the Universe's most massive galaxies through observations - determining their typical mass, temperature, kinematics, and the manner in which they find their way into the galaxies. This is achieved by a new observing technique which takes advantage of the bright and compact active galactic nucleus which encompasses the central supermassive black hole of many large galaxies. As molecular clouds pass in front of this region, they cast shadows. These shadows are signatures of the clouds' properties and make it possible to study them, often individually. These studies are also linked to the variability of active galactic nuclei, which is directly dependant on supermassive black hole accretion.

Declaration

The work in this thesis was carried out between October 2017 and July 2021 while the author was a student under the supervision of Prof. Alastair Edge at the University of Durham's Department of Physics.

No part of this thesis has been submitted in contribution to any other degree or qualification.

Three chapters have appeared in the following published works, listed in order of publication date:

- *Deep and narrow CO absorption revealing molecular clouds in the Hydra-A brightest cluster galaxy* · **Rose, Tom**; Edge, A. C.; Combes, F.; Gaspari, M.; Hamer, S.; Nesvadba, N.; Russell, H.; Tremblay, G. R.; Baum, S. A.; O'Dea, C.; Peck, A. B.; Sarazin, C.; Vantyghem, A.; Bremer, M.; Donahue, M.; Fabian, A. C.; Ferland, G.; McNamara, B. R.; Mittal, R.; Oonk, J. B. R. Salomé, P.; Swinbank, A. M.; Voit · 2019, MNRAS, 485, 229 (view publication)

- *Constraining cold accretion on to supermassive black holes: molecular gas in the cores of eight brightest cluster galaxies revealed by joint CO and CN absorption* · **Rose, Tom**; Edge, A. C.; Combes, F.; Gaspari, M.; Hamer, S.; Nesvadba, N.; Peck, A. B.; Sarazin, C.; Tremblay, G. R.; Baum, S. A.; Bremer, M. N.; McNamara, B. R.; O'Dea, C.; Oonk, J. B. R.; Russell, H.; Salomé, P.; Donahue, M.; Fabian, A. C.; Ferland, G.; Mittal, R. Vantyghem, A. · 2019, MNRAS, 489, 349 (view publication)

- *A molecular absorption line survey towards the AGN of Hydra-A* · **Rose, Tom**; Edge, A. C.; Combes, F.; Hamer, S.; McNamara, B. R.; Russell, H.; Gaspari, M.; Salomé,

P.; Sarazin, C.; Tremblay, G. R.; Baum, S. A.; Bremer, M. N.; Donahue, M.; Fabian, A. C.; Ferland, G.; Nesvadba, N.; O'Dea, C.; Oonk, J. B. R.; Peck, A. B. · 2020, MNRAS, 496, 364 (view publication)

Chapter 2 has also been submitted for publication and is currently under peer review:

- *The variability of brightest cluster galaxies at high radio frequencies* · Tom Rose, Alastair Edge, Sebastian Kiehlmann, Junhyun Baek, Aeree Chung, Tae-Hyun Jung, Jae-Woo Kim, Anthony Readhead, and Aidan Sedgewick

Many of the ideas in thesis were formed in collaboration with those listed as co-authors in the above publications, but the author is responsible for the written content. One exception to this is Chapter 2 Section 2.6, which was jointly written by the author and Alastair Edge.

Acknowledgements

First and foremost, I would like to thank Alastair Edge. Without your encyclopedic knowledge and eye for a good project, none of this work would exist. But even better, you're a lovely person and it's been a pleasure to work with you. A lot has happened over the last few years, and you've been consistently amazing throughout.

Thank you also to David Sobral. I'd never have made it to Durham without your help.

Thank you Mum and Dad, and to my grandparents, sisters, brother, niece, nephews, and all my friends from home in Chester. You're all amazing – even if you don't really have a clue what I do – and I hope you all know how nice it is to have you around and how grateful I am for your continual encouragement without me saying so here. Thank you to those who, because of coronavirus, I've not seen for 18 months, and those I'll sadly never see again.

Thank you as well to all the friends I've made during my time in Durham. I won't name you all, but you know who you are. You've made the last four years a joy and given me many happy memories.

Thank you to the cleaning fairies who have kept the Department tidy and fit for working in. I've never been punctual enough to arrive early enough to see you, but I'm sure you exist.

Finally, I'm also grateful to the UK's tax payers – a group I've skillfully dodged joining for a good few years now, while somehow not ending up as the subject of a Channel 5 documentary. Thanks for the 0.2 pence each of you has given me over the last few years.

Contents

List of Figures

List of Tables

CHAPTER 1

Introduction

1.1 Clusters, galaxies, and supermassive black holes

According to the widely accepted ΛCDM model of cosmology, the Universe is made up of three major components. In order of prevalence, they are (i) a cosmological constant – associated with the dark energy which drives the expansion of the Universe, (ii) non-interacting (or perhaps weakly interacting) cold dark matter, and (ii) ordinary baryonic matter, from which stars and planets are made.

In the ΛCDM model, galaxies and clusters are able to form in locations with a matter density high enough to prevail over the Universe's continued expansion. When galaxy formation was beginning to take place, the size of the initial density perturbations was small, but over time they grew significantly thanks to gravitational collapse, and with help from the merging of dark matter halos (Cole et al., 2000; Schneider et al., 2012). Over time, this led to the formation of large concentrations of mass along web-like structures known as 'galaxy filaments' (Steidel et al., 2010). These are the largest structures in the Universe, and at their nodes are galaxy clusters, the Universe's largest gravitationally bound objects (Edge, 1989). These granular structures are typically composed of a few hundred galaxies of varying size.

Although this collapse is driven by dark matter, significant amounts of baryonic matter followed. However, due to its self-interactions, for baryonic matter to collapse significantly, the gravitational forces acting on it must prevail over its internal pressure. To form a star – a key constituent of galaxies – the cooling of a region of gas must more than compensate for any heating induced by its gravitational collapse. If this is the case, it will eventually become cool and dense enough for nuclear fusion reactions to begin to take place (Stahler & Palla, 2004).

Following their initial formation, galaxies proceeded along a wide range of evolutionary paths, which are determined by their own properties (such as their mass), and the environment in which they find themselves. For example, at the present day, massive galaxies which formed early on in the Universe and which have a large number of neighbours are more likely to have exhausted their reservoirs of cold gas and to have experienced major merger events – this makes them more likely to be elliptical type galaxies with old stellar populations. Conversely, more recently formed galaxies and those that do not belong to a larger galaxy group or cluster (termed 'field galaxies') are more likely to be spirals, with young stellar populations (Kashlinsky, 1982; Graham et al., 1998).

Galaxies are complex structures and contain deep substructure, with each being a gravitationally bound system of dark matter, and baryonic matter in the form of stars, dust, and gas. Galaxies also contain a supermassive black hole at their centre, whose immense mass allows it to accrete matter from its surroundings (Kravtsov & Borgani, 2012).

These supermassive black holes are another significant factor in the evolution of galaxies. The way in which they form is not completely understood, but it is generally agreed that they grow from the merging of many lower mass black holes, as well as by the accretion of matter (Bower et al., 2006).

In many respects, galaxies dwarf their supermassive black holes. Depending on exactly how they are defined, the two are typically several orders of magnitude or more apart in physical size, and around three orders of magnitude separate their masses.

Despite these differences, they appear to be strongly linked. In what's known as the M-sigma relation, the mass of a galaxy's central supermassive black hole, M_{BH}, and

the velocity dispersion in its central bulge of stars, σ, are found to be remarkably well correlated (Magorrian et al., 1998; Robertson et al., 2006; Ferrarese & Merritt, 2000). The relation takes the form $M_{BH} \propto \sigma^{\alpha}$, with α normally found to have a value between 4 and 5 (Robertson et al., 2006; Gültekin et al., 2009). A second example is the Mass-Luminosity relation, which states that a supermassive black hole's mass is approximately proportional to the host galaxy bulge's luminosity (Gültekin et al., 2009; McLure & Dunlop, 2002; Kormendy & Ho, 2013).

These and other correlations between supermassive black holes and their host galaxy's wider properties are a powerful argument that the two are strongly connected and have a significant effect on each other's evolution, even if the exact reasons why remain poorly understood (Bower et al., 2006).

What's known for sure is that supermassive black holes are able to have a profound effect on their host galaxy, and are extremely efficient at converting any mass they accrete into other forms of energy, much more so than the nuclear fusion which takes place in stars. As a result, when a supermassive black hole accretes significant amounts of mass, the surrounding region can become so bright that it outshines the galaxy's entire stellar population (McNamara & Nulsen, 2012). Such a case is termed an 'active galactic nucleus', or AGN. It is observations of these immensely bright and powerful objects which are the focus of this thesis, as well as the ways in which they interact with their host galaxies.

The energy output of AGN varies from object to object, both in terms of brightness, and the relative dominance of radio, X-rays, visible light, and ultra-violet radiation. As an example, Figure 1.1 shows an image of the nearby galaxy Centaurus-A, which hosts a powerful AGN at its centre. This composite image highlights the main features which are typically present in a galaxy hosting a powerful AGN, most notably (i) its disc of stars, gas, and dust, (ii) its radio lobes, and (iii) the bubbles inflated in the X-ray emitting gas by those radio lobes. All of these features will be explored in the rest of this introductory chapter.

More generally, in this thesis, the main focus is on radio and sub-mm observations of AGN hosting galaxies. These are an excellent means of studying the behaviour and interactions of supermassive black holes and their wider environments, but they come with their own difficulties which must be overcome.

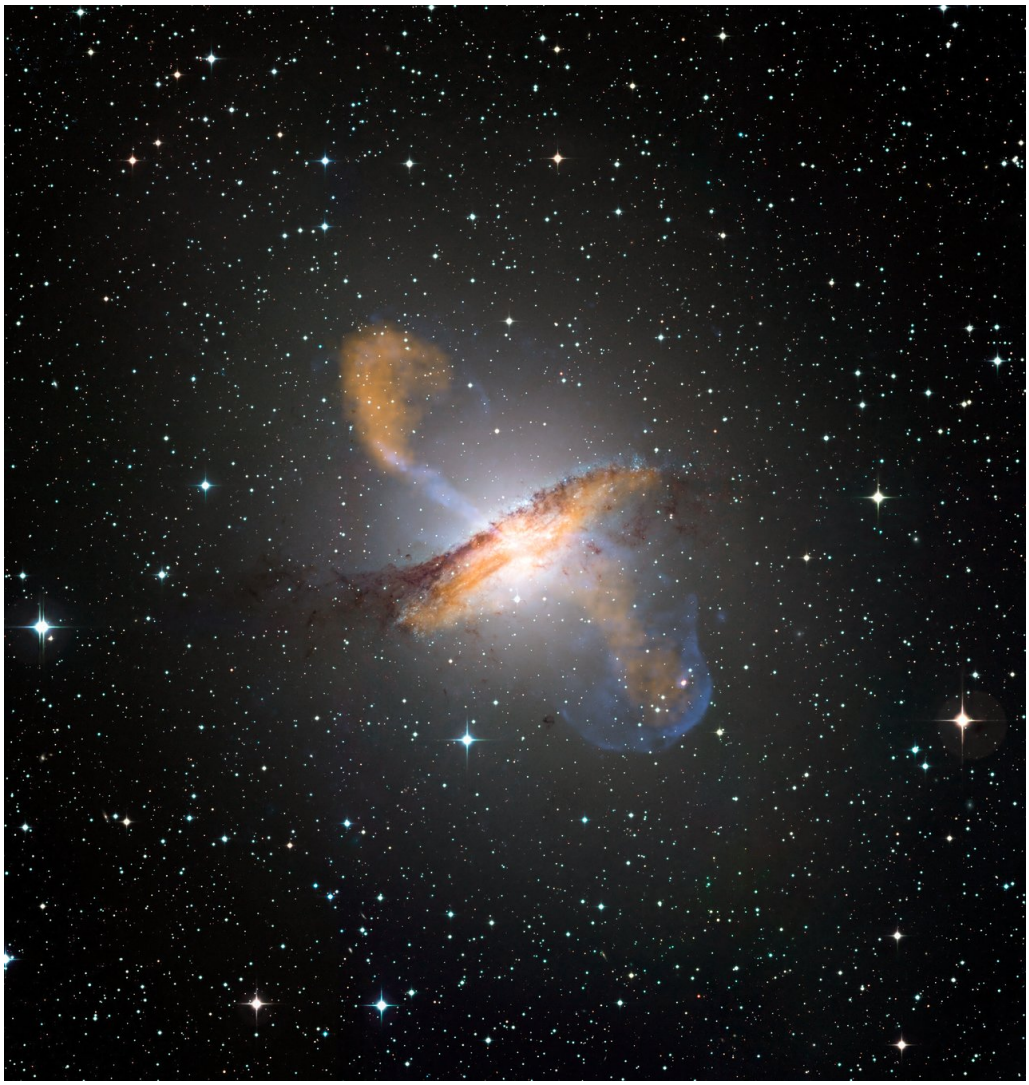

Figure 1.1

A composite image of Centaurus-A, a nearby radio galaxy which hosts a powerful AGN at its centre. The main image is a visible light observation from the MPG/ESO 2.2 m telescope. Sub-millimetre data from LABOCA and APEX is in orange, and data from the Chandra X-ray Observatory in blue. Image: ESO `https://www.eso.org/public/images/eso0903a/`

1.2 Radio Astronomy and its limitations

By human standards astronomical objects of all kinds are at immense and unfathomable distances, so unless an astronomer is content with studying a universe manufactured by computer simulations, they will need to observe the real one using telescopes. The work of this thesis is mainly concerned with the behaviour of AGN and the cool gas within galaxies, and studies them at radio and sub-mm wavelengths, which are at the long wavelength end of the electromagnetic spectrum.

Unfortunately, as the wavelength of the electromagnetic radiation being observed increases, the resolution achievable with a telescope of a given size decreases. The maximum theoretical angular resolution, $\theta_{\max}$, of a telescope of diameter D, and observing at a wavelength λ is:

$$\theta_{\max} = 1.22 \frac{\lambda}{D} \tag{1.2.1}$$

An optical astronomer using the Hubble Space Telescope (*HST*), to study the relatively nearby Hydra-A brightest cluster galaxy could expect to see details on the scale of just a few tens of billions of kilometers thanks to the relatively short wavelengths of the optical light. On the other hand, looking at the same galaxy with a radio telescope whose dish is the same size, it would only be possible to achieve resolution equating to spatial scales of tens of trillions of kilometers – around a thousand times worse.

1.2.1 Radio Interferometry

If persevering with radio astronomy, radio telescopes with dishes of tens of meters or more in diameter are required to achieve images with useful angular resolution. Examples of such telescopes which have been important to this thesis include the Institut de Radioastronomie Millimétrique (IRAM) 30-meter telescope and the Owens Valley Radio Observatory (OVRO) 40-meter telescope.

However, to compete with the angular resolution achievable with an optical telescope such as the *HST* would require dishes stretching to kilometers or more. This presents obvious engineering and financial challenges, and so as an alternative arrays of many smaller dishes,

separated from each other at large distances are used in conjunction with the technique of interferometry. This method connects numerous dishes to make what is in effect a single large telescope. This larger telescope can produce a single combined image with an angular resolution limited by the separation of the dishes, rather than their individual diameters.

An image from a radio telescope is produced by applying a Fourier transform to the sky brightness distribution (also known as the visibility function). Fortunately, a useful image can still be produced from just a sparse sampling of the brightness distribution. Such a sampling can be gained from two or more physically unconnected dishes, which form an array. In interferometry, each dish in the array provides a contribution to the sampling.

The most acute difficulty associated with interferometry is that the sampling of the visibility function is done at discrete baselines set by the placement of the dishes. Put simply, this means that it is incomplete. A less simple explanation is that it makes the true sky brightness an inverse Fourier transform of the convolution of the measured integrated complex visibilities with a point spread function. For a complete sky brightness pattern to be obtained, the Fourier transform must have complete information from the complex visibilities at all angular scales. For an interferometer, which is an array of small dishes with many large gaps in between, a lack of coverage at certain angular angular scales in the visibility function (known as the uv-plane) brings with it a lack of sensitivity at the corresponding angular scales in the image. To produce an image with high sensitivity at a range of angular scales, usually termed as having a good sampling of the uv-plane, the placement of the interferometer's dishes is important. Short baselines provide good sampling of the uv-plane on large angular scales, while long baselines are needed for sampling at small angular scales. A more thorough description of the technique of interferometry can be found in Thompson et al. (2017).

1.2.2 The Atacama Large Millimeter/submillimeter Array

The majority of this thesis has been made possible by the Atacama Large Millimeter/submillimeter Array (ALMA), a radio interferometer composed of 66 ground-based telescopes at an alti-

tude of 5000m in the Atacama Desert's Chajnantor Plateau. In most meaningful respects, it is the best and most advanced radio interferometer in the World, with much higher sensitivity and resolution than any of its predecessors (one possible exception to this is the Event Horizon Telescope – though this is just formed by combining telescopes from a collection of independent observatories, including ALMA). Perhaps most importantly, ALMA lies in one of the most consistently dry places on Earth; a necessity given the tendency of higher frequency radio waves to be reflected, absorbed, scattered, refracted, and diffracted by atmospheric water.

ALMA is itself formed from two sub-arrays – a long baseline array, and the Atacama Compact Array. In total, there are 66 antennas: 54 of them have 12-metre diameter dishes, and the remaining 12 have smaller dishes, with a diameter of 7 metres each (ESO.org, 2021). For the larger array, baselines range between 150 m and 16 km, while the Atacama Compact Array's baselines are of up to 30 m. ALMA is frequently moved into different configurations to provide optimum sampling of the uv-plane for both compact and extended objects. More compact configurations provide more sensitivity for extended sources, making them optimal for larger and dimmer structures, such as giant molecular gas clouds.

ALMA's extended arrays have been particularly vital to this thesis because they are the only ones which can provide the necessary sensitivity and angular resolution with which the bright radio continuum sources associated with the supermassive black holes of radio galaxies can be sufficiently well resolved.

ALMA observations are currently done in 10 wavelength bands which range from 0.3 to 8.5 mm (ESO.org, 2021).

1.3 Active Galactic Nuclei

1.3.1 Classifications of AGN

A wide range of terminology is applied to AGN as a way of grouping together those which have similar properties. These classifications have often depended on which wavelengths

they've been observed with, making exact classifications of many objects the subject of debate among astronomers in different fields.

The first widely used classification system was based on optical wavelength observations and was introduced by Seyfert (1943). This was followed by several others, notably Schmidt (1963) based on optical observations and Fanaroff & Riley (1974) based on radio observations. As astronomy has progressed, various unification models have been proposed in an attempt to relate these and other AGN classifications, with the general consensus being that the appearance of an AGN depends on its orientation, as well as its underlying properties (Urry & Padovani, 1995; Bianchi et al., 2012).

According to unification models, a galaxy's supermassive black hole is surrounded by a disc-like torus of dust and gas. This relatively flat structure forms due to the infalling matter's conservation of angular momentum, and converts the lost gravitational potential energy into radiation. Unless an AGN is viewed edge-on – so that the line of sight passes through the torus – the light reaching an observer will be dominated by the AGN rather than the wider galaxy – this is a Type I AGN. Where an AGN is obscured by the torus, the light an observer sees predominantly originates from the wider galaxy and the presence of the AGN can be inferred from its environmental effects – a Type II AGN.

The most basic elements of the unification model, which explain the major differences in the observed features of AGN, have largely been confirmed. For example, one particularly strong piece of observational evidence in the model's favour has been the discovery of broad optical lines in the polarized spectrum of NGC1068, an archetypal Seyfert II (Antonucci & Miller, 1985). However, in recent years new observations have led to suggestions that the model is something of a simplification. Several high luminosity AGN have now been found either changing from being type I to type II, or doing the reverse (e.g. LaMassa et al., 2015). The explanation for these observations is unclear, but it seems to require some deviation from the unification model – perhaps in the form of variable absorption due to dusty clouds in a clumpy torus, or variable rates of AGN accretion (Bianchi et al., 2012).

In the standard AGN unification model, whether one observes an AGN as being Type I or II depends purely on the geometrical arrangement in which it's observed, and the two are often grouped together as being 'radiative mode' (Heckman & Best, 2014). Radiative mode

AGN are bright, with luminosities of at least $\approx$ 1 per cent of their Eddington limit – the luminosity achievable when there is balance between outward radiative forces and inward gravitational forces. When the luminosity is much lower due to less efficient accretion, AGN are classed as being 'jet mode'.

The differing efficiencies of the accretion in radio and jet mode AGN is normally put down to the mechanism through which the central supermassive black hole acquires its gas.

Radiative mode AGN have an optically thick but geometrically thin accretion disc, which is bright across a broad range of wavelengths. Such discs are efficient at converting accreted mass into radiated energy (Blandford et al., 2019). On the other hand, jet mode AGN are thought to be fuelled by quasi spherical accretion, in which clouds of gas make their way to the supermassive black hole from the region surrounding the AGN (Narayan & Yi, 1994).

1.3.2 Models of supermassive black hole accretion and feedback

The accretion of gas onto a galaxy's central supermassive black hole is extremely powerful, and produces electromagnetic radiation at a range of wavelengths, as well as outflows of up to 10^{46} erg s^{-1}.

It has been suggested that accretion regulates a wide range of physical phenomena. The precise ways in which this might happen are still the subject of debate, but these ideas mainly stem from the positive correlations observed between the intracluster medium's X-ray luminosity and the jet power of the central AGN (e.g. Rafferty et al., 2006). This relationship suggests that rather than being radiated away, most of the jet power is deposited in the surrounding medium, where it is able to affect a wide range of processes such as star formation and further gas accretion (Bower et al., 2006; Croton et al., 2006; King & Pounds, 2015).

For simplicity, many models and simulations of supermassive black hole accretion assume they are fed through highly idealized Bondi accretion – the smooth and spherical inflow of very hot gas (Bondi, 1952) – or a similar process based upon a modified version of this principle (e.g. Proga & Begelman, 2003; Gaspari et al., 2011).

However, models which make use of Bondi accretion do so despite there being a lack of observational evidence indicating that behaviour of this kind is a reality. Instead, recent observations have shown that the central regions of AGN are dominated by the considerably colder atomic and molecular gas phases (e.g. Combes et al., 2013; García-Burillo et al., 2014).

Observations remain difficult however, and in their place a wide range of numerical simulations have been developed to understand the effects that AGN and the surrounding ISM have on each other, as well as their wider group and cluster. These generally point towards supermassive black hole accretion which, at sub-parsec scales, is chaotic, clumpy, and cold, with typical gas temperatures of a few tens of Kelvin, meaning that the accretion is predominantly of gas in the molecular phase (e.g. Pizzolato & Soker, 2005, 2010; Wagner et al., 2012; McNamara et al., 2016).

In this picture, the accretion and feedback processes in massive galaxies are linked, at least in part, by radio jets (Pizzolato & Soker, 2005; Gaspari et al., 2013; Gaspari et al., 2015, 2017). These jets are powered by the accretion, emanate from the central supermassive black hole, and inflate buoyant bubbles within the surrounding X-ray gas. In turn, these bubbles then migrate outwards from the galaxy centre (as can be seen in Centaurus-A in Fig. 1.1).

Turbulent motions driven by AGN outflow, jets and bubbles, together with the uplift of low entropy gas material, drive a top-down non-linear condensation of warm filaments and cold clouds. Behaviour like this is mostly expected close to the core, where the velocity dispersion of the molecular gas dominates over the rotational velocity.

The recurrent inelastic collisions between clouds promotes the cancellation of angular momentum and boosts the supermassive black hole accretion rate. This may then provide more fuel to power subsequent jet activity, and creates a self sustaining process.

Over several gigayears, periods of radio-mode AGN feedback are likely to be of further importance in clusters, with influences being felt on the star formation activity throughout the galaxy, the thermodynamics of the surrounding intracluster medium gas, and the evolution of the galaxies within the whole cluster (Churazov et al., 2001; Nulsen et al., 2005; McNamara & Nulsen, 2012).

1.3.3 AGN variability at radio wavelengths

Radiative and jet mode AGN can both be divided into two groups, depending on if they are 'radio loud' or 'radio quiet'. Whether or not a source is loud or quiet depends on its accretion rate, and over the long term there is a continual drift between the two phases because of the intermittent nature of the fuelling process (Tadhunter, 2008).

When in a radio loud phase, the accretion of significant amounts of mass allows the central supermassive black hole to inject energy into the galaxy via the acceleration of charged particles. Typically, this synchotron radiation is strongest at radio wavelengths and the regions from which it originates can be split into three main physical components: the radio core, radio jets, and radio lobes.

As the name suggests, the radio core is the central component, where emission is produced in close proximity to the supermassive black hole. Radio jets are then formed by the expulsion of highly energetic charged particles from the supermassive black hole, which propels radio plasma out to large distances in the galaxy and cluster. The outward propagation and growth of these jets then leads to the formation of the radio lobes.

The lobes are by far the largest of the three components, and are produced by interactions between the interstellar and intergalactic medium with particles from the jets. Due to their immense size, radio lobes do not vary significantly, and exist over long timescales (McNamara & Nulsen, 2012).

As previously alluded to, alternating periods of energy injection and cooling correlate with a radio core's loud and quiet phases, with the most notable evidence for this being seen in X-ray cavities inflated in the intracluster medium (McNamara et al., 2000; Hlavacek-Larrondo et al., 2012).

Again, a perfect illustration of this is Centaurus-A, shown in Fig. 1.1. The lobes formed by the action of its radio jets can clearly be seen in the orange LABOCA and APEX sub-millimeter data. The interactions of these radio lobes with the interstellar medium can also be inferred from the bubbles they inflate, visible in the blue X-ray image.

The radio variability of AGN is a product of many underlying physical processes which connect the host galaxy to its supermassive black hole. These include the rate and manner of

the black hole fuelling (King et al., 2008; Gaspari et al., 2013), spectral index changes due to interactions within the AGN, and evolving energy densities within radio jets (Blandford et al., 2019). Studying and quantifying variability can therefore inform us about these processes. For example, the variability of a source across several years can indicate the mechanisms through which it is fuelled. Likewise, because a source is unable to vary on timescales which are less than its light crossing time, short-term variability can be used as an indicator of its physical size.

In the long-term, the duration of a radio loud period is relatively short compared with the time frame on which the host galaxy forms and evolves, with estimates generally placing them at around 10^7 to 10^8 years (Parma et al., 2007; Bird et al., 2008). Nevertheless, they can be repeated thanks to further accretion onto the central supermassive black hole (Saikia & Jamrozy, 2009).

Although radio loud AGN are in the minority, their powerful cores, jets, and lobes make them much more enticing objects to study. Their bright central continuum sources are easier to observe, as are their interactions with the interstellar and intergalactic medium in which they lie. Like many others, this thesis focuses on radio loud sources due to the relative ease with which they and their interactions with their surroundings can be studied.

1.4 Cool gas in galaxies

The rate at which a region of gas cools is heavily dependent on its density. For a long while after the beginnings of X-ray and radio astronomy, this led to assumption that in a significant fraction of galaxy clusters (around a third to a half), there should be large amounts of cold gas (< 100 K) present a few billion years after galaxies began to form (McDonald et al., 2018). At first glance, this idea appears to have support from X-ray observations, which show significant amounts of gas cooling toward the centres of clusters (e.g. Peterson & Fabian, 2006).

After discovering such large amounts of energy being lost through radiation, the natural conclusion is that a ‘cool core’ would ultimately be produced – a roughly 100 kpc wide

region at the centre of the cluster to which the cooling gas migrates in a 'cooling flow' and becomes concentrated (Bauer et al., 2005).

Dividing the total intracluster medium mass by the gas's cooling time suggests that cool cores should typically grow at around $100 - 1000 M_{\odot}$ yr^{-1} (Hudson et al., 2010). Over billions of years, this would mean that almost all brightest cluster galaxies in relaxed clusters would find themselves at the centre of vast cooling flows and would have built up massive cool cores (Fabian, 1994).

These predictions have been tested over the last two decades with surveys of the cool gas within clusters at a range of wavelengths e.g. optical lines (Crawford et al., 1999; Tremblay et al., 2018), near infra-red to infra-red (Jaffe et al., 2001; Edge et al., 2002; Egami et al., 2006), atomic cooling lines (Edge et al., 2010) and with H_2 observations (Jaffe et al., 2005; Donahue et al., 2011). These results show significant amounts of cold, < 40 K gas within the majority of relaxed galaxy clusters, with typical column densities of $10^{21} - 10^{23}$ cm^{-2} in the central 3 - 10 kpc of the brightest cluster galaxies (Edge, 2001; Salomé & Combes, 2003).

However, as significant as these masses may be, cooling flows and cool cores failed to materialise to the extent expected (Crawford et al., 1999; Edge, 2001; McDonald et al., 2013).

The reason for this is the AGN, whose powerful outflows transport energy out to large distances in the cluster and influence their environment by preventing runaway gas cooling (Remillard & McClintock, 2006). This ultimately limits the formation of cold gas at the centres of galaxy clusters, and curtails star formation (Salomé & Combes, 2003; Rafferty et al., 2008).

The radio loud and quiet phases AGN pass through are associated with periods of gas heating and cooling, and the two have apparently existed in a fine balance since the earliest times of cluster formation (Pratt et al., 2010; McDonald et al., 2018). As a result, the energy injected into clusters typically offsets any radiative gas cooling and leads to much less dramatic changes in molecular gas content than X-ray cooling lines might suggest. However, though this is true over long time intervals, shorter periods of heating and cooling still occur as AGN cycle through their loud and quiet phases.

1.4.1 HI in massive galaxies

Hydrogen is the most abundant element in the Universe, and in its neutral form (written as H I) significant quantities are found in nearly half of elliptical galaxies, and it is even more ubiquitous in spirals (Serra et al., 2012). H I can be thought of as a temperate phase of hydrogen – hotter than its molecular form, but cooler than its ionized form – and it traces gas at temperatures of around 100 K.

H I is extremely useful because of its 21-centimeter line, which is produced and absorbed by a flipping of the spin state in the atom's sole electron. The resulting energy change is small, which gives the line its long wavelength. Surveys of this line have been ongoing for decades, and large numbers of H I emitting galaxies have been found (e.g. Serra et al., 2012; Haynes et al., 1998, see Fig. 1.2 for an example).

In radio loud galaxies, H I can also be detected in absorption against the bright and compact radio continuum source coincident with the AGN. One example is shown in Fig. 1.3, but many more have been discovered, particularly in recent years (e.g. Jaffe, 1990; Morganti et al., 2009; Geréb et al., 2015; Allison et al., 2020).

Using H I absorption to study the cool gas in galaxy clusters has two significant advantages. Firstly, the strength of the absorption is dependent on the brightness of the background continuum source, which allows for lower column densities and higher redshifts to be studied than is possible with emission lines. This compactness of the background continuum source also means H I absorption only reveals the properties of the gas along a very narrow line of sight, so much smaller regions of gas can be studied than is possible with emission.

Secondly, H I studies can be particularly useful when they use a galaxy's own radio core as the backlight against which absorption is observed, rather than a background quasar which happens to lie along the same line of sight as the absorbing gas. In these cases, the AGN must always lie behind the H I gas, and so the redshift (or blueshift) of the line is determined by the speed at which the gas is moving towards (or away) from the galaxy's core.

H I absorption line systems have been known of for decades, with gas velocities ranging

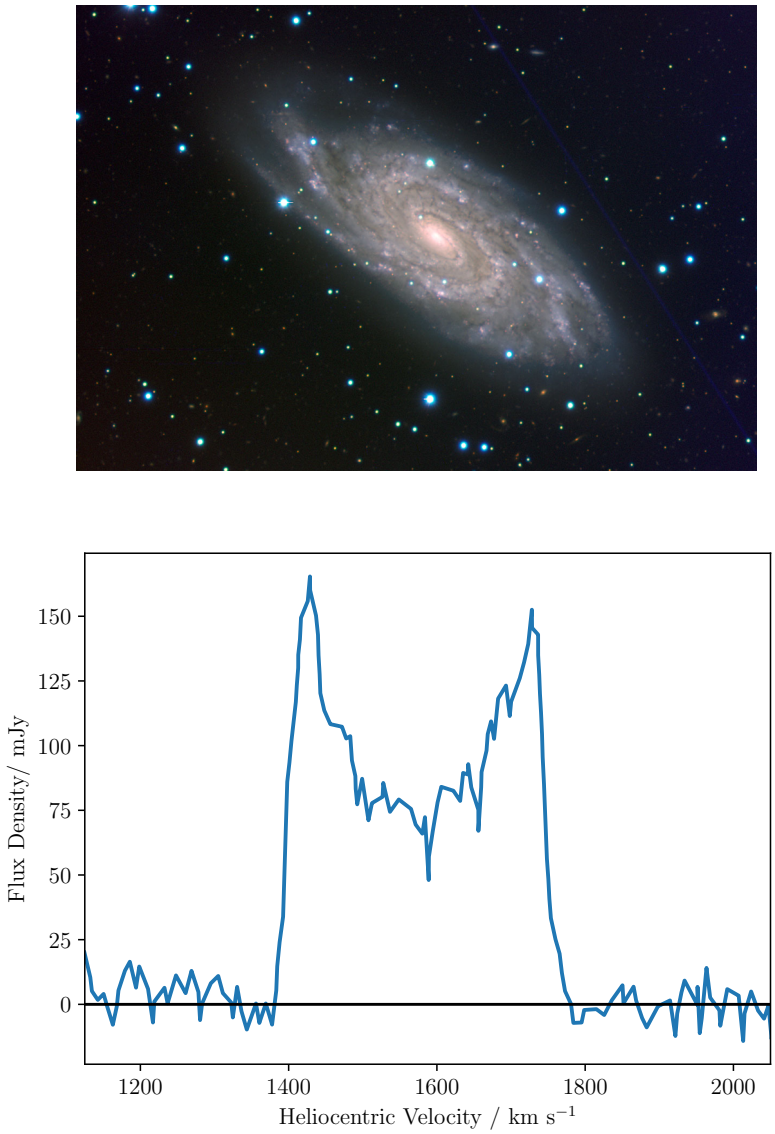

Figure 1.2

Top: A colour composite of the nearby (z = 0.005247) spiral galaxy NGC 6118 made with the multi-mode VIMOS instrument on ESO's Very Large Telescope (`https://www.eso.org/public/images/eso0436a/`). **Bottom**: The H I emission line seen in NGC 6118 (first published by Haynes et al., 1998). The shape of an emission line profile reveals the kinematic make up of the gas which produced it. In this case, the double-horn is characteristic of emission lines in galaxies with well ordered rotation and results from crowding at certain radial velocities. Profiles with single peaks are seen when the galaxy is viewed face-on, or when random motions are comparable or dominant over the rotation.

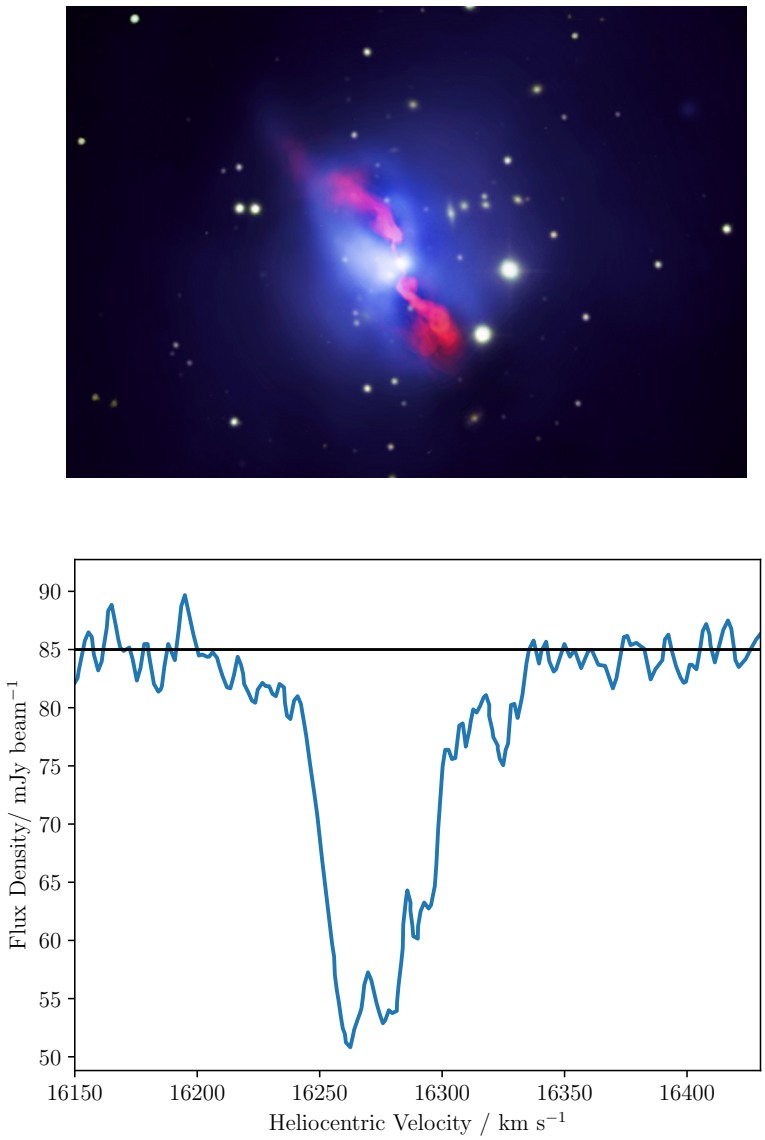

Figure 1.3

Top: A composite image of the Hydra-A brightest cluster galaxy, with X-ray observations from Chandra in blue, and radio emission from the Very Large Array in red. The optical data in yellow is from the Canada-France-Hawaii telescope. (`https://chandra.harvard.edu/photo/2009/hydra/`). **Bottom**: The H I absorption line seen against the radio continuum source at the centre of the galaxy (first published by Taylor, 1996).

from hundreds of km s^{-1} towards the galaxy's core, to hundreds of km s^{-1} away from it (van Gorkom et al., 1989; Morganti et al., 2003, 2009).

An obvious question to ask is whether the H I gas seen in this way tends to be redshifted or blueshifted. Are clouds of atomic hydrogen generally falling towards the core of their host galaxy, or moving away from it? The first case may imply a significant contribution to the AGN fueling and the nuclear activity (van Gorkom et al., 1989), while the second could reveal the properties of expanding radio jets which drive gas outflows (Oosterloo et al., 2000).

However, it's only relatively recently that systems like these have been studied in large numbers e.g. Geréb et al. (2015), where H I absorption in 32 sources was found by observing 101 flux-selected radio AGN (blind searches, which don't hunt out the brightest AGN still struggle to find large numbers of absorbers e.g. Allison et al., 2020). The absorption profiles have a wide range in widths and velocities relative to the associated AGN, though there is no significant bias for motion in either direction (Geréb et al., 2015).

1.4.2 Molecular gas in massive galaxies

Towards the centres of galaxies, where densities are relatively high, H I regions cool efficiently and slowly transform into molecular gas (i.e. H_2). This gas often takes the form of a disc, along with the galaxy's stars and dust.

Although molecular discs and their cooling flows are often thought of as a fuel source for the galaxy's nuclear activity, such a well ordered, rotating disc is far from a universal feature in galaxies with active radio cores (Combes et al., 2013).

In other galaxies, huge outflows of molecular gas are driven by the expansion of radio jets and produce a more disrupted distribution of gas (e.g. Herrera-Camus et al., 2020; Oosterloo et al., 2017). This suggests that a well ordered disc of molecular gas is not the only means through which powerful AGN accrete from their surroundings and subsequently dissipate energy into their host galaxy.

Fig. 1.4 shows one example of the emission lines produced by the molecular gas in the

nearby massive galaxy Hydra-A. The double-peaked structure is similar to the H I emission line shown in Fig. 1.2, and is indicative of a well-ordered, rotating disc.

Although this emission line is able to detect the macroscopic distribution of the molecular gas in the galaxy, the maximum angular scales on which it can be mapped is limited – even with a large radio interferometer – because the emission lines are relatively weak. In particular, as more and more distant galaxies are observed, mapping their molecular gas structure becomes more and more difficult.

Nevertheless, observing gas in the cold molecular phase is still essential if we are to understand the mechanisms of AGN accretion and feedback (recent examples include García-Burillo et al., 2014; Temi et al., 2018a; Ruffa et al., 2019; Olivares et al., 2019). However, since the emission lines of individual molecular clouds are relatively weak, studying the molecular gas in this way can only be used to reveal the behaviour of large ensembles of clouds.

In recent years, several studies have been able to observe molecular gas through absorption, rather than emission. This requires an extremely bright an compact continuum source, so early detections were of molecular gas in galaxies which happened to lie in front of a background quasar (e.g. Wiklind & Combes, 1996b; Muller & Guelin, 2008).

More recently however, ALMA has made it possible to detect a galaxy's molecular gas clouds using its own central continuum source as the backlight for absorption. As molecular clouds pass in front of the radio core, they cast shadows, which acts as signatures of the clouds' properties and make it possible to study them, often individually (see David et al., 2014; Tremblay et al., 2016).

The clouds detected by David et al. (2014) and Tremblay et al. (2016) give a random snapshot of the molecular gas in the galaxy. The molecular gas regions detected have dynamics consistent with their warmer H I clouds and their narrow absorption lines (FWHM~6-30 km s^{-1}) indicate that they may potentially be giant molecular clouds, rather than giant molecular associations, which are falling towards their respective galaxy's supermassive black hole with velocities of between 240 and 335 km s^{-1}.

However, a larger sample of absorbing clouds is needed to constrain their overall properties, and this provides the motivation for Chapters 3, 5, and 4 of this thesis.

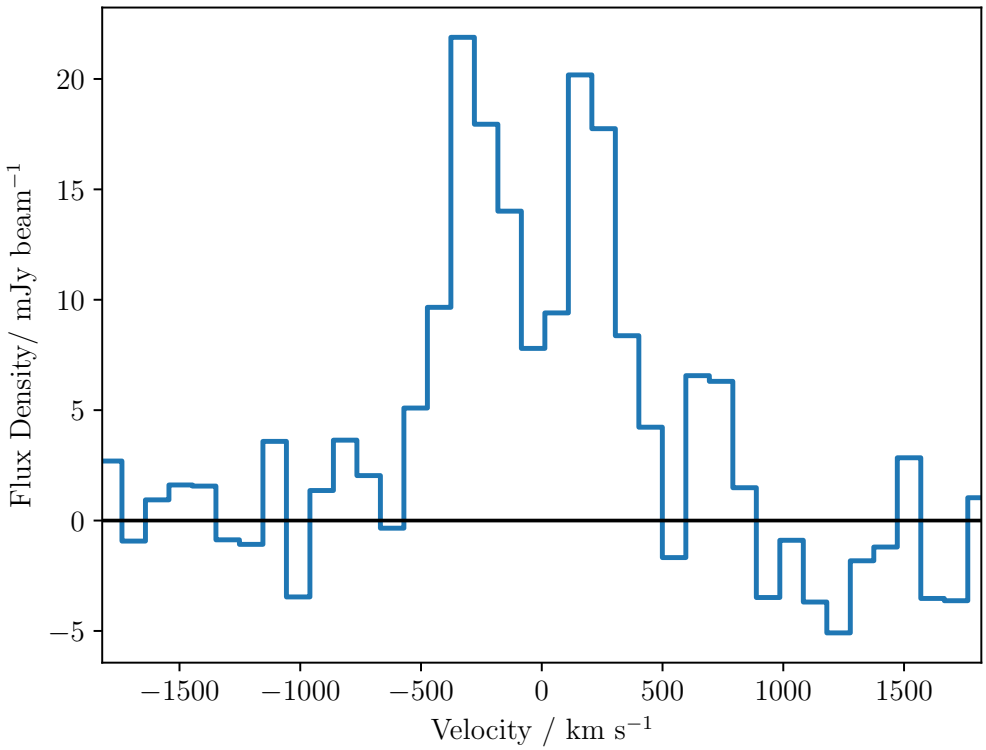

Figure 1.4

The spectrum of CO(2-1) emission seen across the edge on disc of Hydra-A, which traces the galaxy's molecular gas. This data was obtained by the IRAM 30m single dish telescope, and was originally presented in (Hamer et al., 2014).

1.5 Thesis Overview

This rest of thesis aims to reveal the properties of molecular clouds in the cores of the Universe's most massive galaxies, and link these properties to the variability of their core radio sources. It is organised into the following chapters:

- **Chapter 2 – The variability of brightest cluster galaxies at high radio frequencies**

  The core radio sources of massive galaxies frequently change in brightness, a process dependent on the accretion and feedback mechanisms of their black holes. Chapter 2 studies this variability and its importance to other areas of astronomy.

- **Chapter 3 – Molecular absorption in the Hydra-A brightest cluster galaxy**

  An exploration of the properties of Hydra-A's edge-on molecular gas disk. This includes an introduction to the molecular absorption lines visible against the galaxy's bright and compact active galactic nucleus.

- **Chapter 5 – A more in depth look at the molecular absorption lines in Hydra-A**

  This is an extension to the previous chapter, with significantly more molecular species studied. The first evidence of variability in absorption lines observed against a galaxy's own radio core is also presented.

- **Chapter 6 – CO and CN absorption in the cores of eight brightest cluster galaxies**

  This chapter extends the molecular absorption line observations to a larger sample of 18 brightest cluster galaxies. This allows the general properties of the molecular clouds detected by these surveys to be studied.

- **Chapter 7 – Summary and future work**

CHAPTER 2

The variability of brightest cluster galaxies at high radio frequencies

---

This chapter is based on the following paper, which is currently under peer review:

The variability of brightest cluster galaxies at high radio frequencies · Tom Rose, Alastair Edge, Sebastian Kiehlmann, Junhyun Baek, Aeree Chung, Tae-Hyun Jung, Jae-Woo Kim, Anthony C. S. Readhead, and Aidan Sedgewick

2.1 Introduction

The accretion of matter onto an active galactic nucleus (AGN) is associated with compact radio emission from partially self-absorbed synchrotron jets (Remillard & McClintock, 2006). These powerful outflows transport energy out to large distances, where they heavily influence their environment by preventing runaway gas cooling, reducing the cold gas content at the centres of galaxy clusters, and curtailing star formation (Edge, 2001; Salomé & Combes, 2003; Rafferty et al., 2008).

The radio loud and quiet phases of AGN discussed in Chapter 1 are associated with periods of gas heating and cooling, and the two seem to have existed in a fine balance since the earliest times of cluster formation (Pratt et al., 2010; McDonald et al., 2018). As a result, the energy injected into clusters typically offsets any radiative gas cooling. However, though this is true over long time intervals, shorter periods of heating and cooling still occur as AGN pass through their loud and quiet phases.

The radio variability of AGN is a product of a wide range of physical processes which connect the host galaxy to its supermassive black hole (for a review see Hardcastle & Croston, 2020). Among them are the rate and manner in which the black hole us fueled (King & Pringle, 2007; Gaspari et al., 2013), spectral index changes due to interactions within the AGN, and the evolving energy densities found within radio jets (Blandford et al., 2019). By studying and quantifying variability, it's possible to learn about these underlying processes. For example, the timescale on which a source typically varies can indicate the mechanisms through which it is fuelled. Similarly, since a source is unable to vary on timescales less than its light crossing time, the variability on short timescales can be used as an indicator of its physical size.

Despite the importance of radio observations to the study of fuelling and feedback cycles in galaxy clusters, it is not well known how much change the AGN at the centre of the process experience within their radio loud phases. This is particularly true at higher radio frequencies of around 10 - 100 GHz, where there has been a deficit of research.

This chapter presents results from an ongoing 15 GHz survey of 20 X-ray selected brightest cluster galaxies, whose variability is examined on week to decade long timescales. This

work is a continuation of (Hogan et al., 2015a), and includes the addition of several more BCGs. All the monitored sources contain an active core, reside in cool-core clusters, and have a significant radio core component in their spectral energy distributions (SEDs). These properties suggest strong, ongoing feedback, and allow us to detect variability with short observations. The main purpose of this work is to study the amplitude and timescales of variability in the radio cores of these sources, which are dependent upon the short timescale accretion processes of the AGN. This chapter also shows how this variability relates to the sources' spectral properties at radio frequencies of up to 353 GHz.

The paper is laid out as follows. Section 2.2 presents the target sample and give details of the their selection and observations. Section 2.3 shows the lightcurves of the targets and corresponding spectral indices. Section 2.4 discusses the variability detection and quantification parameters, before they are applied to the lightcurves in Section 2.5. Section 2.6 discusses the results and conclusions are presented in Section 2.7.

2.2 Sample and Observations

The brightest, core-dominated radio sources in this study are drawn from the sample presented in Hogan et al. (2015b) and Hogan et al. (2015a). They are hosted by BCGs in X-ray selected clusters from the *ROSAT* All-Sky Survey in the BCS (Ebeling et al., 1998), eBCS (Ebeling et al., 2000), and REFLEX (Böhringer et al., 2004) samples. The uniform X-ray flux limit from the full high Galactic latitude sky ($|b| > 20°$) ensures a representative sampling of host clusters irrespective of the radio properties of the BCG. Only when the BCG hosts a strong BL Lac (objects with strongly variable optical and radio continuum emission, and erratically varying polarization Vermeulen et al., 1995) nucleus that contributes to the total X-ray flux of the cluster does the selection favour a system with a bright radio source (see Green et al., 2017, for a full discussion of this).

From the full *ROSAT* sample of 726 clusters, we selected systems in which the BCG hosted a radio source brighter than 50 mJy (at the time of selection) at 15 GHz and were either known to be core-dominated (Hogan, 2014a) or had a radio SED consistent with a Giga-Hertz peaked spectrum (GPS).

In addition, we added two clusters missed in the original BCS selection because they fell below the X-ray flux limit, RXCJ1350.3+0940 (z = 0.13) and RXCJ1603.5+1554 (z = 0.109). These were mis-identified as being AGN-dominated due to their BCG containing a strong, flat-spectrum radio source. Four clusters with a powerful radio source in their BCG were also added: 4C+55.16 (Iwasawa et al., 1999), A2270 (Green et al., 2016), RGB1745+398/RXCJ1745.6+3951 (Green et al., 2017) and RXCJ2341.1+0018 (Green et al., 2016). This selection completes the 20 sources included in the OVRO BCG monitoring program.

Building on the high frequency monitoring in Hogan et al. (2015a), the size of the sample was increased with regular OVRO monitoring. We also carried out multi-visit observations with the Korean VLBI Network (KVN), IRAM-30m NIKA2, ALMA, and JCMT SCUBA-2 over the period 2015 to 2021. The aim of these observations was to determine the spectral variability of this sample in the 15 to 353 GHz range (a full description of the origins of each of these data sets can be found in the following subsections). Additional higher frequency data were obtained for a further 13 BCGs below the OVRO declination limit of -20°, or which were too faint at 15 GHz. These results are presented in an appendix for completeness (Tables A1 and A3).

2.2.1 OVRO

The Owens Valley Radio Observatory (OVRO), based in California, has carried out a 15 GHz monitoring campaign of more than 1500 radio sources since 2007 using its 40m Telescope. Most of its targets are blazar Fermi-LAT gamma-ray candidates, the full sample of which can be seen in Richards et al. (2011). Table 2.1 lists the subsample of 20 BCGs from this survey whose variability is analysed in this paper, and gives the main details of the observations.

Of this sample of 20 BCGs, five have been included in the OVRO campaign (PI: Anthony Readhead) from its beginning. In January 2013, 11 more were added, followed by several others at various times since. Observations of the entire OVRO sample (including the 20 BCGs this chapter focuses on) were carried out each week, so the median time interval

between observations is 7 days. The mean time interval is slightly higher at 10 days due to occasional poor weather, telescope maintenance, and other observing issues. Nevertheless, this high temporal sampling allows the variability to be evaluated on timescales of weeks to several years.

The OVRO 40m Telescope uses off-axis dual-beam optics and a cryogenic receiver with 2 GHz equivalent noise bandwidth centered at 15 GHz. The observations are conducted in an ON-ON fashion so that one of the beams is always pointed on the source. This double switching technique is used to remove gain fluctuations as well as atmospheric and ground contributions (Readhead et al., 1989).

The two beams were rapidly alternated using a Dicke switch until May 2014. In May 2014 a new pseudo-correlation receiver replaced the old receiver and a 180 degree phase switch has been used since. The change of the receiver resulted in a significant reduction in the observational noise that is reflected in the light curve uncertainty estimates.

Relative calibration is obtained with a temperature-stable noise diode to compensate for gain drifts. The primary flux density calibrator is 3C 286 with an assumed value of 3.44 Jy (Baars et al., 1977), DR21 is used as secondary calibrator source. Details of the observation and data reduction schemes are given in Richards et al. (2011).

Table 2.1

The brightest cluster galaxies monitored by the OVRO 40m Telescope and the main details of the observations. The data below are for the lightcurves after they have been masked according to the criteria given in §2.3.1 and have had their extended emission subtracted according to the process described in §2.3.3. Table continues on next page.

Header clarifications: 'Obs. / day' is the total number of observations divided by the time range over which they were taken, and the 'Detectable variability' is defined as the mean flux density error divided by the mean flux.

Source	RA	Dec	Redshift	Start date MJD (ISO)	Timespan / yrs	Obs. / day	Mean 15 GHz flux density / mJy	Detectable variability / %
3C286 - Calibrator	13:31:08.400	30:30:33.120	0.8493	54474 (2008-01-09)	12.0	0.43	3437	1.2
DR21 - Calibrator	20:39:01.200	42:19:32.880	0.0	54474 (2008-01-09)	12.0	0.46	19061	1.0
RXJ0132.6-0804	01:32:41.112	-8:04:05.880	0.1489	56352 (2013-03-01)	7.7	0.09	102	4.6
J0439+0520	04:39:02.256	05:20:43.080	0.208	54474 (2008-01-09)	12.9	0.12	318	3.7
A646	08:22:09.600	47:05:52.800	0.1268	56323 (2013-01-31)	7.9	0.1	59	6.9
4C55.16	08:34:54.960	55:34:22.080	0.2411	56342 (2013-02-19)	7.8	0.11	519	4.2
A1348	11:41:24.240	-12:16:37.560	0.1195	56336 (2013-02-13)	7.8	0.08	45	9.5
3C264/NGC3862	11:45:05.016	19:36:22.680	0.0217	58432 (2018-11-10)	2.1	0.14	125	8.4
A1644	12:57:11.592	-17:24:34.200	0.0475	58449 (2018-11-27)	2.0	0.05	195	1.9
J1350+0940	13:50:22.080	09:40:09.840	0.13	54476 (2008-01-11)	12.9	0.1	131	7.5
J1459-1810/S780	14:59:28.800	-18:10:45.120	0.2357	54910 (2009-03-20)	11.5	0.08	134	6.9

Source	RA	Dec	Redshift	Start date MJD (ISO)	Timespan / yrs	Obs. / day	Mean 15 GHz flux density / mJy	Detectable variability / %
A2052	15:16:44.640	07:01:18.120	0.0351	56319 (2013-01-27)	7.9	0.1	99	6.1
A2055	15:18:46.560	06:13:58.080	0.1019	56319 (2013-01-27)	7.9	0.1	36	15.4
J1558-1409	15:58:21.840	-14:09:59.040	0.097	54477 (2008-01-12)	12.9	0.09	150	7.7
J1603+1554	16:03:38.160	15:54:02.160	0.109	54696 (2008-08-18)	12.3	0.12	233	4.2
J1727+5510/A2270	17:27:23.520	55:10:53.040	0.24747	54476 (2008-01-11)	12.9	0.11	234	4.2
Z8276	17:44:14.400	32:59:29.400	0.075	56326 (2013-02-03)	7.8	0.09	76	6.1
J1745+398	17:45:37.752	39:51:20.880	0.267	58428 (2018-11-06)	2.0	0.08	39	6.6
A2390	21:53:36.720	17:41:44.880	0.228	56340 (2013-02-17)	7.8	0.13	49	9.1
A2415	22:05:38.640	-5:35:33.720	0.0573	56327 (2013-02-04)	7.8	0.1	134	2.9
A2627	23:36:42.720	23:55:23.880	0.127	56348 (2013-02-25)	7.8	0.12	41	10.9
RXJ2341.1+0018	23:41:06.960	00:18:33.480	0.2768	56328 (2013-02-05)	7.8	0.11	98	4.6

2.2.2 NIKA2

Following on from the success of the IRAM-30m GISMO observations presented in Hogan et al. (2015a), we (PI: Alastair Edge, data reduced by Alastair Edge) obtained data with the NIKA2 bolometer camera on the IRAM-30m that covers both 2 and 1.2mm bands simultaneously (Perotto et al., 2020). These observations were over two pooled campaigns in 2019 and 2020 and maps were made with the resulting data to optimise for faint, unresolved sources.

The flux density measurements obtained with NIKA2 are given in Table A1. For each NIKA2 measurement, the table also provides the nearest OVRO flux, and the spectral indices calculated with these measurements.

2.2.3 KVN

As an additional constraint on the flux density of the core component of these sources we also obtained KVN observations at 22 and 43 GHz over 5 semesters in 2018 to 2020 (PI: Jae-Woo Kim, data reduced by JunHyun Baek). The three telescope interferometry provided by the KVN delivers an angular resolution of 6 mas at 22 GHz and 3 mas at 43 GHz. Therefore the compact core component that will dominate any variability is preferentially detected and the more extended, non-variable emission is resolved out. The data were calibrated using `AIPS` following a standard reduction procedure, and imaged using `DIFMAP`. In order to push the detection limit down to 50 mJy or less, we applied source phase referencing and/or frequency phase transfer techniques at both bands (Rioja & Dodson, 2011; Algaba et al., 2015). The target sources are mostly unresolved or slightly resolved within the KVN synthesized beam, hence the peak flux density is used in further analysis.

The flux density measurements obtained with KVN are given in Table A2. The table also provides the spectral indices calculated with these measurements.

2.2.4 JCMT SCUBA2

JCMT SCUBA2 353 GHz photometry for all 20 OVRO targets and 7 southern or fainter sources was obtained over five semesters in 2019 to 2021 (PI: Alastair Edge, data reduced by Alastair Edge). The data were reduced using the standard SMURF reduction package and the observatory derived calibrations. All the previous observations for the objects were reduced in the same way, so the photometry now supersedes that in Hogan et al. (2015a) and Cheale et al. (2019).

The flux density measurements obtained with SCUBA2 are given in Table A3. For each measurement, the table also provides the nearest OVRO flux, and the spectral indices calculated with these measurements.

2.2.5 ALMA

For seven of the OVRO targets we have single epoch observations with ALMA at either CO(1-0) or CO(2-1) in the rest frame of the target from the absorption line survey of Chapter 5 (PI: Alastair Edge, data reduced by Tom Rose), or observations of extended molecular emission published by Russell et al. (2019). These mm observations can be compared to the other high frequency data and are listed in Appendix A.5.

2.3 Lightcurves

15 GHz lightcurves of the 20 BCGs, obtained with the OVRO 40m Telescope, are shown in Figs. 2.1, 2.2, 2.3, and 2.4. These have been masked according to the procedure outlined in §2.3.1 and had their extended emission subtracted as described in §2.3.3. We also include the KVN 22 GHz flux densities for comparison.

Spectral indices are shown below the lightcurves, calculated with (i) contemporaneous 22 and 43 GHz KVN observations, (ii) 15 GHz OVRO and 150 GHz SCUBA2 observations, (iii) 15 GHz OVRO and 353 GHz NIKA2 observations, and (iv) 15 GHz OVRO and $\approx$ 100 GHz ALMA observations. These pairs of observations are separated by less than

10 days in the majority of cases – a time interval significantly shorter than that in which variability is seen in all of the sources (as is shown later in Section 2.5).

Increases in a source's spectral index have been linked to outbursts due to the high frequency emission that results from accretion events. Conversely, a fading source's spectral index typically decreases (i.e. it becomes more negative and steeper due to a decrease in emission at higher frequencies). However, this relationship generally quite weak, and only becomes apparent with a long period of observations (e.g. NGC1275, which has more than 50 years worth of observations at high radio frequencies Dutson et al., 2014).

2.3.1 Masking

The OVRO lightcurves contain a small but significant number of spurious data points. These either have errors significantly larger than their neighbours, or are implausible measurements. To prevent this affecting the analysis, any observation, i, with flux density, F_i, and error, σ_i, which meets one or both of the following conditions is masked:

$$\sigma_i > 3\bar{\sigma} \tag{2.3.1}$$

$$\left| F_i - \frac{F_{i-2} + F_{i-1} + F_{i+1} + F_{i+2}}{4} \right| > 3\bar{\sigma} \tag{2.3.2}$$

The first condition removes measurements with particularly large errors, while the second removes those which are significantly different to their neighbours. Re-inspection of the masked lightcurves, which are shown in Figs. 2.1, 2.2, 2.3, and 2.4, shows a large reduction in the number of spurious measurements. More conservative masking is not applied to prevent the removal of good data.

It could be argued that the second criterion might falsely mask any short term-variability. However, since a source cannot vary on a timescale less than its light crossing time, and because the median separation of the data points is 7 days (much less than the expected light crossing time), this should not be an issue.

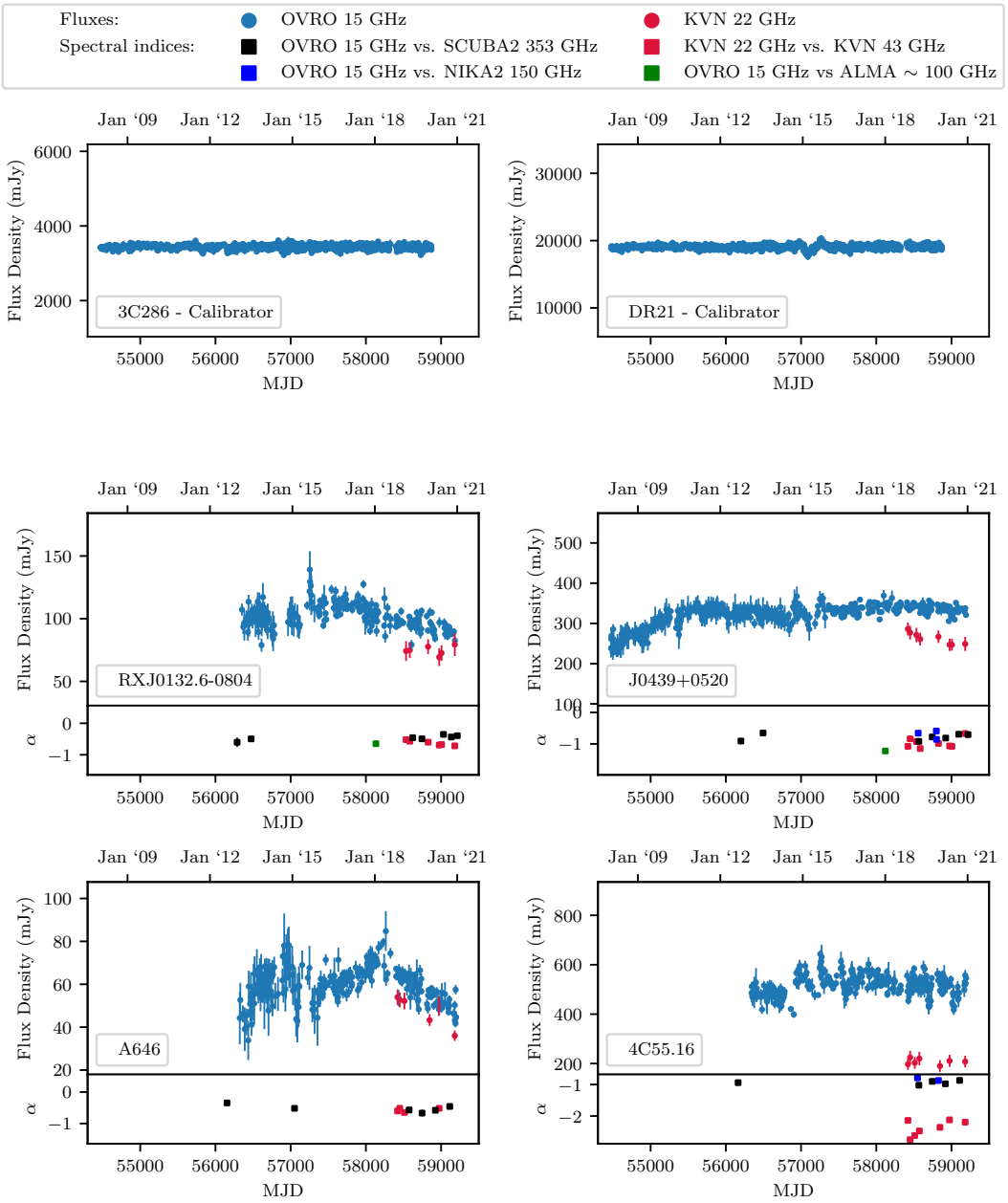

Figure 2.1

15 GHz lightcurves (blue points) of the sample of cool-core BCGs obtained with the OVRO 40m telescope. The data have been masked according to the procedure given in §2.3.1 and extended emission has been removed from several sources as described in §2.3.3. The Y-axes are scaled to each lightcurve's mean flux density to allow for easier comparison of the relative strength of the variability. The plots also include 22 GHz KVN flux densities (red points), and spectral indices calculated over the course of the observations. Continued in Figs. 2.2, 2.3 and 2.4.

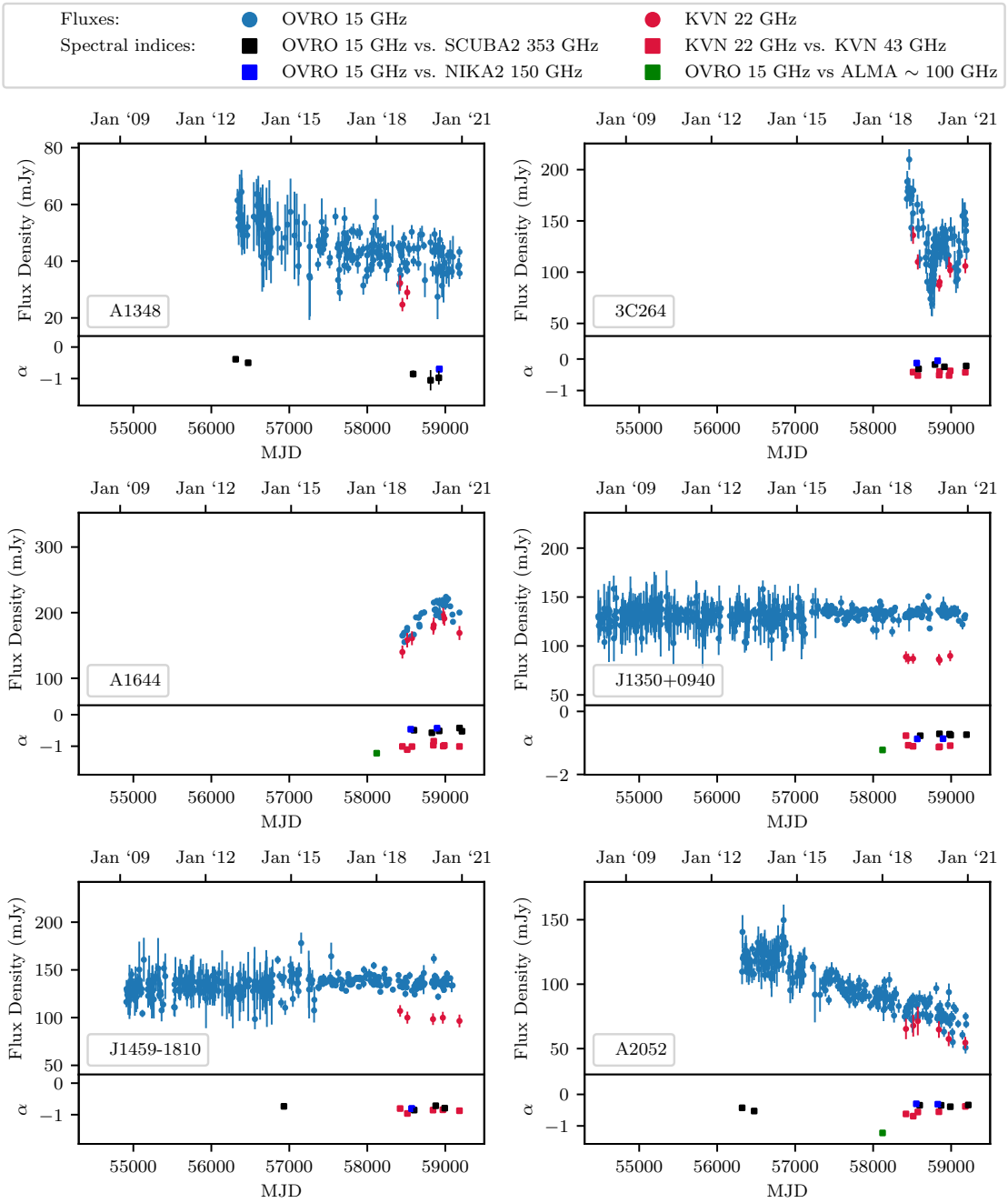

Figure 2.2

Continued from Fig. 2.1. Continued in Figs. 2.3 and 2.4.

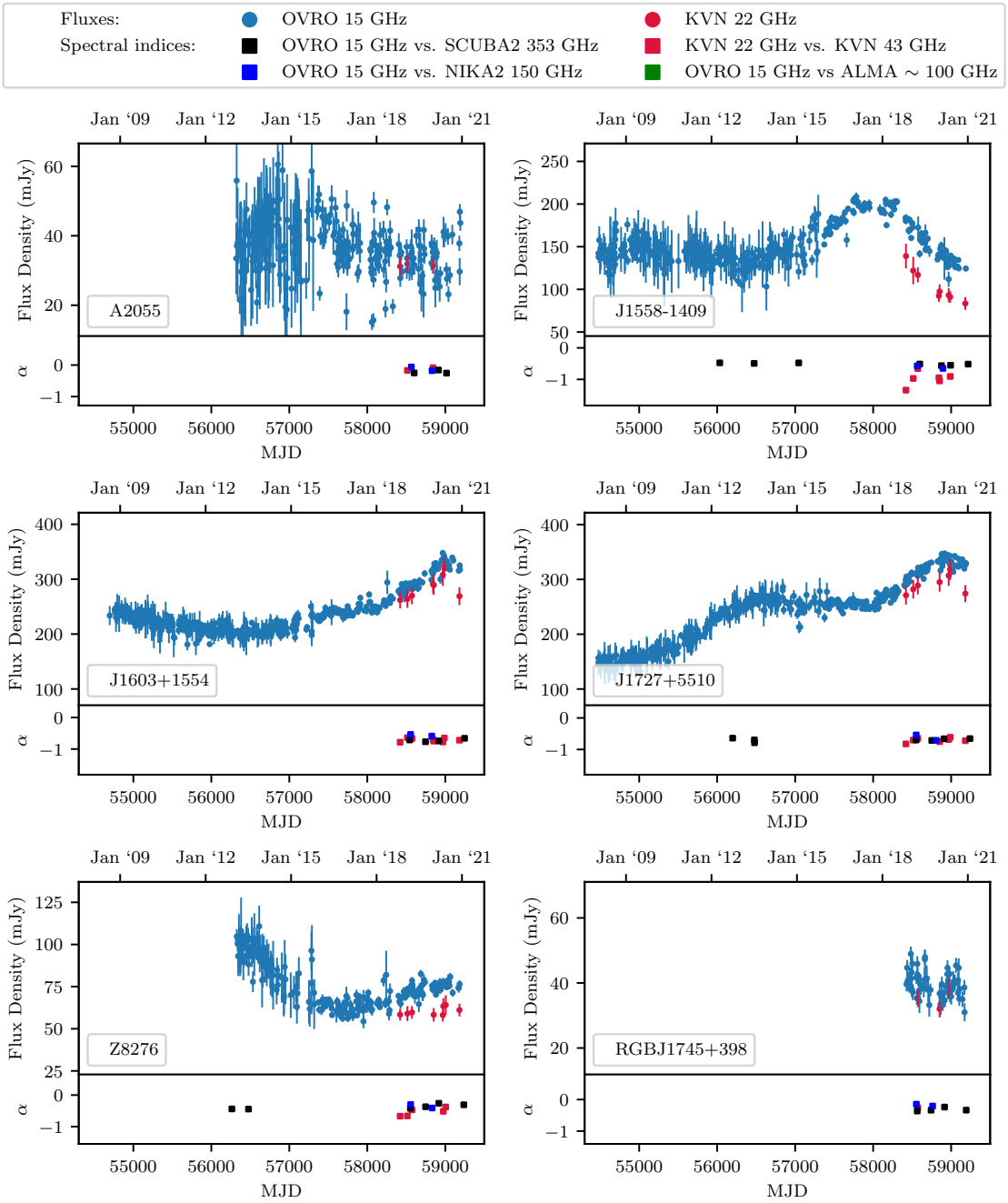

Figure 2.3

Continued from Fig. 2.1 and 2.2. Continued in Fig. 2.4.

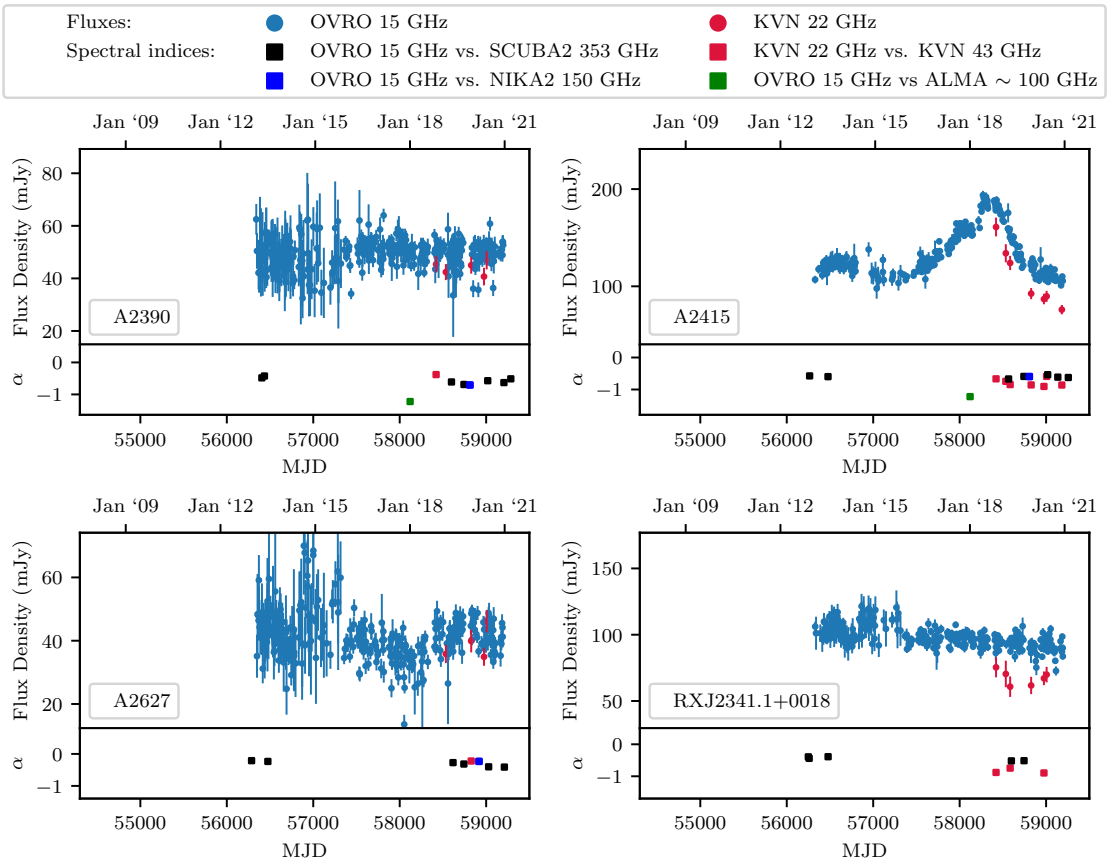

Figure 2.4

Continued from Fig. 2.1, 2.2, and 2.3.

2.3.2 2014 blip in lightcurves

A spurious dimming and brightening appears in some of the lightcurves in 2014/15, most notably in the calibrator source DR21. This is visible in Fig. 2.1, and a similar feature can also be seen in J0439+0520. This effect coincides with the installation of a new receiver on the OVRO 40m telescope in May 2014.

The effect is not so apparent in any of the other sources, and is generally within the 5 per cent absolute calibration uncertainty. Nevertheless, to assess its impact, the variability detection parameters were applied to all the lightcurves with and without this period (mjd 56750 to 57400) being masked. In all cases the difference in the statistics is less than the rounding error, except for the calibrator source DR21. Therefore, in the following analysis this region is masked for DR21, but is left unmasked for all other sources.

2.3.3 Correction for extended emission

The OVRO 40m Telescope with which the 15 GHz lightcurves were obtained is a single dish instrument, so its measurements are of low angular resolution. As a result, the flux densities may incorporate both the radio core and more extended radio lobe components. In cases where the radio lobes - which do not vary on human timescales - are particularly strong, they can dilute the apparent variability of the radio core.

Between around the end of 2018 and the end of 2020, each source was observed by KVN at 22 and 43 GHz. KVN is a very long baseline array, and is able to resolve out the extended emission.

We use these higher resolution observations to correct for the extended emission in many of the OVRO 15 GHz flux densities. To do this, the mean 22 and 43 GHz flux densities are used to estimate the spectral index over the observed period. This spectral index is then used to predict the 15 GHz flux density. Table 2.2 gives the 15 GHz flux densities predicted by KVN, and the values obtained over the same period by OVRO. The table also includes the difference between the two and the implied fraction of the emission which is extended.

In many cases the predicted 15 GHz flux density is significantly lower than that found by OVRO, due to the extended emission. Since we are only interested in the variability of the core component, this difference is subtracted from every point on the 15 GHz OVRO lightcurves, though this is only done for sources where the implied extended emission is more than 25 per cent of the total flux density measured by OVRO. This strikes a balance between removing significant amounts of extended emission, and over-correcting in cases with a non-uniform spectral index over the 15 to 43 GHz range. The correction applied to each lightcurve can be found in Table 2.2.

Table 2.2

The 15 GHz flux densities predicted by 22 and 43 GHz KVN observations between the end of 2018 and the end of 2020, the mean value obtained with the single dish OVRO 40m telescope over the same period, and the resulting correction which has been applied to the spectra in Figs. 2.1, 2.2, 2.3, and 2.4.

Source	15 GHz flux density predicted by KVN / mJy	15 GHz OVRO flux density / mJy	Difference / mJy	Implied extended emission / %	Correction Applied / mJy
RXJ0132.6-0804	95	150	55	36	55
J0439+0520	381	337	-44	-13	0
A646	57	57	0	0	0
4C55.16	514	1572	1058	67	1058
A1348	–	41	–	–	0
3C264	125	731	606	82	606
A1644	250	197	-53	-26	0
J1350+0940	130	134	4	2	0
J1459-1810	140	136	-4	-2	0
A2052	78	232	154	66	154
A2055	33	115	82	71	82
J1558-1409	148	207	59	28	59
J1603+1554	373	304	-69	-22	0
J1727+5510	381	322	-59	-18	0
Z8276	73	74	1	1	0
RGBJ1745+398	39	125	86	68	86
A2390	50	89	39	44	39
A2415	146	134	-12	-8	0
A2627	42	99	57	57	57
RXJ2341.1+0018	93	147	54	36	54

2.4 Variability Detection and Quantification Parameters

To characterize the variability in the 15 GHz lightcurves, a range of numerical parameters is used. Each has advantages and disadvantages, and several are required to give a reliable impression of a source's variability. A combination of four is therefore used to analyse the variability of the observed sources. Each of them is described in the following subsections. Many other methods for quantifying variability in photometric time series data exist, though they are often less effective when applied to AGN versus other astronomical objects, such as variable stars, due to differing relative rates and strengths of variability. Similarly, they may also require many hundreds or thousands of observations to act as robust parameters (Sokolovsky et al., 2017).

The four applied here are standard tests which fare well in the analysis of Sokolovsky et al. (2017), and are also found to produce clear results when applied to our data. Two of them, the variability index and variability amplitude tests, were applied in the earlier analysis of the OVRO data by Hogan et al. (2015b). Due to the significant increase in the timespan covered by the new data, the additional variability parameters can be used to provide a fuller analysis.

2.4.1 Reduced χ^2 Test

A χ^2 test can assess the null hypothesis that a lightcurve is from a non-varying source, and therefore does not change in brightness. With a flat lightcurve model, the reduced χ^2 of the null hypothesis is defined as

$$\chi^2_r = \frac{1}{N} \sum_{i=1}^{N} \left(\frac{F_i - \bar{F}}{\sigma_i} \right)^2 , \tag{2.4.1}$$

where N is the number of measurements of the source's flux density, F_i, and σ_i is the measurement error. If the true lightcurve of the source is flat, this test gives the probability of observing a lightcurve with an apparent level of variability greater than or equal to that which is detected, assuming measurement errors are estimated correctly.

2.4.2 Variability Index

The variability index, VI, is defined as

$$VI = \sqrt{\frac{\sum_{i=1}^{N}(F_i - \bar{F})^2 - \sum_{i=1}^{N}\sigma_i^2}{N}}, \tag{2.4.2}$$

where N is the number of measurements, F_i is the flux density and σ_i is the associated error. If the discriminant of the variability index is negative, the variability index is calculated with the modulus of the discriminant and given a negative sign. Such a result indicates that there is no variability between the two measurements. A variable source is expected to have a VI greater than zero, with larger positive values corresponding to stronger variability.

The most notable advantage of the variability index is that it can be used with as few as two flux density measurements. Since the OVRO observations have a median separation of seven days, this test can in theory be used to assess variability on approximately week long timescales. However, as previously stated, variability cannot take place on timescales less than a source's light crossing time, so week-to-week variability is not expected. Nevertheless, we analyse the spectra on these timescales for completeness.

2.4.3 Variability Amplitude

The variability amplitude, VA, is used to quantify the magnitude of the peak-to-trough variability in a source's lightcurve. It is defined as (Heidt & Wagner, 1996):

$$VA(\%) = \frac{100}{\bar{F}}\sqrt{(F_{\max} - F_{\min})^2 - 2\bar{\sigma^2}}, \tag{2.4.3}$$

where

$$\bar{\sigma^2} = \frac{1}{N}\sum_{i=1}^{N}\bar{\sigma_i^2}. \tag{2.4.4}$$

Here, F represents the observed flux densities and σ the associated errors. The variability amplitude indicates the size of the peak-to-trough variability, and is often calculated with only the single largest and smallest flux density measurements (i.e. $N = 2$).

However, where a light curve has a large number of data points, $F_{\max}$ and $F_{\min}$ can be replaced e.g. by the mean of the several largest and smallest flux densities. This makes it

less prone to selecting outlying data points and overstating the variability in a lightcurve, particularly where the variability is small compared with the measurement error.

2.4.4 Interquartile Range

The interquartile range (IQR) of a lightcurve is found by splitting the data into two halves about the median, then taking the difference between the median value of the upper and lower halves. For a normal distribution, IQR = 1.35σ. The IQR is one of the most robust parameters for quantifying variability due to its low sensitivity to outlying data points. However, to be robust the IQR requires at least several tens of measurements, so with the 15 GHz data it is only useful for multi-year to decade long timescales (Sokolovsky et al., 2017).

2.4.5 Mock Lightcurves

The apparent variability in a lightcurve is a product of a source's true variability and the observational errors, which cannot be known precisely. For some of the weaker sources in the sample, the observational errors are clearly significant. For example, in A2055 of Fig 2.3, the single largest and smallest flux density measurements would suggest a peak-to-trough change in flux density of around 300 per cent in approximately 3 years.

To estimate the true level of variability of each source, mock lightcurves are created based on a flat lightcurve model. By applying the variability detection and quantification parameters described above to the real and mock lightcurves, the level of variability in each source can be more confidently determined.

For each of the 20 sources with OVRO 15 GHz observations, 1000 mock lightcurves are created. These can then be used to find the values given by the variability parameters for a truly flat lightcurve with similar flux density errors. By calculating how often the mock data result in variability greater than or equal to that of the true lightcurves, the probability that the observed variability has arisen as a result of only noise, rather than intrinsic source variability, can be found.

The mock lightcurves are created in the following way:

- The real OVRO observations are split in two at mjd = 56800, the approximate date at which the new phase calibrator was introduced and there was a large reduction in the observational errors. This is done after masking bad data and the removal of extended emission.

- The mean flux density, $\bar{F}$, and flux density error $\bar{\sigma_F}$ of these two parts of the data are calculated.

- Mock flux densities are drawn for the two parts from a Gaussian distribution, centred on $\bar{F}$ and with a standard deviation of $\bar{\sigma_F}$. Each mock flux density is given an error of $\bar{\sigma_F}$. One mock flux density is drawn for each date at which there was a real observation.

Appendix A.1 shows one mock spectrum for each source for illustrative purposes.

2.5 Application of Variability Detection and Quantification

The numerical parameters described in the previous section each have their own strengths and weaknesses, and all have a particular use when applied to the data. As such, we use:

- the reduced χ^2 test to determine whether or not each lightcurve is consistent with that of a non-varying source

- the variability index, VI, to detect variability on short to medium term timescales (weeks to years)

- the variability amplitude, VA, to show the peak-to-trough changes in the lightcurves over medium to long term timescales (year to multi-year)

- the interquartile range, IQR, to categorize each source's variability as undetectable, weak, moderate, strong, or very strong over the full timespan on which they have been observed.

Results from the application of the variability detection parameters to the real and mock lightcurves are described in the following subsections.

2.5.1 Reduced χ^2 Test – determining consistency with a flat lightcurve model

The reduced χ^2 and a corresponding p-value are calculated using the full extent of each source's lightcurve (after masking and the removal of extended emission), and the resulting values are shown in Table 2.3. This p-value does not give the probability that a source is non-varying over the observed period. Instead, it gives the probability of obtaining a lightcurve at least this discrepant from the flat lightcurve model, assuming the model is true and the errors are accurately estimated.

If the p-value is < 5 per cent, the lightcurve is considered to be inconsistent with the flat lightcurve model. According to this criterion, 13 of the sources are inconsistent with a flat lightcurve model, while 7 are consistent.

Table 2.3

Results from the four variability detection techniques applied to the 15 GHz OVRO lightcurves. Bold typeface is used for values indicating variability. Continued on the next page.

1(a) The p-value given by the χ^2 test for a flight lightcurve model when it is applied to the real lightcurves.

2(a-d) The percentage of mock lightcurves for which the median VI at 10, 30, 100, and 300 days exceeds that of the real spectra.

3(a-d) The percentage of mock lightcurves for which the median VA at 100, 300, 1000, and 3000 days exceeds that of the real spectra.

4(a) The percentage of mock lightcurves for which the IQR (calculated over the full timespan of the lightcurve) exceeds that of the real spectra.

4(b) The IQR of each real lightcurve divided by the mean flux density

4(c) The variability classification of each source. This is determined by comparing the IQR/$\bar{F}$ value to that of the calibrator sources (see §2.5).

	(1) χ^2 test	(2) VI				(3) VA			(4) IQR		
Source	(a) p-value /%	(a) 10	(b) 30	(c) 100	(d) 300	(a) 300	(b) 1000	(c) 3000	(a) t_{max}	(b) $/\bar{F}$	(c) Classification
3C286 - Calibrator	11.8	67.8	58.4	27.0	8.6	**0.3**	**<0.1**	**<0.1**	**<0.1**	0.02	negligible
DR21 - Calibrator	12.9	52.7	31.3	7.0	**4.3**	**0.2**	**<0.1**	**<0.1**	**<0.1**	0.02	negligible
RXJ0132.6-0804	**1.4**	23.6	37.0	**4.9**	**<0.1**	**<0.1**	**<0.1**	**<0.1**	**<0.1**	**0.13**	**moderate**
J0439+0520	**0.5**	46.5	73.5	46.0	**0.1**	**<0.1**	**<0.1**	**<0.1**	**<0.1**	**0.08**	**weak**
A646	**0.3**	30.4	47.1	**4.9**	**<0.1**	**<0.1**	**<0.1**	**<0.1**	**<0.1**	**0.15**	**strong**
4C55.16	**2.3**	43.2	67.6	35.3	**0.8**	**1.64**	**0.2**	**<0.1**	**<0.1**	**0.10**	**moderate**
A1348	5.4	20.0	49.4	66.9	46.4	33.61	**0.28**	**0.1**	**<0.1**	**0.20**	**strong**

	(1) χ^2 test	(2) VI				(3) VA			(4) IQR		
Source	(a) p-value /%	(a) 10	(b) 30	(c) 100	(d) 300	(a) 300	(b) 1000	(c) 3000	(a) t_{max}	(b) $/\bar{F}$	(c) Classification
3C264	**0.7**	21.7	25.0	6.6	**<0.1**	**<0.1**	**<0.1**	**<0.1**	**<0.1**	**0.24**	**strong**
A1644	**<0.1**	6.8	8.4	**<0.1**	**<0.1**	**<0.1**	**<0.1**	**<0.1**	**<0.1**	**0.16**	**strong**
J1350+0940	24.6	54.9	78.8	75.7	89.2	83.28	81.91	61.24	33.0	0.05	negligible
J1459-1810	12.6	82.4	73.4	49.8	12.5	39.31	**3.51**	**<0.1**	**<0.1**	**0.08**	**weak**
A2052	**<0.1**	23.9	60.6	66.4	74.3	53.53	**<0.1**	**<0.1**	**<0.1**	**0.29**	**very strong**
A2055	**3.1**	14.8	30.4	18.5	**4.7**	7.49	**<0.1**	**<0.1**	**<0.1**	**0.26**	**very strong**
J1558-1409	**<0.1**	43.7	63.7	58.4	65.0	59.2	68.62	**0.3**	**<0.1**	**0.14**	**moderate**
J1603+1554	**<0.1**	58.9	84.5	87.0	85.4	79.69	**<0.1**	**<0.1**	**<0.1**	**0.15**	**moderate**
J1727+5510	**<0.1**	86.2	79.2	51.9	**2.4**	76.62	**<0.1**	**<0.1**	**<0.1**	**0.42**	**very strong**
Z8276	**<0.1**	22.9	50.3	18.1	**0.5**	**0.18**	**<0.1**	**<0.1**	**<0.1**	**0.28**	**very strong**
RGBJ1745+398	11.3	15.8	22.4	**0.5**	**<0.1**	**<0.1**	**<0.1**	**<0.1**	**1.0**	**0.11**	**moderate**
A2390	16.4	31.4	62.6	28.2	**2.3**	**1.13**	**<0.1**	**<0.1**	**<0.1**	**0.11**	**moderate**
A2415	**<0.1**	35.1	53.7	42.9	18.0	30.62	**<0.1**	**<0.1**	**<0.1**	**0.24**	**strong**
A2627	5.2	32.0	35.0	**4.0**	**<0.1**	**<0.1**	**<0.1**	**<0.1**	**<0.1**	**0.2**	**strong**
RXJ2341.1+0018	6.9	25.1	50.4	46.0	**0.1**	**<0.1**	**<0.1**	**<0.1**	**<0.1**	**0.09**	**weak**

2.5.2 Variability Index – detecting variability on short timescales

The VI is useful in cases where there are a small number of data points, and can be used even with just two flux density measurements. Here, it is used to indicate whether each source shows variability on approximately week to year long timescales. To do this, the parameter is calculated at every available 10, 30, 100, and 300 day timespan within the observations. For example, for the 10 day timespan, the VI is calculated with measurements from between days 1 and 10, 2 and 11, 3 and 12 etc. of the observations; assuming there is a unique set of at least two observations within those time periods.

The percentage of the 1000 mock lightcurves for which the median VI at 10, 30, 100, and 300 days exceeds that of the real lightcurves is then used as a threshold to determine whether or not variability is present. If 5 per cent or fewer of the mock lightcurves result in a VI larger than that of the real lightcurves, the source is classed as variable.

The percentage of the mock lightcurves for which the VI at 10, 30, 100, and 300 days exceeds that of the real lightcurves is shown in Table 2.3. These VI tests suggest that no sources vary on 10 or 30 day timescales, five vary on 100 day timescales, and 13/20 sources (excluding the two calibrator sources) vary on 300 day timescales.

2.5.3 Variability Amplitude – peak-to-trough variability

The VA is used to determine the magnitude of the peak-to-trough changes in the lightcurves over timescales of 100 to 3000 days. Due to the large number of observations, in the calculations we follow the example of Hogan et al. (2015a) and use the mean of the five largest and smallest flux densities in place of $F_{\rm max}$ and $F_{\rm min}$, rather than the single largest and smallest values. This approach provides a good compromise between reducing the effect of outlying flux densities, and the inclusion of more flux densities with less extreme separation reducing the apparent VA.

The percentage of the mock lightcurves for which the VA at 300, 1000, and 3000 days exceeds that of the real lightcurves is shown in Table 2.3. Excluding calibrator sources, and with a threshold of 5 percent, this suggests that 12/20 sources typically vary on 300

day timescales, 18/20 vary on 1000 day timescales, and 19/20 typically vary on 3000 day timescales∗.

Figs. 2.5 and 2.6 show the VA for timespans between approximately 150 and 3600 days for both the real spectra, and the mock lightcurves. As was the case for the variability index, the parameter is calculated at every available timespan within the observations. For example, for the 150 day timespan, the VA is calculated between days 1 and 150, days 2 and 151, days 3 and 152 etc..

The dark blue lines in Figs. 2.5 and 2.6 represent the median VA of the real spectra, while the edges of the shaded blue regions mark the maximum and minimum VA seen within the observations. Similarly, the red lines represent the mock lightcurves. These red lines show that observational errors are responsible for a significant fraction of the apparent VA in many sources, particularly on shorter timespans. However, the excess VA (i.e. the gap between the red and blue lines) is also a clear indicator of variability in many sources.

The width of the shaded regions also indicates how consistent a source's variability is. For example, the range in the VA values calculated for the calibrator source 3C286, which has a consistently flat lightcurve, is very narrow. Similarly, the range of VAs calculated for A2052 is narrow across all timespans because the source varies at a close to constant rate throughout the whole period of observations. On the other hand, the lightcurve of e.g. A646 contains some periods which are much less variable than others, resulting in the wide range of VAs shown by the blue shaded region in Fig. 2.5.

2.5.4 Interquartile Range – quantifying variability over the longest available timescales

The IQR is perhaps the most robust parameter for detecting variability, but is only reliable with several tens of flux measurements (Sokolovsky et al., 2017). Over the full period in which each source was observed, the IQR is therefore used to categorize each source as

∗Three sources (3C264, A1644, and RGBJ1745+398) only have observations spanning 2.1 years, so the VA values calculated at 1000 and 3000 days are lower limits. However, these still meet the variability threshold, in spite of the shorter timespan of the observations.

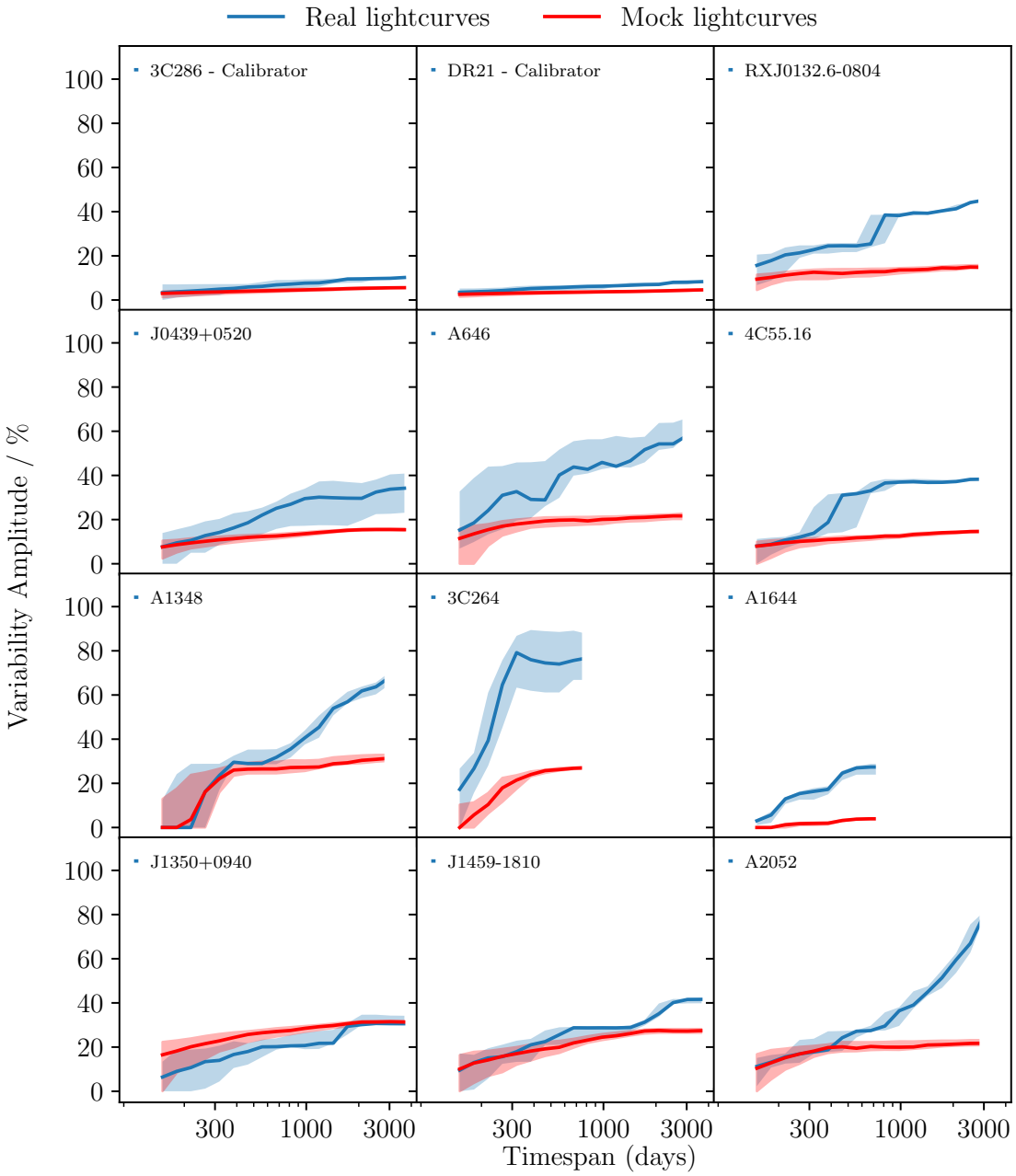

Figure 2.5

Variability amplitudes for timespans of 150 to 3600 days. In most cases, the total time range over which the OVRO 15 GHz observations were carried out is several years, and the dark blue line represents the median VA within that time period. The shaded blue regions mark the maximum and minimum VA within the full period over which each source was observed. The red lines show similar results, but for the mock flat lightcurves. Note that 3C264 and A1644 only have observations spanning 2.1 years ($\sim$ 800 days).

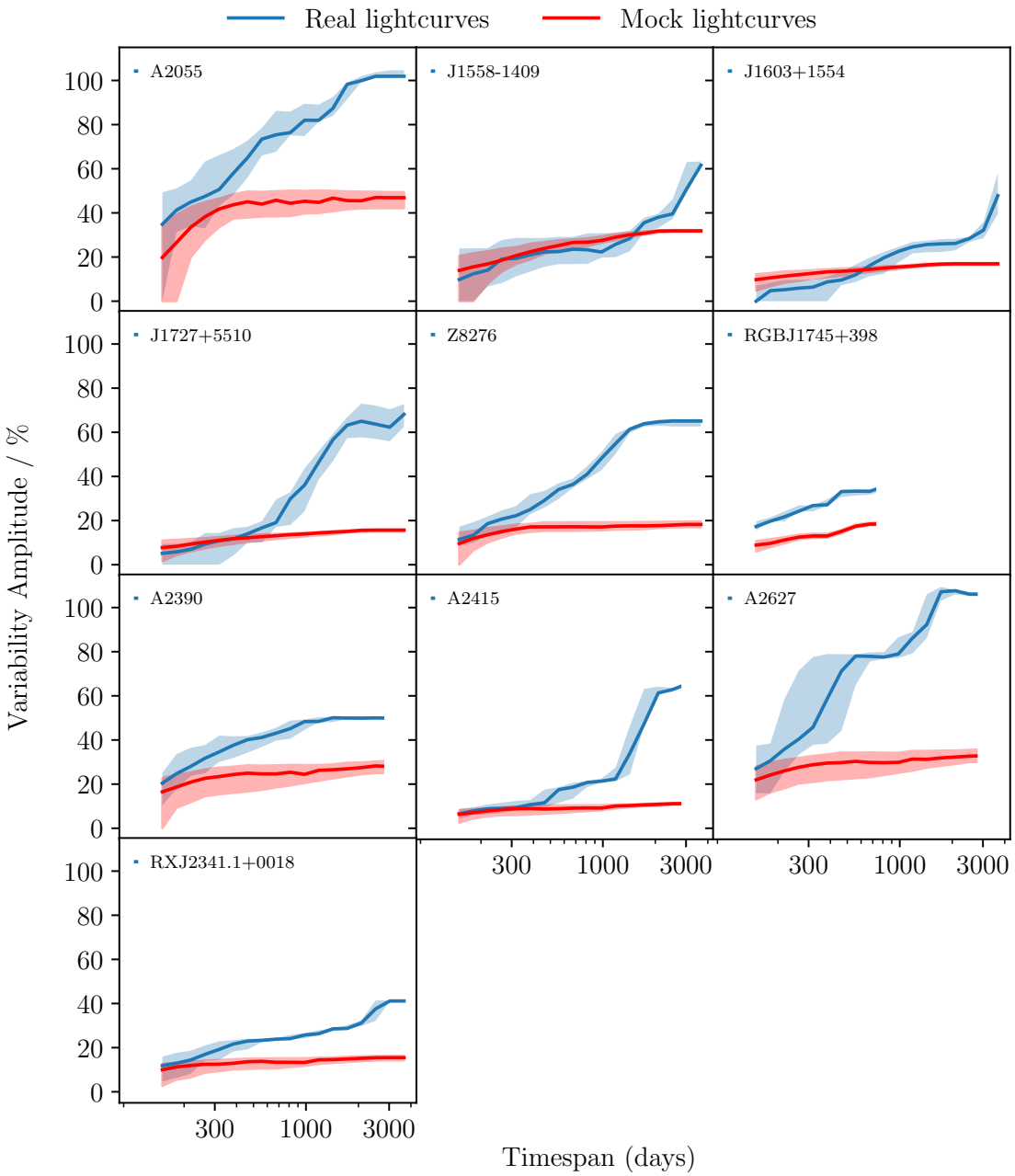

Figure 2.6

Continued from Fig. 2.5. Note that RGBJ1745+398 only has observations spanning 2.1 years (~ 800 days).

having variability which is negligible, weak, moderate, strong, or very strong. In most cases the observations span several years or more, and in this way the strength of the variability in each source can be classified based on the entirety of the available data.

Where the value of $IQR/\bar{F}$ is less than three times the value of the calibrator sources, i.e. < 0.06, the variability is described as negligible. Otherwise, if $IQR/\bar{F}$ is in the range $0.06 - 0.10$ (i.e. three to six times that of the calibrator sources), it is labelled as weak, $0.10 - 0.15$ as moderate, $0.15 - 0.25$ as strong, and > 0.25 as very strong. The IQR and variability classification for each source's lightcurve are shown in Table 2.3 (as well as the percentage of the mock spectra for which the IQR exceeds that of the real lightcurves).

According to this variability characterization parameter, one source has negligible levels of variability over the full timespan in which it was observed, while 3/20 sources show weak levels of variability, 6/20 show moderate levels of variability, 6/20 show strong levels of variability, and 4/20 show very strong levels of variability.

2.6 Discussion

2.6.1 Overall variability within the sample

The precursor to this work, Hogan et al. (2015b), studied the high radio frequency variability of 16 brightest cluster galaxies on timescales of between 1.5 and 6.5 years. The size and high temporal sampling presented here is a significant improvement on this, so it is now possible to draw wider conclusions about the magnitude and ubiquity of variability in brightest cluster galaxy cores than was previously possible.

Fig. 2.7 shows the fraction of sources which vary by between 10 and 60 per cent over a range of timespans from 100 to 2500 days. All sources show 10 per cent peak-to-trough variability on 18 months timescales, but the same is true of the mock lightcurves and so any true variability cannot be separated from the apparent variability caused by observational errors. Variability of 20 per cent is seen in all sources on 3 year timescales versus half of the mock lightcurves, so moderate levels of variability are a feature of at least half these sources.

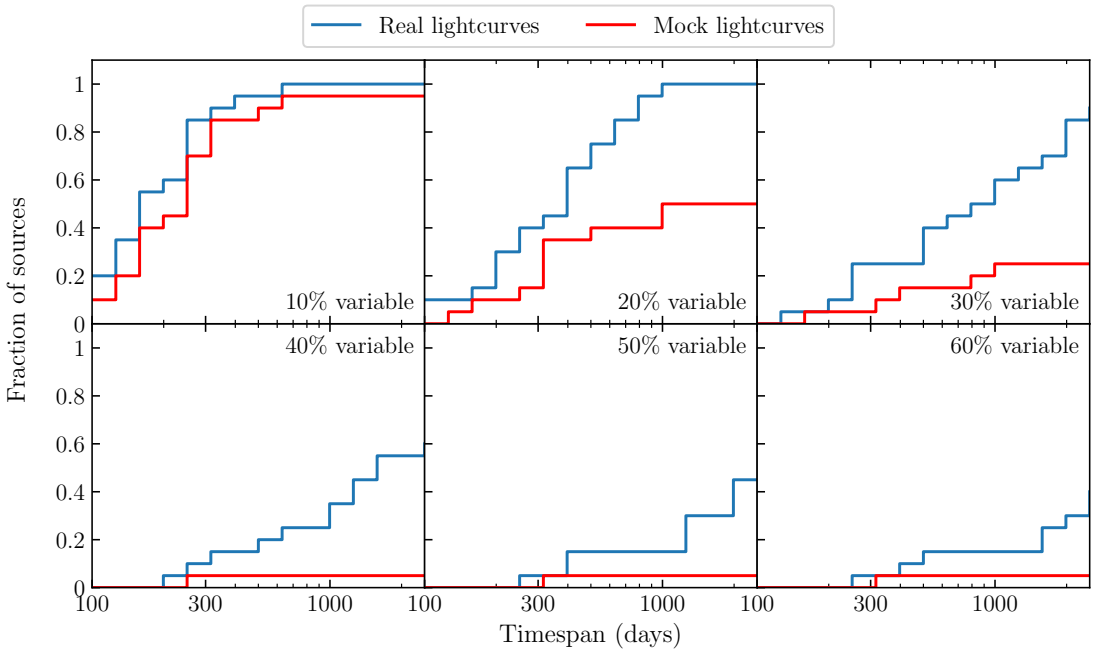

Figure 2.7

The fraction of sources for which the median peak-to-trough variability exceeds 10, 20, 30, 40, 50, and 60 per cent, calculated as a function of the observation timespan. The peak-to-trough variability is determined by the VA, given in equation 2.4.3. Calibrator sources are not included. Note that 3C264, A1644, and RGBJ1745+398 only have observations spanning 2.1 years (~ 800 days).

The total timespan over which the majority of sources have been observed is significantly longer than that on which they are found to vary. If the variability is in any way repetitive and/or predictable on these timescales, it may therefore be possible to observe repeated patterns in the lightcurves and predict future variability. With a by eye inspection of the data, no such patterns obvious. However, to more rigorously assess this, Fourier analysis of the lightcurves would be necessary.

At least a third of the sources vary at the 60 per cent level on the 6 year timescale sampled here. This is important because studies of Sunyaev-Zel'dovich Effect in the radio/sub-mm often involve the subtraction of the radio/sub-mm continuum source from the BCG. This subtraction is often made by extrapolating from a lower frequency radio flux density that was made at least a few years before the Sunyaev-Zel'dovich observations. The complex spectral nature of these radio sources and their intrinsic variability means that these estimates of flux density will be far less certain than assumed.

The OVRO lightcurves themselves show significant changes in variability over the 3–12 years covered. For instance A2415 and J1558-1409 show 3–4 year "outbursts" and several other sources transition from declining to rising over the full lightcurve.

In addition to the sources with OVRO 40m monitoring, we also have multiple high frequency observations of a number of additional sources that were either too far south to be observed with the OVRO 40m telescope (dec$< -20°$) or too faint (< 100 mJy at 15 GHz), but significant variability is implied. This is most notable in (i) A3581, the brightest source detected with SCUBA2, which shows an 80 per cent increase in flux density at 363 GHz between 2013 and 2021, and (ii) Zw8193, which has brightened by a factor of 2 at 150 GHz between 2011 and 2020. The seven other sources with multiple observations do not vary by more than 30 per cent at any frequency. This includes RXJ1745+39, E1821+644 and RXJ1832+68, which have limited Metsähovi 37 GHz monitoring between 2002 and the present day, but the upper limits obtained are consistent with no significantly brighter emission in the recent past for these sources (Lähteenmäki, priv comm). This proportion is consistent with the fraction of sources (2 of 9) expected from Fig. 2.7 for the largest amplitude of variability.

2.6.2 Variability and Spectral Index

The only radio core in a BCG which has a lightcurve with better long term sampling than the OVRO BCG sample presented here is NGC1275/3C264 in the Perseus cluster. This source has varied by over a factor of ten at 30–90 GHz over the 50 years since its first detection at these frequencies (Dutson et al., 2014). The overall variation of peaks in activity with a 30–40 year spacing, short term "flares" during these peaks and then long periods of decline after a peak are consistent with the variety, timescale and amplitude of the variability seen in this sample. Importantly, Dutson et al. (2014) show that the high frequency spectral index of the core changes very significantly over this cycle of activity. As would be expected, the spectral index above 30 GHz is relatively flat when the activity is high and the source is increasing in brightness, then is steeper as it fades.

This dramatic change in the high frequency spectral index also mirrors the gamma-ray emission in NGC1275. Dutson et al. (2013) note the lack of observable gamma-ray emission from NGC1275 in the 1990s with EGRET on *Compton* when the source was in strong decline but very clearly detected in the 1980s with *COS-B* and after 2008 with *Fermi*. Six of the OVRO sample have a significant *Fermi* 4FGL detection in the first 8 years of data: 3C264/NGC3862, RXJ0132-08, A2055, RXJ1558-14, RXJ1745+39, and A2627 (Abdollahi et al., 2020). There are also three other BCGs in the parent X-ray sample with a 4FGL counterpart: A3112, A3392, and A3880. Using the mean OVRO 15 GHz flux density and literature values for the three additional sources and NGC1275 the core radio flux density at 15 GHz can be plotted against the 4FGL photon flux (Fig. 2.8). There are few data points, but there is a clear correlation between these flux densities indicating that these other BCGs show a very similar scaling in radio to gamma-ray emission as NGC1275.

With this link to the gamma-ray and the long timescale behaviour of NGC1275 in mind, we now consider the connection between variability and spectral index for the sample in more detail.

Fig. 2.9 shows the spectral index between 15 GHz and the higher frequency KVN, SCUBA2, NIKA2, and ALMA photometry plotted against the excess amount that the

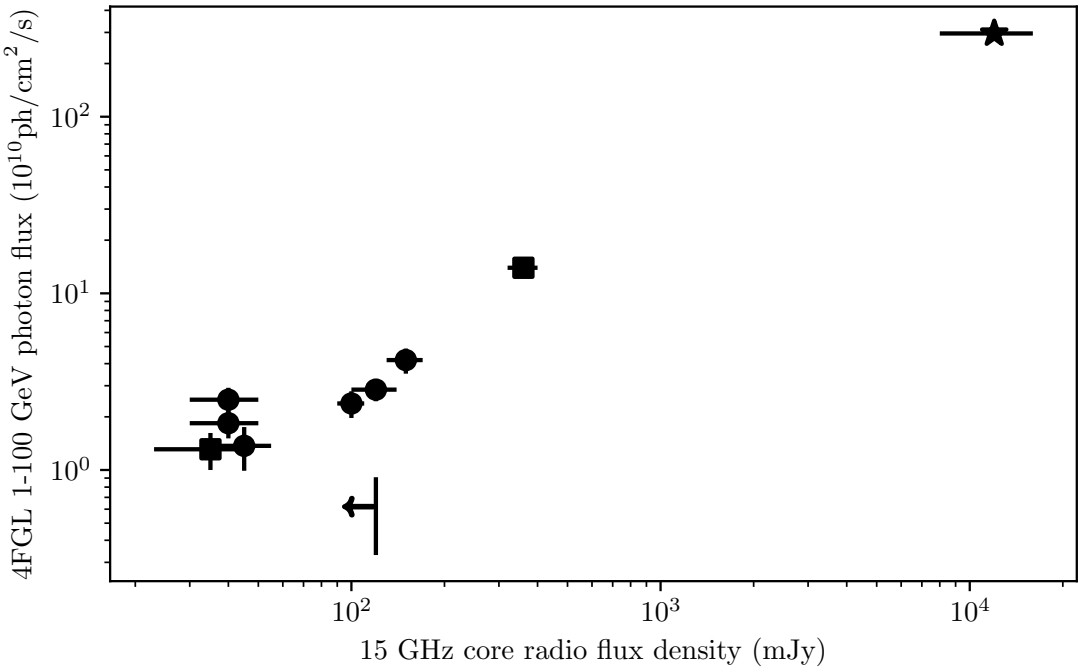

Figure 2.8

The Fermi 4FGL 1–100 GeV photon flux plotted against the mean 15 GHz core flux density for the six OVRO monitored sources (circles), NGC1275 (star) and three southern BCGs (squares and upper limit). Note that there is variability in the properties in both axes, but there is consistency between the two flux densities over the wide range.

source varies over the mock lightcurves in the subsequent two years (i.e. the median VA of the real lightcurve minus the median VA of the mock lightcurves). While the correlation is only moderate to low – with a Pearson's correlation coefficient of 0.30 ± 0.02 – an overall trend that the points are flatter as sources increase in brightness is present. A strict correlation between the variability and spectral index is not necessarily expected due to the intricacies of AGN accretion and feedback mechanisms. For example, the link may be somewhat broken by the complex nature of the formation, expulsion, and breakdown of radio jets, and synchotron opacity effects within the core.

The sources with a *Fermi* 4FGL detection are plotted as stars and these are almost exclusively found in the upper part of the plot with a flatter spectral index but not always brightening. This is consistent with the behaviour of NGC1275 where the gamma-ray

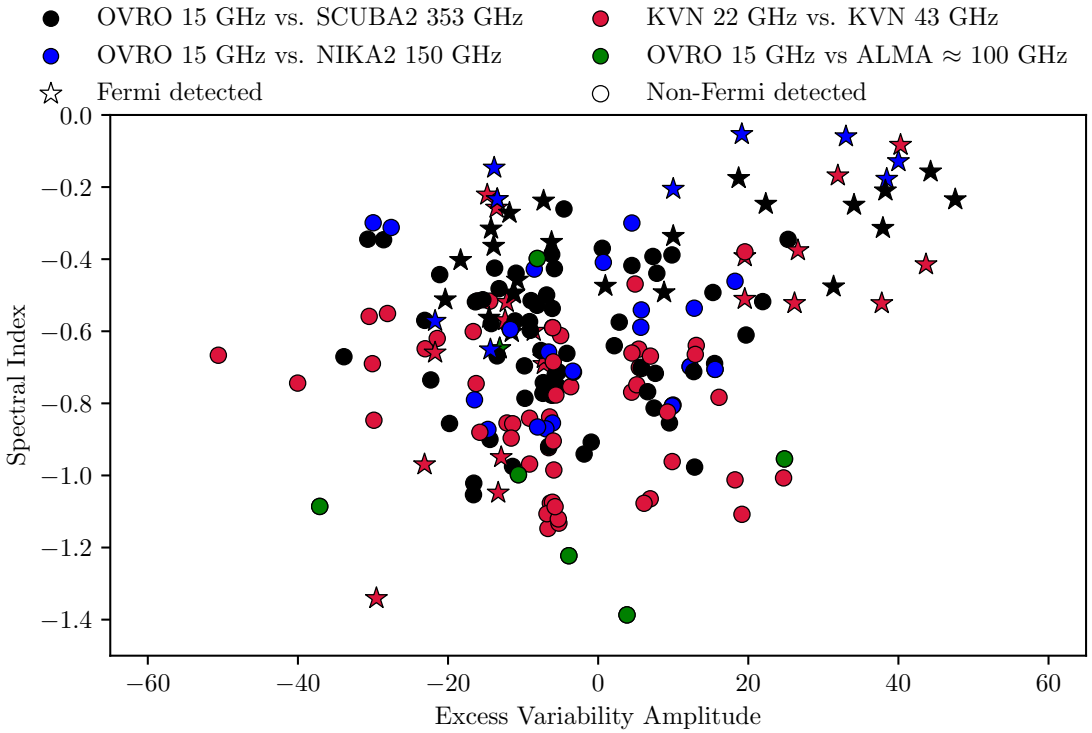

Figure 2.9

The relationship between the spectral index and excess variability amplitude (i.e. the median VA of the real lightcurve minus the median VA of the mock lightcurves) in the following two years. A negative excess VA indicates a fading lightcurve.

emission persists over the shorter term variability on year timescales and only during the long decline, when the high frequency spectral index steepens, does the gamma-ray emission drop appreciably. The general lack of *Fermi* detections of sources with steep high frequency spectral indices – despite having a 15 GHz flux density comparable to the sources with a 4FGL detection – suggests that these are sources in the low activity part of a cycle similar to that seen in NGC1275.

Hogan et al. (2015a) use archival data for two sources, 4C+55.16 and RXCJ1558-14, to show that at least some of the sample have been brighter in the period since the start of radio astronomy. However, sources that have brightened and should enter the sample will continue to be overlooked until we enter the era of regular, high frequency radio surveys. The notable exception is the AT20G survey of Murphy et al. (2010), which selected all the sources in the equatorial overlap area between ATCA and OVRO between declinations of -20 and +0°.

The variation seen in NGC1275 on longer timescales than sampled here suggests that some of the sources in this sample will fade below the OVRO detection limit and other sources will brighten sufficiently to be monitored over the next 3–5 years (Dutson et al., 2014). This makes it worth noting that because of the amplitude of the variability seen, a complete sample of sources for a study like this would be impossible since there will be sources continually rising above or fading below the radio flux density limit. However, we believe that the selection is representative and the properties of these sources can be used to constrain the duty cycle of activity in BCGs in general and act as a comparison for gamma-ray detected radio galaxies more widely.

2.7 Conclusions

The high radio frequency variability of brightest cluster galaxies provides important clues as to the nature of fuelling and feedback cycles in galaxy clusters, but this behaviour is not well understood due to a lack of observational data.

To address this, this chapter has presented the most comprehensive high radio frequency monitoring of brightest cluster galaxies to date. This has primarily been done using the

OVRO 40m telescope at 15 GHz, with additional observations from KVN at 22 and 43 GHz, NIKA2 at 150 GHz, SCUBA2 at 353 GHz, and ALMA at ~ 100 GHz.

Many of the sources have gone through phases in which they have varied significantly on periods of around three years, before returning to a relatively constant state (e.g. J0439+0520, J1558-1409, and J1727+5510). Using a range of variability detection and quantification parameters has shown significant levels of variability in most sources. Over the full timespan on which observations have so far been carried out, typically 8-13 years, 13/20 are inconsistent with a flat lightcurve model. Variability index and variability amplitude tests show that no sources vary on timescales of 10 or 30 days, while 5/20 vary on timescales of 100 days. At 300 days, 12-13/20 sources show evidence of variability, and 18/20 sources vary on timescales of 1000 days. A source cannot vary on timescales less than its light crossing time, so this places an upper limit of 1 - 3 ly (0.3-1 pc) on the sizes of these sources. Variability in the form of AGN outbursts is also a consequence of accretion events, so these can also be concluded to take place on similar timescales.

At least a third of the sample displays 60 per cent variability on 6 year timescales. This is important to studies of the Sunyaev-Zel'dovich effect in the radio/sub-mm, which frequently involve the subtraction of the radio/sub-mm continuum source from the BCG. This is often done by extrapolating from a lower frequency radio flux density made several years before the Sunyaev-Zel'dovich observations. Due to the complex spectral nature of these radio sources and their intrinsic variability, estimates of flux density at higher frequencies will be far less certain than assumed. However, because we find that our sources spend roughly equal amounts of time brightening and fading, the fluxes estimated in this way are as likely to be overestimates as they are underestimates. Therefore, cosmological predictions based on multiple sources will be less certain than assumed, but will not necessarily carry a systemic error (Lin et al., 2015).

We find a weak link between variability and spectral index changes in the sample, with the two being positively correlated. This is particularly true for sources with the strongest levels of variability, where spectral indices tend to be much flatter. This weak trend is similar to that seen in NGC 1275, where fading periods are associated with steep spectral indices, and outbursts with flatter spectral indices (Dutson et al., 2013).

The ‘on-off’ nature of the variability is also consistent with models of clumpy accretion (e.g. Pizzolato & Soker, 2005; Gaspari et al., 2018). These predict that the cores of massive galaxies contain significant quantities of cold molecular gas in the form of distinct clouds, which migrate towards the black hole and provide it with an intermittent source of fuel. The amount of energy provided to a supermassive black hole by an accretion event should be dependent on the mass accreted. In the future, it may be possible to extend this work to find the radiative power associated with outbursts in the lightcurves. Ultimately, once multiple outbursts have been observed this could be used to infer the mass distribution of the accreted clouds. In the mean time however, the chapters which now follow present more direct observations of molecular clouds in brightest cluster galaxies.

CHAPTER 3

Molecular absorption in the Hydra-A brightest cluster galaxy

This chapter is based on the following publication:

Deep and narrow CO absorption revealing molecular clouds in the Hydra-A brightest cluster galaxy · **Rose, Tom**; Edge, A. C.; Combes, F.; Gaspari, M.; Hamer, S.; Nesvadba, N.; Russell, H.; Tremblay, G. R.; Baum, S. A.; O'Dea, C.; Peck, A. B.; Sarazin, C.; Vantyghem, A.; Bremer, M.; Donahue, M.; Fabian, A. C.; Ferland, G.; McNamara, B. R.; Mittal, R.; Oonk, J. B. R. Salomé, P.; Swinbank, A. M.; Voit · 2019, MNRAS, 485, 229 (view publication)

3.1 Introduction

Important observational constraints can be placed on accretion models by studying the gas which is responsible for the process. This means determining the properties of the cold gas close to the supermassive black hole, particularly its typical mass, dynamics, covering fraction, and relative velocity.

To date, the most direct observational evidence supporting clumpy accretion models in brightest cluster galaxies has been provided by David et al. (2014) and Tremblay et al. (2016). Their pencil-beam observations of the NGC 5044 and Abell 2597 brightest cluster galaxies, respectively, detect cold molecular gas inferred to be within ~10 - 100 pc of the galaxy's supermassive black hole.

The clouds are detected through absorption by using the AGN as a bright backlight, and give a random snapshot of the properties of the molecular gas which may go on to fuel the AGN. The cold molecular gas regions detected have dynamics consistent with their warmer H I counterparts and their narrow absorption lines (FWHM~6-30 km s^{-1}) indicate that they may be giant molecular clouds, rather than giant molecular associations, which are falling towards their respective galaxy's supermassive black hole with velocities of between 240 and 335 km s^{-1}.

A larger sample of absorbing clouds is needed to constrain their overall properties, something which is provided by this chapter with the addition of observations of one more particularly interesting brightest cluster galaxy.

This chapter presents ALMA observations of Hydra-A (see Fig. 3.1), a giant elliptical galaxy with a nearly edge-on disc of dust and cool gas which lies at the centre of an X-ray luminous cluster.

Hydra-A is an archetype of a brightest cluster galaxy lying in a cooling flow; it has powerful radio jets and lobes emanating from its centre (Taylor et al., 1990), around which are cavities in the intracluster medium's X-ray emitting gas which have been created by repeated AGN outbursts (McNamara et al., 2000; Wise et al., 2007).

The radio jets and lobes are almost perpendicular to a rotating gas disc and a spatially

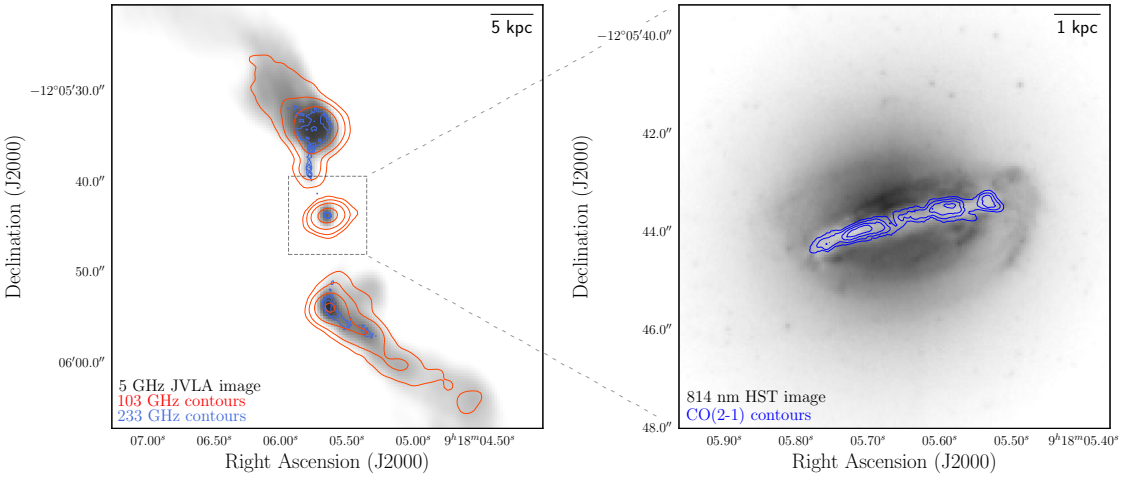

Figure 3.1

Left: A 5GHz *Karl G. Jansky Very Large Array* (VLA) radio image of Hydra-A showing powerful radio lobes emanating from the centre of the brightest cluster galaxy, with 0.19 arcsec pixel^{-1} resolution (Project 13B-088). Contours of the 233 GHz ALMA continuum image are overlaid in blue and lower angular resolution 103 GHz contours are shown in red. **Right:** Contours from a CO(2-1) integrated brightness map (described in §3.3), which mark the 0.15, 0.25, 0.35 and 0.45 mJy beam^{-1} emission regions, overlaid onto a F814W *Hubble Space Telescope* (HST) near-infrared image of the brightest cluster galaxy (Mittal et al., 2015), with a resolution of 0.05 arcsec pixel^{-1}. This highlights how the galaxy's dust lane, which is opaque to optical wavelengths, is spatially coincident with a molecular gas disc.

coincident dust lane (Hansen et al., 1995; Hamer et al., 2013). Hydra-A, or 3C218, is an ideal target for a molecular absorption study for two main reasons.

Firstly, it is an extremely strong radio/mm source with amongst the highest flux density in the 3C catalogue of radio sources (Edge et al., 1959). The ALMA observations measure a flux density of ~60 mJy at 230 GHz and in the sample of 35 brightest cluster galaxies observed by Hogan et al. (2015b), Hydra-A also has the highest flux density at both 150 and 353 GHz. This makes it an ideal backlight against which to observe molecular absorption.

Secondly, previous observations at many different wavelengths suggest that the galaxy's core contains a significant mass of both atomic and molecular gas, making positive detections highly likely e.g. H I absorption by Dwarakanath et al. (1995); Taylor (1996), CO emission by Hamer et al. (2013) and H_2 studies by Edge et al. (2002); Donahue et al. (2011); Hamer et al. (2013).

Our observations show the rotating disc of molecular gas which was previously observed by Hamer et al. (2013) in much greater detail, thanks to the high angular and spectral resolution which is provided by ALMA. They also reveal a series of cold molecular gas clouds lying along the line-of-sight to the galaxy's AGN. These have apparent velocities of between -43 and -4 km s^{-1} relative to the central supermassive black hole and are most likely moving along low ellipticity orbits, with the supermassive black hole at one focus.

This chapter is laid out as follows. §3.2 outlines details of the ALMA observations, §3.3 discusses the kinematic properties of Hydra-A's molecular gas disc and §3.4 estimates its mass. The properties of the molecular clouds which lie along the line-of-sight to the mm-continuum source are discussed in §3.5 and §3.6. Finally, §3.7 discusses the significance and implications of these observations.

Throughout this chapter and thesis, a flat ΛCDM Universe with H_0 = 70 km s^{-1} Mpc^{-1}, Ω_M=0.3 and Ω_Λ=0.7 is assumed. When applying velocity corrections, a stellar redshift of z = 0.0543519 is used, which provides the best estimate of the gravitational centre of the galaxy. This redshift is calculated from MUSE observations (ID: 094.A-0859) and corresponds to a recession velocity of 16294 km s^{-1}. This velocity carries an uncertainty of 15 km s^{-1}. At Hydra-A's redshift, there is a spatial scale of 1.056 kpc $arcsec^{-1}$, meaning that kpc and arcsec scales in figures are approximately equivalent.

3.2 Observations

The Hydra-A brightest cluster galaxy, located at RA 09h18m05.65s, dec. −12°05′44.0″ (J2000), was observed over two ALMA cycles in bands 3 and 6 (PI: Alastair Edge). For these observations, the ALMA receivers were tuned to emission from the J=1-0 and J=2-1 rotational lines of carbon monoxide (CO). This CO emission acts as a tracer for cold molecular hydrogen at temperatures of $\lesssim$50 K. Although molecular hydrogen is significantly more abundant, it is not possible to directly observe it at these temperatures because of a lack of any rotational line emission.

The spectral line observations from ALMA were used to create three dimensional position-velocity maps which trace the brightest cluster galaxy's cold molecular gas. With these high resolution maps, the projected position and line-of-sight velocity of cold molecular gas can be traced throughout the galaxy.

The first observations taken were during ALMA Cycle 4, of CO(2-1) on 2016 October 23, using band 6. The CO(1-0) observations were taken on 2018 July 18 during ALMA Cycle 5, using band 3. Further technical details of each observation are given in Table 3.1.

The data were calibrated using `CASA` version 5.1.1, a software package which is produced and maintained by the ALMA observatory (McMullin et al., 2007). For each of the observed CO lines, the calibrated data were produced by the ALMA observatory. After their delivery, the necessary continuum subtractions were performed.

3.3 Dynamics of the cold gas disc

Fig. 3.2 shows the spectra of the CO(1-0) and CO(2-1) emission observed across Hydra-A's disc. The region from which the spectra are extracted is indicated by the large, blue rectangle on the integrated brightness map shown in Fig. 3.3. A region this size was based on the extent of the weak CO emission ($< 3\sigma$), which is present over a large area – one significantly larger than is suggest by the 3σ map of Fig. 3.3.

	Observation	
	CO(2-1)	CO(1-0)
Observation date	2016 Oct 23	2018 Jul 18
Integration time / s	2700	2700
Velocity resolution / km s^{-1}	1.3	2.7
Frequency resolution / kHz	977	977
Angular resolution / arcsec	0.19	1.63
PWV / mm	1.11	2.85
Field of view / arcsec	27.8	62.1
Central frequency / GHz	218.55	109.33
Maximum spacing / km	1.1	0.16
RMS noise per channel / mJy	1.4	0.7

Table 3.1

Observational details for the CO(2-1) and CO(1-0) data.

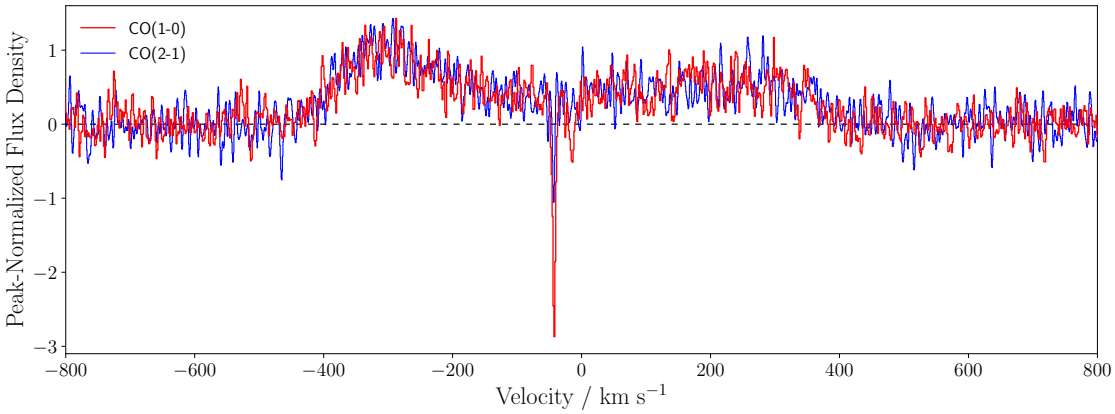

Figure 3.2

Peak-normalized CO(1-0) and CO(2-1) spectra of Hydra-A's disc from the ALMA observations, extracted using the region indicated by the large blue box shown in Fig. 3.3. The spectra both show a double-peaked structure with a trough at the galaxy's dynamical centre, which itself shows some absorption close to the systemic velocity. The peak-normalization applied to the spectra aids comparison of the emission, but due to the CO(1-0) having a much lower peak, it over emphasizes the strength of the CO(1-0) absorption at the centre. The emission from the CO(2-1) and CO(1-0) continuum-subtracted spectra peak at 13 mJy and 3 mJy, respectively. Additionally, both peak-normalized spectra appear to have a similar noise levels because each observation was done while working towards a similar signal-to-noise ratio. The CO(1-0) and CO(2-1) absorption features are discussed in more detail in §3.5 and §3.6.

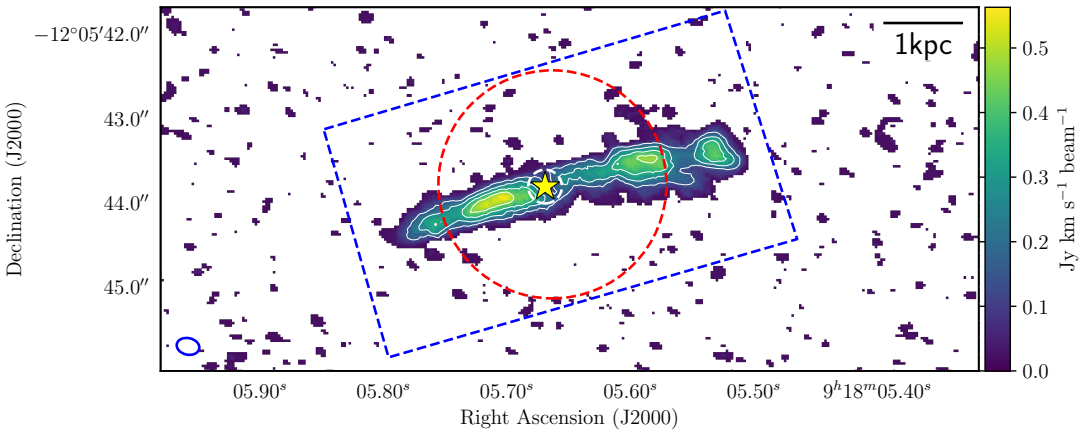

Figure 3.3

An integrated brightness map of $\geq 3\sigma$ CO(2-1) emission in the Hydra-A brightest cluster galaxy. The brightness is integrated from -500 km s^{-1} to +500 km s^{-1} about the galaxy's systemic velocity. Contours marking 0.15, 0.25, 0.35 and 0.45 Jy km s^{-1} beam^{-1} emission are shown in white. The yellow star indicates the position of the mm-continuum source while the large, dashed blue box and dashed white circle indicate the respective regions from which the spectra in Fig. 3.2 and 3.6 are extracted. The large, dashed red circle, which is approximately the same size as the CO(1-0) beam, indicates the region from which the spectra in Fig. 3.8 are extracted. The CO(2-1) beam size is shown in blue in the bottom-left corner.

Due to its considerably higher angular resolution, only an integrated brightness map of the CO(2-1) data is shown, which was produced using the `immoments` task in `CASA`. The map reveals a close to edge-on disc of cold molecular gas, with two peaks in brightness on either side of the centre corresponding to those seen in Fig. 3.2. Brightness contours from Fig. 3.3 overlaid onto the HST F814 image of Fig. 3.1 show a cold molecular gas disc that is spatially coincident with the dust lane of the galaxy. The molecular disc and dust lane are aligned with the ~5 kpc diameter disc of ionized and warm molecular hydrogen identified by Hamer et al. (2013).

The strong, broad, and double-peaked line emission seen in Fig. 3.2 results from the disc's rotation and has a large full width zero intensity of ~1000 km s^{-1}, consistent with previous CO observations of Hydra-A (O'Dea et al., 1994; Edge, 2001; Hamer et al., 2013).

The double-peaked nature of the CO emission, also previously identified by Hamer et al. (2013), has so far only been detected in a small fraction of elliptical brightest cluster galaxies (e.g. Lim et al., 2000; Salomé et al., 2011). This is due to the low probability of a galactic disc lying almost perfectly edge-on along the line-of-sight.

Moments maps of the high angular resolution CO(2-1) data, also produced using `CASA`'s `immoments` task, show the velocity structure of the disc in greater detail. The intensity-weighted velocity map in the left panel of Fig. 3.4 shows that the brightest cluster galaxy has an average line-of-sight velocity gradient of ~140 km s^{-1} kpc^{-1}.

Throughout, the intensity-weighted velocity dispersion shown in the right panel of Fig. 3.4, remains small and never exceeds ~50 km s^{-1}, implying that the cold gas within the disc is undergoing relatively ordered rotation without large proportions deviating from this significantly.

The shape of the molecular emission from Hydra-A is strongly suggestive that its molecular gas is being viewed edge-on, and is either in the form of a smooth disc, or a ring. The rotational velocities of brightest cluster galaxies with disc shaped molecular gas distributions tend to peak at low radii, before flattening out. However, Fig. 3.4 shows that the rotational velocity continues to increase at large radii, making a ring shaped distribution more plausible.

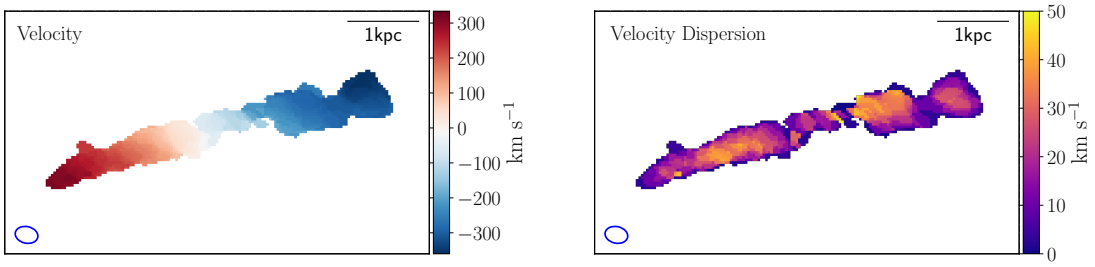

Figure 3.4

Moments maps of $\geq 5\sigma$ CO(2-1) emission produced using `CASA`'s `immoments` task (McMullin et al., 2007). **Left:** The intensity-weighted velocity of the CO(2-1) line emission relative to the galaxy's systemic recession velocity, showing a disc of cold molecular gas with a line-of-sight velocity gradient of ~140 km s^{-1} kpc^{-1} running across the galaxy's dust lane. **Right:** The intensity-weighted velocity dispersion of the CO(2-1) emission, which remains significantly smaller than the rotation velocity throughout all but the very centre of the disc. This suggests that the cold molecular gas within Hydra-A's disc is undergoing relatively ordered rotation.

This is further demonstrated by the turbulent Taylor number, the ratio of the rotational velocity to the velocity dispersion. The values found here may be affected by beam smearing, but should nevertheless be provide a good approximation, thus making it clear from Fig. 3.4 that the turbulent Taylor number is > 1 throughout the majority of the disc i.e. the rotation velocity dominates over the velocity dispersion.

It does however appear to fall below unity in a small region which is coincident with the mm-continuum source – probably because at this point the disc rotation is transverse to the line-of-sight. Chaotic cold accretion simulations (e.g. Gaspari et al., 2015, 2017), show that where the turbulent Taylor number does reach unity, gas condensation becomes increasingly clumpy (as is seen in the example of NGC 7049, described by Juráňová et al., 2018).

Although the velocity dispersion remains small throughout the disc, there are small increases approximately half-way between the galaxy centre and the edges of its visible disc of cold gas which coincide with the peaks in the intensity of the CO emission seen in both Fig. 3.2 and 3.3.

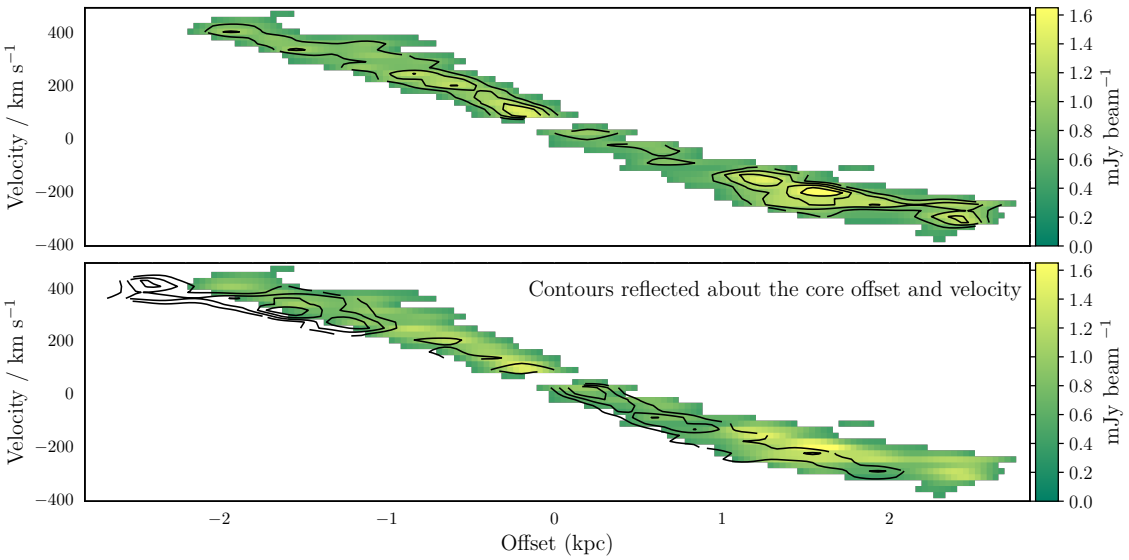

Figure 3.5

Top: Position-velocity diagram of Hydra-A's $\geq 5\sigma$ CO(2-1) emission along the kinematic axis of the disc, with integrated brightness contours of 0.75, 1.0, 1.25 and 1.5 mJy beam^{-1}. The offset is centred at the position of the continuum source and the velocity is centred at Hydra-A's recession velocity. **Bottom:** Integrated brightness contours reflected about the velocity and offset of the core highlight the slight asymmetry within the disc. Though the disc has a largely symmetric velocity distribution, there is an extended emission region at the extreme edge of the blueshifted side of the disc.

The increase in the velocity dispersion occurs where the change in the rotational velocity of the disc with respect to the orbital radius is highest, as is demonstrated by the position-velocity diagram shown in Fig. 3.5.

The position-velocity diagram also shows that there are no significant inflows or outflows of cold molecular gas from the disc, as well as highlighting some asymmetry; the blueshifted side of the disc extends to around 2.5 kpc, while the redshifted side extends to around 2 kpc.

3.4 Molecular Gas Mass of the Disc

The total mass of cold molecular gas in Hydra-A can be estimated from both the CO(1-0) and CO(2-1) emission measured along the galaxy's disc using the following relation from Bolatto et al. (2013),

$$M_{\rm mol} = \frac{1.05\times10^4}{F_{ul}}\left(\frac{X_{\rm CO}}{2\times10^{20}\,\frac{\rm cm^{-2}}{\rm K\ km\ s^{-1}}}\right)\left(\frac{1}{1+z}\right) \times\left(\frac{S_{\rm CO}\Delta v}{\rm Jy\ km\ s^{-1}}\right)\left(\frac{D_{\rm L}}{\rm Mpc}\right)^2 M_\odot\ , \tag{3.4.1}$$

where $M_{\rm mol}$ is the mass of molecular hydrogen, $X_{\rm CO}$ is the CO-to-H_2 conversion factor, z is the redshift of the source, $S_{\rm CO}\Delta v$ is the CO emission integral, $D_{\rm L}$ is the luminosity distance in Mpc and $M_\odot$ is a solar mass. F_{ul} is a factor which is included as an approximate conversion between the expected flux density ratios of the two lines, where u and l represent the upper and lower levels.

For CO(1-0), $F_{10} = 1$ and for CO(2-1) a value of $F_{21} = 3.2$ has been used. This value is consistent with similar studies (e.g. David et al., 2014; Tremblay et al., 2016; Temi et al., 2018b), and originates from a combination of the factor of two between the frequencies of the lines and the brightness temperature ratio observed for molecular clouds in spiral galaxies of 0.8 (Braine & Combes, 1992).

Hydra-A is at a redshift of $z = 0.0543519$ and a distance of $D_{\rm L} = 242.4$ Mpc. A standard

value of $X_{\rm CO} = 2 \times 10^{20}$ cm^{-2} (K km s^{-1})$^{-1}$ is used for the CO-to-H_2 conversion factor, as previously done by e.g. Bolatto et al. (2013); David et al. (2014); Tremblay et al. (2016).

To determine the mass of cold molecular hydrogen in Hydra-A's disc and its uncertainties, Monte Carlo simulations which allow us to estimate the emission integral for the spectra shown in Fig. 3.2 are performed in the following way.

Firstly, for each spectrum the noise in the observed spectrum was estimated from the root mean square (rms) of the continuum emission. This was calculated after excluding the region where the emission is clearly visible (-600 km s^{-1} to +600 km s^{-1}).

Following this, 100 000 simulated spectra are created based upon the observed spectrum. To produce each simulated spectrum, a Gaussian distribution is created for each velocity channel. This Gaussian distribution is centred at the intensity in the observed spectrum for that particular velocity channel, and has a variance equal to the rms noise squared.

A random value for the intensity is drawn from the Gaussian distribution and when this has been done across all velocity channels, a simulated spectrum is produced. A double-Gaussian line provides the best fit and for each of the 100 000 spectra produced such a fit is found using χ^2 minimisation.

Finally, the molecular mass is found by using Eq. 3.4.1 and the median value resulting from the 100 000 estimates of $S_{\rm CO}\Delta v$. The upper and lower 1σ errors are taken from the values which delimit the 15.865 per cent highest and lowest results for each of the fits (i.e. 68.27 per cent of the fitted parameters will therefore lie within this 1σ range).

This procedure treats the CO(1-0) and CO(2-1) spectra independently and provides two inferred masses for Hydra-A's cold molecular gas. Using the CO(1-0), gives an estimated mass of $M_{\rm mol} = 1.06^{+0.02}_{-0.02} \times 10^9$ M$_\odot$, while for the CO(2-1), gives an estimated mass of $M_{\rm mol} = 5.6^{+0.1}_{-0.1} \times 10^9$ $M_\odot$.

It is important to note that the errors quoted in these values are due to the noise seen in each of the spectra. In reality, the molecular mass may differ from the estimated values by as much as an order of magnitude due to the uncertainty surrounding the values of the X-factor and the conversion factor, F_{ul}.

However, given these larger errors, the masses found are consistent with the value of $M_{\rm mol} = 2.26 \pm 0.29 \times 10^9\ M_\odot$ found from *Institut de RadioAstronomie Millimétrique* (IRAM) 30m observations of CO(2-1) emission presented in Hamer et al. (2013) and are typical molecular gas masses when compared with those found through CO detections for other brightest cluster galaxies with cooling flows (e.g. Edge, 2001; Salomé & Combes, 2003).

3.5 Cold, Clumpy Gas Clouds

As can be seen in Fig. 3.2, the CO(1-0) and CO(2-1) spectra from Hydra-A's disc show the presence of a narrow absorption feature close to the zero-velocity point, caused by molecular clouds which lie along the line-of-sight to the bright mm-continuum source.

Due to the high angular resolution of the CO(2-1) observations, this absorption can be seen in more detail by extracting spectra from a much smaller region. The left panel of Fig. 3.6 shows the continuum-normalized CO(2-1) spectrum along the line-of-sight to the mm-continuum source, taken from the region shown by the small, dashed white circle in Fig. 3.3. The spectrum, which is centred on the stellar recession velocity of the galaxy, has two main features.

Firstly, there is a broad emission component. This can also be seen across the rest of the galaxy's disc and is produced by a large-scale ensemble of molecular gas clouds. It is this component which, when summed across the disc, produces the double-peaked spectrum seen in Fig. 3.2.

Secondly, the spectrum reveals a group of absorption features which are produced by the cold molecular gas clouds which lie along the line-of-sight to the bright and unresolved continuum source. Importantly, the compact nature of the continuum source ensures that we are probing a single line-of-sight and seeing no contamination from more extended emission. These absorption features appear to be unique to the radio core of the galaxy and do not arise elsewhere, such as along the line-of-sight to the bright spots in galaxy's radio lobes.

To show the strength of the absorption more clearly, the broad emission component is removed by fitting and subtracting a Gaussian line to the spectrum, with the Gaussian fit excluding the spectral bins where absorption can be seen (approximately -48 to -1 km s^{-1}, as indicated by the vertical grey lines in Fig. 3.6).

This region was chosen by performing Gaussian fits to the emission after applying masks to the spectrum with limits at every spectral bin between -55 ± 10 km s^{-1} and +5 ± 10 km s^{-1}. The selected range produces a spectrum with the lowest χ^2_ν value when the non-masked region is fitted to a flat line after the removal of the emission. The right panel of Fig. 3.6 shows the spectrum after the subtraction of the optimum Gaussian fit.

Following this correction, an apparent optical depth profile, τ_a, was calculated from the observed intensities using the relation (Savage & Sembach, 1991),

$$\tau_a = \ln\left[I_0/I_{obs}(\lambda)\right], \tag{3.5.1}$$

where I_0 is the continuum intensity (independent of λ over the wavelength range observed) and $I_{obs}(\lambda)$ is the observed intensity.

Due to the high signal to noise ratio and because the spectrum's velocity resolution is relatively high compared with the line widths, the calculations of τ_a are likely to be minimally affected by the instrumental spread function. In this case τ_a is a good representation of the optical depth, τ, and so the two are treated as being equivalent.

Gaussian lines are used for simplicity, and the combination of three provides the best fit to the absorption features seen in Fig. 3.6. As such, the properties of these emission lines can be estimated using an appropriately modified version of the Monte Carlo method previously described in §3.4.

By assuming a filling factor of 1, the calculations provide a lower limit on the optical depths of the absorbing regions. The estimates for the optical depths of the absorbing regions are shown in Table 3.2, along with their velocities, v_{cen}, and the FWHM of the lines. As well as the observed MUSE stellar redshift the spectrum is centred on, the velocities of the absorption regions relative to the line-of-sight emission are shown, since this provides a second plausible value for the zero velocity reference point.

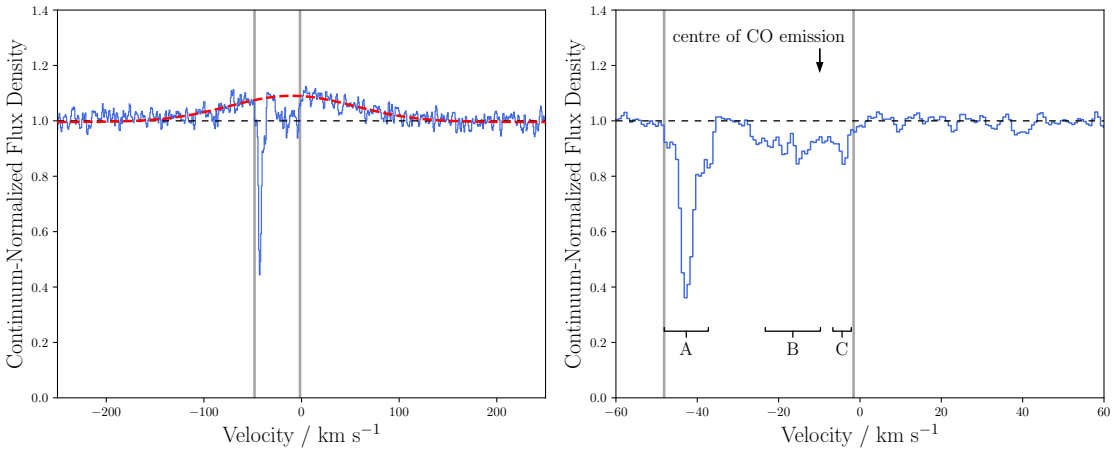

Figure 3.6

Left: Hydra-A's continuum-normalized CO(2-1) spectrum, extracted from the region lying along the line-of-sight to the bright mm-continuum source (the exact region is shown by a dashed, white circle in Fig. 3.3). The spectrum shows a broad emission component (FWHM=151^{+8}_{-7} km s^{-1}) and very clear absorption regions. The broad component is present throughout the disc and is produced by emission from a large scale ensemble of cold molecular gas clouds. To show the strength of the absorption regions more clearly, a Gaussian line is fitted to the spectrum (shown in red). This fit is made after excluding the spectral bins where absorption is visible (approximately -48 km s^{-1} to -1 km s^{-1}, indicated by the vertical grey lines). **Right:** The continuum-normalized CO(2-1) spectrum extracted from the region lying along the line-of-sight to the mm-continuum source, with the broad emission component removed. The absorption features are due to cold molecular gas clouds which are likely to be within ~200 pc of the supermassive black hole. The best fit parameters of the absorbing regions labelled 'A', 'B' and 'C' are shown in Table 3.2.

Region	v_{cen} / km s^{-1}	v_{cen} - $v_{emission}$ / km s^{-1}	FWHM / km s^{-1}	τ_{max}
Emission	-10^{+2}_{-2}	-	151^{+8}_{-7}	-
A	$-42.8^{+0.1}_{-0.1}$	-33^{+2}_{-2}	$4.4^{+0.3}_{-0.3}$	$0.88^{+0.06}_{-0.06}$
B	$-16.5^{+0.8}_{-0.8}$	-7^{+2}_{-2}	17^{+2}_{-2}	$0.11^{+0.01}_{-0.01}$
C	$-4.4^{+0.2}_{-0.3}$	$+6^{+2}_{-2}$	$2.3^{+1.6}_{-0.8}$	$0.13^{+0.03}_{-0.03}$

Table 3.2

Best fit parameters for the broad emission and absorption regions along the line of sight to Hydra-A's mm-continuum source, as seen in Fig. 3.6. The 1σ errors in the v_{cen} values are in addition to the systemic uncertainty of 15 km s^{-1} in the recession velocity of Hydra-A taken from MUSE observations of stellar absorption lines. The velocities of the absorption regions relative to the centre of the CO(2-1) line-of-sight emission are also included, since this provides a second plausible value for the zero velocity reference point.

One particularly strong absorption feature (labelled 'A' in Fig. 3.6) can be seen in the spectrum, where a peak of around 60 per cent of the continuum emission is absorbed. This has a narrow line width of FWHM=$4.4^{+0.2}_{-0.3}$ km s^{-1}. At the time this chapter was published, it was the narrowest such absorption feature found in a brightest cluster galaxy – and was only superseded by higher resolution observations of the same galaxy which are presented in Chapter 4.

Previous observations by David et al. (2014); Tremblay et al. (2016) have comparable velocity resolution, so this is unlikely to be the narrowest feature observed purely because their absorption regions are not sufficiently resolved in velocity.

This absorption region is found to have a high peak optical depth of τ=$0.88^{+0.06}_{-0.06}$. Therefore, it is also by far the deepest intrinsic CO absorption line detected so far in a brightest cluster galaxy, with the next strongest being found in Abell 2597 with an optical depth of τ ~0.3 (Tremblay et al., 2016).

At the line's peak around ~60 per cent of the emission from the continuum source is being absorbed, either by optically thick gas which covers ~60 per cent of the continuum source spatially, or by more diffuse gas which completely covers the source's synthesised beam with an optical depth of τ ~0.9.

Further absorption regions due to clouds moving away from the mm-continuum source at slightly lower velocities are also present. The central velocity, FWHM and peak optical depth of each of these absorption features are also shown in Table 3.2.

Collectively, these absorption features reveal the presence of cold molecular gas clouds moving relative to the galaxy's central supermassive black hole at velocities of between -43 and -4 km s^{-1}. However, these are simply apparent motions along the line-of-sight and do not necessarily imply that the gas clouds are flowing away from the galaxy centre at those velocities.

Nevertheless, simulations predict that over long periods of time clouds such as those observed here experience collisions in the inner region which reduce their angular momentum. This disrupts their relatively stable, slightly elliptical orbits and funnels them towards the galaxy's supermassive black hole (Gaspari et al., 2017; Gaspari et al., 2018). However, it

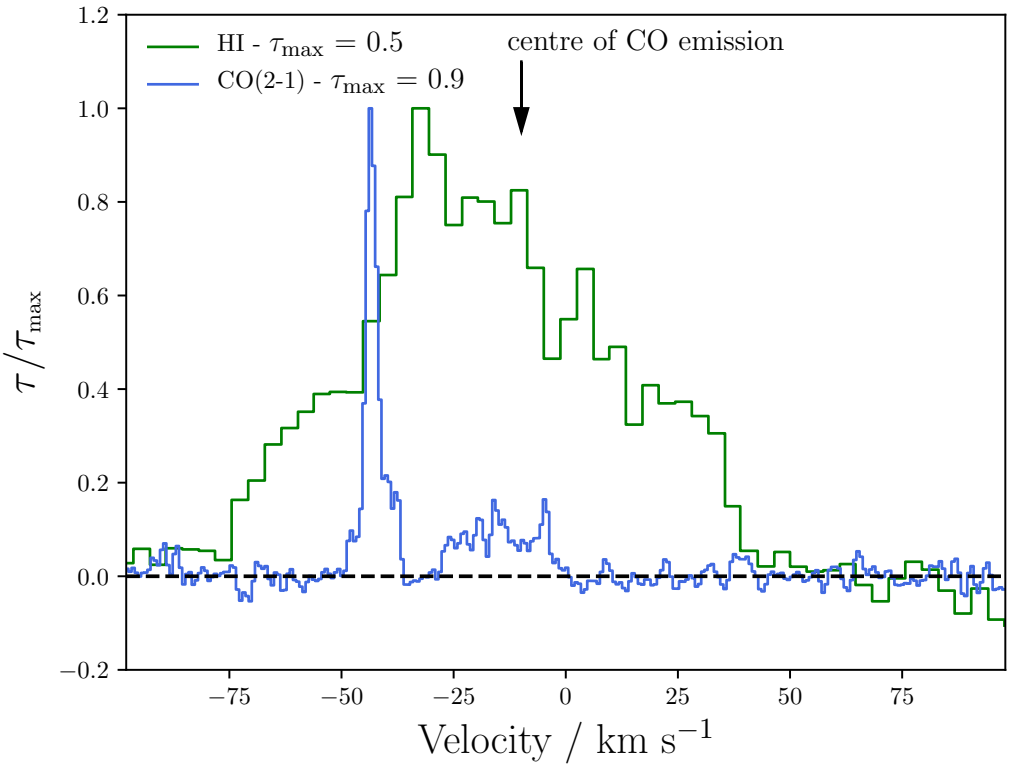

Figure 3.7

Hydra-A's normalized CO(2-1) and H I optical depth profiles for the region co-spatial with the mm-continuum source. The CO(2-1) optical depth profile is produced using the spectrum shown in the the right panel of Fig. 3.6, and the H I profile is taken from VLBA observations presented in Taylor (1996).

is also possible that the slightly blueshifted velocities seen could be due to a bar, though this would typically associated with lower mass spiral galaxies.

As well as cold molecular gas, warmer atomic gas has also been detected in Hydra-A with the *Very Long Baseline Array* (VLBA) telescope (Taylor, 1996). These observations detect H I gas in absorption along multiple lines-of-sight close to the centre of the galaxy; absorption is seen against the knots of the active galactic nucleus's jets, as well as against the extremely bright continuum source.

The optical depth profiles of the H I and CO(2-1) absorption for the line-of-sight to the continuum source are shown in Fig. 3.7, where both have been peak-normalized to aid

comparison.

The H I line lies at 1.4 GHz and the CO(2-1) line lies at 230 GHz. Due to the large difference in these frequencies, if there are spectral index variations or synchrotron opacity effects in the radio core, it is possible that different parts of the core would dominate at the different frequencies. However, in both cases the absorption is observed against an unresolved core and so this should not be an issue when comparing the two spectra.

Both the warm atomic gas and cold molecular gas appear to be centred at slightly blueshifted velocities relative to the supermassive black hole. Additionally, both absorption profiles have velocity ranges with comparable widths and profiles which may suggest that the clouds detected as a narrow CO(2-1) line are visible as a blended H I line. Given that the clouds are spatially coincident, if this is the case it would be consistent with the hypothesis that when heated, cold molecular gas regions produce an encompassing skin of warm atomic gas (e.g. Jaffe et al., 2005). With the exception of the small velocity discrepancy between the peaks in the optical depths of the atomic and molecular gas, this relationship is similar to that seen in Abell 2597 (Tremblay et al., 2016) and demonstrates the need for an increase in the number of joint CO and H I observations to advance our understanding of the link between the atomic and molecular gas and how they fit into the predictions of accretion models and simulations.

Nevertheless, if Hydra-A and similar absorption lines systems (e.g. David et al., 2014; Tremblay et al., 2016) are shown to be caused by gas in the central regions of these galaxies, they will provide a strong argument against models related to Bondi accretion, which rely upon the smooth and spherically symmetric accretion of hot gas. The detections made so far are more consistent with the predictions of clumpy accretion models such as chaotic cold accretion.

3.6 Temperature and Column Density Derivations

Although the angular resolution of the CO(2-1) observations is considerably higher than those of CO(1-0), both have sufficient spectral resolution to show the narrow absorption

along the line-of-sight to the mm-continuum source. Fig. 3.8 shows the spectra for each CO line, extracted from the region shown by the large, dashed red circle in Fig. 3.3, which is of a similar size to the CO(1-0) beam.

The strength of the CO(1-0) absorption line is primarily dependent on the number of CO molecules in the ground rotational state (J=0), whereas the absorption line observed in CO(2-1) primarily depends on the number of molecules in the first rotational state (J=1).

The relative number of molecules in these two states is determined by the temperature of the gas. Therefore, the ratio of the optical depth values for these two absorption lines will give a direct measure of the gas temperature, assuming that the lines are not optically thick.

Due to the lower resolution and larger beam size of the CO(1-0) observations, only the most strongly absorbing region remains clearly visible in both spectra when the larger extraction region is used, so it is only possible to estimate the temperature for this absorption region.

For optically thin gas in local thermodynamic equilibrium, the CO(1-0) and CO(2-1) velocity integrated optical depths are related by,

$$\frac{\int \tau_{21} dv}{\int \tau_{10} dv} = 2 \frac{1 - e^{-h\nu_{21}/kT_{\rm ex}}}{e^{h\nu_{10}/kT_{\rm ex}} - 1} \ , \tag{3.6.1}$$

where h and k are the Planck and Boltzmann constants, ν_{10} and ν_{21} are the rest frequencies of the CO(1-0) and CO(2-1) lines and $T_{\rm ex}$ is the excitation temperature (Bolatto et al., 2003; Godard et al., 2010; Mangum & Shirley, 2015).

In the above, CO is approximated to being a stiff molecule such that ν_{10} and ν_{21} differ by a factor of two. To estimate $T_{\rm ex}$ for the strongly absorbing cloud, calculations using a Monte Carlo approach similar the one described in §3.4 were carried out, again using 100 000 simulated spectra for each line.

For each pair of simulated spectra, the emission is removed and the optical depth integrals are estimated using a single Gaussian fit to each line. Eq. 3.6.1 can then be used to calculate $T_{\rm ex}$ numerically, and this gives a cloud excitation temperature of $T_{\rm ex} = 42^{+25}_{-11}$ K.

Using the derived excitation temperature, it is also possible to estimate the total column density, $N_{\rm tot}$, of the absorption region. In general,

$$N_{\rm tot} = Q(T_{\rm ex}) \frac{8\pi\nu_{ul}^3}{c^3} \frac{g_l}{g_u} \frac{1}{A_{ul}} \frac{1}{1 - e^{-h\nu_{ul}/kT_{\rm ex}}} \int \tau_{ul} dv \ , \tag{3.6.2}$$

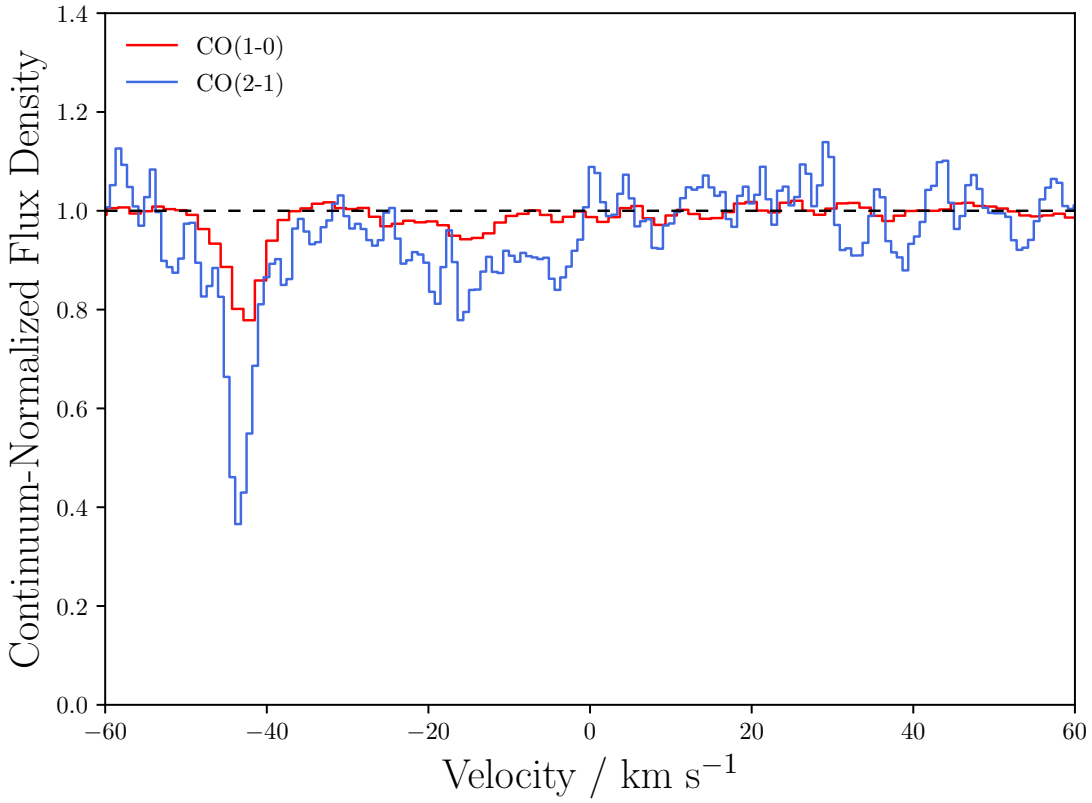

Figure 3.8

Hydra-A's continuum-normalized CO(1-0) and CO(2-1) flux density after the removal of the emission which is seen across the galaxy's disc. These spectra are both extracted from the region indicated by the large, dashed red circle in Fig 3.3. A wider region is used to extract these spectra due to the larger beam size of the CO(1-0) images. By comparing the strength of the absorption seen for the two lines, one finds that the absorbing gas has a temperature of $T_{\rm ex} = 42^{+25}_{-11}$ K and line-of-sight column densities of $N_{\rm CO} = 2^{+3}_{-1} \times 10^{17}{\rm cm}^{-2}$ and $N_{\rm H_2} = 7^{+10}_{-4} \times 10^{20}{\rm cm}^{-2}$.

where $Q(T_{ex})$ is the partition function, c is the speed of light, A_{ul} is the Einstein coefficient of the observed transition and g the level degeneracy, with the subscripts u and l representing the upper and lower levels (Godard et al., 2010; Mangum & Shirley, 2015).

Using the derived excitation temperature and the velocity integrated optical depth of the CO(2-1) line gives a line-of-sight CO column density of $N_{CO} = 2^{+3}_{-1} \times 10^{17}\text{cm}^{-2}$; a similar CO column density to the absorption regions identified by e.g. (Wiklind et al., 2018).

This value can also be used to estimate the column density of molecular hydrogen by assuming a carbon abundance equal to the Milky Way gas phase, and assuming that all gas-phase carbon exists in CO molecules (Sofia et al., 2004). In this case, there is a conversion factor of $CO/H_2 = 3.2 \times 10^{-4}$, giving an H_2 column density of $N_{H_2} = 7^{+10}_{-4} \times 10^{20}\text{cm}^{-2}$.

Observations of Hydra-A's X-ray emission by Russell et al. (2013) have also been used to estimate the total H_2 column density along the line-of-sight to the core. They find a value of $N_{H_2} = 3.5 \pm 0.3 \times 10^{22}$ cm^{-2}, many times larger than the value estimated here. However, this difference is likely due to the estimate calculated here being for the mass of gas which lies in the most strongly absorbing region. The X-ray observations of Russell et al. (2013) would instead probe all of the gas along this line-of-sight.

3.7 Discussion

The near edge-on orientation of Hydra-A's dust and gas discs is a rarity and so these observations provide a unique opportunity to analyse the dynamics of its molecular gas disc with crucial knowledge of how it is placed within the overall structure of the galaxy.

The principal absorption line detected in Hydra-A is by far the deepest found to date in a brightest cluster galaxy, with a peak CO(2-1) optical depth of $\tau = 0.88^{+0.06}_{-0.06}$, a temperature of $T_{ex} = 42^{+25}_{-11}$ K and line-of-sight column densities of $N_{CO} = 2^{+3}_{-1} \times 10^{17}\text{cm}^{-2}$ and $N_{H_2} = 7^{+10}_{-4} \times 10^{20}\text{cm}^{-2}$.

The strength of this absorption is likely due to the edge-on nature of the disc. As a result of this orientation, the column density of the molecular gas intersecting the line-of-sight to the mm-continuum source is particularly high and so very strong absorption is seen.

Although it is not possible to directly measure the velocity component of the molecular gas clouds orthogonal to the line-of-sight, the ∼140 km s^{-1} kpc^{-1} line-of-sight velocity gradient across the disc of the galaxy implies that unless they lie at very large radii, they should be significantly larger than the infall velocities of the molecular clouds. However, it is unlikely that the clouds detected lie at large distances from the supermassive black hole. Simulations by Gaspari et al. (2017) of clumpy molecular gas condensation show that the volume filling factor and internal density of molecular clouds are both inversely proportional to radius. Most of the dense, absorbing gas contributing to the line-of-sight obscuration is therefore expected to reside in the inner region, within radii of up to ∼200 pc.

Conversely, the clouds' low velocities relative to the supermassive black hole suggest that they lie beyond the Bondi capture radius of ∼10 pc, within which they would gain large velocities towards the core due to the increasing likelihood of collisions and the strength of the supermassive black hole's gravitational field.

Regarding the velocity structure of the disc, the large inferred horizontal velocities, combined with the comparatively small line-of-sight velocities of a few tens of km s^{-1} away from the core, suggest the molecular clouds are moving within a relatively stable, slightly elliptical disc.

The asymmetry seen in Hydra-A's position-velocity diagram also point towards a low ellipticity disc. However, it is also possible that the non-circular motion inferred in the absorbing clouds may be caused by a bar, though this would typically be associated with spiral galaxies of lower mass.

In terms of the line-of-sight velocities of the molecular clouds, this observation is in contrast to those of David et al. (2014) and Tremblay et al. (2016), where velocities of $\sim 200 - 300$ km s^{-1} towards the supermassive black hole were observed.

Additionally, in Hydra-A's case the absorbing clouds along the line-of-sight to the core lie roughly at the centre of the broad CO emission (shown in the left panel of Fig. 3.6). According to CCA simulations, this implies that clouds are not yet falling within the black hole's region of influence (< 10 pc), but drifting in the turbulent field at up to ~ 200 pc

(Gaspari et al., 2017). However, as Fig. 3.3 shows, the molecular gas disc extends out to radii of around 2.5 kpc, so the majority of the molecular gas lies much further out than this.

In other words, these observations are simply showing a random sample of molecular clouds from a very narrow line-of sight, and their velocity dispersion correlates well with that which is found close to the core.

At the time of publication, this work represented one of very few detections of cold molecular gas lying in front of a brightest cluster galaxy's strong and unresolved mm-continuum source. As such, more general predictions regarding the properties of the molecular gas in other brightest cluster galaxies were difficult to make.

A more in depth survey of Hydra-A's absorption lines was needed to understand the properties of these molecular clouds in more detail, and a larger sample needed to investigate the properties of this molecular gas across a wider range of targets – and this provides the motivation for Chapters 4 and 5.

CHAPTER 4

A more in depth look at the molecular absorption lines in Hydra-A

This chapter is based on the following publication:

A molecular absorption line survey towards the AGN of Hydra-A · **Rose, Tom**; Edge, A. C.; Combes, F.; Hamer, S.; McNamara, B. R.; Russell, H.; Gaspari, M.; Salomé, P.; Sarazin, C.; Tremblay, G. R.; Baum, S. A.; Bremer, M. N.; Donahue, M.; Fabian, A. C.; Ferland, G.; Nesvadba, N.; O'Dea, C.; Oonk, J. B. R.; Peck, A. B. · 2020, MNRAS, 496, 364 (view publication)

4.1 Introduction

Most absorption line surveys, like the one described in the previous chapter, trace molecular gas using rotational lines of carbon monoxide. So far, all intrinsic absorption lines detected in BCGs have been in found this way.

Although the detection of these systems with CO alone is of great value, observing the same absorption regions with multiple molecular species has the potential to reveal the chemistry and history of the gas in the surroundings of supermassive black holes in much more detail, significantly increasing our understanding of the origins of the gas responsible for their accretion and feedback mechanisms.

This chapter presents high spectral resolution observations of the molecular absorption lines already detected in Hydra-A – previously identified with CO lines – but now seen with many more molecular species.

The observations in this chapter are from an *Atacama Large Millimeter/submillimeter Array* (ALMA) Cycle 6 survey originally designed to detect the absorption lines of several molecular species in Hydra-A, namely CO, ^{13}CO, C^{18}O, CN, HCN and HCO^{+}. A multi-wavelength view of Hydra-A, which highlights its main features can be seen in Fig. 4.1.

As shown in Chapter 3, Hydra-A has by far the most optically thick CO absorption of its kind, caused by clouds of cold, molecular gas lying along the line of sight to the bright radio source which is spatially coincident with the supermassive black hole. These clouds are almost entirely composed of hydrogen, though small but significant amounts of these less common molecules are present at sufficient abundances to produce detectable absorption lines.

Although no study of a single source can ever be representative of a whole family of astronomical objects, Hydra-A is a prime target for a study of this type for several reasons, perhaps most importantly because it is a giant elliptical galaxy with a near perfectly edge-on disc of dust and molecular gas, which should readily produce absorption lines in the spectrum of any radio source lying behind it (Hamer et al., 2014).

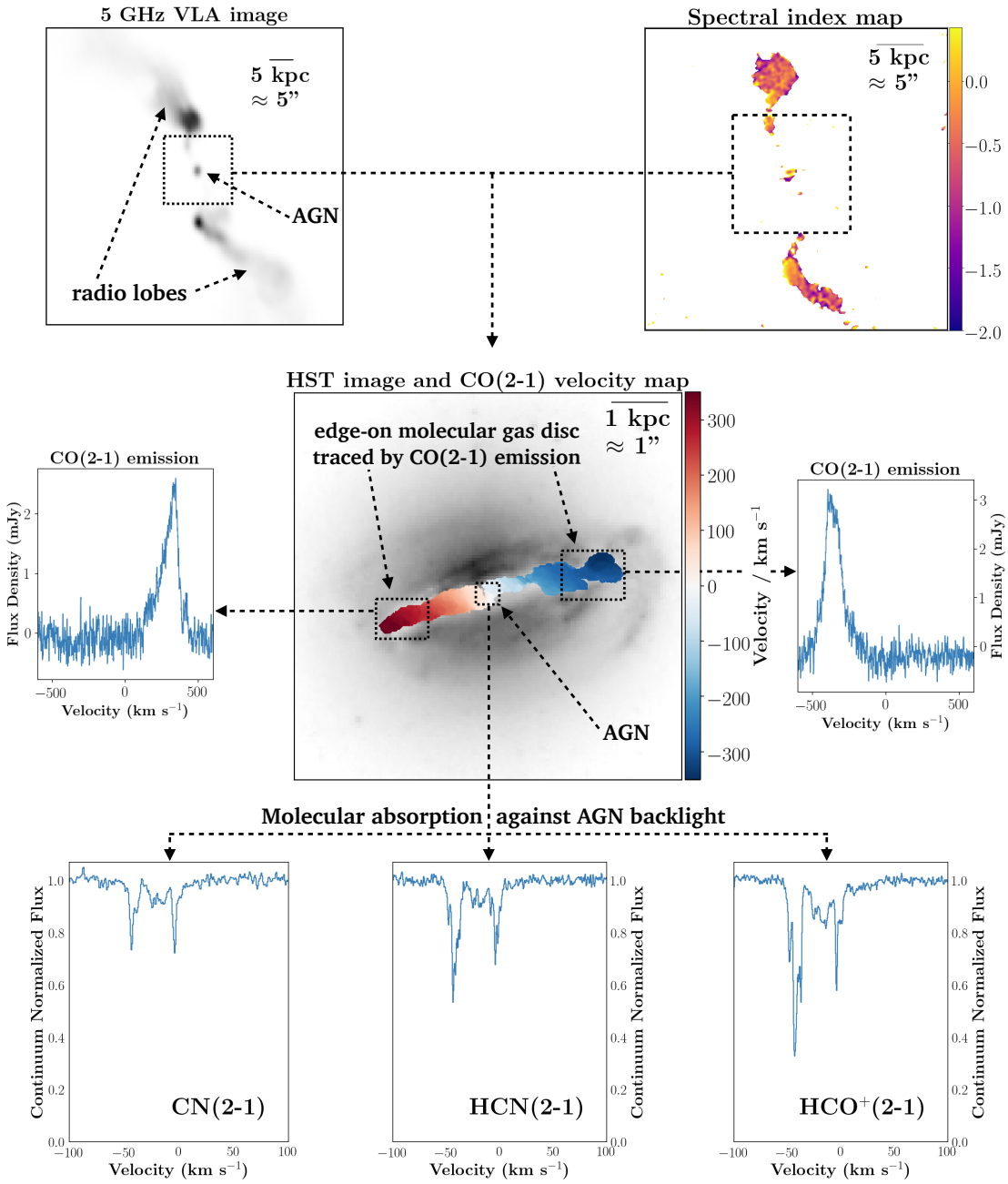
5 GHz VLA image
5 kpc
≈ 5”
AGN
radio lobes
Spectral index map
5 kpc
≈ 5”
0.0
−0.5
−1.0
−1.5
−2.0
HST image and CO(2-1) velocity map
edge-on molecular gas disc
traced by CO(2-1) emission
1 kpc
≈ 1”
AGN
300
200
100
0
−100
−200
−300
Velocity / km s−1
CO(2-1) emission
Flux Density (mJy)
Velocity (km s−1)
CO(2-1) emission
Flux Density (mJy)
Velocity (km s−1)
Molecular absorption against AGN backlight
Continuum Normalized Flux
CN(2-1)
Velocity (km s−1)
Continuum Normalized Flux
HCN(2-1)
Velocity (km s−1)
Continuum Normalized Flux
HCO+(2-1)
Velocity (km s−1)

Figure 4.1

A multi-wavelength view of Hydra-A's AGN, radio lobes and edge-on molecular gas disc. **Top left:** An unmasked 5 GHz *Karl G. Jansky Very Large Array* (VLA) image showing the galaxy's AGN and its radio lobes emanating to the north and south, with 0.19 arcsec pixel^{-1} resolution (Project 13B-088). **Top right:** A 0.29 arcsec pixel^{-1} spectral index map of the AGN and radio lobes, produced from continuum images at 92 and 202 GHz which were taken as part of the ALMA survey. **Centre:** A 0.05 arcsec pixel^{-1} F814W *Hubble Space Telescope* (HST) near-infrared image (Mittal et al., 2015). Overlaid is a velocity map which traces the galaxy's edge-on disc of cold molecular gas, produced using the ALMA observations of CO(2-1) emission. **Centre left and right:** The spectra of CO(2-1) emission from the red and blueshifted sides of the edge-on disc, also extracted from the ALMA data presented in this paper. **Bottom:** Some of the principal absorption lines seen against the continuum source at the galaxy centre, which is explored in this chapter. The absorption is produced by the cold molecular gas within the disc which lies along the line of sight to the bright radio core.

Combined with its compact and unresolved nature, this high flux density makes it an ideal backlight for an absorption line survey, particularly on searching for rarer molecular species than have ever been found in this type of system. This is especially true in this case, where the aim is to detect molecular species with relatively low column densities, such as CO isotopologues.

Throughout this chapter, velocity corrections applied to the spectra of Hydra-A use a redshift of $z = 0.0544 \pm 0.0001$, which provides the best estimate of the systemic velocity of the galaxy. This redshift is calculated from MUSE observations of stellar absorption lines (ID: 094.A-0859) and corresponds to a recession velocity of 16294 ± 30 km s^{-1}. Note that this is different to the error of 15 km s^{-1} used in Chapter 3. This is due to a change in the uncertainty in the redshift estimated from the MUSE observations. Rather than amending the the Chapters 3 and 4, they are kept in their original published form because the change has no significant impact on the results or their interpretation.

At the redshift used, there is a spatial scale of 1.056 kpc arcsec^{-1}, meaning that kpc and arcsec scales are approximately equivalent. The CO(2-1) emission line produced by the molecular gas disc also provides a second estimate for the galaxy's recession velocity of 16284 km s^{-1}, though this value has a larger uncertainty due to potential gas sloshing.

4.2 Observations and target lines

Observations at the expected frequencies of the CO(1-0), CO(2-1), ^{13}CO(2-1), C^{18}O(2-1), CN(2-1), HCO$^+$(1-0), HCO$^+$(2-1), HCN(1-0), HCN(2-1) and HNC(1-0) rotational lines in Hydra-A were carried out between 2018 July 18 and 2018 Dec 12 (PI: Alastair Edge). The CO(1-0) observation was carried out as part of an ALMA Cycle 4 survey (2016.1.01214.S), and the remaining were part of an ALMA Cycle 6 survey (2018.1.01471.S). Absorption from all of these lines except C^{18}O(2-1) was detected. Serendipitous detections of SiO(5-4) and H_2CO(3-2) were also made during the observations of the target lines.

The main details for each observation are given in Table 4.1. For these observations, Fig. 4.2 shows the spectra seen against the bright radio source at the centre of the galaxy. All

are extracted from a region centered on the continuum source with a size equal to the synthesized beam's FHWM.

Target lines	CO(1-0)	^{13}CO(2-1) C^{18}O(2-1) SiO(5-4)	CO(2-1) CN(2-1) H_2CO(3-2)	HCO$^+$(1-0) HCN(1-0) HNC(1-0)	HCO$^+$(2-1) HCN(2-1)
Observation date	2018 Jul 18	2018 Dec 12	2018 Oct 30	2019 Sep 24	2018 Nov 16
Integration time (mins)	44	215	95	48	85
Velocity width per channel (km s^{-1})	2.7	1.4	0.7	1.7	0.9
Frequency width per channel (kHz)	977	977	488	488	488
Beam dimensions (")	2.3×1.6	0.60×0.46	0.27×0.25	0.47×0.29	0.38×0.32
Spatial resolution (kpc)	1.71	0.54	0.29	0.44	0.36
Precipitable water vapour (mm)	2.85	1.59	0.96	3.21	1.04
Field of view (arcsec)	56.9	28.9	26.1	63.3	33.4
ALMA band	3	5	6	3	5
ALMA configuration	C43-1	C43-4	C43-5	C43-6	C43-5
Maximum baseline (m)	161	784	1400	2500	1400
Noise/channel (mJy/beam)	1.01	0.27/0.27/0.27	1.33/0.47/0.47	0.58/0.56/0.58	0.57/0.63

Table 4.1

A summary of the observational details for the ALMA data presented in this chapter. Each column of the table represents a different observation, with most containing multiple target lines.

With such a wide range of molecular lines targeted, the properties of the gas clouds responsible for the absorption can be revealed in significant detail. A short summary of the particular properties each molecular species can reveal about the absorbing gas clouds is provided below, as well as references to more in depth information. The dipole moments for the molecules observed are given in Table 4.2, along with the critical density and rest frequency of each line.

- **CO** (carbon monoxide) has a relatively small electric dipole moment which allows it to undergo collisional excitation easily. This makes it readily visible in emission and as a result it is commonly used as a tracer of molecular hydrogen, which has no rotational lines due to its lack of a dipole moment. CO is relatively abundant within the centres of brightest cluster galaxies and has many rotational lines which are sufficiently populated to produce observable emission and absorption lines. The variation in the absorption strengths of these different rotational lines can be used to estimate the excitation temperature of the gas (Mangum & Shirley, 2015). The strength of each absorption line is dependent on the number of CO molecules in each rotational state, which itself is determined by the gas excitation temperature. Therefore, the ratio of the optical depths for various absorption lines of CO can give a direct measure of the gas excitation temperature, assuming that the lines are not optically thick.

- ^{13}**CO**, when seen at high column densities, is normally associated with galaxy mergers and ultra-luminous infrared galaxies (Taniguchi et al., 1999; Glenn & Hunter, 2001). Interestingly, CO/^{13}CO values have been shown to correlate with star formation and top heavy initial mass functions (Davis, 2014; Sliwa et al., 2017). Variation in the CO/^{13}CO ratio is also seen within the Milky Way and other galaxies, with decreasing values associated with proximity to the galaxy centre as a result of astration (Wilson, 1999; Paglione et al., 2001; Vantyghem et al., 2017). ^{13}CO is typically at least an order of magnitude less abundant than CO, so the absorption lines of this isotopologue can be used to distinguish between optically thick clouds with a low covering fraction and more diffuse clouds which cover an entire continuum

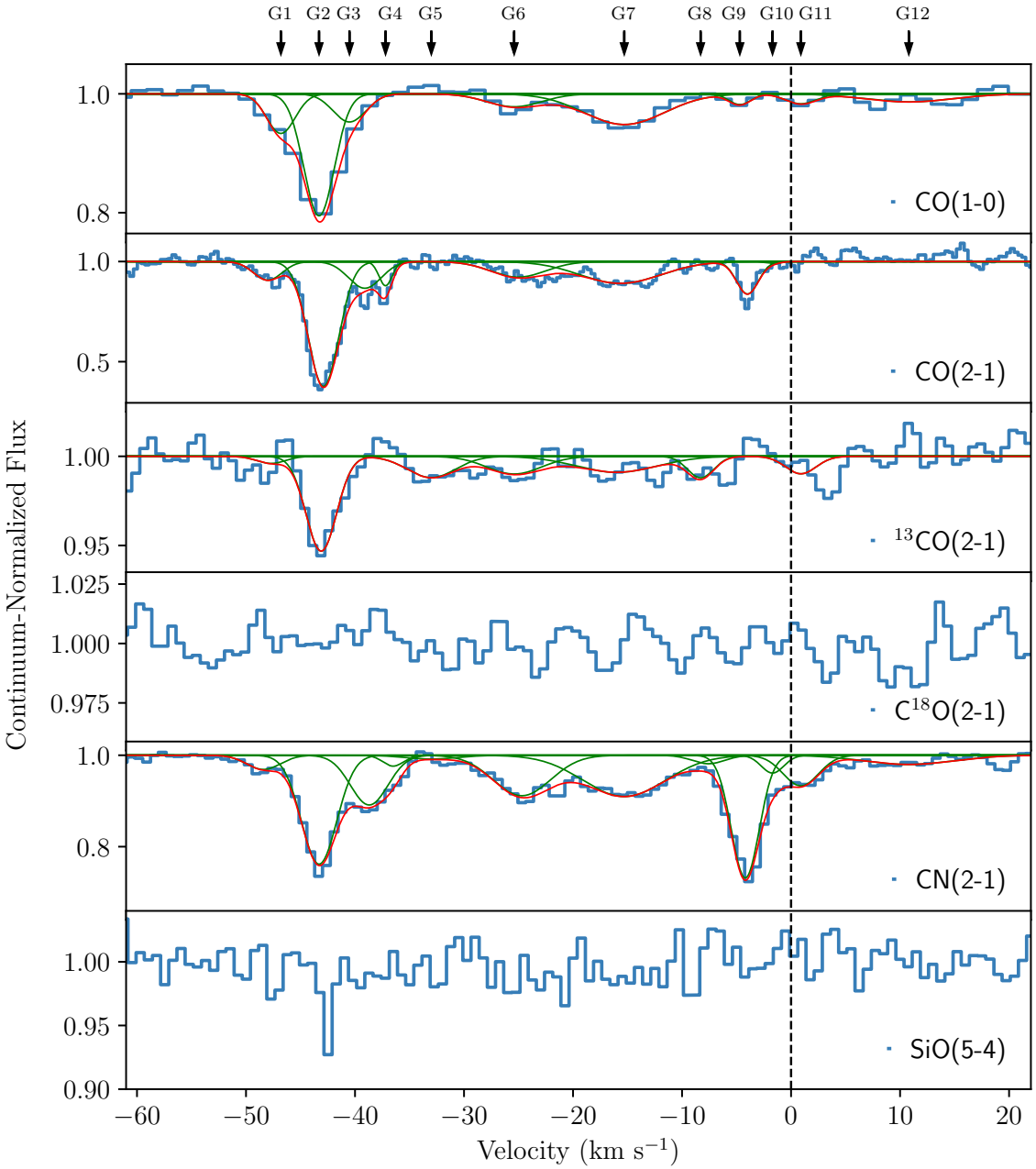
G1
G2
G3
G4
G5
G6
G7
G8
G9
G10
G11
G12
CO(1-0)
CO(2-1)
^{13}CO(2-1)
C^{18}O(2-1)
CN(2-1)
SiO(5-4)
Continuum-Normalized Flux
Velocity (km s^{-1})

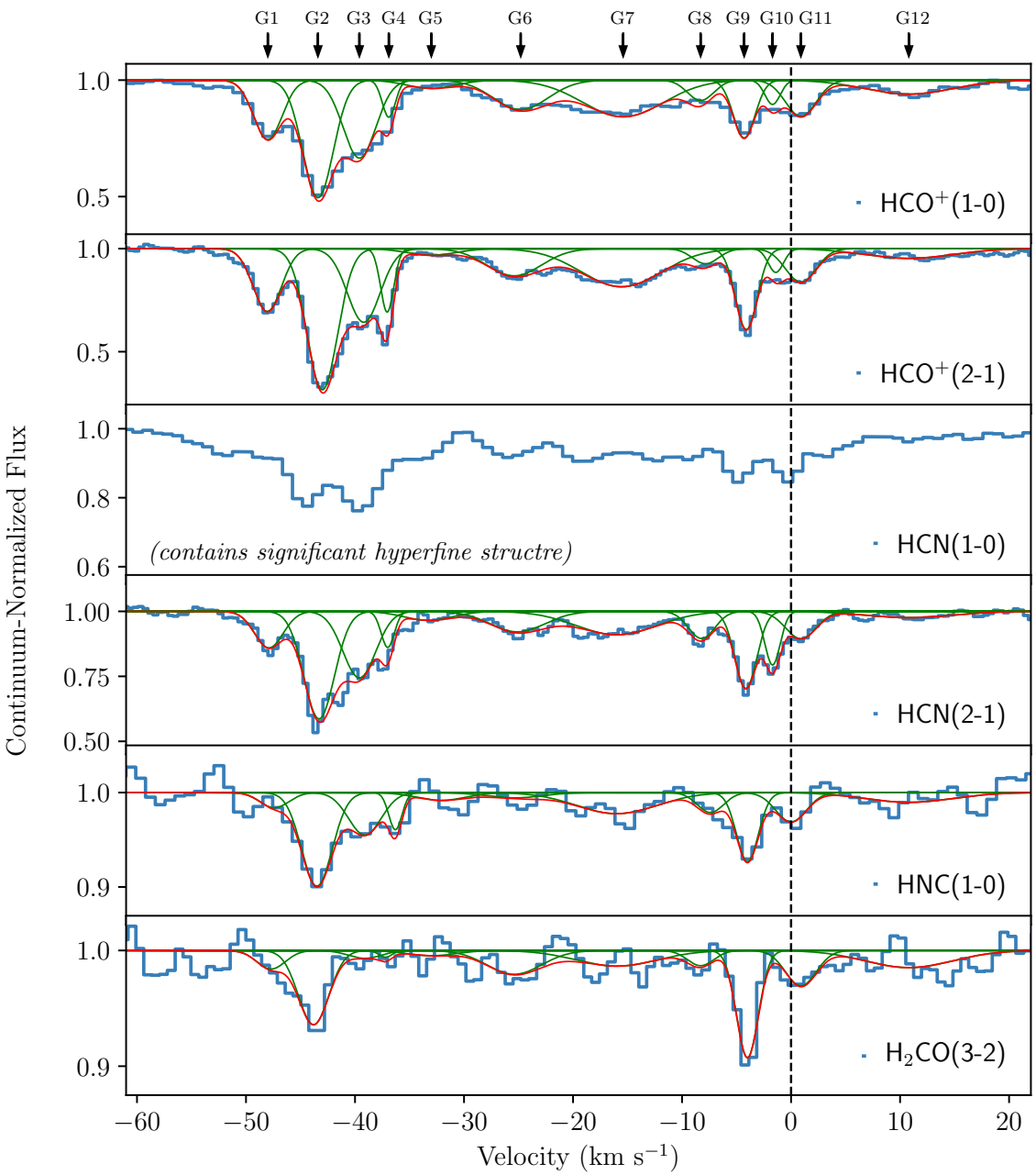
G1
G2
G3
G4
G5
G6
G7
G8
G9
G10
G11
G12
HCO+(1-0)
HCO+(2-1)
(contains significant hyperfine structre)
HCN(1-0)
HCN(2-1)
HNC(1-0)
H2CO(3-2)
Continuum-Normalized Flux
Velocity (km s−1)

Figure 4.2

Absorption profiles observed against the bright and compact radio continuum source at the centre of Hydra-A, which is spatially coincident with the brightest cluster galaxy's AGN and supermassive black hole. These spectra have a very narrow velocity range of approximately 80 km s^{-1} in order to show the absorption features clearly. The full width of the observed spectra is typically 2000 km s^{-1}, though no absorption features outside the velocity range shown are apparent. The spectra are extracted from a region with a size equal to the FWHM of each observation's synthesized beam. Green and red lines show the individual and combined 12-Gaussian best fits, where each of the 12 Gaussians has a freely varying amplitude across all of the spectra, but a fixed FWHM and central velocity (as indicated by the arrows at the top of the plot). The process by which the best fits are found is described in §4.3. Some of the 12 Gaussian lines may appear weak and unconvincing in some spectra, but all are resolved and detected to high significance in at least one absorption line. No reliable best fits are found for $C^{18}O$(2-1) or SiO(5-4).

source. For example, if a molecular cloud extinguishes 10 per cent of a continuum source's flux in CO(1-0), it may be an optically thin cloud with $\tau = 0.1$, or an optically thick cloud (i.e. $\tau \gg 1$) covering 10 per cent of the continuum. ^{13}CO(1-0) could distinguish between these scenarios; relative to ^{12}CO(1-0), its absorption would be more easily detected in the case of an optically thick cloud.

- **C^{18}O** contains the stable oxygen-18 isotope, which is predominantly produced in the cores of stars above 8 $M_\odot$ (Iben, 1975). The ratio of the absorption strength seen from ^{13}CO, C^{18}O, and other CO isotopologues can therefore be used as a probe of the star formation history of the molecular gas in which the molecules are observed (see Papadopoulos et al., 1996; Zhang et al., 2018; Brown & Wilson, 2019).

- **CN** (cyanido radical) molecules are primarily produced by photodissociation reactions of HCN. Its emission lines are therefore normally indicative of molecular gas in the presence of a strong ultraviolet radiation field (for a detailed overview of the origins of CN, see Boger & Sternberg, 2005). Models have shown that the production of CN at high column densities can also be induced by the strong X-ray radiation fields found close to AGN (Meijerink et al., 2007). Observations of CN emission lines from nearby galaxies show internal variation in the CO/CN line ratios of around a factor of three Wilson (2018). System to system variation in the CO/CN ratio of at least an order of magnitude is also observed in the absorption lines of brightest cluster galaxies (Chapter 5).

- **SiO** (silicon monoxide) is associated with warm, star-forming regions of molecular gas, where it is enhanced by several orders of magnitude compared with darker and colder molecular gas clouds. As a result, SiO is normally linked to dense regions and shocks, though it has occasionally been detected in low density molecular gas via absorption (e.g. Peng et al., 1995; Muller et al., 2013).

- **HCO$^+$**(formyl cation) and **HCN** (hydrogen cyanide) are tracers of low density molecular gas when seen in absorption, since it is only at low densities that the molecules are not collisionally excited to high J-levels. Their absorption lines have been detected in a handful of intervening absorber systems, e.g. Wiklind &

Combes (1997a); Muller et al. (2011). Due to their large electric dipole moments, the molecules have often been detected with relative ease despite being much less abundant than e.g. CO or CN (e.g. Lucas & Liszt, 1996; Liszt & Lucas, 2001; Gerin et al., 2019; Kameno et al., 2020).

- **HNC** (hydrogen isocyanide) is a tautomer of HCN. Thanks to its similar structure, it can be used as a tracer of gas properties in a similar manner to HCN and HCO^+. HNC detections may also useful in combination with those of HCN because of an observed dependence of the I(HCN)/I(HNC) ratio on the gas kinetic temperature (Hernández Vera et al., 2017; Hacar et al., 2019).

- **H_2CO** (formaldehyde) is highly prevalent towards H II regions and has been found throughout the interstellar medium at relatively high abundances which do not vary significantly, even in particularly chaotic regions (Henkel et al., 1983; Downes et al., 1980; Ginard et al., 2012). The molecule has several pathways of formation within the interstellar medium, split into two main groupings. First, it can form on the icy surfaces of dust grains. Second, it can be produced more directly in the gas phase. The formation of H_2CO on dust grains requires CO to be frozen onto the surface, so this mechanism mainly contributes to H_2CO gas at distances of hundreds of AU from stars, where temperatures are low enough for volatile molecules to condense (Qi et al., 2013; Loomis et al., 2015).

4.3 Data Processing

Transition	Dipole Moment / D	Critical Density / cm^{-3}	Frequency / GHz	Detected
CO(1-0)	0.112	4.1×10^2	115.271208	Yes
CO(2-1)	"	2.7×10^3	230.538000	Yes
^{13}CO(2-1)	0.112	2.7×10^3	220.398684	Yes
C^{18}O(2-1)	0.112	2.7×10^3	219.560354	No
CN(2-1)	1.450	1.4×10^6	226.874783*	Yes
SiO(5-4)	3.098	1.7×10^6	217.104980	Yes
HCO$^+$(1-0)	3.300	2.3×10^4	89.188525	Yes
HCO$^+$(2-1)	"	2.2×10^5	178.375056	Yes
HCN(1-0)	2.980	1.1×10^5	88.631602*	Yes
HCN(2-1)	"	1.1×10^6	177.261117*	Yes
HNC(1-0)	3.050	7.0×10^4	90.663568	Yes
H_2CO(3-2)	2.331	4.5×10^5	225.697775	Yes

*intensity weighted mean of hyperfine structure lines

Table 4.2

Dipole moments, critical densities and rest frequencies for the molecules discussed in this chapter. The critical densities are calculated at kinetic temperatures of 100 K.

The data presented throughout this chapter were handled using CASA version 5.6.0, a software package which is produced and maintained by the National Radio Astronomy Observatory (NRAO) (McMullin et al., 2007). The calibrated data were produced by the ALMA observatory and following their delivery, channel maps were made at maximal spectral resolution. The self-calibration of the images was done as part of the pipeline calibration.

The values used when converting from the observed frequencies to velocities are given in Table 4.2. The CN absorption profile in Fig. 4.2 is composed of three unresolved hyperfine structure lines of the N= 2-1, J=5/2-3/2 transition. The intensity weighted mean of these lines is used as the rest frequency.

The full CN(2-1) spectrum, including all of its observed hyperfine structure lines, can be seen in Appendix B. HCN(2-1) also contains hyperfine structure, though it is closely spaced enough that it does not significantly affect the appearance of the spectrum. HCN(1-0) contains hyperfine structure at separations which make resolving the 12 absorption regions unfeasible.

4.3.1 Line fitting procedure

Fig. 4.2 shows that the relative strengths of the absorption seen in a given velocity range of the spectrum can vary significantly between the molecular tracers. For example, in the CO(2-1) and H_2CO(3-2) spectra, the absorption features represented by G2 and G9 are the strongest. In CO(2-1) the first is significantly stronger than the second, wheres for H_2CO(3-2) the reverse is true.

The absorption is nevertheless produced by the same two regions of molecular gas, which will have the same velocity dispersion, σ, and central velocity, $v_{\rm cen}$, since they are determined by the clouds' gas dynamics and not the abundance of the molecular tracer they are observed with. To reflect this, a common multi-Gaussian best fit line is found which is composed of several Gaussian lines. Gaussian lines are used for simplicity, and each has a fixed σ and $v_{\rm cen}$ across all of the spectra, but a freely varying amplitude.

Line	v_{cen} / km s^{-1}	σ / km s^{-1}	T_{ex} / K	D / pc	M_{tot} / $M_\odot$
G1	−47.7	1.3	$5.1^{+0.5}_{-0.4}$	1.7	330
G2	−43.1	1.4	$21.0^{+54.6}_{-7.6}$	2.0	450
G3	−39.1	1.5	$4.7^{+0.3}_{-0.3}$	2.3	600
G4	−37.2	0.6	$9.7^{+3.8}_{-2.4}$	0.4	33
G5	−33.0	2.2	$4.3^{+4.6}_{-1.3}$	4.8	2.7×10^3
G6	−25.4	2.5	$4.6^{+0.7}_{-0.5}$	6.3	4.6×10^3
G7	−16.0	3.7	$4.8^{+0.3}_{-0.3}$	13.7	2.2×10^4
G8	−8.3	1.2	$3.4^{+0.6}_{-0.4}$	1.0	430
G9	−4.0	1.0	$7.2^{+1.0}_{-0.8}$	1.0	430
G10	−1.7	0.7	$4.9^{+1.8}_{-1.0}$	0.5	40
G11	0.9	1.4	$4.5^{+0.5}_{-0.4}$	2.0	450
G12	10.8	4.0	$3.5^{+0.7}_{-0.5}$	16.0	7.5×10^3

Table 4.3

The central velocities, velocity dispersions, excitation temperatures and corresponding diameters and masses of the absorption regions which make up the 12-Gaussian fit applied to each of the spectra shown in Fig. 4.2 . The fitting procedure by which the central velocities and velocity dispersions are found is described in detail in §4.3. The excitation temperatures are estimated from the HCO^+(1-0) and HCO^+(2-1) lines using using Equation 4.4.1, while the sizes and masses are found using a size-linewidth relation and with the assumption of virial equilibrium (see §4.6.2).

To find the minimum number of Gaussian lines needed for a good fit, and their σ and v_{cen}, the procedure starts with the three best resolved absorption lines: CO(2-1), HCO^+(2-1) and HCN(2-1). An initial fit was made using 10 Gaussian lines. This is the number which are clearest to the eye on initial inspection of the spectra. In the final fits to the data shown in the plots, these initial 10 are labeled as G1, G2, G3, G4, G6, G7, G8, G9, G10, and G11. G1, G2, G3, G4, G6, and G7 are most easily seen in the HCO^+(2-1) profile, while G8, G9, G10, and G11 are clearest in the HCN(2-1) profile. For the three spectra, best fits are found for a range of σ and v_{cen}. The values which provide the lowest reduced χ^2 across the three spectra are then used as the basis of the best fit line for all of the spectra. With a fixed σ and v_{cen}, the amplitudes of the Gaussian lines are then the only free parameters.

The initial 10 Gaussian fit is found to be insufficient, with $> 5\sigma$ absorption remaining in the residuals across several neighbouring channels. Two more Gaussians are added to the best fit line (labelled G5 and G12 in the final fit) to account for this extra absorption. Once again, the values of σ and v_{cen} which provide the lowest reduced χ^2 across the three spectra are then used as the basis of the best fit line for all of the spectra. The minimum number of Gaussians required to provide a good fit for all of the lines is found to be 12. The σ and v_{cen} of these lines is given in Table 4.3.

It is possible that some of the regions represented by each Gaussian line are made up from absorption due to multiple molecular clouds, rather than an individual one. If this is true a small shift in the central velocity of each Gaussian line across the different molecular transitions may result from any temperature, density or velocity dispersion gradient which exists along the line of sight. This was investigated for each molecular absorption line by allowing the v_{cen} of each Gaussian line to vary as a free parameter during the fitting process. The v_{cen} values resulting from this process were consistent with the fixed values, so it is not evident that this issue affects the fits shown in Fig. 4.2.

When applying the final 12 Gaussian fit to all of the spectra, the σ are fixed while the v_{cen} are pinned to a common value, but allowed to vary by up to an amount equal to the spectrum's velocity resolution. The amplitude of each Gaussian is the only free parameter and is able to take any value less than or equal to zero.

To find a final best fit line and errors for the spectra, the Monte Carlo approach described

in Chapter 3 is used. For each spectrum the noise was estimated from the root mean square (RMS) of the continuum emission. This was calculated after excluding the region where any emission or absorption is visible. Following this, 10 000 simulated spectra are created based upon the observed spectrum. To produce each simulated spectrum, a Gaussian distribution is created for each velocity channel. This Gaussian distribution is centred at the intensity in the observed spectrum for that particular velocity channel, and has a variance equal to the RMS noise squared.

A random value for the intensity is drawn from the Gaussian distribution and when this has been done across all velocity channels, a simulated spectrum is produced. The fitting procedure described above is then applied to each simulated spectrum to estimate the strength of each of the 12 Gaussian absorption regions. The upper and lower 1σ errors are taken from the values which delimit the 15.865 per cent highest and lowest results for each of the fits (i.e. 68.27 per cent of the fitted parameters will therefore lie within this 1σ range).

The $\sim 10^9 M_\odot$ of molecular gas present across the disc of the galaxy produces broad CO(1-0) and CO(2-1) emission lines with FWHM of hundreds of km s^{-1}. Since the primary interest is the significantly more narrow absorption features which lie at the centre of the emission, the emission is removed from the spectra in the following way.

First, a Gaussian fit is made to the emission. During the fitting process, the spectral bins in which absorption can be seen are masked, approximately -50 to $+10$ km s^{-1}. This masking region was chosen by performing Gaussian fits to the emission after applying masks to the spectra with limits at every spectral bin between -55 ± 10 km s^{-1} and $+5 \pm 10$ km s^{-1}.

The chosen range produces a spectrum with the lowest χ^2_ν value when the non-masked, emission-subtracted region is fitted to a flat line. Corresponding emission lines are not visible in the other molecular species due to their higher electric dipole moments, which makes collisional excitation less likely. The molecular emission lines are therefore so faint as to be undetectable given the integration times of the observations.

		G1	G2	G3	G4	G5	G6
v_{cen} / km s^{-1}		−47.7	−43.1	−39.1	−37.2	−33.0	−25.4
σ / km s^{-1}		1.3	1.4	1.5	0.6	2.2	2.5
CO(1-0)	τ_{max}	$0.07^{+0.02}_{-0.02}$	$0.35^{+0.04}_{-0.04}$	< 0.07	< 0.04	< 0.01	< 0.03
	$\int \tau dv$ / km s^{-1}	$0.10^{+0.03}_{-0.03}$	$0.52^{+0.06}_{-0.05}$	< 0.1	< 0.06	< 0.02	< 0.05
	N / $\times 10^{15}$cm^{-2}	$0.2^{+0.1}_{-0.1}$	$13.1^{+1.5}_{-1.3}$	< 0.2	< 0.4	< 0.1	< 0.2
CO(2-1)	τ_{max}	$0.10^{+0.01}_{-0.01}$	-	$0.15^{+0.01}_{-0.01}$	$0.13^{+0.02}_{-0.02}$	< 0.02	$0.086^{+0.007}_{-0.008}$
	$\int \tau dv$ / km s^{-1}	$0.15^{+0.02}_{-0.02}$	-	$0.22^{+0.02}_{-0.02}$	$0.20^{+0.03}_{-0.03}$	< 0.03	$0.13^{+0.01}_{-0.01}$
	N / $\times 10^{14}$cm^{-2}	$4.0^{+0.3}_{-0.5}$	-	$5.4^{+0.4}_{-0.4}$	$11.8^{+1.8}_{-1.2}$	< 0.5	$3.0^{+0.3}_{-0.2}$
^{13}CO(2-1)	τ_{max}	< 0.03	$0.07^{+0.01}_{-0.02}$	< 0.02	< 0.01	< 0.02	< 0.02
	$\int \tau dv$ / km s^{-1}	< 0.04	$0.103^{+0.022}_{-0.022}$	< 0.01	< 0.01	< 0.03	< 0.03
	N / $\times 10^{13}$cm^{-2}	< 9.0	$224.5^{+41.4}_{-54.5}$	< 3	< 1	< 7	< 8
CN(2-1)*	τ_{max}	$0.03^{+0.01}_{-0.01}$	$0.43^{+0.02}_{-0.02}$	$0.11^{+0.01}_{-0.01}$	$0.02^{+0.01}_{-0.01}$	< 0.03	$0.09^{+0.01}_{-0.01}$
	$\int \tau dv$ / km s^{-1}	$0.04^{+0.01}_{-0.01}$	$0.64^{+0.03}_{-0.03}$	$0.17^{+0.02}_{-0.02}$	$0.04^{+0.02}_{-0.02}$	< 0.04	$0.14^{+0.01}_{-0.01}$
	N / $\times 10^{12}$cm^{-2}	$1.0^{+0.3}_{-0.3}$	159^{+8}_{-8}	$4.1^{+0.5}_{-0.5}$	$2.3^{+1.2}_{-1.2}$	< 0.8	$3.3^{+0.2}_{-0.2}$
HCO$^+$(1-0)	τ_{max}	$0.29^{+0.02}_{-0.02}$	$1.29^{+0.07}_{-0.06}$	$0.40^{+0.02}_{-0.02}$	$0.18^{+0.02}_{-0.02}$	$0.04^{+0.01}_{-0.01}$	$0.13^{+0.01}_{-0.01}$
	$\int \tau dv$ / km s^{-1}	$0.44^{+0.03}_{-0.03}$	$1.9^{+0.1}_{-0.1}$	$0.59^{+0.03}_{-0.03}$	$0.26^{+0.04}_{-0.03}$	$0.05^{+0.02}_{-0.02}$	$0.19^{+0.02}_{-0.02}$
	N / $\times 10^{12}$cm^{-2}	$1.8^{+0.1}_{-0.1}$	310^{+20}_{-20}	$2.3^{+0.1}_{-0.1}$	$3.1^{+0.5}_{-0.4}$	$0.1^{+0.1}_{-0.1}$	$0.6^{+0.1}_{-0.1}$
HCO$^+$(2-1)	τ_{max}	$0.36^{+0.01}_{-0.01}$	-	$0.44^{+0.01}_{-0.01}$	$0.37^{+0.02}_{-0.02}$	$0.03^{+0.01}_{-0.01}$	$0.14^{+0.01}_{-0.01}$
	$\int \tau dv$ / km s^{-1}	$0.54^{+0.02}_{-0.02}$	-	$0.66^{+0.02}_{-0.02}$	$0.55^{+0.03}_{-0.03}$	$0.05^{+0.01}_{-0.01}$	$0.21^{+0.01}_{-0.01}$
	N / $\times 10^{12}$cm^{-2}	$2.4^{+0.1}_{-0.1}$	-	$2.7^{+0.1}_{-0.1}$	$6.0^{+0.3}_{-0.3}$	$0.2^{+0.1}_{-0.1}$	$0.7^{+0.1}_{-0.1}$
HCN(2-1)	τ_{max}	$0.15^{+0.02}_{-0.02}$	$0.88^{+0.06}_{-0.06}$	$0.30^{+0.02}_{-0.02}$	$0.15^{+0.03}_{-0.03}$	$0.03^{+0.01}_{-0.01}$	$0.08^{+0.01}_{-0.01}$
	$\int \tau dv$ / km s^{-1}	$0.22^{+0.03}_{-0.03}$	$1.31^{+0.09}_{-0.09}$	$0.45^{+0.04}_{-0.04}$	$0.23^{+0.05}_{-0.05}$	$0.05^{+0.02}_{-0.02}$	$0.12^{+0.02}_{-0.02}$
	N / $\times 10^{12}$cm^{-2}	$1.1^{+0.2}_{-0.2}$	$84.6^{+5.8}_{-5.8}$	$2.2^{+0.2}_{-0.2}$	$2.9^{+0.6}_{-0.6}$	$0.2^{+0.1}_{-0.1}$	$0.5^{+0.1}_{-0.1}$
HNC(1-0)	τ_{max}	$0.02^{+0.01}_{-0.01}$	$0.15^{+0.02}_{-0.02}$	$0.04^{+0.01}_{-0.01}$	$0.02^{+0.02}_{-0.02}$	$0.01^{+0.01}_{-0.01}$	$0.01^{+0.01}_{-0.01}$
	$\int \tau dv$ / km s^{-1}	$0.02^{+0.02}_{-0.02}$	$0.23^{+0.03}_{-0.03}$	$0.07^{+0.02}_{-0.02}$	$0.03^{+0.03}_{-0.03}$	$0.02^{+0.01}_{-0.01}$	$0.01^{+0.01}_{-0.01}$
	N / $\times 10^{11}$cm^{-2}	$0.8^{+0.8}_{-0.8}$	$114.6^{+14.9}_{-14.9}$	$2.6^{+0.7}_{-0.7}$	$3.5^{+3.5}_{-3.5}$	$0.6^{+0.3}_{-0.3}$	$0.4^{+0.4}_{-0.4}$
H_2CO(3-2)	τ_{max}	< 0.02	$0.10^{+0.01}_{-0.01}$	< 0.02	< 0.02	< 0.02	< 0.01
	$\int \tau dv$ / km s^{-1}	< 0.03	$0.15^{+0.01}_{-0.01}$	< 0.04	< 0.03	< 0.02	< 0.02
	N / $\times 10^{13}$cm^{-2}	< 4	55^{+6}_{-3}	< 6	< 9	< 4	< 7

		G7	G8	G9	G10	G11	G12
v_{cen} / km s^{-1}		−16.0	−8.3	−4.0	−1.7	0.9	10.8
σ / km s^{-1}		3.7	1.2	1.0	0.7	1.4	4.0
CO(1-0)	τ_{max}	$0.05^{+0.01}_{-0.01}$	< 0.02	< 0.06	< 0.04	< 0.06	< 0.03
	$\int \tau dv$ / km s^{-1}	$0.08^{+0.02}_{-0.02}$	< 0.02	< 0.06	< 0.06	< 0.08	< 0.04
	N / $\times 10^{15}$cm^{-2}	$0.20^{+0.04}_{-0.04}$	< 0.1	< 0.3	< 0.3	< 0.3	< 0.2
CO(2-1)	τ_{max}	$0.12^{+0.01}_{-0.01}$	< 0.03	$0.18^{+0.01}_{-0.01}$	< 0.03	< 0.02	< 0.01
	$\int \tau dv$ / km s^{-1}	$0.18^{+0.01}_{-0.01}$	< 0.05	$0.27^{+0.02}_{-0.02}$	< 0.06	< 0.03	< 0.02
	N / $\times 10^{14}$cm^{-2}	$4.4^{+0.3}_{-0.2}$	< 0.5	$11.3^{+0.7}_{-0.9}$	< 1	< 0.6	< 0.2
^{13}CO(2-1)	τ_{max}	< 0.01	< 0.3	< 0.01	< 0.01	< 0.02	< 0.01
	$\int \tau dv$ / km s^{-1}	< 0.02	< 0.04	< 0.007	< 0.01	< 0.03	< 0.02
	N / $\times 10^{13}$cm^{-2}	< 3	< 7	< 2	< 3	< 10	< 3
CN(2-1)*	τ_{max}	$0.10^{+0.01}_{-0.01}$	$0.03^{+0.01}_{-0.01}$	$0.32^{+0.02}_{-0.02}$	$0.04^{+0.01}_{-0.01}$	$0.07^{+0.01}_{-0.01}$	$0.02^{+0.01}_{-0.01}$
	$\int \tau dv$ / km s^{-1}	$0.14^{+0.01}_{-0.01}$	$0.04^{+0.02}_{-0.02}$	$0.48^{+0.02}_{-0.02}$	$0.06^{+0.02}_{-0.02}$	$0.11^{+0.02}_{-0.02}$	$0.03^{+0.01}_{-0.01}$
	N / $\times 10^{12}$cm^{-2}	$3.5^{+0.2}_{-0.2}$	$0.7^{+0.3}_{-0.3}$	$22.0^{+0.9}_{-0.9}$	$1.5^{+0.5}_{-0.5}$	$2.5^{+0.5}_{-0.5}$	$0.5^{+0.2}_{-0.2}$
HCO$^+$(1-0)	τ_{max}	$0.18^{+0.01}_{-0.01}$	$0.10^{+0.02}_{-0.02}$	$0.29^{+0.02}_{-0.02}$	$0.11^{+0.02}_{-0.02}$	$0.17^{+0.02}_{-0.02}$	$0.06^{+0.01}_{-0.01}$
	$\int \tau dv$ / km s^{-1}	$0.26^{+0.01}_{-0.01}$	$0.15^{+0.02}_{-0.02}$	$0.43^{+0.03}_{-0.03}$	$0.16^{+0.03}_{-0.03}$	$0.25^{+0.02}_{-0.02}$	$0.09^{+0.01}_{-0.01}$
	N / $\times 10^{12}$cm^{-2}	$0.90^{+0.01}_{-0.01}$	$0.30^{+0.01}_{-0.01}$	$3.4^{+0.2}_{-0.2}$	$0.6^{+0.1}_{-0.1}$	$0.8^{+0.1}_{-0.1}$	$0.20^{+0.01}_{-0.01}$
HCO$^+$(2-1)	τ_{max}	$0.2^{+0.01}_{-0.01}$	$0.07^{+0.01}_{-0.01}$	$0.49^{+0.02}_{-0.02}$	$0.13^{+0.01}_{-0.01}$	$0.18^{+0.01}_{-0.01}$	$0.05^{+0.01}_{-0.0}$
	$\int \tau dv$ / km s^{-1}	$0.3^{+0.01}_{-0.01}$	$0.11^{+0.01}_{-0.01}$	$0.74^{+0.02}_{-0.02}$	$0.19^{+0.02}_{-0.02}$	$0.27^{+0.01}_{-0.01}$	$0.07^{+0.01}_{-0.01}$
	N / $\times 10^{12}$cm^{-2}	$1.10^{+0.01}_{-0.01}$	$0.30^{+0.01}_{-0.01}$	$5.6^{+0.2}_{-0.2}$	$0.7^{+0.1}_{-0.1}$	$1.00^{+0.01}_{-0.01}$	$0.20^{+0.01}_{-0.01}$
HCN(2-1)	τ_{max}	$0.10^{+0.01}_{-0.01}$	$0.10^{+0.02}_{-0.02}$	$0.34^{+0.03}_{-0.03}$	$0.21^{+0.03}_{-0.03}$	$0.12^{+0.02}_{-0.02}$	< 0.04
	$\int \tau dv$ / km s^{-1}	$0.14^{+0.02}_{-0.02}$	$0.15^{+0.03}_{-0.03}$	$0.51^{+0.05}_{-0.04}$	$0.31^{+0.05}_{-0.05}$	$0.18^{+0.03}_{-0.03}$	< 0.08
	N / $\times 10^{12}$cm^{-2}	$0.6^{+0.1}_{-0.1}$	$0.5^{+0.1}_{-0.1}$	$4.6^{+0.4}_{-0.4}$	$1.5^{+0.2}_{-0.2}$	$0.8^{+0.1}_{-0.1}$	< 0.3
HNC(1-0)	τ_{max}	$0.02^{+0.01}_{-0.01}$	$0.02^{+0.01}_{-0.01}$	$0.08^{+0.02}_{-0.02}$	< 0.04	$0.03^{+0.01}_{-0.01}$	< 0.03
	$\int \tau dv$ / km s^{-1}	$0.03^{+0.01}_{-0.01}$	$0.03^{+0.02}_{-0.02}$	$0.11^{+0.02}_{-0.02}$	< 0.04	$0.04^{+0.02}_{-0.02}$	< 0.04
	N / $\times 10^{11}$cm^{-2}	$1.1^{+0.4}_{-0.4}$	$0.7^{+0.5}_{-0.5}$	$8.1^{+1.5}_{-1.5}$	< 2	$1.4^{+0.7}_{-0.7}$	< 0.7
H_2CO(3-2)	τ_{max}	$0.02^{+0.01}_{-0.01}$	$0.02^{+0.01}_{-0.01}$	$0.10^{+0.01}_{-0.01}$	< 0.02	$0.03^{+0.01}_{-0.01}$	$0.02^{+0.01}_{-0.01}$
	$\int \tau dv$ / km s^{-1}	$0.02^{+0.01}_{-0.01}$	$0.02^{+0.01}_{-0.01}$	$0.16^{+0.01}_{-0.01}$	< 0.02	$0.05^{+0.01}_{-0.01}$	$0.02^{+0.01}_{-0.01}$
	N / $\times 10^{13}$cm^{-2}	$3.7^{+0.2}_{-1.4}$	$3.2^{+0.8}_{-1.7}$	29^{+2}_{-3}	< 2	$7.0^{+2.0}_{-0.8}$	$3.3^{+0.3}_{-1.1}$

Table 4.4

See previous two pages: The peak optical depths, velocity integrated optical depths and line of sight column densities for the 12-Gaussian fits applied to each of the spectra shown in Fig. 4.2 . A fit composed of 12 individual Gaussian lines (labelled G1 to G12) of fixed v_{cen} and σ, but varying amplitude, is used when fitting to the spectra. Column densities for G2 could not always be reliably calculated because it is optically thick in some of the lines.

*The values for CN(2-1) are calculated from three overlapping hyperfine structure lines representing ∼ 60 per cent of the total absorption. The full CN(2-1) spectrum is shown in Appendix B.

4.3.2 Optical depth calculations

The apparent optical depth of an absorption line, τ, can be derived according to the equation,

$$\tau = -\ln\left(1 - \frac{1}{f_c}\frac{I_{obs}}{I_{cont}}\right), \tag{4.3.1}$$

where f_c is the fraction of the background continuum source covered by the absorbing molecular cloud, I_{obs} is the depth of the absorption, and I_{cont} is the continuum level.

A covering factor of 0.7 is assumed for the G2 absorption feature at −43.1 km s^{-1}. Simply assuming $f_c = 1$ gives a relatively high ^{13}CO(2-1) optical depth of $\tau = 0.07$, so for the significantly more ubiquitous CO(2-1), one would expect $\tau \gg 1$ and for the continuum normalized flux to drop to 0. In fact, the line flattens out when around 30 percent of the continuum can still be seen, despite being covered by an optically thick cloud. This in turn implies that the G2 feature covers around 70 per cent of the continuum source.

No highly significant ^{13}CO(2-1) absorption is detected in the rest of the absorption profile, as would be expected in the case of optically thick clouds which cover a small fraction of the continuum. Hence, a covering factor of $f_c = 1$ is assumed for the remaining absorption features.

It is nevertheless possible that we are observing optically thin clouds which do not cover the entire continuum source, so the estimates of τ are essentially lower limits. Additionally,

it is generally assumed that as frequency increases, the emission from an AGN originates closer to its core, so the covering factor may also increase with frequency.

For each spectrum, the implied optical depths of the 12 Gaussian regions are given in Table 4.4. The tables also give their velocity integrated optical depths and the implied line of sight column densities, the calculations of which are described in a later section.

4.4 Temperature Estimates

4.4.1 Excitation temperature estimates

The absorption profiles seen in Fig. 4.2 are produced by what is best described as the combination of 12 Gaussian absorption regions. Most of the absorption regions have extremely narrow velocity dispersions of $\sim$ 1 km s^{-1}, which are comparable to those of individual clouds in the Milky Way (Roman-Duval et al., 2010). Therefore, most of the absorption regions detected can be approximated as individual molecular gas clouds, for which the excitation temperature can be estimated.

Even for the broader absorption regions (G7 and G12), which are likely small associations of clouds, an average excitation temperature can still be found. Though it is worth noting that this concept of individual molecular clouds is an approximation given that there is no clear point where they will start and end, they will have internal structure, and there will always be some interstellar medium which exists between them.

The observations of HCO$^+$(1-0) and HCO$^+$(2-1) provide two well resolved absorption profiles from which it is possible to estimate the excitation temperature of the absorption regions represented by each of the 12 Gaussian best fit lines. This requires that the gas is optically thin and in local thermodynamic equilibrium, but as is shown in §4.4.2, this is not the case, so the values should only be treated as approximations.

Nevertheless, with this assumption the HCO$^+$(1-0) and HCO$^+$(2-1) velocity integrated optical depths are related by

$$\frac{\int \tau_{21} dv}{\int \tau_{10} dv} = 2 \frac{1 - \exp(-h\nu_{21}/kT_{\rm ex})}{\exp(h\nu_{10}/kT_{\rm ex}) - 1} \ , \tag{4.4.1}$$

where h and k are the Planck and Boltzmann constants, ν_{10} and ν_{21} are the rest frequencies of the HCO^+(1-0) and HCO^+(2-1) lines and T_{ex} is the excitation temperature (Bolatto et al., 2003; Godard et al., 2010; Mangum & Shirley, 2015). The excitation temperatures found using Equation 4.4.1 are given in Table 4.3.

The hyperfine structure components of the HCN(1-0) line are separated by frequencies similar to those of the 12 Gaussian absorption lines seen in this system. It is therefore not possible to estimate the excitation temperature of the individual absorption regions using the HCN(1-0) and HCN(2-1) spectra, though an average can be estimated from the total velocity integrated optical depth of the whole absorption profile. This gives an excitation temperature of $5.5^{+2.0}_{-1.6}$ K, which compares well with the value of $5.8^{+0.7}_{-0.7}$ K when the same method is applied to the HCO^+(1-0) and HCO^+(2-1) spectra.

In Chapter 3, a much higher excitation temperature of 42^{+25}_{-11} Kelvin was found. However, this temperature estimate was made exclusively for the deepest absorption region, and was also made using much lower angular resolution CO(1-0) data. This lower resolution means that the core spectrum contains significantly more extended CO emission. Errors can arise while attempting to compensate for this emission, which explains why this earlier estimate carries a large uncertainty.

4.4.2 Kinetic temperature estimate

The relative abundance of the HCN and HNC tautomers depends on the gas kinetic temperature, with the ratio HCN/HNC increasing at higher temperatures due to reactions which preferentially destroy the HNC molecule (Hernández Vera et al., 2017; Hacar et al., 2019). Where the intensity ratio satisfies $I(\mathrm{HCN})/I(\mathrm{HNC}) \leq 4$, it is found to correlate with kinetic temperature according to:

$$T_{\mathrm{kin}} = 10 \times \left[\frac{I(\mathrm{HCN})}{I(\mathrm{HNC})} \right]. \tag{4.4.2}$$

Due to the HCN(1-0) line's hyperfine structure, it is only possible to estimate an average kinetic temperature for the absorption profile as a whole, which is found to be 33^{+9}_{-8}K.

The errors quoted are determined from the combination of the uncertainty in the velocity integrated intensities of both spectra and the uncertainty given by Hacar et al. (2019) for Eq. 4.4.2. Since $T_{ex} < T_{kin}$, the absorbing gas is sub-thermally excited i.e. it is not in thermal equilibrium. This means there are fewer molecules in the J = 1 rotational state than would be expected, resulting in a change to the absorption strength.

4.5 Column Density Estimates

The total line of sight column density, N_{tot}, of the absorption regions can be found by using an estimated excitation temperature and assuming that the absorption is optically thin. In general,

$$N_{tot}^{thin} = Q(T_{ex}) \frac{8\pi\nu_{ul}^3}{c^3} \frac{g_l}{g_u} \frac{1}{A_{ul}} \frac{1}{R} \frac{1}{1 - e^{-h\nu_{ul}/kT_{ex}}} \int \tau_{ul}\, dv\,, \tag{4.5.1}$$

where $Q(T_{ex})$ is the partition function, c is the speed of light, A_{ul} is the Einstein coefficient of the observed transition and g the level degeneracy, with the subscripts u and l representing the upper and lower levels (Godard et al., 2010; Mangum & Shirley, 2015). The factor R is the total intensity of the hyperfine structure lines in the absorption profile, where the combined intensity of all hyperfine lines is normalized to 1.

As previously stated, this calculation assumes that the absorption is optically thin. However, in some cases where $\tau \gtrapprox 1$ e.g. G2 of CO(2-1), HCO^+(2-1) and HCN(2-1), the true column densities may be significantly higher than calculated. An optical depth correction factor from Mangum & Shirley (2015) is therefore applied to give a more accurate value for the line of sight column densities,

$$N_{tot} = N_{tot}^{thin} \frac{\tau}{1 - \exp(-\tau)}. \tag{4.5.2}$$

The line of sight column densities of the molecular species whose absorption spectra are shown in Fig. 4.2 are given in Table 4.4, where the assumed excitation temperature for each of the 12 absorption regions is equal to that calculated as described in §4.4.1 and shown in Table 4.3.

Using these bespoke excitation temperatures tightens the correlation seen in the column densities compared with when a fixed excitation temperature is assumed for all absorption regions. A corner plot showing how these column densities correlate to one another can be seen in Fig. 4.3. Where a molecular species has been observed with multiple rotational lines, e.g. CO(1-0) and CO(2-1), the column densities shown in Fig. 4.3 are those calculated from the better resolved (2-1) line.

4.6 Discussion

4.6.1 A comparison to Milky Way and extragalactic absorption profiles

Fig. 4.4 shows the HCO^+, HCN, and HNC column densities of the molecular clouds in Hydra-A, as well as those found in the Milky Way and other extragalactic sources up to relatively high redshifts of $z = 0.89$. The column densities occupy a similar region in the plot as those seen in the Milky Way. However, they are typically lower than those in intervening absorber systems by two to three orders of magnitude. A difference this large is not likely to be due to the high quality of the ALMA observations or lower than assumed covering factors. Even if the 12 absorption regions were combined, this would still place the column densities at the low end of the scale.

Fig. 4.5 shows a comparison of the velocity dispersion, excitation temperature, and line of sight velocity for each of the 12 absorption regions. Included in the top panel are molecular clouds towards the galactic plane of the Milky Way, as well as those at radii of 4 - 8 kpc. This highlights further similarities between the absorption regions of Hydra-A, which reside in the high pressure environment of a brightest cluster galaxy, and those in the Milky Way.

Although there is no strong indication of the distances of Hydra-A's molecular clouds from the centre of the galaxy, this suggests that the locations in which these two sets of clouds reside are fairly interchangeable and that their self-gravitation is significantly more important than the ambient pressures. The properties of the molecular clouds seen

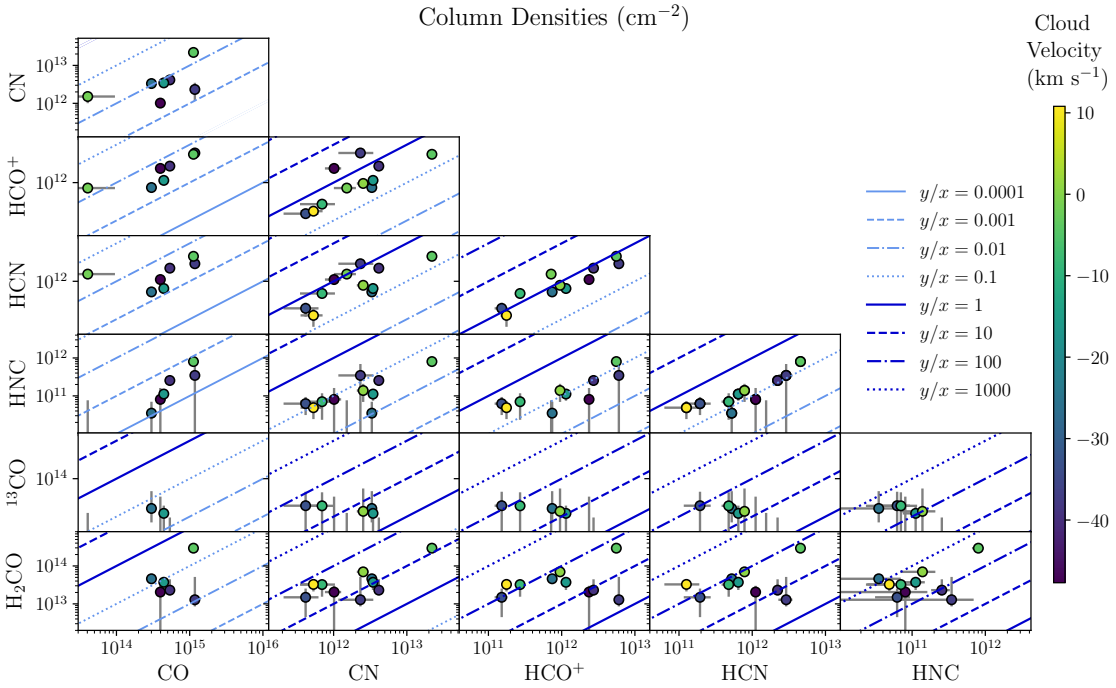

Figure 4.3

A comparison of the line of sight column densities of CO, CN, HCO^+, HCN, HNC, ^{13}CO, and H_2CO. The column densities are calculated from the 12 Gaussian fits applied to the absorption profiles shown in Fig. 4.2 , using Equation 4.5.2. The excitation temperature assumed for each absorption region is that estimated in §4.4.1 and given in Table 4.3. The colour of each point represents the central velocity of the absorption region relative to the stellar recession velocity of the galaxy, which itself is a good approximation for the velocity of the central supermassive black hole. For CO, $HCO^+$and HCN, which were observed with both the (1-0) and (2-1) rotational lines, the column densities are calculated using the (2-1) line in which the absorption is best resolved.

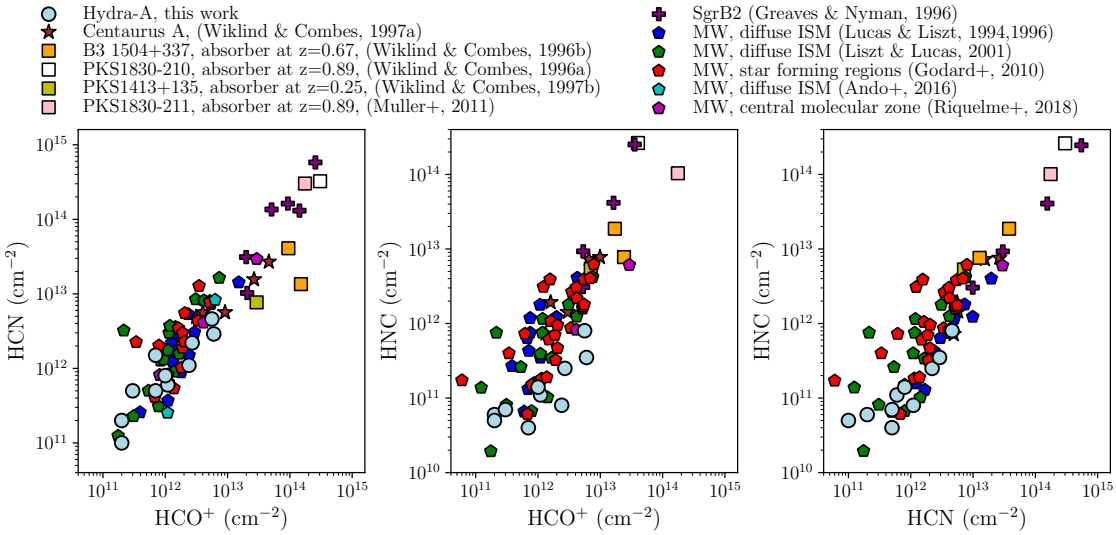

Figure 4.4

The column densities of HCO^+, HCN and HNC seen in Hydra-A (circles), Centaurus-A (stars), intervening absorbers i.e. extragalactic sources lying in front of background quasars (squares), Sagittarius B2 (crosses), and the Milky Way (pentagons). The original data are taken from Wiklind & Combes (1997a, 1996b,a, 1997b); Muller et al. (2011); Greaves & Nyman (1996); Lucas & Liszt (1994, 1996); Liszt & Lucas (2001); Godard et al. (2010); Ando et al. (2016); Riquelme et al. (2018).

in Hydra-A and the Milky way are also both similar to those predicted by accretion simulations (e.g. those of Gaspari et al., 2017).

If the absorbing regions of molecular gas lie on elliptical orbits, their velocities could have apparent shifts relative to the galaxy's systemic velocity of up to a few tens of km s^{-1}. In the Keplerian regime, the most blueshifted absorption should lie closest to the galaxy centre. In turn, this could produce a trend between the cloud excitation temperature and velocity as a result of heating from the AGN.

Although in Hydra-A the highest excitation temperatures are seen in the most blueshifted clouds, the trend is not especially strong (see the centre panel of Fig. 4.5). This correlation has been observed within the Milky Way, though it is weak and only visible with the detection of hundreds of molecular clouds (Roman-Duval et al., 2010).

The velocity dispersions of most clouds, shown in the lower plot of Fig. 4.5, are very low and lie between 0.5 and 1.4 km s^{-1}, indicating that they are due to individual molecular clouds. The outlying absorption regions with higher velocity dispersions are likely small associations of molecular clouds which are not resolved by the observations.

The absorption profiles seen in Hydra-A also bear a strong resemblance to those seen in other systems such as Centaurus-A, and the less well studied brightest cluster galaxy NGC6868 (Israel et al., 1990, Chapter 5). In all three cases there are two deep absorption lines separated by $\sim 50-100$ km s^{-1}, as well as a more extended absorption complex. Like Hydra-A, Centaurus-A also has a close to edge-on molecular gas disc and an extremely compact core (Israel et al., 1990).

4.6.2 Cloud size and mass estimates

The similarities between the clumpy interstellar medium of the Milky Way and that seen along the line of sight to the core of Hydra-A allow estimates of the size and mass of the molecular clouds to be derived. Within the Milky Way, the velocity dispersion, σ, and diameter, D, of molecular clouds are related by:

$$\left(\frac{\sigma}{\text{km s}^{-1}}\right) = \left(\frac{D}{\text{pc}}\right)^{0.5}. \tag{4.6.1}$$

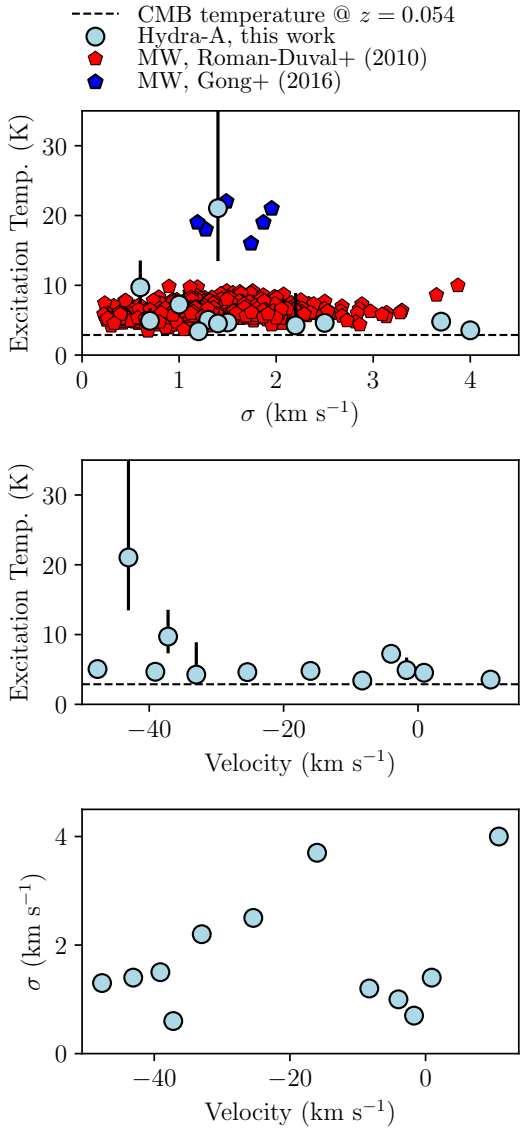

Figure 4.5

A comparison of the velocity dispersions, σ, excitation temperatures and line of sight velocities of the absorbing clouds traced by the absorption profiles shown in Fig. 4.2 . The excitation temperatures are those derived from the HCO^+(1-0) and HCO^+(2-1) spectra. The top plot shows molecular clouds of the Milky Way observed at galactocentric radii of 4 - 8 kpc (red pentagons, Roman-Duval et al., 2010) and those in star forming regions towards the galactic plane (blue pentagons, Gong et al., 2016).

This relation was first shown by Larson (1981) and its approximate form has been supported by many more recent works (e.g. Solomon et al., 1987; Vazquez-Semadeni et al., 2007; McKee & Ostriker, 2007; Ballesteros-Paredes et al., 2011). Hydra-A is a brightest cluster galaxy and so its thermal pressure is many times higher than that of the Milky Way. If the molecular gas behaves in a reactive way to this different environment, then the relation may be less applicable. However, as Fig. 4.4 shows, the clouds' environment does not result in significantly higher line of sight column densities and so the relation should still hold true.

The implied sizes of the 12 absorption regions detected in Hydra-A are given in Table 4.3.

By further assuming the absorption regions are in virial equilibrium, their total masses, $M_{\rm tot}$, can be estimated using the virial theorem:

$$M_{\rm tot} = \frac{D\sigma^2}{2G}, \tag{4.6.2}$$

where D is the cloud diameter and G is the gravitational constant. The total masses of the 12 absorption regions are also given in Table 4.3.

4.6.3 An estimate of the continuum source's size

The above estimate of the total cloud mass can be used in conjunction with the line of sight column density of molecular hydrogen derived from X-ray observations to estimate the size of the continuum source against which absorption is seen. This will only provide a rough estimate due to the uncertainties in the cloud masses and the likely difference in the size of the continuum source between the frequencies of the X-ray and radio observations.

The total mass inferred from the molecular absorption seen in Hydra-A is $4 \times 10^4 M_\odot$ and Russell et al. (2013) find a line of sight column density of $N_H = 3.5 \times 10^{22}{\rm cm}^{-2}$ from X-ray observations. These values imply that Hydra-A's central continuum source has an apparent diameter of 7 pc, assuming it appears circular along the line of sight.

The above value is likely an overestimate because most of the mass in the estimates of §4.6.2 come from the broadest absorption regions. These are unlikely to be individual

molecular clouds in virial equilibrium, but rather collections of unresolved molecular clouds.

To make some correction for this, it is simply assumed that the widest clouds, G7 and G12, are each in fact the combination of two molecular clouds, with a velocity dispersion half of the original value. This reduces their estimated diameters by a factor of four, and their masses by a factor of sixteen. There are now twice as many clouds, so the overall mass of these absorption features is reduced by a factor of eight. This new mass results in an estimated continuum diameter of 4 pc. VLBA observations by Taylor (1996) at the lower frequency 1.35 GHz show hints of structure on similar scales.

4.6.4 Continuum variability

Hydra-A has been attentively studied at a wide range of frequencies over several decades. The left panel of Fig. 4.6 shows the galaxy's spectral energy distribution and the right shows the continuum variability of its core and radio lobes, as seen with the ALMA observations presented in this chapter.

The right panel of Fig. 4.6 shows that no significant change in the flux density of the core, against which the absorption is detected, has taken place over the two year time range in which the observations were taken. The flux density of the lobes is expected to be constant and the significant scatter present is a result of the limited angular resolution of the observations, with the lobes often spreading out close to the edge of the field of view where beam corrections are large.

4.6.5 Absorption variability

CO(2-1) absorption was first detected in Hydra-A in October 2016 (as described in Chapter 3), and a repeat observation was carried out in October 2018 as part of the main survey presented in this chapter. Fig. 4.7 shows the absorption profiles seen against the galaxy's bright radio core for these two observations.

Across the majority of the absorption profile, the two spectra are consistent within the noise levels and there is little hint of variability. However, between -20 and -5 km s^{-1} a decrease

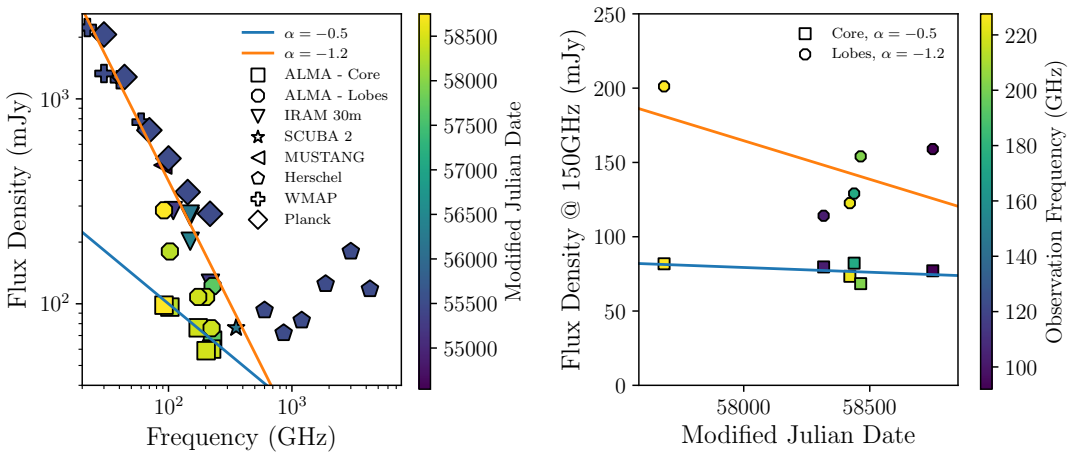

Figure 4.6

Left: The spectral energy distribution of Hydra-A, produced with data taken since March 2008 using a range of observatories. With the exception of those from ALMA, the observations are of a low angular resolution and consequently include flux from both the radio core and radio lobes. The orange and blue lines show power law fits to the core plus radio lobes and to the resolved core. The increase in emission at 10^3 GHz is from infrared emission due to dust heating. **Right**: Six ALMA flux density measurements of Hydra-A, all adjusted to give the implied flux density at 150 GHz assuming a power-law spectrum with $\alpha = -0.5$ for the radio core and $\alpha = -1.2$ for the radio lobes. This shows a stable continuum flux density from Hydra-A's core and from its lobes (more scatter is seen in the flux density of the lobes because in some cases, they spread out close to the edge of the observation's the field of view where beam corrections are large).

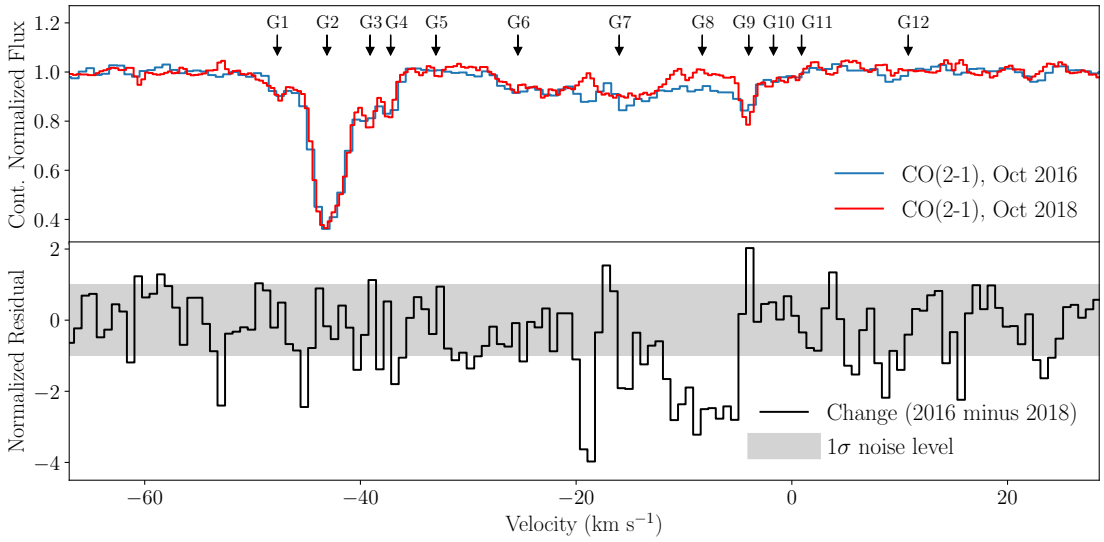

Figure 4.7

Top: The overlaid absorption profiles of two CO(2-1) spectra taken in October 2016 and October 2018. The two spectra are extracted from a region with a size equal to the synthesized beam's FWHM centred on Hydra-A's bright and compact radio core. The absorption is largely consistent given the noise levels, though a small difference appears between -20 and -5 km s^{-1}. The G1-12 markers indicate the central velocities of each component of the 12-Gaussian fit made to the spectra in Fig. 4.2 . **Bottom:** The change seen in the absorption between the two observations, with the grey band indicating the 1σ noise level of the residual. The variability of the spectrum over the velocity range in which absorption is seen (approximately -50 to 10 km s^{-1}) has a combined significance of 3.4σ, as calculated from a χ^2 distribution test.

in the absorption strength appears to have taken place over the intervening two years. This velocity range does not correspond well to any component of the multi-Gaussian best fit and so is unlikely to be due to a change in the absorption of any individual molecular cloud.

The variability of the spectrum over the velocity range in which absorption is seen (approximately -50 to 10 km s^{-1}) has a combined significance of 3.4σ (calculated from a χ^2 distribution test). Note that a shift of $\sim$ 0.1 mJy has been applied to the spectrum extracted from the 2018 observation. This error appears as a result of the subtraction of the emission from the two spectra, where the degree to which the emission compensates for the absorption cannot be known precisely (see Chapter 3 for a plot showing the CO(2-1) emission from the around core).

If this apparent change in the absorption profile is real, then it will almost certainly be due to either a change in the continuum source against which the absorption is observed, or due to a movement of the molecular clouds responsible for the absorption. Below these explanations are discussed, though both are likely to be true to a greater or lesser extent.

The unresolved continuum source the absorption is observed against may be made up of several components, each covered to varying degrees by different gas clouds. This would produce absorption along multiple lines of sight, which then combines to make the single absorption profile against the unresolved continuum source. This is consistent with 1.35 GHz VLBA observations by Taylor (1996), which show the continuum source at high angular resolution. Spatially resolved H I absorption is seen, most likely caused by different lines of sight towards the radio core and the knots of the galaxy's jets. If this is the case, no absorption which appears to be optically thick would be detected, and the reduced strength of the absorption may be due to a decrease in flux from one particular component of the continuum source. This would result in weaker absorption from that line of sight, but leave the remaining absorption unaffected. Although there is no significant change in the continuum's strength over this time period (see Fig. 4.6), the dimming required to produce the small decrease in absorption could well be within the noise levels of the measurements of the continuum flux density. Even if the total continuum emission is not varying, relativistic and transverse motions in the hot spots of the continuum source could

change the background illumination of the absorbing clouds.

An angular precession of the continuum source could also result in a change in the background illumination of the molecular gas. Nawaz et al. (2016) found a precession period of $\sim$ 1 Myr in Hydra-A from hydrodynamical simulations of its jet-intracluster medium interactions. In a two year time frame this translates to an angular precession of 2.6", which sweeps over a transverse distance of 0.01 pc at a radius of 1 kpc from the continuum source, or 0.1 pc at a radius of 10 kpc. Given the typical size of the molecular clouds of around 1 pc (see Table 4.3) and that they likely have a fractal substructure, the latter seems plausible. However, with a precessing continuum source the level of variability would increase as the distance of the clouds from the nucleus increases. To observe a significant level of variability between -20 and -5 km s^{-1}, but little hint of it anywhere else requires there to be a group of clouds close to the continuum source where the angular change encompasses a negligible linear scale relative to the cloud size, and one group at very large distances, with no clouds in between. Further, the edge on disc of Hydra-A has a radius of around 2.5 kpc, so at 10 kpc the column density of cold molecular gas present is likely low compared with smaller radii.

A variation in the absorption could also be produced by transverse movement of the molecular gas responsible for the absorption between -20 and -5 km s^{-1}. However, even a relatively small molecular cloud with a diameter of 0.1 pc and a large transverse velocity of 500 km s^{-1} will take $\sim$ 200 years to fully cross the line of sight, assuming a point-like continuum source. Particularly small and dense, inhomogeneous, or fast moving molecular clouds would therefore be required for this effect to be seen within a two year time frame. The transverse velocities of molecular clouds are orders of magnitude less than the relativistic and potentially superluminal motions of the knots in the jets at the core of the continuum source, so this can be ruled out with a fair degree of confidence.

Alterations in the cloud chemistry could also result in variability. Although this can occur on cosmologically short timescales on the order of 10^5 years (Harada et al., 2019), this is much greater than the two year interval over which the variability is detected. Only a change induced by significant alterations to the local cosmic ray field, for example, by a nearby supernova could occur quickly enough. Although physically feasible, this

by chance explanation is unlikely given that absorption variability has also been seen in several similar intervening absorber systems (e.g. Wiklind & Combes, 1997b; Muller et al., 2011).

Variability caused by internal changes to the molecular clouds as a result of turbulence, heating, or cooling can also be ruled out. Such changes are only predicted to take place on megayear timescales, rather than the two year timescale on which the variability is seen in Hydra-A (Chira et al., 2019; Sander & Hensler, 2019).

When considering the above explanations it should be noted that clear absorption is still seen within this velocity range in CN(2-1), HCO^+(2-1) and HCN^+(2-1), though this may well have been stronger still if all of the observations had been taken in October 2016 rather than October 2018. Further observations of these lines, where this absorption is strongest and any changes would be more evident, would therefore track any variability and give clues as to its cause. For example, if variability occurs on timescales of months or less, superluminal motions within the jets of the background radio source would be a much more plausible explanation than the comparatively slow transverse motion of the molecular clouds.

4.7 Conclusions

This chapter presents ALMA observations of CO, ^{13}CO, CN, SiO, HCO^+, HCN, HNC, and H_2CO molecular absorption lines seen against the bright radio core of Hydra-A. Their narrow velocity dispersions (typically $\sim$ 1km s^{-1}) are similar to those seen in molecular cloud complexes of the Milky Way and indicate that the observations are tracing individual clouds of cold molecular gas. The molecular gas clouds typically have excitation temperatures of 5 - 10 K, diameters of 1 - 10 pc, and masses of a few tens to a few thousands of $M_\odot$.

The precise origins and locations of the absorbing molecular clouds within Hydra-A are difficult to constrain, though they are most likely to be within the inner few kpc of the disc where the column densities of molecular gas are highest.

The line of sight column densities, velocity dispersions and excitation temperatures of the molecular clouds seen in Hydra-A have been compared to those of the Milky Way. The two populations are largely indistinguishable, implying that the high pressure environment of a brightest cluster galaxy has negligible effect on the molecular clouds when compared with their self-gravitation. Therefore, although the observations of a clumpy ISM are consistent with the galaxy-wide fuelling and feedback cycles predicted by e.g. Pizzolato & Soker (2005); Peterson & Fabian (2006); McNamara et al. (2016); Gaspari et al. (2018), they are not necessarily evidence in favour of them because clouds with similar properties are seen in the Milky Way, which does not have a comparable AGN.

Future surveys targeting molecular absorption in brightest cluster galaxies are likely to be most successful when searching for $HCO^+$and HCN lines, which are found to be stronger, more ubiquitous, and more consistent tracers than CO. A further advantage of these molecules over CO is a lack of significant emission, which can counteract any absorption and make the true optical depths unclear. HCO^+ is particularly useful because it lacks any hyperfine structure.

The line of sight absorption seen against Hydra-A's bright radio core has shown variation at 3.4 σ significance between ALMA Cycle 4 and 6 observations. These observations are separated by two years, so if this variability is genuine it is occurring on galactically short timescales. The first of two likely explanations for the variability is a multi-component continuum source, one component of which has decreased in brightness or has seen relativistic movement in a hot spot, in turn giving decreased absorption along one particular line of sight. A second possible but less likely explanation is that one of the many absorbing clouds, or groups of absorbing clouds, has significant transverse motion such that it no longer covers the continuum source in the same way.

Extending this study of Hydra-A to a much larger sample will be a useful way in which to determine the more general properties of molecular gas clouds in the cores of massive galaxies. This provides the motivation for the following chapter.

CHAPTER 5

CO and CN absorption in the cores of eight brightest cluster galaxies

---

This chapter is based on the following publication:

Constraining cold accretion on to supermassive black holes: molecular gas in the cores of eight brightest cluster galaxies revealed by joint CO and CN absorption · **Rose, Tom**; Edge, A. C.; Combes, F.; Gaspari, M.; Hamer, S.; Nesvadba, N.; Peck, A. B.; Sarazin, C.; Tremblay, G. R.; Baum, S. A.; Bremer, M. N.; McNamara, B. R.; O'Dea, C.; Oonk, J. B. R.; Russell, H.; Salomé, P.; Donahue, M.; Fabian, A. C.; Ferland, G.; Mittal, R. Vantyghem, A. · 2019, MNRAS, 489, 349 (view publication)

5.1 Introduction

A small number of recent studies of the molecular gas in the central regions of massive galaxies have begun to focus on molecular absorption, rather than emission – including chapters 3 and 4 of this thesis (other examples are David et al., 2014; Tremblay et al., 2016). Such absorption line studies have two principal benefits. First, observing absorption against a bright and unresolved backlight makes it possible to study the behaviour and properties of molecular gas on much smaller scales than is achievable from emission. Second, in absorption line studies using a galaxy's bright radio core as a backlight, redshifted absorption unambiguously indicates inflow while blueshifted lines indicate outflow – in the case of emission lines, there is ambiguity as to whether the gas being traced lies in front of or behind the core of the galaxy.

Despite these advantages, molecular absorption studies remain rare, with only a handful of intrinsic absorbing systems having been found in this way. In terms of brightest cluster galaxies, five associated absorbers have been detected, where the absorption is observed in the spectrum of the bright radio source spatially coincident with the galaxy's supermassive black hole (David et al., 2014; Tremblay et al., 2016; Ruffa et al., 2019; Rose et al., 2019; Nagai et al., 2019). A small selection of intervening absorbers have also been detected in gravitational lens systems, where absorption is observed in a galaxy separate from, but along the same line of sight as a distant and bright radio continuum source such as a quasi-stellar object (Combes, 2008; Wiklind et al., 2018; Combes et al., 2019).

Two of the associated absorbers detected so far have provided some indication of cold, molecular gas clouds falling towards their host galaxy's core and thus potentially going on to fuel the supermassive black hole. These observations of NGC 5044 by David et al. (2014) and of Abell 2597 by Tremblay et al. (2016) both show regions of cold molecular gas moving towards the galaxy centre at $\sim 200 - 300$ km s^{-1}. Additionally, Ruffa et al. (2019) and Chapter 3 both show molecular gas which appears to be in stable, slightly elliptical orbits where they most likely drift in a turbulent velocity field, rather than undergoing any significant inflow or outflow.

The molecular gas detected in these systems provides some evidence in line with theories

and simulations which predict a gradual drifting of molecular clouds towards a galaxy's central supermassive black hole.

However, with such a small number of detections having been made so far, it is difficult to draw concrete conclusions about the typical behaviour and properties of the molecular gas in the central regions of massive galaxies and how it interacts with the central supermassive black hole. This chapter presents the results of an Atacama Large Millimeter/submillimeter Array (ALMA) survey of 18 brightest cluster galaxies, all of which are extremely bright and core dominated in the radio.

A clear conclusion of Chapter 4 was that molecular absorption lines surveys are likely to be most successful when searching for HCO^+, rather than CO (which is commonly used in emission line surveys). Unfortunately, the observations which are presented in this chapter were carried out before that became apparent.

As a result, the principal target in this survey is the more standard CO(1-0) line. Nevertheless, several serendipitous detections of CN absorption were also made. There is also a detection of one SiO absorption line. Across the eight systems in which molecular absorption is detected, the survey presented here found 15 new and individual CO, CN, or SiO absorption lines.

This chapter is laid out as follows. §5.2 gives details of the observations and introduces the sample, while §5.3 explains the data reduction carried out. §5.4 presents the eight systems with detections of CO, CN, and SiO absorption lines. §5.5 shows the sources which have CO and CN emission, but lack absorption features, and §5.6 briefly discusses the sources which have no absorption or emission features. In §5.7 the CO and CN column densities from the observed absorption features are derived. §5.8 discusses the significance and implications of the results and §5.9 presents the main conclusions. Throughout, a flat ΛCDM Universe with $H_0 = 70$ km s^{-1} Mpc^{-1}, Ω_M=0.3 and Ω_Λ=0.7 is assumed.

5.2 Target sample and observed lines

The observations presented in this paper are from an ALMA Cycle 5 survey of core dominated brightest cluster galaxies with extremely high flux densities (PI: Alastair Edge,

project 2017.1.00629.S). In total, time was awarded for observations of 23 targets but three observations were not attempted and two were not sufficiently well calibrated to extract a reliable spectrum.

All 23 targets have unresolved emission at 85 - 110 GHz of >10 mJy, so they are both bright and compact enough to probe the behaviour of cold molecular gas along very narrow, uncontaminated lines of sight. In all but one case the ALMA observations of each galaxy's radio core are unresolved. The exception to this is Abell 3112, though there does not appear to be any detectable molecular absorption in this system. For the interested reader, all of the observations presented in this paper, including all continuum images, are publicly available via the ALMA Science Archive.

The sample of 23 brightest cluster galaxies was drawn from over 750 X-ray selected clusters with complete, multi-frequency radio coverage (Hogan et al., 2015b) that extends to the sub-mm for the brightest sources (Hogan et al., 2015a). Each source has either a detection at 2 mm above 7 mJy (Hogan et al., 2015a), an AT20G 20 GHz (Murphy et al., 2010) detection and/or is included in the OVRO 40m 15 GHz monitoring sample (Richards et al., 2011). There are at most two sources below the declination limit ($< 33°$) not included in the original Cycle 5 request (Abell 2055 and Abell 2627) which meet these high frequency selection criteria but are both excluded to avoid issues of source orientation (Green et al., 2017). This is because they are potential BL Lacs – objects with strongly variable optical and radio continuum emission, and erratically varying polarization (Vermeulen et al., 1995). Therefore, the sample will be representative and an essentially complete selection of the brightest mm-bright cores in cluster centres. All of the objects observed, 11 of which appear in the optical emission line sample of Hamer et al. (2016), would most likely be classified as low-ionization nuclear emission-line regions (LINERs) in terms of the line widths of their optical spectra. LINERs represent the most numerous local Active Galactic Nuclei population, and are similar to Seyfert 2 galaxies. The key difference between them is the low-ionization lines, such as [O I] λ6300, which are relatively strong in LINERs (Singh et al., 2013). As a result of their low X-ray luminosities, they have also been suggested as a link between normal and active galaxies (Márquez et al., 2017).

Observations were taken between 2018 January 02 and 2018 September 20. The survey

focused on detecting emission and absorption due to transitions between the $J = 0$ and $J = 1$ rotational states of CO. This line acts as a tracer for molecular hydrogen at temperatures of up to a few tens of Kelvin; H_2 is significantly more abundant, but not directly observable at these low temperatures. Assuming a carbon abundance equal to that of the Milky Way gas phase, and that all gas phase carbon exists in CO molecules, the ratio of carbon monoxide to molecular hydrogen is $CO/H_2 = 3.2 \times 10^{-4}$ (Sofia et al., 2004).

As well as the spectral window in which CO lines were anticipated, the brightest cluster galaxies were observed in neighbouring spectral windows in order to estimate the flux densities of their continuum sources. These observations, which are done at a much lower spectral resolution, also provide serendipitous detections of CN lines from the N = 0 - 1 transition. CN molecules are primarily produced by photodissociation reactions of HCN, and its presence is therefore indicative of dense, molecular gas in the presence of a strong ultraviolet radiation field (for a detailed overview of the origins of CN, see Boger & Sternberg, 2005). Additionally, models have shown that CN production at high column densities can be induced by strong X-ray radiation near active galactic nuclei (Meijerink et al., 2007).

As well as CO and CN lines, in one case SiO absorption is also detected. This dense gas tracer is often indicative of shocks due to outflows and jet-cloud interactions, and its abundance is highest around galactic centres (Rodriguez-Fernandez et al., 2006; Rodríguez-Fernández et al., 2010).

Table 5.1 summarises the observations and detections of CO, CN, and H I lines which have been made both in this survey and archival observations. The top section of the table gives details for sources in which there is some form of molecular absorption – discussed fully in §5.4. The middle section shows sources later discussed in §5.5 in which there is emission, but no absorption. The lower section gives details for sources in which there is no molecular absorption or emission – discussed in §5.6. This table provides a useful reference for the reader throughout the chapter and helps to place these detections within a wider context. Details of the observations for all sources in which there is evidence of molecular gas from emission and/or absorption lines are given in Table 5.2.

Source	CO(1-0)	CN-A	CN-B	SiO(3-2)	Archival CO(2-1)	Archival H I
Hydra-A	✓✓	✓✗	✓✗	-	✓✓	✓✗
S555	✓✓	✓✗	✓✗	-	-	✗✗
Abell 2390	✓✗	✓✗	✓✗	✓✗	-	✓✗
RXCJ0439.0+0520	✓✗	✗✗	✗✗	✗✗	-	✗✗
Abell 1644	✗✓	✓✗	✓✗	-	-	✓✗
NGC 5044	✗✗	✓✗	✓✗	-	✓✗	✗✗
NGC 6868	✓✓	✓✗	✓✗	-	-	✓✗
Abell 2597	✗✓	✓✗	✓✗	-	✓✓	✓✗
RXCJ1350.3+0940	✗✓	✗✓	✗✓	-	-	✓✗
MACSJ1931.8-2634	✗✓	-	-	-	-	-
RXCJ1603.6+1553	✗✓	✗✗	✗✗	-	-	✓✗
RXCJ0132.6-0804	✗✗*	✗✗	✗✗	✗✗	-	-
MACSJ0242-2132	✗✗	-	✗✗	✗✗	-	-
Abell 3112	✗✗	✗✗	✗✗	-	-	✗✗
Abell 496	✗✗	✗✗	✗✗	-	-	✗✗
Abell 2415	✗✗	✗✗	✗✗	-	-	✓✗
Abell 3581	✗✗	✗✗	✗✗	-	-	-
RXCJ1356-3421	✗✗	✗✗	✗✗	✗✗	-	✓✗

- Not observed

✗✗ Not detected in emission or absorption

✓✗ Absorption detected, emission undetected

✗✓ Absorption undetected, emission detected

✓✓ Absorption and emission detected

Table 5.1

For the 18 sources observed in this survey, the above table highlights the lines for which observations have been carried out and detections of emission and absorption lines have been made. Archival CO(2-1) and H I observations and detections are also indicated. The top section of the table gives these details for the sources shown in Fig. 5.2 and 5.3, where there is $\geq 3\sigma$ CO(1-0), CN-A, and/or CN-B absorption lines. The CN-A and CN-B lines are produced when CN N = 0 - 1 absorption, which has two groupings of hyperfine structure, is observed at low spectral resolution (a more detailed description of this is given in §5.3). In the middle section of the table are the sources which have clear CO(1-0)/CN-A/CN-B emission but no $\geq 3\sigma$ absorption lines (Fig. 5.4). In the lower section are the sources which do not show any $\geq 3\sigma$ CO(1-0) or CN-A/CN-B emission and absorption along the line of sight the galaxy's continuum source.

*Detected in emission on scales significantly larger than the beam size.

	Hydra-A	S555	Abell 2390	RXCJ0439.0+0520	Abell 1644	NGC 5044
Observation date	2018 Jul 18	2018 Jan 23	2018 Jan 07	2018 Jan 11	2018 Aug 21	2018 Sep 20
Integration time (s)	2700	2800	8000	1300	2800	2400
CO(1-0) vel. resolution (km s^{-1})	2.7	2.6	3.1	3.0	2.6	2.5
CN vel. resolution (km s^{-1})	46	45	63	60	45	42
SiO(3-2) vel. resolution (km s^{-1})	-	-	54	-	-	-
Angular resolution (arcsec)	1.63	0.81	0.37	0.43	1.97	0.56
Spatial Resolution (kpc)	1.72	0.70	1.36	1.46	1.83	0.11
PWV (mm)	2.85	2.23	2.12	2.58	1.39	0.49
FoV (arcsec)	61.6	71.0	63.8	62.7	61.1	58.8
ALMA configuration	C43-1	C43-5	C43-6	C43-5	C43-3	C43-5
Maximum spacing (m)	161	1400	2500	1400	500	1400
CO(1-0) noise/channel (mJy/beam)	1.00	0.45	0.25	0.76	0.65	0.59
CN noise/channel (mJy/beam)	0.16	0.064	0.030	0.11	0.10	0.073
SiO noise/channel (mJy/beam)	-	-	0.064	-	-	-
115 GHz cont. flux density (mJy)	81.5	12.8	7.7	72.0	41.8	14.6
CO(2-1) channel width (km s^{-1})	-	-	-	-	-	1.3
CO(2-1) noise per channel (mJy)	-	-	-	-	-	0.95

	NGC 6868	Abell 2597	RXCJ1350.3+0940	MACSJ1931.8-2634	RXCJ1603.6+1553
Observation date	2018 Jan 25	2018 Jan 02	2018 Sep 16	2018 Jan 02	2018 Sep 16
Integration time (s)	5100	7300	5600	5300	1500
CO(1-0) vel. resolution (km s^{-1})	2.5	2.7	2.9	3.4	2.8
CN vel. resolution (km s^{-1})	42	48	53	-	51
Angular resolution (arcsec)	0.81	0.35	0.66	0.47	0.68
Spatial Resolution (kpc)	0.15	0.54	1.55	2.33	1.36
PWV (mm)	6.52	1.87	0.66	3.19	0.82
FoV (arcsec)	58.8	63.3	66.5	68.3	65.0
ALMA configuration	C43-5	C43-6	C43-4	C43-6	C43-4
Maximum spacing (m)	1400	2500	784	2500	784
CO(1-0) noise/channel (mJy/beam)	0.53	0.34	0.31	0.24	0.62
CN noise/channel (mJy/beam)	0.064	0.054	0.047	-	0.12
115 GHz cont. flux density (mJy)	14.3	7.8	10.6	3.1	54.3
CO(2-1) channel width (km s^{-1})	-	4.3	-	-	-
CO(2-1) noise per channel (mJy)	-	0.23	-	-	-

Table 5.2

A summary of the ALMA observations presented in this chapter. All were taken using ALMA band 3 and have a frequency resolution of 977 kHz. The field of view (FoV) is defined as the FWHM of the primary beam.

For context, a short description of previous observations of each galaxy in this survey is provided below. Any previous detections of H I absorption, a tracer of warm atomic gas, are highlighted. In ambiguous cases where a source's name is often used to describe both the individual brightest cluster galaxy and the wider cluster, the name is used in reference to the former.

- **Hydra-A** is a giant elliptical galaxy with a close to edge-on disk of dust and molecular gas lying at the centre of an X-ray luminous cluster (Hamer et al., 2014). Hydra-A is an archetype of a brightest cluster galaxy lying in a cooling flow, with powerful radio jets and lobes projected outwards from its centre (Taylor et al., 1990). These are surrounded by cavities in the X-ray emitting gas of the intracluster medium created by repeated AGN outbursts (McNamara et al., 2000; Wise et al., 2007). Previous observations of Hydra-A show extremely strong CO(2-1) absorption against the bright radio core ($\tau_{\rm max} \sim 0.9$) due to molecular gas moving away from the galaxy centre at a few tens of km s^{-1}(Chapter 3). H I absorption has been detected against the core of the galaxy with a peak optical depth of $\tau = 0.0015$ (Taylor, 1996).

- **S555** is a relatively anonymous low X-ray luminosity cluster selected by the REFLEX survey (Böhringer et al., 2004) which has a strong compact radio source (Hogan et al., 2015b), is known to be core dominated, and has a significant radio and gamma-ray flux density (Dutson et al., 2013). Against the core of the galaxy, H I absorption has been searched for, providing an upper limit of $\tau_{\rm max} < 0.013$ (Hogan, 2014b).

- **Abell 2390** lies at the centre of a highly X-ray luminous cluster ($L_X \sim 10^{45}$ erg s^{-1}, Ebeling et al., 1996) with a significant cooling flow of 300 $M_\odot$ yr^{-1} (Allen et al., 2001). The galaxy has extended optical emission lines (Le Borgne et al., 1991) and contains a significant mass of dust showing up as strong absorption in optical and submillimetre continuum emission (Edge et al., 1999). Against the core of the galaxy, H I absorption has been detected with $\tau_{\rm max} = 0.084 \pm 0.011$ (Hogan, 2014b).

- **RXCJ0439.0+0520** has been found to be highly variable in the radio, with significant changes occurring in its 15 GHz spectrum over year long timescales (Hogan et al.,

2015b). Optical emission line studies also show a significant Hα luminosity of 6×10^{40} erg s^{-1} (Hamer et al., 2016). Against the core of the galaxy, H I absorption has been searched for, providing an upper limit of $\tau_{\rm max} < 0.133$ (Hogan, 2014b).

- **Abell 1644** is a poorly studied source lying at the centre of the brighter of two X-ray peaks in its host cluster, which itself has evidence of gas sloshing (Johnson et al., 2010). H I absorption has also been detected (Baek et al., 2020).

- **NGC 5044** is a highly perturbed brightest cluster galaxy which contains a significant mass of multiphase gas. It is surrounded by numerous cavities and X-ray filaments which have been inflated by the AGN (Buote et al., 2004; David et al., 2011; Gastaldello et al., 2013). CO(2-1) observations show significant emission and give an inferred molecular gas mass of $6.1{\times}10^7$ M$_\odot$ (Temi et al., 2018a). CO(2-1) absorption has also been observed due to a series of molecular gas clouds lying along the line of sight to the continuum source, with velocities of approximately 250 km s^{-1} (David et al., 2014).

- **NGC 6868** is poorly studied, though it has been found to have a flat spectrum with a core flux density of 105 mJy at 5 GHz (Hogan et al., 2015a). H I absorption has been observed against the galaxy's core at a velocity of v $\sim$ 50 km s^{-1} and FWHM $\sim$ 80 km s^{-1} (Tom Oosterloo, private communications)

- **Abell 2597** is a giant elliptical brightest cluster galaxy surrounded by a dense halo of hot, X-ray bright plasma of megaparsec scales. Observations by Tremblay et al. (2016); Tremblay et al. (2018) show CO(2-1) emission at the systemic velocity of the galaxy. There are also three distinct regions of CO(2-1) absorbing molecular gas along the line of sight to the galaxy's radio core, with optical depths of $\tau \sim 0.2 - 0.3$ and velocities of $240 - 335$ km s^{-1}.

- **RXCJ1350.3+0940** lies in an extremely strong cool-core cluster which, while selected as part of the ROSAT Bright Source catalogue (RBS1322, Schwope et al., 2000), was misidentified as a BL-LAC (Massaro et al., 2009; Richards et al., 2011; Green et al., 2017) because it is dominated by a 300 mJy, flat-spectrum radio core. Despite

having radio, optical, MIR, and sub-mm properties which are similar to many of the best known cool-core clusters (e.g. Abell 1068, Abell 1835 and Zw3146), overall the galaxy remains poorly studied (Hogan et al., 2015a; Green et al., 2016). However, around the core of the galaxy, H I absorption has been searched for, giving an upper limit of $\tau_{\rm max} < 0.0054$ (Hogan, 2014b).

- **MACSJ1931.8-2634** lies within an extremely X-ray luminous cool-core containing large cavities and an equivalent mass cooling rate of ~ 700 $M_\odot$ yr^{-1} in the central 50 kpc (Allen et al., 2004, 2008). Clear structure exists within the cluster core and the brightest cluster galaxy itself is strongly elongated in the North-South direction (Ehlert et al., 2011). ALMA data at higher frequencies have recently been published by (Fogarty et al., 2019) but no attempt to determine the extent of any absorption against the core was made in that paper.

- **RXCJ1603.6+1553** is another relatively poorly studied cluster, likely due to its brightest cluster galaxy being dominated by a flat-spectrum radio core. Like RXCJ1350.3+0940, the source was selected in the ROSAT Bright Source catalogue (RBS1552) but the bright radio core led to the X-ray source being classified as a BL Lac. HI absorption has been detected close to the galaxy's systemic recession velocity with a peak optical depth of $\tau_{\rm max} = 0.125$ and FWHM ~ 400 km s^{-1}(Geréb et al., 2015).

- **MACSJ0242.5-2132** contains one of the most radio powerful core sources in the sample presented in Hogan et al. (2015a). The redshift of this source at $z = 0.31$ means that the H I absorption is strongly affected by RFI, so in the past sensitive observations of this source have not been attempted.

- **Abell 3112** has a strong source at its core in the ALMA continuum image consistent with the position of the published Long Baseline Array observation. However, a second unresolved source is visible to the North-West of the core consistent with a compact, off nuclear source seen in archival HST imaging. The galaxy has an upper limit for H I absorption of $\tau_{\rm max} < 0.007$, made with the Australia Telescope Compact Array (ATCA) and shown in Hogan (2014b).

- **Abell 496** is poorly studied, though has an upper limit for H I absorption from the Very Large Array (VLA) presented by Hogan (2014b).

- **RXCJ0132.6-0804** is highly X-ray luminous (3.6×10^{44} erg s^{-1} Bohringer et al., 2002) and core dominated, with evidence of AGN activity (Hamer, 2012). It also has a highly variable radio flux density, with up to $\sim$ 80 per cent variability at 150 GHz found by Hogan et al. (2015b).

- **Abell 2415** is poorly studied, though has an as yet unpublished H I absorption detection from the *Jansky* VLA from 2015 (PI: Edge) with an estimated peak optical depth of $\tau_{\rm max} = 0.02$.

- **Abell 3581** hosts one of the best studied, low redshift and radio loud brightest cluster galaxies, PKS 1404-267 (Johnstone et al., 1998, 2005). The cluster shows evidence of multiple AGN outbursts (Canning et al., 2013) and ALMA observations detect strong CO(2-1) emitting gas filaments (Olivares et al., 2019). Johnstone et al. (1998) present a VLA spectrum showing no significant H I absorption.

- **RXCJ1356.0-3421** has X-ray properties consistent with a strong cooling flow. It should therefore have been included in the REFLEX cluster sample that is one of the two primary X-ray samples that make up the parent sample for this study, but was assumed to be AGN dominated (Somboonpanyakul et al., 2018). H I absorption with $\tau_{\rm max} = 0.125$ and a full-width-zero-intensity of $\sim$ 500 km s^{-1} has been published by (Véron-Cetty et al., 2000), implying that a significant column density of atomic gas is present in this system.

5.3 Data processing and the origin of the CN-A and CN-B absorption lines

The data presented in this chapter were handled using CASA version 5.1.1, a software package which is produced and maintained by the National Radio Astronomy Observatory (NRAO) (McMullin et al., 2007). The calibrated data were produced by the ALMA

observatory and following their delivery, channel maps at maximal spectral resolution were made. The self-calibration and continuum subtraction of the images were done as part of the pipeline calibration. When converting the frequencies of the observed CO(1-0) spectra to velocities, a rest frequency of $f_{\mathrm{CO(1\text{-}0)}} = 115.271208$ GHz is used. The CN absorption is more complex than that of CO due to its hyperfine structure and the lower spectral resolution with which it was observed. Two lines are seen in CN for each absorption region detected, with relative peak line strengths of approximately 2:1. These two poorly resolved absorption features are themselves composed of a mixture of hyperfine structure lines, details of which are given in Table 5.3 and Fig. 5.1. The CN lines covered are of the N = 0 - 1 transition, which consists of nine hyperfine structure lines split into two distinct groups. The stronger group being J = 3/2 - 1/2 transitions and the weaker group J = 1/2 - 1/2 transitions. Throughout the paper, the label CN-A is used to denote the stronger absorption line, and CN-B to denote the weaker line. The intensity weighted mean of the component hyperfine structure lines is used to calculate the rest frequencies, resulting in $f_{\mathrm{CN\text{-}A}} = 113.49485$ GHz and $f_{\mathrm{CN\text{-}B}} = 113.16883$ GHz. For the single detection of SiO(3-2), the rest frequency is $f_{\mathrm{SiO(3\text{-}2)}} = 130.268610$ GHz.

We use a range of sources to determine the velocity of the emission and absorption features in each galaxy relative to its recession velocity. The velocities used for each galaxy and their sources are listed in Table 5.4.

5.4 Molecular absorption in the cores of eight brightest cluster galaxies

From the sample of 18 brightest cluster galaxies observed, there is $\geq 3\sigma$ evidence of molecular absorption in eight. Their absorption spectra, each extracted from a region centred on the continuum source with a size equal to the synthesized beam's FHWM, are shown in Fig. 5.2 and 5.3. The continuum emission against which this absorption is observed is unresolved in all of these sources, and therefore the absorption itself is not spatially resolved.

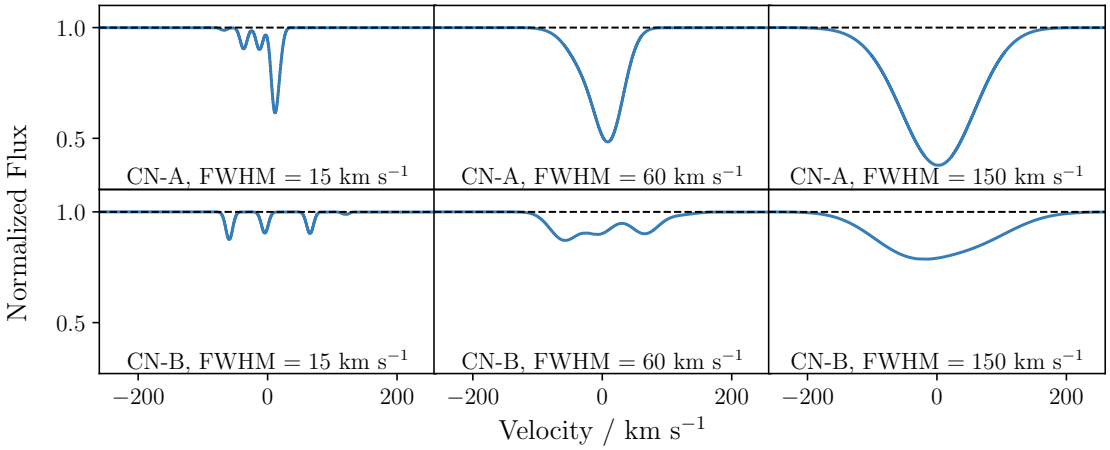

Figure 5.1

Our observations show detections of two CN lines, labelled as CN-A and CN-B throughout the paper. These are respectively formed by the combination of five and four hyperfine structure lines, details of which are shown in Table 5.3. The low spectral resolution CN observations do not resolve this hyperfine structure, and as such, each of the two groups of lines is treated as a single Gaussians during the analysis. Here, the appearance of these two sets of lines is simulated for increasing FWHM and a constant, arbitrary peak intensity to show how they appear as they blend together. The velocities are calculated using the intensity weighted mean of the CN-A and CN-B line centres rather than the individual line frequencies (see Table 5.3). The same calculations are applied to the CN spectra. Even without including noise, the hyperfine structure lines merge together as the FWHM increases towards the CN channel widths of the observations shown in Fig. 5.2 and 5.3 ($\sim$ 60 km s^{-1}). Gaussian fits to these lines show that CN-B has the larger FWHM, consistent with the observations. The slight asymmetry which is particularly prominent in the blended CN-B line is also seen in the majority of the spectra shown in Fig. 5.2 and 5.3.

Line	Rest frequency (GHz)
CO(1-0)	115.271208
CO(2-1)	230.538000
CN-A	113.49485
CN-B	113.16883
SiO(3-2)	130.268610

CN transition $N, J, F \rightarrow N', J', F'$	Rest frequency (GHz)	Relative intensity
1,3/2,3/2 → 0,1/2,1/2	113.48812	0.125
1,3/2,5/2 → 0,1/2,3/2	113.49097	0.333
1,3/2,1/2 → 0,1/2,1/2	113.49964	0.099
1,3/2,3/2 → 0,1/2,3/2	113.50890	0.096
1,3/2,1/2 → 0,1/2,3/2	113.52043	0.012
1,1/2,1/2 → 0,1/2,1/2	113.12337	0.012
1,1/2,1/2 → 0,1/2,3/2	113.14415	0.098
1,1/2,3/2 → 0,1/2,1/2	113.17049	0.096
1,1/2,3/2 → 0,1/2,3/2	113.19127	0.125

Table 5.3

Top: The rest frequencies used throughout this paper when converting from frequencies to velocities. The frequencies of the CN-A and CN-B lines are the intensity weighted means of the component hyperfine structure lines. **Bottom:** The individual hyperfine structure lines of CN existing in the frequency range of the observed absorption regions (Muller et al., 2005). From the hyperfine structure lines listed here, the first five and last four each blend together to form two separate lines in the relatively low spectral resolution observations. When fitting to these two lines, an intensity weighted mean for the line frequency is used. For the lines labelled CN-A, this frequency is 113.49485 GHz and for those labelled CN-B, is 113.16883 GHz. Fig. 5.1 demonstrates how this hyperfine structure of CN blends to give the CN-A and CN-B lines.

Source	Redshift	Recession velocity (km s^{-1})	Redshift source
Hydra-A	0.0544±0.0001	16294±30	MUSE
S555	0.0446±0.0001	13364±30	MUSE
Abell 2390	0.2304±0.0001	69074±30	VIMOS
RXCJ0439.0+0520	0.2076±0.0001	62237±30	VIMOS
Abell 1644	0.0473±0.0001	14191±30	MUSE
NGC 5044	0.0092±0.0001	2761±30	MUSE
NGC 6868	0.0095±0.0001	2830±30	FORS
Abell 2597	0.0821±0.0001	24613±30	MUSE
RXCJ1350.3+0940	0.13255±0.00003	39737±10	SDSS
MACS1931.8-2634	0.35248±0.00004	105670±10	MUSE
RXCJ1603.6+1553	0.10976±0.00001	32905±3	SDSS

Table 5.4

Stellar redshifts and their corresponding velocities used as zero-points for the spectra shown in Figs. 5.2, 5.3 and 5.4. All redshifts are barycentric and use the optical convention. The stellar redshifts of Hydra-A, Abell 1644, and NGC 5044 are taken from Multi Unit Spectroscopic Explorer (MUSE) observations (ID: 094.A-0859). Further details of the MUSE stellar redshift used for Abell 2597 can be found in Tremblay et al. (2018). The stellar redshifts of RXCJ1350.3+0940 and RXCJ1603.6+1553 are from the Sloan Digital Sky Survey (SDSS) (Abazajian et al., 2009). The stellar redshift of MACS1931.8-2634 is taken from Fogarty et al. (2019) and is found using MUSE observations. Crosschecking with FOcal Reducer and low dispersion Spectrograph (FORS) observations of S555, Abell 1644, NGC 5044, and Abell 2597 provides redshifts in good agreement with those listed below. The redshifts used for Abell 2390 and RXCJ0439.0+0520 are taken from Visible Multi-Object Spectrograph (VIMOS) observations previously presented by Hamer et al. (2016) and are based primarily on stellar emission lines. The observed wavelengths of the single stellar absorption line in these two VIMOS spectra are consistent with the quoted redshifts. The VIMOS redshift of RXCJ0439.0+0520 also matches that derived from the multiple absorption lines found from an archival William Hershel Telescope (WHT) observation using the ISIS spectrograph.

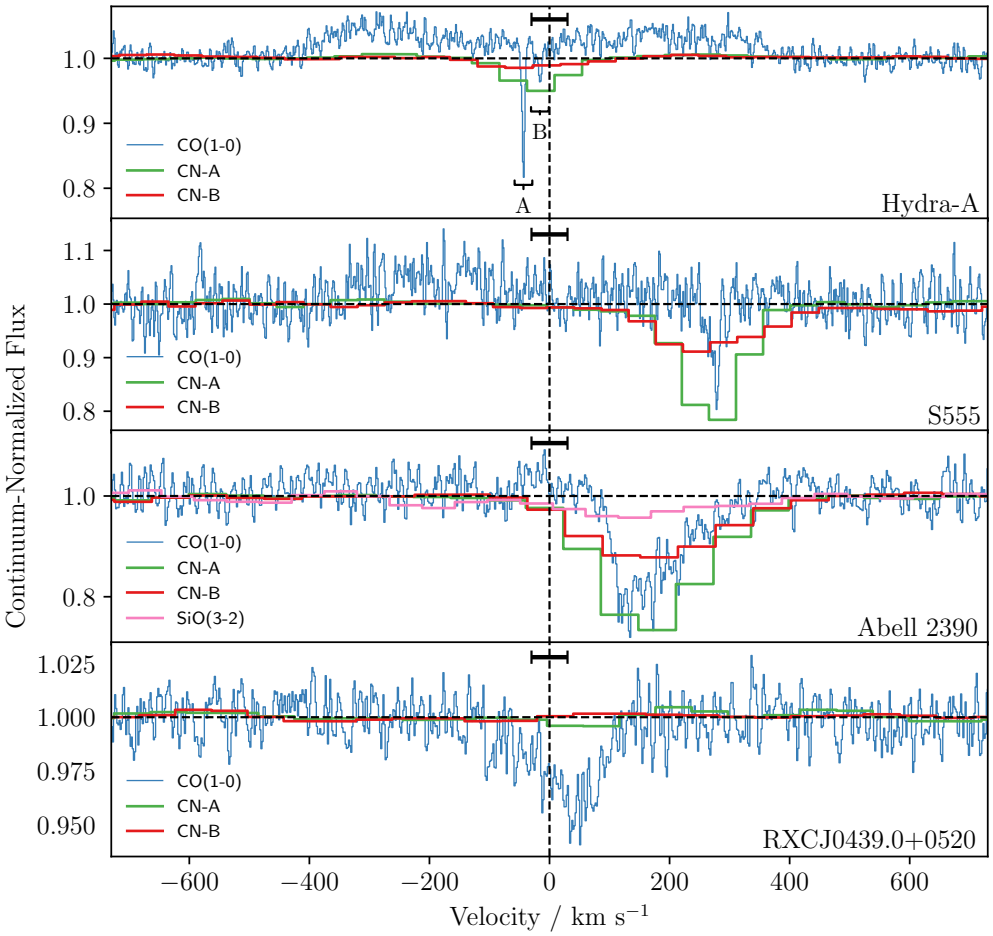

Figure 5.2

CO(1-0) and CN-A/CN-B spectra from along the line of sight to each object's continuum source, extracted from a region with a size equal to the synthesized beam's FHWM. The spectra shown here are those with $\geq 3\sigma$ detections of CO and/or CN absorption out of the sample of 18 observed. Each of the two CN lines shown is produced by the combination of several of the molecule's hyperfine structure lines (see Fig. 5.1 and Table 5.3 for further details). One source, Abell 2390, also shows a SiO(3-2) absorption line detection. Where available, archival observations of CO(2-1) have been included. The recession velocity on which each spectrum is centred can be found in Table 5.4 and the error bars shown in the top-middle of each spectrum indicate the systematic uncertainty of this value. Continued in Fig. 5.3.

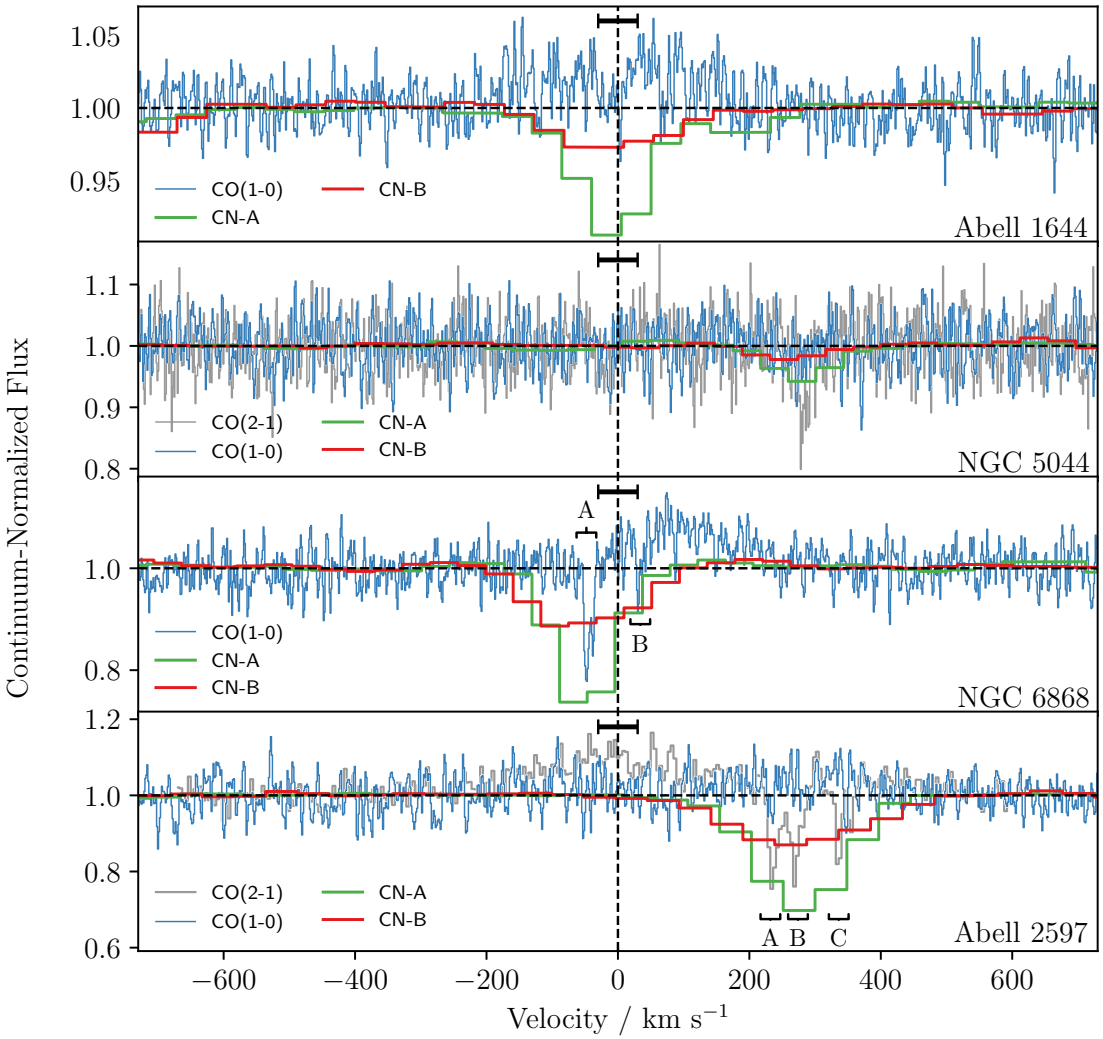

Figure 5.3

CO(1-0) and CN-A/CN-B spectra extracted from regions centred on each object's continuum source and with a size equal to the synthesized beam's FHWM. Continued from Fig. 5.2.

Table 5.5 shows the central velocity, FWHM, amplitude, peak optical depth, and velocity integrated optical depth of the emission and absorption features. The values and errors are calculated by performing Monte Carlo simulations which re-simulate the noise seen in each spectrum, along the same lines as described in Chapter 3. To summarise, for each observed spectrum the noise level is estimated from the root mean square (rms) of the continuum source's emission. This is calculated after excluding the region where the emission is clearly visible. Following this, 10 000 simulated spectra are produced. To make each simulated spectrum, a Gaussian distribution is created for each velocity channel. This distribution is centred at the intensity in the observed spectrum for that particular velocity channel, with a variance equal to the rms noise squared. A value for the intensity is drawn at random from the Gaussian distribution. When this has been done for all velocity channels, a simulated spectrum is produced. For each of the 10 000 simulated spectra, Gaussian lines are fitted to the absorption and emission line features. The values which delimit the 15.865 per cent highest and lowest results for each of the fits give the upper and lower 1σ errors, meaning that 68.27 per cent of the fitted parameters will lie within the 1σ range.

Below is a brief description of the emission and absorption features seen in each source.

- **Hydra-A** shows double peaked CO(1-0) emission due to the edge-on orientation of its disk and the large beam size of the observations. Close to the zero velocity point, two CO(1-0) absorption features can be seen, one of which is strong and extremely narrow ($\tau_{\rm max} = 0.22^{+0.1}_{-0.1}$, FWHM $= 5.2^{+0.4}_{-0.3}$ km s^{-1}). These are also matched by CN-A/CN-B absorption lines. This feature appears stronger still in previous CO(2-1) absorption, where the optical depth peaks at $\tau_{\rm max} = 0.9$. In order to show the CO(1-0) and CN-A/CN-B absorption more clearly, the CO(2-1) absorption line of Hydra-A is not included (due to its significantly larger optical depth. It can however be found in Chapter 3).

- **S555** shows a CO(1-0) emission line, as well as CO(1-0) and CN-A/CN-B absorption lines at large redshifted velocities of $\sim$ 270 km s^{-1}. These high velocities imply significant line of sight motion towards the mm-continuum source. The combined

integrated optical depth of the CN-A/CN-B absorption lines is around 20 times larger than that of CO(1-0), implying a low molecular ratio of CO/CN.

- **Abell 2390** has no visible CO(1-0) emission, but does show CO(1-0), CN-A/CN-B and SiO(3-2) absorption lines. All of these lines are wide, slightly skewed Gaussians centred at a velocity of $\sim$ 170 km s^{-1}. Despite its large FWHM, the absorption feature has a sharp onset in the high spectral resolution CO(1-0) spectrum.

- **J0439+05** has no CO(1-0) emission, though a wide CO(1-0) absorption feature (FWHM= 126^{+10}_{-10} km s^{-1}) is present close to the zero velocity point, which is unique among the sample in that there are no corresponding CN-A/CN-B lines.

- **Abell 1644** has a broad CO(1-0) emission region, but no statistically significant CO(1-0) absorption. However, strong CN-A/CN-B absorption is present at the centre of the CO(1-0) emission.

- **NGC 5044**, which was previously found to have redshifted CO(2-1) absorption at $\sim$ 300 km s^{-1} (David et al., 2014), has corresponding CN-A/CN-B lines with a total of around four times the velocity integrated optical depth. However, perhaps due to the relatively high noise level, there is no statistically significant CO(1-0) absorption feature. Likewise, there is no clear CO(1-0) emission.

- **NGC 6868** has the narrowest CO(1-0) emission feature of the sample (FWHM = 207^{+18}_{-18} km s^{-1}), though it is consistent with the range of line widths found in single dish studies (Edge, 2001; Salomé & Combes, 2003). At the blueshifted edge of this emission there are two narrow CO(1-0) absorption features. CN absorption centred on the stronger, more blueshifted of the two CO(1-0) absorption features is also present. As with the other sources, its CN-A/CN-B absorption has a much larger velocity integrated optical depth than that of the CO(1-0). By this measure, the two CN absorption lines are around 10 times stronger than those of CO(1-0).

- **Abell 2597** has previously been shown to have CO(2-1) emission for which the central velocity matches that of the galaxy's stellar recession velocity. There are also three narrow absorption features at velocities of between 240 and 335 km s^{-1}

(Tremblay et al., 2016). These absorption features are also detected at low resolution in CN-A/CN-B, but not in CO(1-0). A weak CO(1-0) emission line is present in the spectrum. However, this is centred at approximately the same velocity as the CO(2-1) and CN-A/CN-B absorption features, rather than close to the systemic velocity where the CO(2-1) emission is seen. This velocity difference between the weak but broad CO(1-0) emission and stronger CO(2-1) emission indicates that the warmer gas, which likely lies closer to the core, traces gas with different dynamics compared with the colder gas traced by the CO(1-0).

In many cases, it should be noted that the optical depth calculations simply provide lower limits. This is due to the difficulty of establishing to what extent emission is compensating for absorption in some spectra. For example, in Abell 2390 there are hints of emission either side of the absorption region, which could reduce the level of absorption inferred. Where the emission is clearer, such as in NGC 6868 and Abell 1644∗, it can be compensated for. This is done by fitting and subtracting a Gaussian line to the CO(1-0) emission after excluding the velocity channels in which the absorption regions lie. For the CN-A/CN-B lines, this effect is unlikely to have an impact because it is only expected to be present very weakly in emission (Wilson, 2018).

∗In the case of Abell 1644, the tentative absorption feature at $v \sim 0$ km s^{-1} is of less than 3σ significance.

Source	Region	$v_{\rm cen}$ (km s^{-1})	FWHM (km s^{-1})	Amplitude (mJy)	$\tau_{\rm max}$	$\int \tau dv$ (km s^{-1})
Hydra-A	CO(1-0) emission	-275^{+6}_{-7}	235^{+16}_{-16}	$3.6^{+0.1}_{-0.1}$	-	-
	CO(1-0) emission	158^{+10}_{-13}	346^{+26}_{-21}	$2.98^{+0.10}_{-0.09}$	-	-
	CO(1-0) absorption 'A'	$-43.4^{+0.1}_{-0.1}$	$5.2^{+0.4}_{-0.3}$	$-15.9^{+0.8}_{-0.8}$	$0.22^{+0.01}_{-0.01}$	$1.17^{+0.06}_{-0.06}$
	CO(1-0) absorption 'B'	-16^{+1}_{-1}	9^{+5}_{-3}	$-4.2^{+0.8}_{-1.0}$	$0.05^{+0.02}_{-0.01}$	$0.5^{+0.2}_{-0.1}$
	CN-A absorption	-22^{+2}_{-2}	102^{+4}_{-4}	$-4.2^{+0.1}_{-0.1}$	$0.052^{+0.002}_{-0.002}$	$5.6^{+0.2}_{-0.2}$
	CN-B absorption	-32^{+9}_{-9}	157^{+15}_{-15}	$-1.2^{+0.1}_{-0.1}$	$0.015^{+0.001}_{-0.001}$	$2.5^{+0.2}_{-0.2}$
S555	CO(1-0) emission	-186^{+10}_{-10}	260^{+19}_{-18}	$0.65^{+0.04}_{-0.04}$	-	-
	CO(1-0) absorption	276^{+2}_{-2}	17^{+6}_{-6}	$-1.8^{+0.3}_{-0.5}$	$0.16^{+0.04}_{-0.03}$	$2.7^{+0.5}_{-0.5}$
	CN-A absorption	270^{+1}_{-1}	113^{+3}_{-3}	$-2.9^{+0.1}_{-0.1}$	$0.26^{+0.01}_{-0.01}$	$29.6^{+0.6}_{-0.6}$
	CN-B absorption	265^{+4}_{-4}	210^{+11}_{-10}	$-1.09^{+0.04}_{-0.04}$	$0.089^{+0.004}_{-0.004}$	$19.6^{+0.8}_{-0.8}$
Abell 2390	CO(1-0) absorption	164^{+2}_{-2}	122^{+4}_{-4}	$-1.55^{+0.05}_{-0.05}$	$0.22^{+0.1}_{-0.1}$	$28.2^{+0.9}_{-0.9}$
	CN-A absorption	167^{+1}_{-1}	200^{+3}_{-3}	$-2.09^{+0.02}_{-0.02}$	$0.31^{+0.01}_{-0.01}$	$63.5^{+0.8}_{-0.7}$
	CN-B absorption	171^{+3}_{-3}	251^{+6}_{-6}	$-1.00^{+0.02}_{-0.02}$	$0.137^{+0.003}_{-0.003}$	$36.0^{+0.7}_{-0.7}$
	SiO(3-2) absorption	120^{+30}_{-30}	400^{+100}_{-100}	$-0.28^{+0.04}_{-0.05}$	$0.037^{+0.007}_{-0.006}$	15^{+3}_{-3}
RXCJ0439.0+0520	CO(1-0) absorption	35^{+3}_{-3}	126^{+10}_{-10}	$-2.9^{+0.2}_{-0.2}$	$0.041^{+0.002}_{-0.002}$	$5.4^{+0.3}_{-0.3}$

Source	Region	$v_{\rm cen}$ (km s^{-1})	FWHM (km s^{-1})	Amplitude (mJy)	$\tau_{\rm max}$	$\int \tau dv$ (km s^{-1})
Abell 1644	CO(1-0) emission	0^{+12}_{-12}	308^{+19}_{-17}	$0.85^{+0.6}_{-0.6}$	-	-
	CN-A absorption	-6^{+1}_{-1}	120^{+4}_{-4}	$-3.6^{+0.1}_{-0.1}$	$0.089^{+0.002}_{-0.002}$	$11.2^{+0.3}_{-0.3}$
	CN-B absorption	-11^{+5}_{-5}	170^{+10}_{-10}	$-1.09^{+0.06}_{-0.06}$	$0.026^{+0.002}_{-0.002}$	$4.7^{+0.3}_{-0.3}$
NGC 5044	CO(2-1) absorption	283^{+1}_{-1}	14^{+2}_{-2}	$-2.6^{+0.4}_{-0.4}$	$0.14^{+0.02}_{-0.02}$	$2.2^{+0.4}_{-0.3}$
	CN-A absorption	280^{+4}_{-4}	101^{+10}_{-9}	$-0.85^{+0.07}_{-0.07}$	$0.06^{+0.01}_{-0.01}$	$6.4^{+0.5}_{-0.5}$
	CN-B absorption	258^{+10}_{-9}	103^{+19}_{-17}	$-0.34^{+0.06}_{-0.06}$	$0.024^{+0.00}_{-0.004}$	$2.6^{+0.5}_{-0.4}$
NGC 6868	CO(1-0) emission	93^{+7}_{-7}	207^{+18}_{-18}	$1.09^{+0.07}_{-0.07}$	-	-
	CO(1-0) absorption 'A'	-45^{+1}_{-1}	15^{+2}_{-1}	$-3.0^{+0.2}_{-0.2}$	$0.24^{+0.04}_{-0.04}$	$3.8^{+0.4}_{-0.4}$
	CO(1-0) absorption 'B'	32^{+1}_{-2}	10^{+5}_{-5}	$-1.6^{+0.4}_{-0.4}$	$0.12^{+0.04}_{-0.04}$	$1.2^{+0.3}_{-0.3}$
	CN-A absorption	-50^{+1}_{-1}	101^{+2}_{-2}	$-4.09^{+0.06}_{-0.06}$	$0.3^{+0.01}_{-0.01}$	$34.4^{+0.5}_{-0.5}$
	CN-B absorption	-52^{+2}_{-2}	168^{+4}_{-4}	$-1.73^{+0.04}_{-0.04}$	$0.12^{+0.01}_{-0.01}$	$22.7^{+0.6}_{-0.6}$
Abell 2597	CO(1-0) emission	233^{+46}_{-42}	400^{+100}_{-100}	$0.24^{+0.08}_{-0.04}$	-	-
	CO(2-1) emission	-5^{+12}_{-8}	330^{+40}_{-30}	$0.89^{+0.05}_{-0.05}$	-	-
	CO(2-1) absorption 'A'	237^{+1}_{-1}	17^{+12}_{-8}	$-2.4^{+0.2}_{-0.2}$	$0.29^{+0.03}_{-0.03}$	$4.9^{+0.6}_{-0.5}$
	CO(2-1) absorption 'B'	269^{+1}_{-1}	21^{+15}_{-10}	$-1.9^{+0.2}_{-0.2}$	$0.23^{+0.03}_{-0.02}$	$4.8^{+0.7}_{-0.6}$
	CO(2-1) absorption 'C'	336^{+1}_{-1}	8^{+7}_{-3}	$-2.1^{+0.4}_{-0.3}$	$0.24^{+0.04}_{-0.04}$	$2.2^{+0.4}_{-0.3}$
	CN-A absorption	279^{+1}_{-1}	156^{+3}_{-3}	$-2.40^{+0.04}_{-0.04}$	$0.36^{+0.01}_{-0.01}$	57^{+1}_{-1}
	CN-B absorption	273^{+4}_{-4}	234^{+8}_{-8}	$-1.03^{+0.03}_{-0.03}$	$0.141^{+0.005}_{-0.005}$	34^{+1}_{-1}

Source	Region	v_{cen} (km s^{-1})	FWHM (km s^{-1})	Amplitude (mJy)	τ_{max}	$\int \tau dv$ (km s^{-1})
RXCJ1350.3+0940	CO(1-0) emission	-50^{+6}_{-6}	318^{+14}_{-14}	$0.77^{+0.03}_{-0.03}$	-	-
	CN-A emission	-14^{+26}_{-26}	310^{+40}_{-50}	$0.19^{+0.03}_{-0.02}$	-	-
	CN-B emission	-30^{+30}_{-30}	160^{+50}_{-50}	$0.14^{+0.04}_{-0.04}$	-	-
MACSJ1931.8-2634	CO(1-0) emission	24^{+5}_{-6}	176^{+20}_{-15}	$0.66^{+0.04}_{-0.05}$	-	-
RXCJ1603.6+1553	CO(1-0) emission	-50^{+7}_{-7}	318^{+18}_{-17}	$1.49^{+0.07}_{-0.06}$	-	-

Table 5.5

The central velocity, FWHM (equivalent to 2.355 σ), amplitude, peak optical depth, and velocity integrated optical depth for the absorption and emission regions shown in Fig. 5.2, 5.3, 5.4. The velocity zero-point used for each source is given in Table 5.4. All velocities are barycentric and use the optical convention. The values and errors are calculated by performing Monte Carlo simulations which re-simulate the noise seen in each spectrum, along the same lines as described in Chapter 3. The residuals of these best fits are shown in Fig. C.1, C.2 and C.3 in Appendix C.1.

5.5 Sources with emission which lack absorption lines

As well as the eight brightest cluster galaxies which have $\geq 3\sigma$ evidence of CO(1-0) and/or CN-A/CN-B absorption lines, there are three systems which have clear emission but no absorption features. The spectra of these sources are shown in Fig. 5.4 and the best fit parameters for the emission lines are given in the lower section of Table 5.5. These spectra are once again extracted from a region which is centered on each object's continuum source and with a size equal to the synthesized beam's FWHM. This is the smallest region from which the spectra can feasibly be extracted and it therefore maximises the strength of any tentative absorption features which may be present.

The three sources which show CO(1-0) emission but lack any absorption features are:

- **RXCJ1350.3+0940**, which also shows clear emission from the CN-A and CN-B lines.
- **MACSJ1931.8-2634**, which is also known to have extended CO(3-2) and CO(4-3) emission (Fogarty et al., 2019).
- **RXCJ1603.6+1553**, in which H I absorption has been detected close to the systemic recession velocity of the galaxy with a peak optical depth of $\sim$ 10 and FWHM = $\sim$ 400 km s^{-1}.

5.6 Sources without emission or absorption lines

As well as the detections shown in Fig. 5.2, 5.3, and 5.4, a large number of the sources observed in this ALMA survey show no clear evidence of any emission or absorption along the line of sight to their continuum source. The details of their observations are given in Table C.1 of Appendix C. The spectra of these sources are not shown, though their observations, including all continuum images, are publicly available via the ALMA Science Archive.

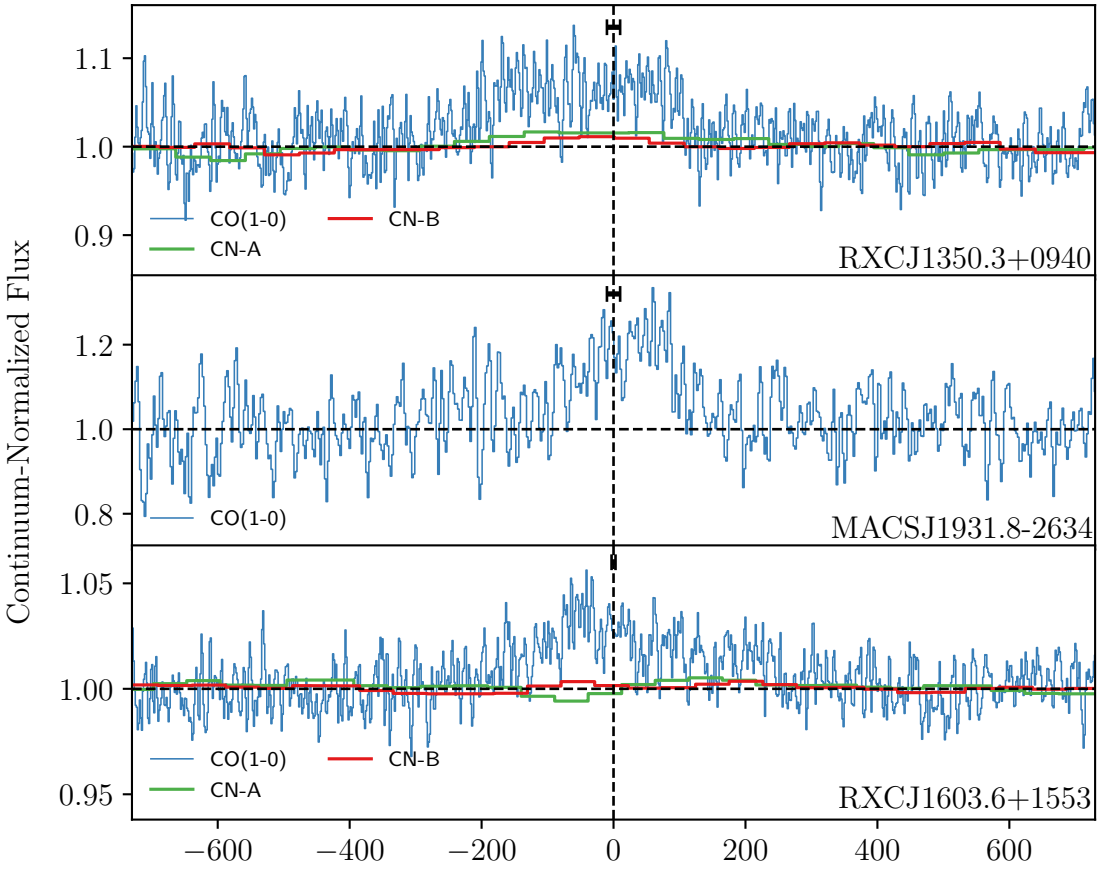

Figure 5.4

CO(1-0) and CN-A/CN-B spectra of sources which do not have $\geq 3\sigma$ absorption features of either CO(1-0) or CN-A/CN-B despite having significant masses of molecular gas in their cores, evidenced by clear CO(1-0) emission. These spectra are each extracted from a region centred on the continuum source with a size equal to the synthesized beam's FHWM. This is the smallest region from which they can feasibly be extracted from and maximises the strength of any tentative absorption features in the spectra. The error bars shown in the top-middle of each spectrum indicate the systematic uncertainty in the recession velocity on which each spectrum in centered.

In total there are seven sources observed for which there is no $\geq 3\sigma$ evidence of molecular gas along the line of sight to their bright radio cores from emission or absorption:

- **MACSJ0242.5-2132**
- **Abell 3112**
- **Abell 496**
- **RXCJ0132.6-0804**
- **Abell 2415**
- **Abell 3581**
- **RXCJ1356.0-3421.**

Additionally, none of the galaxies listed above have CO(1-0) emission which is visible on larger galaxy-wide scales, with the exception of RXCJ0132.6-0804. The extended CO(1-0) emission seen in this system follows the morphology previously found with optical emission lines (Hamer et al., 2016).

In systems such as those observed here, the line of sight covering fraction of molecular gas is expected to be less than its maximum physical value of 1. In other words, molecular gas is not expected to exist along all lines of sight to the galaxies' bright radio cores. Therefore, the lack of absorption lines in the systems listed above does not necessarily mean that significant masses of cold molecular gas are absent. Overall, the eight absorbing systems found from the sample of 18 observed implies a line of sight covering fraction in line with expectations and is similar to that predicted by accretion simulations, such as those by Gaspari et al. (2018).

However, sources which have both CO(1-0) and CO(2-1) observations (Hydra-A, NGC 5044, and Abell 2597) all show the higher energy CO(2-1) line to be significantly stronger in both emission and absorption. It is therefore likely that the 8/18 detection rate is only indicating the covering fraction of particularly cool molecular gas at a up to few tens of Kelvin. Above $\sim$ 50 K, the fraction of CO molecules occupying the ground state energy

level is negligible, and so CO(1-0) absorption from this line is no longer seen. Large proportions of the molecular gas in the cores of these galaxies is likely to exist at higher temperatures not traced well by CO(1-0), as shown by Hydra-A, NGC 5044, and Abell 2597. Therefore, the total covering fraction of molecular gas is likely to be higher than indicated by the CO(1-0) and CN-A/CN-B† observations alone.

5.7 Column Density Estimates

Fig. 5.5 shows the relationship between the velocity integrated optical depths of the CO(1-0) and CN-A/CN-B lines for the eight sources in which they are detected. In the majority of cases the sum of the CN-A and CN-B absorption, i.e. the combination of all CN N = 0 - 1 hyperfine structure lines, is ∼ 10 times as strong as that of CO(1-0). Using an estimated excitation temperature and treating the absorption as optically thin, it is possible to calculate the total column density, $N_{\rm tot}$, of the absorption regions, and therefore estimate the CO/CN ratio of the absorbing gas. In general,

$$N_{\rm tot} = Q(T_{\rm ex}) \frac{8\pi\nu_{ul}^3}{c^3} \frac{g_l}{g_u} \frac{1}{A_{ul}} \frac{1}{1 - e^{-h\nu_{ul}/kT_{\rm ex}}} \int \tau_{ul}\, dv\,, \tag{5.7.1}$$

where $Q(T_{\rm ex})$ is the partition function, c is the speed of light, A_{ul} is the Einstein coefficient of the observed transition and g the level degeneracy, with the subscripts u and l representing the upper and lower levels (Godard et al., 2010; Mangum & Shirley, 2015).

The values from this calculation are given in Table 5.6 and shown in Fig. 5.6. The CO/CN ratio for sources with both CO and CN absorption ranges from ∼ 9 to ∼ 44. This is similar to the values found by Wilson (2018) for nearby galaxies from ALMA observations of CO and CN emission, meaning that the gas seen through absorption has ratios of CO/CN typical of much larger distributions of gas.

Repeat observations of CN at high spectral resolution would be required to fully understand the relationship between CN and CO. Additionally, in the three cases where there are both

†Although the CN observations appear ∼ 10 times stronger than those of CO(1-0), they are likely to lack sufficient spectral resolution to reveal all but the widest and strongest absorption lines.

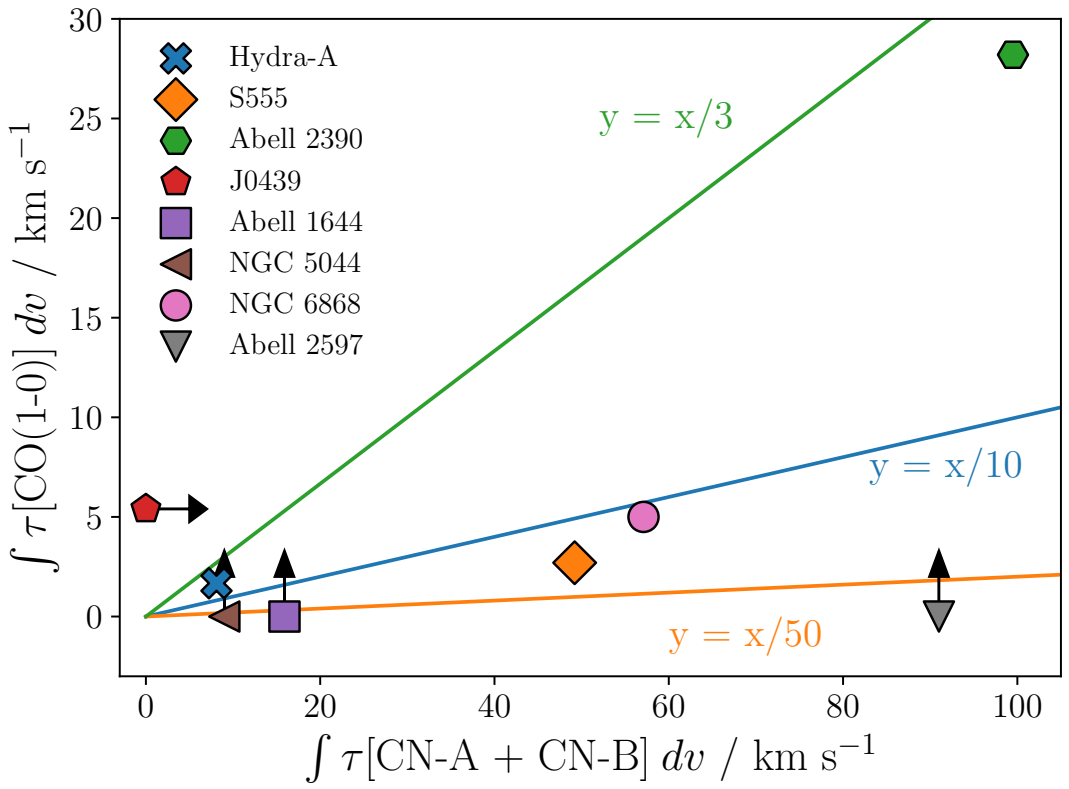

Figure 5.5

The velocity integrated optical depths of the CN-A + CN-B and CO(1-0) absorption lines. For most sources, the CN-A + CN-B absorption (i.e. the sum of the absorption from the various hyperfine structure lines of the $N = 0 - 1$ transition), is typically around ~10 times stronger than that of CO(1-0), indicating a molecular number ratio of CO/CN ~ 10. The CN line appears stronger in absorption than that of CO despite its lower abundance because of its higher electric dipole moment.

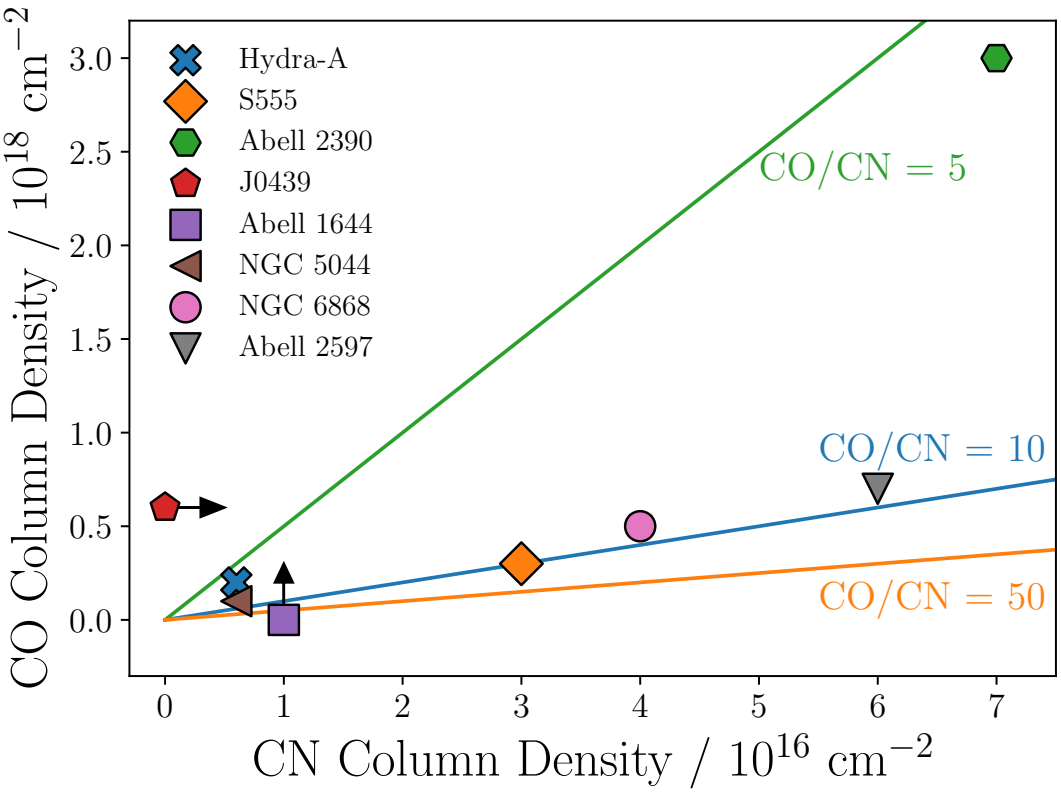

Figure 5.6

The total line of sight CO and CN column densities of the absorption regions shown in Fig. 5.2 and 5.3, values of which are given in Table 5.6. These are mostly derived from the integrated optical depths shown in Table 5.5 and Fig. 5.5. However, for NGC 5044 and Abell 2597, archival CO(2-1) observations are used because they show the absorption more clearly. The column densities are calculated using Eq. 5.7.1 and assuming a gas temperature of 40 K. For most sources, the CO/CN ratio is ~ 10.

Source	Temp. (K)	CO column density (cm^{-2})	CN column density (cm^{-2})	CO/CN ratio
Hydra-A	20	5×10^{16}	2×10^{15}	32^{+4}_{-2}
	40	2×10^{17}	6×10^{15}	32^{+4}_{-2}
	80	7×10^{17}	2×10^{16}	32^{+4}_{-2}
S555	20	8×10^{16}	9×10^{15}	9^{+2}_{-2}
	40	3×10^{17}	3×10^{16}	9^{+2}_{-2}
	80	1×10^{18}	1×10^{17}	9^{+2}_{-2}
Abell 2390	20	8×10^{17}	2×10^{16}	44^{+2}_{-2}
	40	3×10^{18}	7×10^{16}	44^{+2}_{-2}
	80	1×10^{19}	3×10^{17}	44^{+2}_{-2}
J0439+05	20	2×10^{17}	-	-
	40	6×10^{17}	-	-
	80	2×10^{18}	-	-
Abell 1644	20	-	3×10^{15}	-
	40	-	1×10^{16}	-
	80	-	4×10^{16}	-
NGC 5044*	20	4×10^{16}	2×10^{15}	22^{+2}_{-1}
	40	1×10^{17}	6×10^{15}	20^{+2}_{-1}
	80	5×10^{17}	2×10^{16}	20^{+2}_{-2}
NGC 6868	20	1×10^{17}	1×10^{16}	14^{+1}_{-1}
	40	5×10^{17}	4×10^{16}	14^{+1}_{-1}
	80	2×10^{18}	1×10^{17}	14^{+1}_{-1}
Abell 2597*	20	2×10^{17}	2×10^{16}	12^{+1}_{-1}
	40	7×10^{17}	6×10^{16}	11^{+1}_{-1}
	80	2×10^{18}	2×10^{17}	10^{+1}_{-1}

Table 5.6

The CO column densities, CN column densities and molecular number ratio of CO/CN for the sources in Fig. 5.2 and 5.3 which have absorption regions detected. *For NGC 5044 and Abell 2597, where the are no detections of CO(1-0) absorption, archival CO(2-1) absorption is used to estimate the CO column density.

CO(1-0) and CO(2-1) observations, the latter show stronger and clearer absorption lines. A survey of CO(2-1) is therefore vital in order to show the CO gas in more detail.

5.8 Discussion

Following the works of David et al. (2014); Tremblay et al. (2016); Ruffa et al. (2019), and Chapters 3 and 4, the eight detections of molecular absorption presented here significantly increases the number of brightest cluster galaxies in which cold, molecular gas has been observed in absorption against the host galaxy's bright radio core. These detections are made through CO absorption and emission lines, as well as previously undetected CN lines. In seven out of eight cases where there is a CO(1-0) detection there is also CN-A/CN-B, with the exception being RXCJ0439.0+0520. Conversely, one source, NGC 5044 shows clear CN-A/CN-B absorption, but no CO(1-0) absorption despite having been previously detected in CO(2-1) by David et al. (2014). A weak CN line has previously been observed in the intervening absorber G0248+430 (Combes et al., 2019) and was one of many lines detected in the nearby galaxy Centarus-A (Eckart et al., 1990; McCoy et al., 2017). However, these detections are notable due to their rarity, with CN absorption lines being much less commonly observed than those of CO. Further, the line has never previously been detected in absorption against a brightest cluster galaxy's bright continuum source, making the seven detections especially noteworthy.

Fig. 5.7 shows a Venn diagram highlighting the detections of CO, CN and H I which have been made for sources with a complete set of observations for these lines. This emphasises the wide range in the absorption properties of these systems and implies that surveys searching for many different molecular absorption lines are justifiable, even in cases which have previous non-detections of H I and CO absorption.

5.8.1 Potential fuelling of supermassive black holes

In many cases, there is clear evidence of cold molecular gas moving towards its host galaxy's mm-continuum source at significant velocities. S555, NGC 5044, and Abell 2597

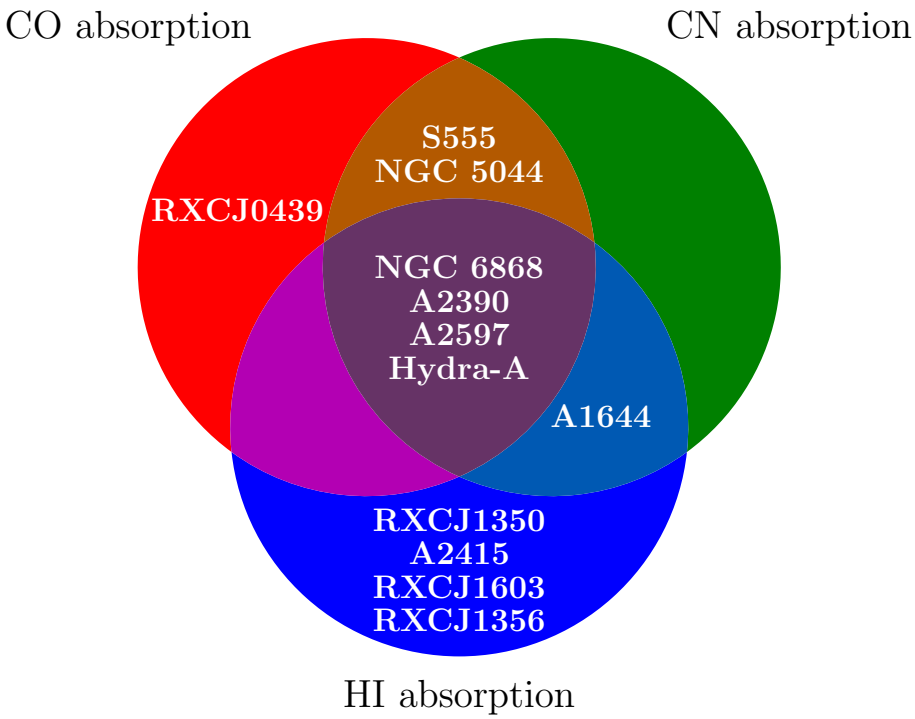

No CN, CO or HI absorption: **Abell 3112, Abell 496**

Figure 5.7

Venn diagram showing the combination of absorption lines which have been detected for sources which have a complete set of CO, CN, and H I observations. Note that the CO detection of NGC 5044 has been made with the (2-1) line and there is no detection with the (1-0) line.

all have absorption regions with velocities towards the core of $\gtrsim 250$ km s^{-1}. Abell 2390 also has redshifted absorbing gas, albeit moving at lower velocities – though in this case the large width of the absorption implies that there is likely to be a systemic motion towards the core.

Hydra-A, J0439+05, Abell 1644, and NGC 6868 all have molecular gas moving at lower blue and redshifted velocities, implying that the clouds are drifting in non-circular orbits and not experiencing any significant inflow or outflow.

Overall these eight detections, combined with those of NGC 5044 (David et al., 2014), Abell 2597 (Tremblay et al., 2016), Hydra-A (Chapter 3) and IC 4296 (Ruffa et al., 2019) do not present any evidence of significantly blueshifted absorption. Though there are some moderately blueshifted regions of molecular gas, overall there is a bias for motion towards the galaxies' supermassive black holes, as shown by Fig. 5.8. In the chaotic cold accretion scenario, most clouds are expected to drift in the large-scale turbulent field (with low $v_{\rm cen}$), while only a few outliers are found to reach velocities of several 100 km s^{-1} (see Gaspari et al., 2018), which is consistent with the findings presented here. Nevertheless, the number of detections these conclusions are based upon remains small.

5.8.2 Constraining the location of the absorbing clouds

It is physically plausible that the absorbing clouds detected in these systems lie anywhere from a few tens of parsecs from the central supermassive black hole, to several kilo parsecs away. Indeed, many of the galaxies in this sample have molecular gas seen in emission out to several kpc, most notably Hydra-A where there is an edge-on gas disc with a diameter of 5 kpc. However, the covering fraction of molecular gas as a function of radius significantly constrains the distance at which the gas is likely to be, as predicted by simulations such as chaotic cold accretion (Gaspari et al., 2017). These simulations of clumpy molecular gas condensation show that the volume filling factor and internal density of molecular clouds are both inversely proportional to radius. This means that the vast majority of dense clouds which contribute to the line of sight absorption are expected to reside in the inner region, within radii of up to ~ 200 pc. Conversely, two properties of the absorbing clouds imply

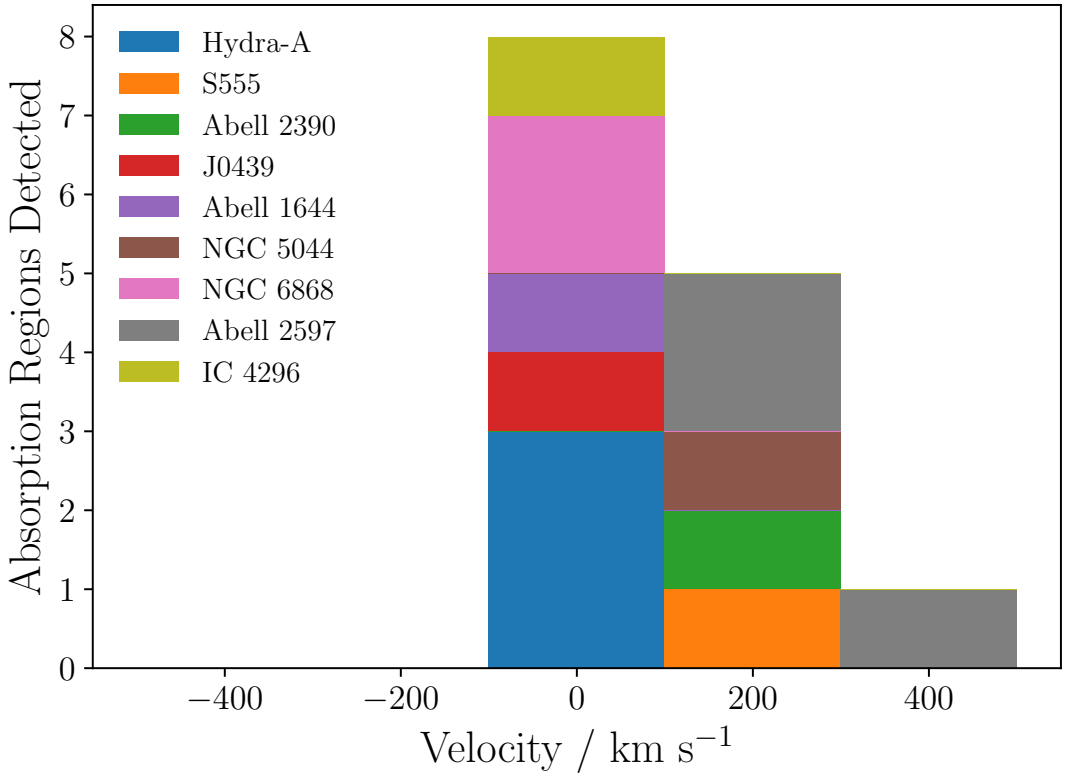

Figure 5.8

Histogram showing the velocities of absorbing regions detected for the nine such brightest cluster galaxy systems known to date, which has a bias for redshifted absorption. Note that from a combination of CO(1-0), CO(2-1), and CN-A/CN-B detections, each galaxy's absorption feature(s) are represented by the line which best resolves the absorption. In most cases, this is CO(1-0). However, for Hydra-A, NGC 5044, and Abell 2597, CO(2-1) is used. For Abell 1644, CN-A is used. Also note that some sources have multiple absorption regions. The histogram is also unweighted by the velocity integrated optical depth of each absorption region due to the uncertainties associated with doing this for the multiple lines from different molecular species.

that they lie outside the approximate Bondi capture radius in each system of a few tens of parsecs. First, the fact that the clouds are detectable by CO(1-0) absorption implies that they are all relatively cool and not being significantly heated by the high radiative power of the central AGN. Given that dust grains are found with ubiquity in interstellar gas, the approximate level of heating a molecular gas cloud will experience can be demonstrated by providing an estimate for the equilibrium dust temperature. For a dust grain radiating with a black-body spectrum, the balance between radiation and emission can be written as

$$F = Q\,\sigma T^4\,, \tag{5.8.1}$$

where F is the flux of the radiation field, Q is the Planck average emissivity, σ is the Stefan-Boltzmann constant and T is the equilibrium temperature. Alternatively,

$$\frac{L}{4\pi R^2} = Q\,\sigma T^4\,, \tag{5.8.2}$$

where the radiation field is assumed to be from a point source of luminosity L at a distance R. The AGN of brightest cluster galaxies such as those in this survey have typical luminosities of $10^{39} - 10^{44}$ erg s^{-1}, though at the higher end these are dominated by radiatively powerful AGN (see Russell et al., 2013). For a dust grain at a distance of 10 pc from a 10^{42} erg s^{-1} point source, the equilibrium temperature is therefore $\sim$ 100 K, assuming a Q value of 0.1 (an approximate value from Draine & Lee, 1984). If self-shielding effects are sufficiently small that the gas and dust can be approximated as being in thermal equilibrium, the existence of cold molecular gas clouds inside these distances is unlikely.

A second property of the absorbing clouds which implies that they lie outside the Bondi capture radius of $\sim$ 10 pc is their velocities. Within these distances they would be expected to obtain highly redshifted velocities, perhaps of thousands of km s^{-1}, due to the gravitational influence of the central supermassive black hole. For example, in Abell 2390 which has a 3×10^8 M$_\odot$ supermassive black hole (Tremblay et al., 2012), a circular orbit at 10 pc requires a velocity of $\sim$ 400 km s^{-1}. Due to the high number density of gas clouds at these low radii, stable orbits are difficult to maintain for long periods due the the high likelihood of cloud-cloud collisions.

5.8.3 Differences between the absorption of different molecules

The significant differences which are seen between the strengths of the CO(2-1) absorption line detections and the lower energy CO(1-0) and CN-A/CN-B lines of NGC 5044 and Abell 2597 have a number of possible explanations. First, the CO(2-1) absorption is enhanced by a factor of three due to its statistical weight. Second, due to the time difference between the observations of CO(2-1) and CO(1-0)/CN-A/CN-B, the clouds may have moved across the line of sight to the bright radio core.

The time difference between the observations is approximately 5 years in the case of NGC 5044 and 6 years for Abell 2597, whereas individual clouds are expected to take at least hundreds of years to cross the line of sight; a relatively small molecular cloud with a diameter of 0.1 pc and a large transverse velocity of 500 km s^{-1} will take $\sim$ 200 years to fully cross the line of sight, assuming a point-like continuum source. A third explanation is that due to the energy difference of the lines, molecular gas regions of different temperatures are being revealed by the different lines. The CO(2-1) absorption line will trace higher temperature gas than the CO(1-0) and CN-A/CN-B lines due to its higher excitation energy. Therefore, if there are multiple regions of molecular gas of significantly different temperatures along the line of sight, the lower and higher energy lines may reveal different absorption features.

However, in the case of NGC 5044, absorption is detected in the low energy CN-A/CN-B lines, but not the similarly low energy CO(1-0) line. The same absorption region is nevertheless detected in the higher energy CO(2-1) line, suggesting that whether or not absorption is present is dependent on more than just the gas temperature alone. A further factor which is likely to play a large role in affecting the strength of the absorbing regions across different lines is the molecular number ratio of CO/CN. In the case of NGC 5044, the absorption may be due to relatively warm gas with a low CO/CN ratio, resulting in modest CO(2-1) and CN-A/CN-B absorption, but no clear CO(1-0) line.

5.9 Conclusions

This chapter presents results from an ALMA survey of 18 brightest cluster galaxies which lie in cool cores and have extremely bright mm-continuum sources at their centres. Molecular absorption is found in eight of this sample via the detections of seven CO(1-0) absorption lines, seven CN N = 1 - 0 lines and one SiO(3-2) line, shown in Figs. 5.2 and 5.3.

Our survey doubles the number of systems in which molecular absorption has been observed against a brightest cluster galaxy's bright continuum source from five to ten and provides new molecular absorption lines for two of those systems previously discovered.

The absorption regions detected have velocities of between -45 to 283 km s^{-1} relative to the systemic recession velocity of the galaxies and overall there is a bias for motion towards the supermassive black holes, though this is found from what is still a relatively small number of sources. These results appear to be consistent with the chaotic cold accretion scenario of Gaspari et al. (2018).

Given that eight absorbing systems are found from the observed sample of 18, it is highly unlikely that a detection rate this high could be produced by absorption at large distances. Instead, they are most likely cases of absorption due to molecular gas at distances within which they could feasibly be accreted onto the supermassive black hole under the right conditions. At these distances of up to a few hundred parsecs, slightly elliptical orbits would be expected to produce offsets of just a few tens of km s^{-1}, rather than the hundreds of km s^{-1} seen in some of the observations i.e. these large velocities are not due to orientation effects. To more precisely estimate the effects of the disc morphology and how this may relate the the velocities of the absorbing clouds, an obvious next step is to map and analyse the molecular emission lines in these galaxies.

CN is found to be a significantly stronger tracer of molecular absorption than CO due to the molecule's higher electric dipole moment. From the eight sources which have detections of both lines, the velocity integrated optical depths are $\sim$ 10 times higher for CN. This implies a typical molecular number ratio of CO/CN $\sim$ 10.

The CO(2-1) line also appears to be a more efficient tracer of molecular absorption than the lower energy CO(1-0) line. Observations of both lines now exist for three sources: Hydra-A, Abell 2597, and NGC 5044. In all cases, the absorption features appear significantly deeper and clearer in the higher energy line.

With the additions from this survey, a complete set of CO, CN, and H I observations now exists for 14 sources (Fig. 5.7). From these, many different combinations of absorption lines are detected. For four sources, all three lines are detected while for a further four only H I absorption is seen. Two show both CO and CN absorption but not that of H I. One source shows only CO absorption while another shows both CN and H I absorption but not that of CO. For two sources, none of the three absorption lines are seen. In relation to future surveys, these results imply that non-detections of a particular absorption line do not rule out subsequent detections of other lines.

CHAPTER 6

Summary and Future Work

6.1 Key Results

Over the last few decades, galaxies and the active galactic nuclei which lie at their centres have come to be understood as incredibly important factors in each other's evolution, and this thesis has explored some new ways in which the links between the two can be better understood. First, the behaviour of active galactic nuclei was explored by observing their variability at high radio frequencies. This was then followed by observations of the molecular gas clouds within the galaxy. It is clumpy molecular clouds like these which are thought to be largely responsible for the accretion process which result in that variability.

The research presented in this thesis was written over the course of four years, and the chapters in which it is presented are largely in their original published form. Naturally however, as the research progressed a more complete picture emerged and the interpretations of the data have been made more precise, and in some cases have changed. Below are the most significant conclusions which can be drawn from this research, with some reflections on the ways in which the original conclusions have now changed.

- At high radio frequencies, the core radio sources of cool-core brightest cluster galaxies exhibit significant levels of variability on relatively short timescales. At

least half of the sources in the representative sample studied in Chapter 2 vary by 20 percent or more on timescales of 1000 days. This is a lower limit because in the remaining half, the apparent variability due to observational errors cannot be separated from the true variability. Additionally, since a source is unable to vary on timescales less than its light crossing time, an upper limit on physical size can be inferred from the timescale on which it varies. This puts the upper limit at 1 - 3 ly (0.3-1 pc) in most cases. Because variability (in the form of AGN outbursts) is a consequence of accretion events, such events can also be concluded to take place on similar timescales.

- The same study also suggests that at least a third of cool-core brightest cluster galaxies vary by 60 per cent on 6 year timescales. This is important to studies of the Sunyaev-Zel'dovich effect in the radio/sub-mm, which frequently involve the subtraction of the radio/sub-mm continuum source from the brightest cluster galaxy. This is often done by extrapolating from a lower frequency radio flux made several years before the Sunyaev-Zel'dovich observations. Due to the complex spectral nature of these radio sources and their intrinsic variability, estimates of flux density at higher frequencies will be far less certain than is often assumed.

- The clumpy nature of the molecular gas in massive galaxies which seems to be implied by the variability study was then studied using the absorption lines of 13 molecular species in the Hydra-A brightest cluster galaxy. This made it possible to compare the line of sight column densities, velocity dispersions, and excitation temperatures of the molecular clouds seen in Hydra-A to those of the Milky Way. Due to the significant differences between a brightest cluster galaxy and the Milky Way (such as mass, galaxy type, AGN activity), it's not obvious their regions of molecular gas should be in any way similar. However, in terms of their column densities, the two populations appear to be largely indistinguishable. This implies that the high pressure environment of a brightest cluster galaxy has negligible effect on the molecular clouds when compared with their self-gravitation.

- The line of sight absorption seen against Hydra-A's bright radio core has shown

temporal variation on astronomically short timescales of two years. The first of two likely explanations for the variability is a multi-component continuum source, one component of which has decreased in brightness or has seen relativistic movement in a hot spot, in turn giving decreased absorption along one particular line of sight. A second possible but less likely explanation is that one of the many absorbing clouds, or groups of absorbing clouds, has significant transverse motion such that it no longer covers the continuum source in the same way.

- A survey of molecular absorption in a larger sample has doubled the number of systems in which molecular absorption has been observed against a brightest cluster galaxy's bright continuum source, with an increase from five to ten.

- In Chapters 3, 4, and 5, it was said that the molecular gas clouds detected were likely to be in the central regions of their galaxies, with radii of around 10 to 200 pc. This was largely based on the predictions of simulations (e.g. Pizzolato & Soker, 2005; Gaspari et al., 2017), which in hindsight, may have been too heavily relied upon. In Hydra-A, the shape of the molecular emission suggests that its molecular gas is being viewed edge-on, and is either in the form of a smooth disc, or a ring which extends out across approximately 5 kpc. The majority of its molecular gas is therefore likely to lie further out than initially suggested, and the precise location of the absorbing clouds cannot be known precisely. Furthermore, for the larger survey presented in Chapter 5, the likely radii of the clouds which happen to be picked out by the molecular absorption line surveys cannot be known without first studying the larger scale molecular gas distribution through the galaxy's emission lines.

- The absorption regions detected against the radio cores of brightest cluster galaxies have a bias for motion towards the supermassive black holes, though this is found from what is still a relatively small number of sources. This has two plausible explanations. The first is that there is a net movement of cold molecular gas towards the supermassive black holes, thus providing it with a significant source of fuel. Second, there is a cyclical process in which the cold clouds are warmed as they move toward the AGN. In time, the same AGN activity also drives them back in the

opposite direction. Testing these ideas will require observations of molecular and atomic absorption lines in at least a few tens more galaxies, which will reveal any differences in the bulk motions of the two gas phases in a statistically meaningful way.

6.2 Potential Future Work

For every question this thesis goes some way to answering, several others appear. Below is a brief description of three projects which would build on the work of this thesis and answer some of the questions it raises.

Project I: A longer-term study of BCG variability: Chapter 2 of this thesis presented results from the most comprehensive ever monitoring campaign of the high radio frequency variability of brightest cluster galaxies. This showed that significant levels of variability are a common feature of brightest cluster galaxy radio cores lying at the centres of cool-cores. At least half of the sample of 20 studied vary by more than 20 per cent on timescales of three years, and at least a third vary by 60 per cent of timescales of several years.

However, the conclusions of this study are limited by the length of time the survey has been ongoing for – currently 12 years – which is still short by astronomical standards. Fortunately, the OVRO 15 GHz monitoring campaign is still active, so a longer term study is entirely possible and will refine and enhance all of the conclusions made in Chapter 2. This will establish a much better understanding of the link between variability and spectral index changes and will be more likely to show rarer patterns of variability such as short outbursts, which are linked to more extreme but infrequent accretion events.

Project II: Further observations of the molecular absorption lines in Hydra-A: Observing individual gas clouds in the cores of the Universe's most massive galaxies is extremely difficult, and despite the work of this thesis, their properties could still be far better understood.

Studying the properties of a single system like Hydra-A in-depth is an important step in testing models of gas accretion onto supermassive black holes. Hydra-A continues to

provide an excellent opportunity to do this because wealth of the molecular absorption lines already detected is far greater than in any other extragalactic intrinsic absorption line system. This is largely thanks to its bright and compact AGN, which lies at the center of a near perfectly edge-on disc of molecular gas. This orientation maximises our line-of-sight through the disc and toward the AGN, increasing the chance of intercepting an absorbing molecular cloud.

Further ALMA and lower frequency JVLA and ngVLA observations will improve constraints on the properties of the clouds in the core of this archetypal galaxy. For example, the isotopic ratios of carbon, nitrogen, oxygen, silicon, and sulphur are a product the elements' origins. As a result, more precise relative abundances and absorption strengths will be able to tell us the primary channel for the production of metals in the cores of brightest cluster galaxies (Kobayashi & Nakasato, 2011).

Chapter 4 presented the first evidence of variability in the intrinsic absorption lines of an extragalactic radio source. Variable absorption has previously been seen against a background quasar, but not in a system like this which uses the galaxy's own AGN as a backlight.

The most likely cause of this is a change in the illumination of the clouds due to relativistic motions of knots in the galaxy's central continuum source. Further observations of Hydra-A with the aim of monitoring changes in its absorption features would be extremely revealing. CO(2-1) absorption was observed in Hydra-A in 2016 and 2018, so this will provide the longest timeline for observing any variability. Observations of HCO^+(2-1) and HCN(2-1), which were first observed in 2018, may be even more useful. These lines have turned out to be the clearest tracers of the molecular absorption, and so will best show variation in the absorption features. The difference between the strength of the two CO(2-1) absorption lines in Hydra-A is currently dominated by the earlier CO(2-1) spectrum, so further observations will be able to show the already clear variability in even finer detail.

Isotopologues containing carbon-12 and carbon-13 were searched for in Chapter 4 as a means of estimating the fraction of the background continuum source covered by the absorbing molecular clouds. Carbon-13 is typically at least an order of magnitude less abundant than carbon-12, so its absorption lines can be used to distinguish between

optically thick clouds with a low covering fraction, and more diffuse clouds which cover an entire continuum source. For example, if a molecular cloud extinguishes 10 per cent of a continuum source in CO(2-1), it may be a large, optically thin cloud with $\tau = 0.1$ covering the entire continuum source, or an optically thick cloud with $\tau \gg 1$ covering 10 per cent of the continuum. Molecules containing carbon-13 can distinguish between these scenarios; their absorption lines would be much more significant and relatively easily detected in the case of an optically thick cloud.

In Chapter 4, this technique was applied using ^{12}CO and ^{13}CO. This allowed for the covering factor of one of the absorbing clouds to be estimated, so there was some degree of success. However, the same chapter also unexpectedly showed that H^{12}CO$^+$ was a significantly clearer tracer of absorption than ^{12}CO. In turn, a future survey targeting H^{13}CO$^+$ will be more successful than ^{13}CO at constraining the covering factor of many more of Hydra-A's absorption regions. These covering factors will then allow for more accurate estimates of optical depths, sizes, densities, and masses and will significantly improve on the unique comparisons made between the environments of the Milky Way and the core of this archetypal brightest cluster galaxy.

Project III: Constraining Cold Accretion onto Supermassive Black Holes The make-up of the gas fuelling supermassive black hole accretion - such as what fraction is hot, warm, and cold - remains poorly understood. Molecular absorption line surveys are one route to solving this problem because they offer the possibility of determining how large a contribution cold gas makes to the process. This is possible because the AGN backlight and absorbing gas clouds are in the same galaxy, so redshifted absorption unambiguously indicates that gas is moving towards the central supermassive black hole, while blueshifted lines indicate outflow. In many cases we know the absorbing cold gas clouds detected are moving toward their host supermassive black hole due to their positive velocities, which far exceed the uncertainty in the galaxies' recession velocities. From the nine associated absorber systems found in brightest cluster galaxies, this thesis has revealed a strong tendency for molecular gas clouds to be in motion towards their host supermassive black hole, often at hundreds of km s^{-1}.

Further observations will distinguish between these scenarios, and detections of even just

a few tens more absorption line systems will make these statistics compelling. Until now, findings have been limited by observations of a small, but not insignificant number of absorbers. As with the first suggested project, we will also gain insight into the origins of the clouds and improve upon comparisons made between the environments of the Milky Way and the cores of brightest cluster galaxies.

Additionally, this can act as a test of accretion simulations (e.g. Gaspari et al., 2013), and be compared with them to elicit information about the interstellar gas detected. These comparisons will yield an estimate of the accretion rate of cold clouds onto supermassive black holes, which could be related to statistical studies of radio-mode feedback (e.g. Rafferty et al., 2008; Hlavacek-Larrondo et al., 2012).

Chapter Acknowledgements

The acknowledgements below were made when the following chapters were published.

Chapter 2

This chapter has made use of data from the OVRO 40m monitoring program which was supported in part by NASA grants NNX08AW31G, NNX11A043G and NNX14AQ89G, and NSF grants AST-0808050 and AST-1109911, and private funding from Caltech and the MPIfR.

We are grateful to the staff of the KVN who helped to operate the array and to correlate the data. The KVN and a high-performance computing cluster are facilities operated by the KASI (Korea Astronomy and Space Science Institute). The KVN observations and correlations are supported through the high-speed network connections among the KVN sites provided by the KREONET (Korea Research Environment Open NETwork), which is managed and operated by the KISTI (Korea Institute of Science and Technology Information). The following people contributed to the acquisition and analysis of the KVN data: Jae-Woo Kim and Tae-Hyun Jung. Their affiliations are given on the title page of this paper.

We would like to thank the IRAM staff for their support during the numerous campaigns. The NIKA2 dilution cryostat has been designed and built at the Institut Néel.

We are grateful to the staff of the James Clerk Maxwell Telescope, which is operated by the East Asian Observatory on behalf of The National Astronomical Observatory of Japan;

Academia Sinica Institute of Astronomy and Astrophysics; the Korea Astronomy and Space Science Institute; Center for Astronomical Mega-Science (as well as the National Key R&D Program of China with No. 2017YFA0402700). Additional funding support is provided by the Science and Technology Facilities Council of the United Kingdom and participating universities and organizations in the United Kingdom and Canada. Additional funds for the construction of SCUBA-2 were provided by the Canada Foundation for Innovation.

This chapter makes use of the following ALMA data: ADS/JAO.ALMA#2017.1.00629.S. ALMA is a partnership of ESO (representing its member states), NSF (USA) and NINS (Japan), together with NRC (Canada), NSC and ASIAA (Taiwan), and KASI (Republic of Korea), in cooperation with the Republic of Chile. The Joint ALMA Observatory is operated by ESO, AUI/NRAO and NAOJ.

T.R. is supported by the Science and Technology Facilities Council (STFC) through grant ST/R504725/1. A.C.E. acknowledges support from STFC grant ST/P00541/1. JWK acknowledges support from the National Research Foundation of Korea (NRF), grant No. NRF-2019R1C1C1002796, funded by the Korean government (MSIT).

This research made use of Astropy (The Astropy Collaboration et al., 2013, 2018), matplotlib (Hunter, 2007), numpy (van der Walt et al., 2011; Harris et al., 2020), python (Van Rossum & Drake, 2009), and scipy (Jones et al., 2011; Virtanen et al., 2020). We thank their developers for maintaining them and making them freely available.

This publication makes use of data obtained at Metsähovi Radio Observatory, operated by Aalto University in Finland.

Chapter 3

T.R. is supported by the Science and Technology Facilities Council (STFC) through grant ST/R504725/1.

A.C.E. acknowledges support from STFC grant ST/P00541/1.

The work of S.B. and C.O. was supported by NSERC (Natural Sciences and Engineering Research Council of Canada).

M.G. is supported by NASA through Einstein Postdoctoral Fellowship Award Number PF5-160137 issued by the Chandra X-ray Observatory Center, which is operated by the SAO for and on behalf of NASA under contract NAS8-03060. Support for this work was also provided by Chandra grant GO7-18121X.

G.R.T. acknowledges support from the National Aeronautics and Space Administration (NASA) through Chandra Award Number GO7-8128X8, issued by the Chandra X-ray Center, which is operated by the Smithsonian Astrophysical Observatory for and on behalf of NASA under contract NAS8-03060.

This paper makes use of the following ALMA data: ADS/JAO.ALMA#2016.1.01214.S, ADS/JAO.ALMA#2017.1.00629.S. ALMA is a partnership of ESO (representing its member states), NSF (USA) and NINS (Japan), together with NRC (Canada) and NSC and ASIAA (Taiwan) and KASI (Republic of Korea), in cooperation with the Republic of Chile. The Joint ALMA Observatory is operated by ESO, AUI/NRAO and NAOJ.

This work used the DiRAC Data Centric system at Durham University, operated by the Institute for Computational Cosmology on behalf of the STFC DiRAC HPC Facility (www.dirac.ac.uk). This equipment was funded by BIS National E-infrastructure capital grant ST/K00042X/1, STFC capital grant ST/H008519/1, and STFC DiRAC Operations grant ST/K003267/1 and Durham University. DiRAC is part of the National E-Infrastructure.

This research made use of APLpy, an open-source plotting package for Python (Robitaille & Bressert, 2012).

The authors gratefully acknowledge the referee Dr. Rick Perley for his comments, which helped us to improve the paper. We give him extra thanks for providing the JVLA dataset used in Fig. 3.1.

Chapter 4

We thank the referee for their time and comments, which have helped us to improve the paper. We are grateful to Rick Perley for providing the VLA image used in Fig. 4.1.

T.R. is supported by the Science and Technology Facilities Council (STFC) through grant ST/R504725/1.

A.C.E. acknowledges support from STFC grant ST/P00541/1.

M.G. is supported by the Lyman Spitzer Jr. Fellowship (Princeton University) and by NASA Chandra GO8-19104X/GO9-20114X and HST GO- 15890.020-A grants.

This paper makes use of the following ALMA data: ADS/JAO.ALMA#2016.1.01214.S, ADS/JAO.ALMA#2017.1.00629.S and ADS/JAO.ALMA#2018.1.01471.S. ALMA is a partnership of ESO (representing its member states), NSF (USA) and NINS (Japan), together with NRC (Canada), MOST and ASIAA (Taiwan), and KASI (Republic of Korea), in cooperation with the Republic of Chile. The Joint ALMA Observatory is operated by ESO, AUI/NRAO and NAOJ.

Chapter 5

The authors gratefully acknowledge the anonymous referee for their comments, which helped us to improve the paper.

We thank Tom Oosterloo for generously providing the H I detection of NGC 6868.

T.R. is supported by the Science and Technology Facilities Council (STFC) through grant ST/R504725/1.

A.C.E. acknowledges support from STFC grant ST/P00541/1.

M.G. is supported by the Lyman Spitzer Jr. Fellowship (Princeton University) and by NASA Chandra grants GO7-18121X and GO8-19104X.

S.B. and C.O. are grateful for support from the Natural Sciences and Engineering Research Council of Canada.

G.R.T. acknowledges support from the National Aeronautics and Space Administration (NASA) through Chandra Award Number GO7-8128X8, issued by the Chandra X-ray Center, which is operated by the Smithsonian Astrophysical Observatory for and on behalf of NASA under contract NAS8-03060.

This paper makes use of the following ALMA data: ADS/JAO.ALMA#2017.1.00629.S. ALMA is a partnership of ESO (representing its member states), NSF (USA) and NINS (Japan), together with NRC (Canada), NSC and ASIAA (Taiwan), and KASI (Republic of Korea), in cooperation with the Republic of Chile. The Joint ALMA Observatory is operated by ESO, AUI/NRAO and NAOJ. We also use archival data: ADS/JAO.ALMA#2016.1.00533.S of NGC 5044 and of Abell 2597.

APPENDIX A

Appendix: The variability of brightest cluster galaxies at high radio frequencies

---

.1 Mock Lightcurves

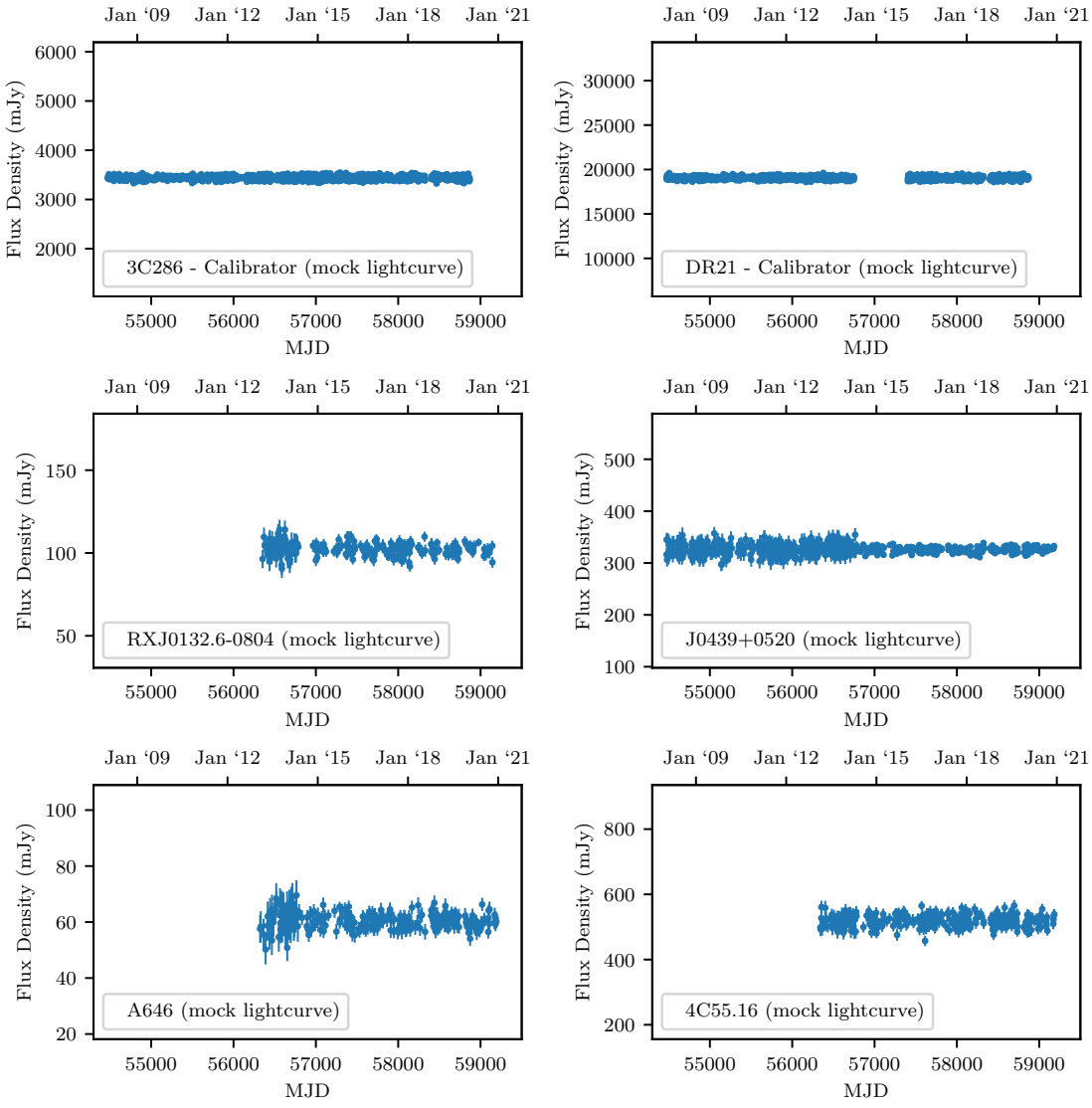

Figure 1

Example mock lightcurves produced along the lines described in §2.4.5

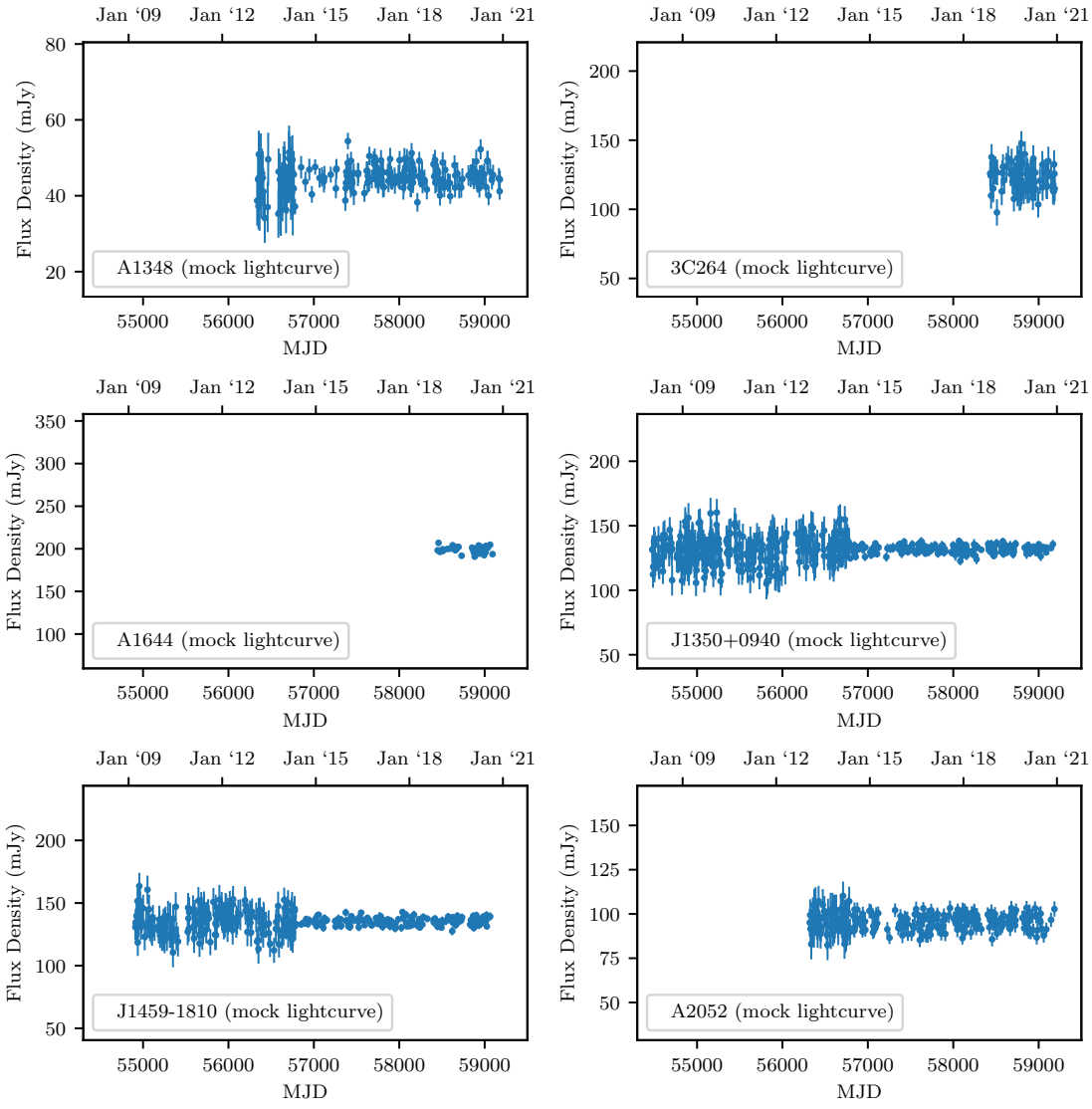

Figure 2

Example mock lightcurves produced along the lines described in §2.4.5

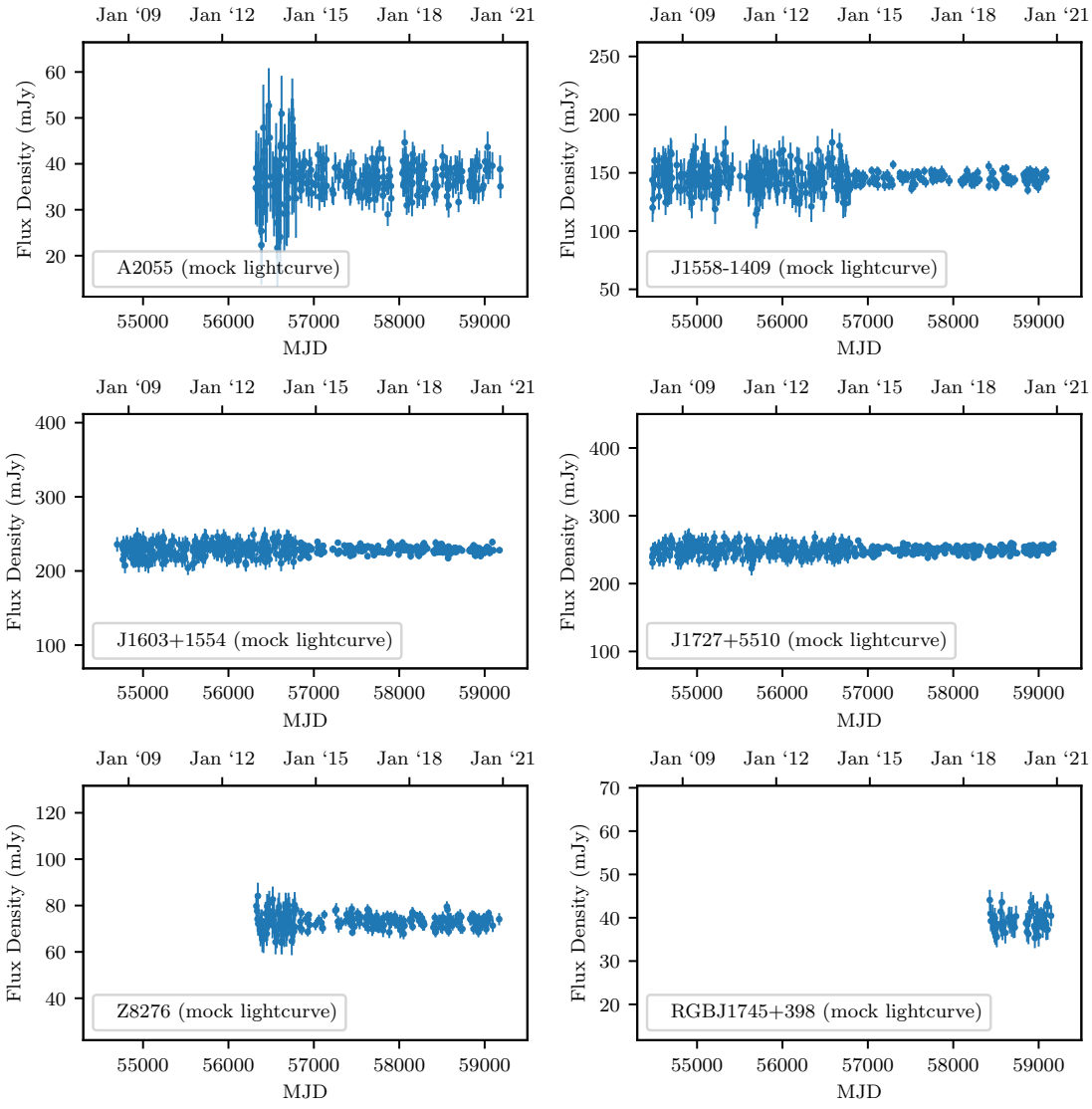

Figure 3

Example mock lightcurves produced along the lines described in §2.4.5

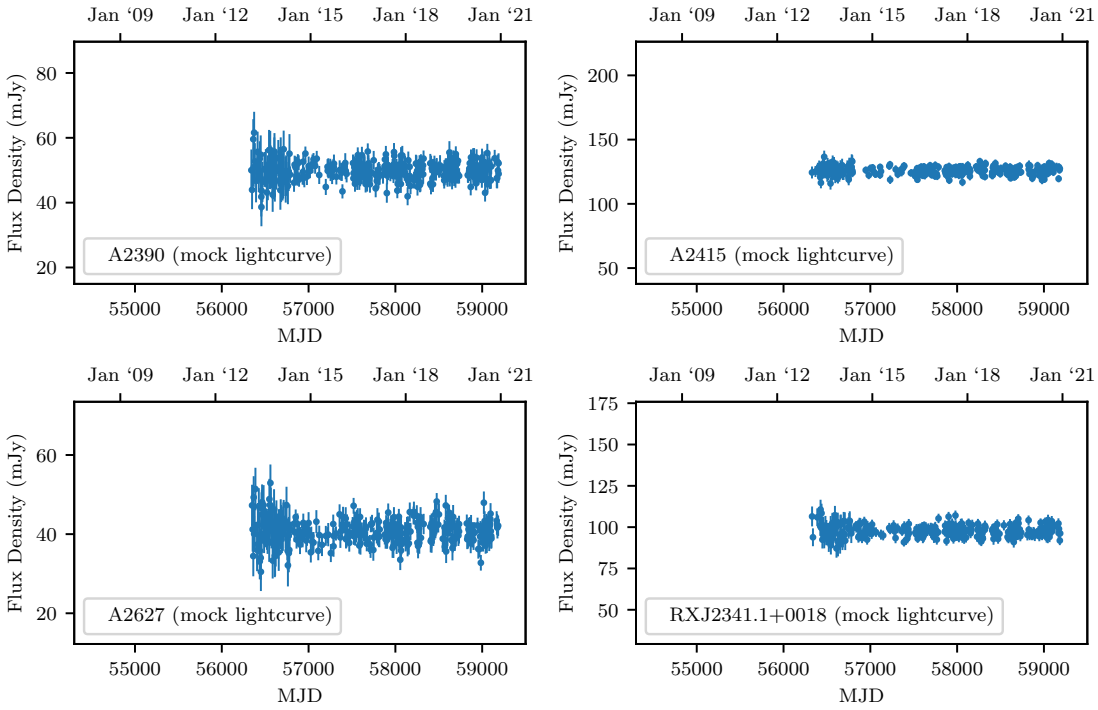

Figure 4

Example mock lightcurves produced along the lines described in §2.4.5

.2 NIKA2 Data

Table 1

150 GHz NIKA2 flux densities, and the spectral indices calculated with the nearest 15 GHz OVRO 40m observations. We also include NIKA2 flux densities of several core-dominated BCGs not included in the OVRO BCG sample.

Source	NIKA2 Obs. mjd (ISO)	NIKA2 flux density / mJy	OVRO Obs. mjd (ISO)	OVRO flux density / mJy	Time Difference / days	α
J0439+0520	58549 (2019-03-07)	75 ± 1	58565 (2019-03-22)	342 ± 4	16	-0.66 ± 0.0
J0439+0520	58786 (2019-10-30)	89 ± 5	58811 (2019-11-24)	347 ± 5	25	-0.59 ± 0.02
J0439+0520	58791 (2019-11-04)	49 ± 1	58811 (2019-11-24)	347 ± 5	20	-0.85 ± 0.01
4C55.16	58550 (2019-03-08)	86 ± 1	58546 (2019-03-04)	523 ± 21	4	-0.79 ± -0.01
4C55.16	58828 (2019-12-11)	74 ± 1	58827 (2019-12-10)	562 ± 13	1	-0.87 ± -0.01
A1348	58922 (2020-03-14)	8 ± 1	58926 (2020-03-18)	38 ± 2	4	-0.7 ± 0.02
3C264	58550 (2019-03-08)	125 ± 1	58567 (2019-03-25)	166 ± 10	17	-0.13 ± -0.02
3C264	58828 (2019-12-11)	111 ± 1	58825 (2019-12-08)	117 ± 9	3	-0.05 ± -0.02
A1644	58553 (2019-03-11)	59 ± 1	58561 (2019-03-19)	164 ± 3	8	-0.46 ± 0.0
A1644	58897 (2020-02-18)	77 ± 1	58893 (2020-02-13)	218 ± 3	4	-0.43 ± 0.0
J1350+0940	58565 (2019-03-23)	18 ± 1	58567 (2019-03-25)	135 ± 3	2	-0.87 ± 0.01
J1350+0940	58897 (2020-02-18)	18 ± 1	58895 (2020-02-16)	136 ± 2	2	-0.87 ± 0.02
J1459-1810	58567 (2019-03-25)	21 ± 1	58572 (2019-03-30)	128 ± 2	5	-0.81 ± 0.01

Source	NIKA2 Obs. mjd (ISO)	NIKA2 flux density / mJy	OVRO Obs. mjd (ISO)	OVRO flux density / mJy	Time Difference / days	α
A2052	58550 (2019-03-08)	44 ± 1	58557 (2019-03-15)	88 ± 4	7	-0.3 ± -0.01
A2052	58829 (2019-12-12)	37 ± 1	58830 (2019-12-12)	75 ± 3	1	-0.31 ± -0.01
A2055	58565 (2019-03-23)	30 ± 1	58566 (2019-03-24)	30 ± 2	1	-0.06 ± -0.01
A2055	58831 (2019-12-14)	24 ± 1	58830 (2019-12-12)	37 ± 2	1	-0.18 ± -0.01
J1558-1409	58553 (2019-03-11)	47 ± 1	58577 (2019-04-04)	172 ± 13	24	-0.57 ± -0.01
J1558-1409	58897 (2020-02-18)	32 ± 2	58894 (2020-02-14)	142 ± 3	3	-0.65 ± 0.01
J1603+1554	58553 (2019-03-11)	84 ± 1	58557 (2019-03-15)	290 ± 4	4	-0.54 ± -0.0
J1603+1554	58829 (2019-12-12)	79 ± 1	58825 (2019-12-07)	315 ± 6	4	-0.59 ± -0.0
J1727+5510	58550 (2019-03-08)	89 ± 1	58555 (2019-03-12)	309 ± 5	5	-0.54 ± -0.0
J1727+5510	58790 (2019-11-03)	64 ± 2	58829 (2019-12-11)	333 ± 5	39	-0.71 ± 0.01
Z8276	58554 (2019-03-12)	36 ± 1	58557 (2019-03-15)	73 ± 2	3	-0.3 ± -0.0
Z8276	58831 (2019-12-14)	30 ± 1	58832 (2019-12-14)	76 ± 2	1	-0.41 ± 0.0
RGBJ1745+398	58554 (2019-03-12)	30 ± 1	58555 (2019-03-12)	42 ± 2	1	-0.15 ± -0.01
RGBJ1745+398	58790 (2019-11-03)	23 ± 1	58735 (2019-09-09)	38 ± 2	55	-0.21 ± -0.01
A2627	58922 (2020-03-14)	25 ± 1	58913 (2020-03-04)	37 ± 2	9	-0.23 ± -0.01

Source	NIKA2 Obs. mjd (ISO)	NIKA2 flux density / mJy	OVRO Obs. mjd (ISO)	OVRO flux density / mJy	Time Difference / days	α
NGC5044	58553 (2019-03-11)	37.4 ± 0.9				
NGC5044	58897 (2020-02-18)	35.4 ± 1.3				
A496	58550 (2019-03-08)	21.0 ± 1.0				
A496	58831 (2019-12-14)	12.4 ± 0.9				
A1795	58829 (2019-12-12)	4.7 ± 0.6				
A3581	58553 (2019-03-11)	99.9 ± 1.7				
E1821+64	58790 (2019-11-03)	9.1 ± 1.0				
NGC6338	58565 (2019-03-23)	4.2 ± 0.7				
NGC6338	58790 (2019-11-03)	4.9 ± 0.8				
R1504-02	58565 (2019-03-23)	5.7 ± 0.7				
R1504-02	58828 (2019-12-11)	16.8 ± 2.0				
R1504-02	58831 (2019-12-14)	4.0 ± 0.6				
R1832+68	58790 (2019-11-03)	6.1 ± 0.9				
Z8193	58554 (2019-03-12)	28.5 ± 0.6				
Z8193	58790 (2019-11-03)	17.0 ± 1.8				
Z8193	58831 (2019-12-14)	21.1 ± 0.8				

.3 KVN Data

Table 2

Contemporaneous 22 and 43 GHz KVN flux densities and their spectral indices. Continued on the next page.

Source	mjd (ISO)	22 GHz flux density / mJy	43 GHz flux density / mJy	α
RXJ0132.6-0804	58534 (2019-02-20)	74.2 ± 7.9	52.4 ± 4.0	-0.5 ± 0.2
RXJ0132.6-0804	58584 (2019-04-11)	75.0 ± 6.4	51.2 ± 3.6	-0.6 ± 0.1
RXJ0132.6-0804	58827 (2019-12-10)	77.7 ± 5.9	52.0 ± 4.4	-0.6 ± 0.2
RXJ0132.6-0804	58975 (2020-05-06)	69.3 ± 7.0	43.6 ± 3.2	-0.7 ± 0.2
RXJ0132.6-0804	59006 (2020-06-06)	72.6 ± 6.3	46.2 ± 3.9	-0.7 ± 0.2
RXJ0132.6-0804	59182 (2020-11-29)	79.4 ± 9.2	49.1 ± 9.3	-0.7 ± 0.3
J0439+0520	58421 (2018-10-30)	286.0 ± 16.1	139.0 ± 11.3	-1.1 ± 0.2
J0439+0520	58450 (2018-11-28)	277.0 ± 17.1	158.0 ± 9.6	-0.8 ± 0.2
J0439+0520	58534 (2019-02-20)	271.0 ± 18.0	146.0 ± 17.5	-0.9 ± 0.2
J0439+0520	58584 (2019-04-11)	261.0 ± 16.0	121.0 ± 8.5	-1.1 ± 0.2
J0439+0520	58827 (2019-12-10)	267.0 ± 15.7	138.0 ± 11.2	-1.0 ± 0.2
J0439+0520	58975 (2020-05-06)	247.0 ± 15.4	121.0 ± 7.6	-1.1 ± 0.2
J0439+0520	59006 (2020-06-06)	247.0 ± 14.7	120.0 ± 8.2	-1.1 ± 0.2
J0439+0520	59182 (2020-11-29)	249.0 ± 17.5	159.0 ± 9.4	-0.7 ± 0.2
A646	58421 (2018-10-30)	54.0 ± 3.6	36.1 ± 3.3	-0.6 ± 0.2
A646	58450 (2018-11-28)	52.7 ± 3.4	37.3 ± 3.0	-0.5 ± 0.1

Source	mjd (ISO)	22 GHz flux density / mJy	43 GHz flux density / mJy	α
A646	58512 (2019-01-29)	52.2 ± 3.9	33.8 ± 3.0	-0.6 ± 0.2
A646	58847 (2019-12-30)	43.3 ± 2.7	–	–
A646	58974 (2020-05-05)	49.9 ± 4.4	35.3 ± 3.1	-0.5 ± 0.2
A646	59182 (2020-11-29)	36.0 ± 2.4	–	–
4C55.16	58421 (2018-10-30)	197.0 ± 22.6	47.0 ± 5.2	-2.1 ± 0.5
4C55.16	58450 (2018-11-28)	225.0 ± 26.4	35.6 ± 4.3	-2.8 ± 0.6
4C55.16	58512 (2019-01-29)	203.0 ± 23.8	35.1 ± 4.3	-2.6 ± 0.6
4C55.16	58573 (2019-03-31)	220.0 ± 27.1	41.9 ± 5.8	-2.5 ± 0.5
4C55.16	58847 (2019-12-30)	190.0 ± 23.6	39.1 ± 4.3	-2.4 ± 0.5
4C55.16	58974 (2020-05-05)	211.0 ± 24.5	50.9 ± 5.1	-2.1 ± 0.5
4C55.16	59182 (2020-11-29)	208.0 ± 23.6	47.8 ± 5.7	-2.2 ± 0.5
A1348	58421 (2018-10-30)	32.3 ± 2.7	–	–
A1348	58450 (2018-11-28)	24.7 ± 2.4	–	–
A1348	58512 (2019-01-29)	29.0 ± 2.5	–	–
3C264	58512 (2019-01-29)	136.0 ± 8.4	103.0 ± 7.2	-0.4 ± 0.1
3C264	58573 (2019-03-31)	110.0 ± 7.4	77.5 ± 5.6	-0.5 ± 0.1

Source	mjd (ISO)	22 GHz flux density / mJy	43 GHz flux density / mJy	α
3C264	58847 (2019-12-30)	87.3 ± 6.2	62.0 ± 4.8	-0.5 ± 0.1
3C264	58852 (2020-01-04)	90.4 ± 6.7	69.5 ± 4.6	-0.4 ± 0.1
3C264	58974 (2020-05-05)	107.0 ± 7.8	75.4 ± 5.4	-0.5 ± 0.1
3C264	58988 (2020-05-19)	102.0 ± 7.2	79.3 ± 5.7	-0.4 ± 0.1
3C264	59182 (2020-11-29)	106.0 ± 7.0	79.9 ± 4.9	-0.4 ± 0.1
A1644	58450 (2018-11-28)	140.0 ± 10.0	71.3 ± 6.2	-1.0 ± 0.2
A1644	58512 (2019-01-29)	158.0 ± 11.1	75.2 ± 7.1	-1.1 ± 0.3
A1644	58573 (2019-03-31)	161.0 ± 10.6	81.7 ± 6.8	-1.0 ± 0.2
A1644	58847 (2019-12-30)	177.0 ± 10.4	92.5 ± 7.7	-1.0 ± 0.2
A1644	58852 (2020-01-04)	181.0 ± 11.5	103.0 ± 8.2	-0.8 ± 0.2
A1644	58974 (2020-05-05)	195.0 ± 12.4	100.0 ± 8.3	-1.0 ± 0.2
A1644	58988 (2020-05-19)	191.0 ± 10.9	99.4 ± 8.1	-1.0 ± 0.2
A1644	59182 (2020-11-29)	169.0 ± 10.7	86.0 ± 7.5	-1.0 ± 0.2
J1350+0940	58421 (2018-10-30)	88.9 ± 5.6	53.1 ± 5.0	-0.8 ± 0.2
J1350+0940	58450 (2018-11-28)	86.9 ± 5.3	42.3 ± 3.8	-1.1 ± 0.2
J1350+0940	58512 (2019-01-29)	87.1 ± 5.1	41.5 ± 2.9	-1.1 ± 0.2
J1350+0940	58843 (2019-12-26)	86.5 ± 5.3	40.5 ± 2.9	-1.1 ± 0.2

Source	mjd (ISO)	22 GHz flux density / mJy	43 GHz flux density / mJy	α
J1350+0940	58852 (2020-01-04)	85.4 ± 5.2	40.3 ± 2.7	-1.1 ± 0.2
J1350+0940	58988 (2020-05-19)	89.9 ± 5.5	43.4 ± 3.6	-1.1 ± 0.2
J1459-1810	58421 (2018-10-30)	107.0 ± 6.1	62.4 ± 7.9	-0.8 ± 0.2
J1459-1810	58514 (2019-01-31)	100.0 ± 6.3	52.5 ± 3.8	-1.0 ± 0.2
J1459-1810	58843 (2019-12-26)	98.4 ± 6.1	55.5 ± 3.3	-0.9 ± 0.2
J1459-1810	58969 (2020-04-30)	99.9 ± 6.2	56.7 ± 4.1	-0.8 ± 0.2
J1459-1810	59182 (2020-11-29)	96.5 ± 6.7	53.7 ± 3.8	-0.9 ± 0.2
A2052	58421 (2018-10-30)	65.3 ± 8.0	43.1 ± 6.9	-0.6 ± 0.2
A2052	58514 (2019-01-31)	67.8 ± 8.5	42.7 ± 4.5	-0.7 ± 0.2
A2052	58573 (2019-03-31)	71.4 ± 11.1	49.1 ± 4.1	-0.6 ± 0.2
A2052	58843 (2019-12-26)	64.8 ± 6.4	44.8 ± 3.2	-0.6 ± 0.2
A2052	58969 (2020-04-30)	57.5 ± 5.6	–	–
A2052	59182 (2020-11-29)	54.6 ± 4.6	42.3 ± 4.1	-0.4 ± 0.1
A2055	58421 (2018-10-30)	31.2 ± 2.7	–	–
A2055	58514 (2019-01-31)	31.9 ± 2.5	28.5 ± 2.2	-0.2 ± 0.1
A2055	58843 (2019-12-26)	31.3 ± 2.2	29.6 ± 2.6	-0.1 ± 0.1

Source	mjd (ISO)	22 GHz flux density / mJy	43 GHz flux density / mJy	α
J1558-1409	58421 (2018-10-30)	139.0 ± 14.4	56.6 ± 9.2	-1.3 ± 0.3
J1558-1409	58514 (2019-01-31)	122.0 ± 16.1	63.7 ± 10.9	-1.0 ± 0.3
J1558-1409	58573 (2019-03-31)	117.0 ± 8.8	75.2 ± 5.6	-0.7 ± 0.2
J1558-1409	58843 (2019-12-26)	92.4 ± 7.0	48.9 ± 3.5	-0.9 ± 0.2
J1558-1409	58852 (2020-01-04)	97.5 ± 8.4	48.3 ± 4.8	-1.0 ± 0.2
J1558-1409	58969 (2020-04-30)	93.2 ± 8.2	–	–
J1558-1409	58988 (2020-05-19)	91.1 ± 6.9	49.6 ± 3.9	-0.9 ± 0.2
J1558-1409	59182 (2020-11-29)	83.5 ± 7.5	–	–
J1603+1554	58421 (2018-10-30)	262.0 ± 15.1	155.0 ± 13.0	-0.8 ± 0.2
J1603+1554	58514 (2019-01-31)	264.0 ± 16.2	172.0 ± 10.2	-0.6 ± 0.1
J1603+1554	58573 (2019-03-31)	270.0 ± 15.5	173.0 ± 9.5	-0.7 ± 0.2
J1603+1554	58843 (2019-12-26)	291.0 ± 16.8	182.0 ± 10.6	-0.7 ± 0.2
J1603+1554	58852 (2020-01-04)	289.0 ± 17.5	175.0 ± 10.6	-0.7 ± 0.2
J1603+1554	58969 (2020-04-30)	308.0 ± 20.2	183.0 ± 11.4	-0.8 ± 0.2
J1603+1554	58988 (2020-05-19)	320.0 ± 18.3	207.0 ± 11.8	-0.6 ± 0.2
J1603+1554	59182 (2020-11-29)	269.0 ± 16.3	166.0 ± 9.5	-0.7 ± 0.2
J1727+5510	58421 (2018-10-30)	271.0 ± 17.0	156.0 ± 10.6	-0.8 ± 0.2
J1727+5510	58514 (2019-01-31)	282.0 ± 16.9	176.0 ± 10.3	-0.7 ± 0.2
J1727+5510	58573 (2019-03-31)	289.0 ± 16.5	187.0 ± 10.8	-0.6 ± 0.2

Source	mjd (ISO)	22 GHz flux density / mJy	43 GHz flux density / mJy	α
J1727+5510	58852 (2020-01-04)	295.0 ± 17.4	178.0 ± 11.0	-0.8 ± 0.2
J1727+5510	58969 (2020-04-30)	307.0 ± 19.0	194.0 ± 12.6	-0.7 ± 0.2
J1727+5510	58988 (2020-05-19)	318.0 ± 19.1	211.0 ± 12.0	-0.6 ± 0.1
J1727+5510	59182 (2020-11-29)	274.0 ± 15.6	169.0 ± 9.6	-0.7 ± 0.2
Z8276	58421 (2018-10-30)	58.4 ± 3.5	37.3 ± 3.8	-0.7 ± 0.2
Z8276	58514 (2019-01-31)	59.0 ± 4.4	37.9 ± 2.9	-0.7 ± 0.2
Z8276	58573 (2019-03-31)	59.7 ± 3.8	43.6 ± 3.7	-0.5 ± 0.1
Z8276	58852 (2020-01-04)	58.3 ± 4.0	–	–
Z8276	58969 (2020-04-30)	58.1 ± 3.8	–	–
Z8276	58975 (2020-05-06)	63.4 ± 4.8	44.9 ± 4.4	-0.5 ± 0.2
Z8276	59006 (2020-06-06)	64.1 ± 5.7	49.8 ± 7.0	-0.4 ± 0.2
Z8276	59182 (2020-11-29)	61.1 ± 3.8	–	–
RGBJ1745+398	58573 (2019-03-31)	35.3 ± 2.7	29.7 ± 2.7	-0.3 ± 0.1
RGBJ1745+398	58852 (2020-01-04)	32.0 ± 2.6	–	–
RGBJ1745+398	58969 (2020-04-30)	38.3 ± 2.8	–	–
A2390	58827 (2019-12-10)	45.0 ± 3.2	–	–

Source	mjd (ISO)	22 GHz flux density / mJy	43 GHz flux density / mJy	α
A2390	58975 (2020-05-06)	40.7 ± 3.4	–	–
A2390	59006 (2020-06-06)	46.9 ± 3.5	–	–
A2415	58421 (2018-10-30)	161.0 ± 9.6	103.0 ± 6.6	-0.7 ± 0.2
A2415	58534 (2019-02-20)	134.0 ± 9.3	81.4 ± 5.6	-0.7 ± 0.2
A2415	58584 (2019-04-11)	124.0 ± 7.3	70.3 ± 4.4	-0.8 ± 0.2
A2415	58827 (2019-12-10)	92.5 ± 5.7	52.1 ± 4.0	-0.9 ± 0.2
A2415	58975 (2020-05-06)	86.9 ± 5.4	47.4 ± 4.0	-0.9 ± 0.2
A2415	59006 (2020-06-06)	89.7 ± 5.6	60.4 ± 5.6	-0.6 ± 0.2
A2415	59182 (2020-11-29)	76.0 ± 4.8	42.7 ± 3.1	-0.9 ± 0.2
A2627	58534 (2019-02-20)	35.8 ± 2.9	–	–
A2627	58827 (2019-12-10)	39.9 ± 3.6	34.4 ± 3.0	-0.2 ± 0.1
A2627	58975 (2020-05-06)	34.9 ± 2.8	–	–
A2627	59006 (2020-06-06)	46.2 ± 3.5	–	–
RXJ2341.1+0018	58421 (2018-10-30)	75.4 ± 7.5	41.8 ± 5.7	-0.9 ± 0.2
RXJ2341.1+0018	58534 (2019-02-20)	70.4 ± 10.0	–	–
RXJ2341.1+0018	58584 (2019-04-11)	60.8 ± 7.7	36.9 ± 3.9	-0.7 ± 0.2
RXJ2341.1+0018	58827 (2019-12-10)	61.7 ± 6.5	–	–
RXJ2341.1+0018	58975 (2020-05-06)	67.1 ± 5.1	36.8 ± 4.5	-0.9 ± 0.2
RXJ2341.1+0018	59006 (2020-06-06)	69.9 ± 5.9	–	–

.4 SCUBA2 Data

Table 3

353 GHz SCUBA2 flux densities, and the spectral indices calculated with the nearest 15 GHz OVRO 40m observations. Continued on the next page.

Source	SCUBA2 Obs. mjd (ISO)	SCUBA2 flux density / mJy	OVRO Obs. mjd (ISO)	OVRO flux density / mJy	Time Difference / days	α
RXJ0132.6-0804	56223 (2012-10-23)	14 ± 9	56353 (2013-03-01)	107 ± 5	130	-0.6 ± 0.15
RXJ0132.6-0804	56476 (2013-07-03)	21 ± 8	56473 (2013-06-29)	103 ± 6	3	-0.5 ± 0.08
RXJ0132.6-0804	58628 (2019-05-25)	22 ± 3	58618 (2019-05-14)	96 ± 3	10	-0.46 ± 0.03
RXJ0132.6-0804	58751 (2019-09-25)	20 ± 3	58739 (2019-09-13)	106 ± 3	12	-0.49 ± 0.03
RXJ0132.6-0804	59021 (2020-06-21)	30 ± 2	59042 (2020-07-11)	97 ± 4	21	-0.35 ± 0.01
RXJ0132.6-0804	59127 (2020-10-05)	23 ± 3	59143 (2020-10-21)	88 ± 2	16	-0.44 ± 0.03
RXJ0132.6-0804	59248 (2021-02-03)	25 ± 3	59183 (2020-11-30)	82 ± 3	65	-0.39 ± 0.02
J0439+0520	56201 (2012-10-01)	18 ± 5	56200 (2012-09-30)	318 ± 8	1	-0.91 ± 0.06
J0439+0520	56496 (2013-07-23)	41 ± 13	56494 (2013-07-20)	326 ± 40	2	-0.65 ± 0.07
J0439+0520	58568 (2019-03-26)	19 ± 4	58565 (2019-03-22)	342 ± 4	3	-0.92 ± 0.06
J0439+0520	58750 (2019-09-24)	29 ± 2	58738 (2019-09-11)	346 ± 5	12	-0.78 ± 0.02
J0439+0520	58920 (2020-03-12)	26 ± 2	58926 (2020-03-18)	336 ± 5	6	-0.81 ± 0.02
J0439+0520	59096 (2020-09-04)	37 ± 2	59097 (2020-09-04)	336 ± 5	1	-0.69 ± 0.01
J0439+0520	59247 (2021-02-02)	36 ± 2	59193 (2020-12-10)	321 ± 4	54	-0.7 ± 0.01
A646	55984 (2012-02-27)	16 ± 6	56323 (2013-01-31)	44 ± 12	339	-0.35 ± 0.07

Source	SCUBA2 Obs. mjd (ISO)	SCUBA2 flux density / mJy	OVRO Obs. mjd (ISO)	OVRO flux density / mJy	Time Difference / days	α
A646	57047 (2015-01-25)	12 ± 4	57055 (2015-02-02)	59 ± 9	8	-0.52 ± 0.05
A646	58576 (2019-04-03)	10 ± 2	58573 (2019-03-30)	65 ± 4	3	-0.57 ± 0.05
A646	58756 (2019-09-30)	8 ± 3	58738 (2019-09-11)	57 ± 2	18	-0.67 ± 0.1
A646	58917 (2020-03-09)	9 ± 2	58930 (2020-03-22)	55 ± 1	13	-0.58 ± 0.06
A646	59120 (2020-09-28)	12 ± 3	59109 (2020-09-16)	53 ± 2	11	-0.46 ± 0.05
4C55.16	55984 (2012-02-27)	27 ± 6	56342 (2013-02-19)	486 ± 37	358	-0.94 ± 0.05
4C55.16	58567 (2019-03-25)	21 ± 4	58565 (2019-03-23)	538 ± 19	2	-1.02 ± 0.05
4C55.16	58750 (2019-09-24)	31 ± 3	58739 (2019-09-12)	546 ± 13	11	-0.9 ± 0.01
4C55.16	58917 (2020-03-09)	24 ± 2	58920 (2020-03-12)	510 ± 20	3	-0.98 ± 0.01
4C55.16	59117 (2020-09-25)	31 ± 3	59100 (2020-09-07)	486 ± 13	17	-0.87 ± 0.01
A1348	56288 (2012-12-27)	14 ± 5	56336 (2013-02-13)	61 ± 4	48	-0.39 ± 0.08
A1348	56479 (2013-07-06)	10 ± 5	56465 (2013-06-22)	52 ± 4	14	-0.5 ± 0.09
A1348	58583 (2019-04-10)	3 ± 2	58593 (2019-04-20)	40 ± 2	10	-0.86 ± 0.11
A1348	58813 (2019-11-26)	2 ± 3	58811 (2019-11-23)	47 ± 3	2	-1.05 ± 0.32
A1348	58917 (2020-03-09)	2 ± 2	58917 (2020-03-09)	43 ± 4	0	-0.97 ± 0.21
3C264	58583 (2019-04-10)	56 ± 3	58582 (2019-04-09)	142 ± 9	1	-0.31 ± -0.01
3C264	58793 (2019-11-06)	65 ± 3	58793 (2019-11-05)	115 ± 23	0	-0.18 ± -0.03

Source	SCUBA2 Obs. mjd (ISO)	SCUBA2 flux density / mJy	OVRO Obs. mjd (ISO)	OVRO flux density / mJy	Time Difference / days	α
3C264	58914 (2020-03-06)	58 ± 2	58913 (2020-03-05)	128 ± 9	1	-0.25 ± -0.01
3C264	59194 (2020-12-11)	73 ± 2	59192 (2020-12-08)	140 ± 10	2	-0.22 ± -0.01
A1644	58600 (2019-04-27)	36 ± 3	58597 (2019-04-24)	166 ± 3	3	-0.49 ± 0.02
A1644	58803 (2019-11-16)	34 ± 3	58854 (2020-01-05)	215 ± 3	51	-0.57 ± 0.02
A1644	58917 (2020-03-09)	42 ± 2	58926 (2020-03-18)	214 ± 9	9	-0.51 ± 0.01
A1644	59184 (2020-12-01)	51 ± 2	59182 (2020-11-28)	200 ± 3	2	-0.42 ± 0.01
J1350+0940	58980 (2020-05-11)	14 ± 5	58979 (2020-05-10)	135 ± 3	1	-0.72 ± 0.09
J1350+0940	58605 (2019-05-02)	12 ± 3	58603 (2019-04-30)	133 ± 3	2	-0.77 ± 0.05
J1350+0940	58847 (2019-12-30)	14 ± 2	58854 (2020-01-05)	135 ± 2	7	-0.71 ± 0.04
J1350+0940	58994 (2020-05-25)	12 ± 3	58994 (2020-05-25)	134 ± 3	0	-0.75 ± 0.05
J1350+0940	59214 (2020-12-31)	13 ± 1	59181 (2020-11-27)	131 ± 2	33	-0.74 ± 0.03
J1459-1810	56931 (2014-10-01)	13 ± 6	56931 (2014-09-30)	142 ± 11	0	-0.74 ± 0.1
J1459-1810	58599 (2019-04-26)	9 ± 2	58603 (2019-04-30)	133 ± 3	4	-0.85 ± 0.07
J1459-1810	58879 (2020-01-31)	15 ± 3	58877 (2020-01-28)	135 ± 3	2	-0.72 ± 0.05
J1459-1810	58991 (2020-05-22)	11 ± 3	58995 (2020-05-26)	141 ± 3	4	-0.79 ± 0.06
A2052	56320 (2013-01-28)	22 ± 7	56320 (2013-01-27)	110 ± 10	0	-0.43 ± 0.07
A2052	56476 (2013-07-03)	22 ± 6	56472 (2013-06-29)	108 ± 5	4	-0.53 ± 0.06

Source	SCUBA2 Obs. mjd (ISO)	SCUBA2 flux density / mJy	OVRO Obs. mjd (ISO)	OVRO flux density / mJy	Time Difference / days	α
A2052	58599 (2019-04-26)	27 ± 2	58594 (2019-04-21)	90 ± 6	5	-0.34 ± 0.01
A2052	58871 (2020-01-23)	26 ± 2	58873 (2020-01-24)	71 ± 5	2	-0.35 ± 0.01
A2052	58994 (2020-05-25)	23 ± 3	58985 (2020-05-16)	69 ± 4	9	-0.39 ± 0.02
A2052	59247 (2021-02-02)	22 ± 3	59193 (2020-12-09)	69 ± 3	54	-0.34 ± 0.02
A2055	58599 (2019-04-26)	15 ± 2	58603 (2019-04-30)	32 ± 3	4	-0.25 ± 0.02
A2055	58917 (2020-03-09)	18 ± 2	58909 (2020-02-29)	27 ± 3	8	-0.16 ± 0.01
A2055	59017 (2020-06-17)	17 ± 2	59015 (2020-06-15)	30 ± 2	2	-0.25 ± 0.02
J1558-1409	56032 (2012-04-15)	33 ± 4	56034 (2012-04-17)	141 ± 13	2	-0.47 ± 0.01
J1558-1409	56476 (2013-07-03)	28 ± 6	56472 (2013-06-29)	129 ± 13	4	-0.49 ± 0.04
J1558-1409	57047 (2015-01-25)	31 ± 4	57045 (2015-01-22)	121 ± 9	2	-0.48 ± 0.01
J1558-1409	58599 (2019-04-26)	32 ± 2	58596 (2019-04-23)	142 ± 4	3	-0.51 ± 0.01
J1558-1409	58879 (2020-01-31)	24 ± 3	58873 (2020-01-24)	151 ± 5	6	-0.56 ± 0.03
J1558-1409	58991 (2020-05-22)	24 ± 2	58995 (2020-05-26)	139 ± 3	4	-0.55 ± 0.02
J1558-1409	59247 (2021-02-02)	25 ± 3	59189 (2020-12-05)	124 ± 3	58	-0.52 ± 0.02
J1603+1554	58547 (2019-03-05)	30 ± 3	58540 (2019-02-26)	292 ± 5	7	-0.71 ± 0.02
J1603+1554	58757 (2019-10-01)	27 ± 3	58736 (2019-09-10)	310 ± 6	21	-0.77 ± 0.03
J1603+1554	58914 (2020-03-06)	31 ± 3	58917 (2020-03-08)	325 ± 4	3	-0.74 ± 0.02

Source	SCUBA2 Obs. mjd (ISO)	SCUBA2 flux density / mJy	OVRO Obs. mjd (ISO)	OVRO flux density / mJy	Time Difference / days	α
J1603+1554	59306 (2021-04-02)	40 ± 3	59189 (2020-12-05)	318 ± 5	117	-0.66 ± 0.02
J1727+5510	56200 (2012-09-30)	31 ± 4	56197 (2012-09-27)	251 ± 25	3	-0.64 ± 0.02
J1727+5510	56476 (2013-07-03)	29 ± 6	56478 (2013-07-05)	260 ± 8	2	-0.7 ± 0.04
J1727+5510	56480 (2013-07-07)	22 ± 4	56478 (2013-07-05)	260 ± 8	2	-0.79 ± 0.04
J1727+5510	58547 (2019-03-05)	34 ± 3	58555 (2019-03-12)	309 ± 5	8	-0.7 ± 0.02
J1727+5510	58756 (2019-09-30)	35 ± 3	58747 (2019-09-21)	331 ± 4	9	-0.71 ± 0.02
J1727+5510	58908 (2020-02-29)	41 ± 2	58909 (2020-02-29)	335 ± 4	1	-0.66 ± 0.01
J1727+5510	59292 (2021-03-19)	41 ± 2	59191 (2020-12-07)	329 ± 6	101	-0.66 ± 0.01
Z8276	56200 (2012-09-30)	21 ± 4	56327 (2013-02-03)	105 ± 4	127	-0.44 ± 0.05
Z8276	56476 (2013-07-03)	24 ± 5	56477 (2013-07-04)	88 ± 7	1	-0.44 ± 0.04
Z8276	58547 (2019-03-05)	19 ± 3	58557 (2019-03-15)	73 ± 2	10	-0.42 ± 0.04
Z8276	58756 (2019-09-30)	24 ± 3	58739 (2019-09-12)	78 ± 2	17	-0.37 ± 0.02
Z8276	58918 (2020-03-10)	33 ± 2	58917 (2020-03-08)	76 ± 2	1	-0.26 ± 0.01
Z8276	59292 (2021-03-19)	28 ± 2	59184 (2020-11-30)	77 ± 2	108	-0.31 ± 0.01
RGBJ1745+398	58564 (2019-03-22)	13 ± 2	58567 (2019-03-24)	46 ± 2	3	-0.36 ± 0.02
RGBJ1745+398	58751 (2019-09-25)	13 ± 3	58735 (2019-09-09)	38 ± 2	16	-0.34 ± 0.04

Source	SCUBA2 Obs. mjd (ISO)	SCUBA2 flux density / mJy	OVRO Obs. mjd (ISO)	OVRO flux density / mJy	Time Difference / days	α
RGBJ1745+398	58914 (2020-03-06)	16 ± 2	58917 (2020-03-08)	35 ± 2	3	-0.24 ± 0.02
RGBJ1745+398	59214 (2020-12-31)	12 ± 1	59173 (2020-11-19)	31 ± 3	41	-0.34 ± 0.01
A2390	56406 (2013-04-24)	11 ± 4	56405 (2013-04-22)	48 ± 4	1	-0.48 ± 0.03
A2390	56433 (2013-05-21)	12 ± 6	56438 (2013-05-25)	43 ± 8	5	-0.42 ± 0.08
A2390	58599 (2019-04-26)	7 ± 3	58599 (2019-04-25)	47 ± 2	0	-0.61 ± 0.08
A2390	58752 (2019-09-26)	6 ± 3	58734 (2019-09-08)	54 ± 3	18	-0.69 ± 0.11
A2390	59018 (2020-06-18)	9 ± 2	59018 (2020-06-18)	52 ± 2	0	-0.57 ± 0.06
A2390	59214 (2020-12-31)	7 ± 1	59197 (2020-12-14)	53 ± 3	17	-0.63 ± 0.04
A2390	59373 (2021-06-08)	11 ± 3	59197 (2020-12-14)	53 ± 3	176	-0.51 ± 0.06
A2415	56201 (2012-10-01)	18 ± 6	56328 (2013-02-04)	107 ± 4	127	-0.57 ± 0.08
A2415	56475 (2013-07-02)	18 ± 9	56479 (2013-07-06)	123 ± 4	4	-0.6 ± 0.11
A2415	58567 (2019-03-25)	20 ± 2	58565 (2019-03-22)	159 ± 3	2	-0.67 ± 0.02
A2415	58750 (2019-09-24)	19 ± 2	58736 (2019-09-10)	122 ± 2	14	-0.59 ± 0.03
A2415	59018 (2020-06-18)	21 ± 2	59019 (2020-06-18)	107 ± 2	1	-0.54 ± 0.03
A2415	59127 (2020-10-05)	16 ± 3	59144 (2020-10-22)	107 ± 2	17	-0.61 ± 0.05
A2415	59322 (2021-04-18)	15 ± 2	59192 (2020-12-09)	106 ± 3	130	-0.62 ± 0.04

Source	SCUBA2 Obs. mjd (ISO)	SCUBA2 flux density / mJy	OVRO Obs. mjd (ISO)	OVRO flux density / mJy	Time Difference / days	α
A2627	56224 (2012-10-24)	21 ± 5	56349 (2013-02-25)	35 ± 7	125	-0.21 ± 0.04
A2627	56475 (2013-07-02)	23 ± 7	56475 (2013-07-01)	43 ± 8	0	-0.23 ± 0.02
A2627	58615 (2019-05-12)	16 ± 2	58619 (2019-05-15)	37 ± 3	4	-0.27 ± 0.02
A2627	58751 (2019-09-25)	17 ± 3	58733 (2019-09-07)	45 ± 3	18	-0.32 ± 0.03
A2627	59029 (2020-06-29)	13 ± 3	59028 (2020-06-28)	49 ± 2	1	-0.4 ± 0.05
A2627	59230 (2021-01-16)	12 ± 2	59191 (2020-12-08)	41 ± 3	39	-0.41 ± 0.04
RXJ2341.1+0018	56170 (2012-08-31)	27 ± 4	56329 (2013-02-05)	106 ± 4	159	-0.39 ± 0.03
RXJ2341.1+0018	56189 (2012-09-19)	23 ± 4	56329 (2013-02-05)	106 ± 4	140	-0.44 ± 0.04
RXJ2341.1+0018	56476 (2013-07-03)	30 ± 5	56481 (2013-07-07)	104 ± 6	5	-0.39 ± 0.03
RXJ2341.1+0018	58598 (2019-04-25)	18 ± 2	58599 (2019-04-25)	98 ± 2	1	-0.52 ± 0.03
RXJ2341.1+0018	58751 (2019-09-25)	19 ± 2	58738 (2019-09-12)	96 ± 3	13	-0.51 ± 0.02

.5 ALMA Data

Table 4

ALMA flux densities, and the spectral indices calculated with the nearest 15 GHz OVRO 40m observations. *The observation of A2052 was completed on two separate dates (mjd 57611 and 57623), and we use the central date to find the nearest OVRO measurement for calculating the spectral index.

Source	ALMA Obs. mjd (ISO)	ALMA Freq. / GHz	ALMA flux den. / mJy	OVRO Obs. mjd (ISO)	OVRO flux den. / mJy	Time diff. / days	α
RXJ0132.6-0804	58134.0 (2018-01-16)	92.7	31.6 ± 0.6	58132 (2018-01-14)	101 ± 2	1	-0.65 ± -0.03
J0439+0520	58119.0 (2018-01-01)	100.1	34.6 ± 1.0	58122 (2018-01-04)	341 ± 5	3	-1.22 ± 0.01
A1644	58351.0 (2018-08-21)	103.1	29.2 ± 1.0	58449 (2018-11-27)	164 ± 2	98	-0.95 ± 0.03
J1350+0940	58377.0 (2018-09-16)	94.8	10.2 ± 0.4	58408 (2018-10-17)	129 ± 2	31	-1.39 ± 0.01
A2052	57617 (2016-08-17)*	229.5	32.5 ± 0.1	57612 (2016-08-12)	93 ± 3	4	-0.40 ± -0.04
A2390	58125.0 (2018-01-07)	98.3	7.3 ± 0.4	58131 (2018-01-13)	44 ± 2	6	-1.0 ± 0.01
A2415	58141.0 (2018-01-23)	102.0	19.7 ± 0.3	58141 (2018-01-23)	152 ± 2	0	-1.09 ± -0.01

APPENDIX B

Hyperfine Structure of CN and HCN

The spectra of the CN(2-1) and HCN(2-1) observations contain absorption features of several hyperfine structure lines. The frequencies of these lines and their relative strengths are given in Tables B.1 and B.2.

Fig. B.1 shows the full spectrum of CN(2-1), as well as markers which indicate where absorption would be expected due to the hyperfine structure lines for the strong absorption features at -43.1 and -4.0 km s^{-1}(see Fig. 4.2). The main body of this chapter focuses on the strongest set of absorption features which can be seen at approximately $215.15-215.25$ GHz and disregard the rest (note that in Fig. B.1 the frequency axis is reversed such that the direction of left to right implies increasing velocity for each of the lines, in keeping with the chapter's other plots). This set of absorption features is produced by the combination of four hyperfine structure lines. However, three of these lines are very close to each other in frequency and the fourth is of negligible strength (5 per cent of the other three lines combined) and so is ignored for simplicity.

Although the three remaining hyperfine structure lines are very close to each other in frequency, the difference between them does have a tangible effect on the apparent velocity dispersion, σ, of the absorption features. A slight modification is therefore made to the rigid Gaussian fitting process used for the other spectra which have no or negligible

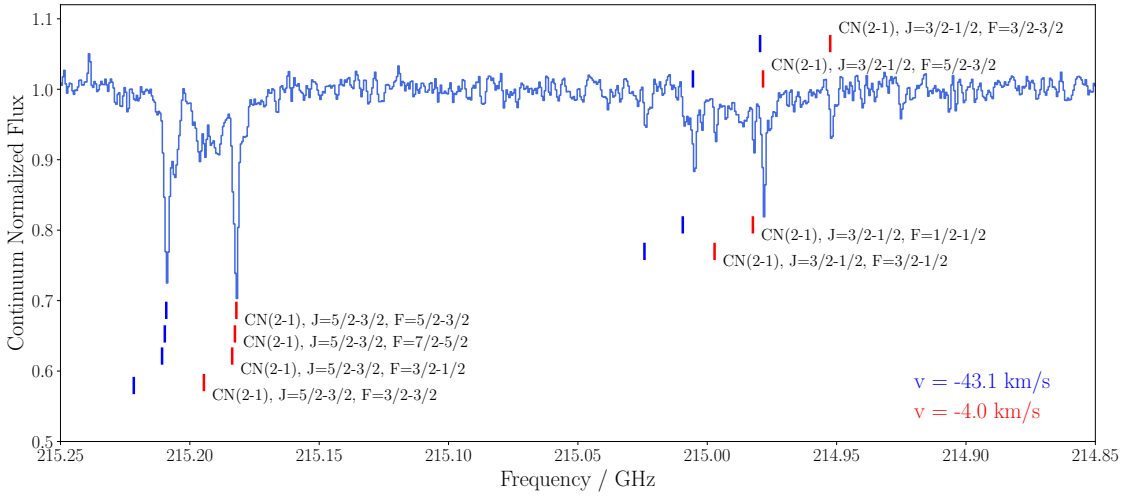

Figure B.1

The spectrum of CN(2-1) seen against the line of sight to Hydra-A's bright radio core, which contains absorption from several of the molecule's hyperfine structure lines. The intensity and rest frequencies of these hyperfine structure lines are given in Table B.1. Markers on the plot indicate where absorption would be expected from the dominant hyperfine structure lines due to the two strongest points of absorption at -43.1 and -4.0 km s^{-1}. Analysis of the CN(2-1) absorption in the main body of this chapter focuses on the combination of hyperfine structure lines seen between approximately 215.15 – 215.25 GHz and disregard the rest.

hyperfine structure. When fitting to all of the other spectra a 12-Gaussian line is used, where each Gaussian has a fixed $v_{\rm cen}$ and σ, but varying amplitude. To estimate the effect of the CN molecule's hyperfine structure, each of the 12 Gaussian features is simulated as they would appear due to the three overlapping hyperfine structure lines. This produces what appears to be a single, stronger Gaussian absorption line with a slightly wider σ than the individual lines. This slightly wider σ is due the separation of the hyperfine structure lines. When a single Gaussian is fitted to each of these simulated absorption features, the increase in the σ caused by the hyperfine structure (typically $0.1 - 0.3$ km s^{-1}) is found. When making the 12-Gaussian fit to the CN(2-1) spectrum shown in Fig. 3, the σ of each component Gaussian line is increased accordingly. This process has also been tested for HCN(2-1), which contains similar hyperfine structure. However, an unmodified fit works best, most likely because for HCN(2-1), around 70 percent of the flux is contained within two hyperfine lines just 0.0001 GHz apart.

Rest frequency (GHz)	CN Transition	Relative intensity
226.28741850	J=3/2-3/2, F=1/2-1/2	0.0060
226.29894270	J=3/2-3/2, F=1/2-3/2	0.0048
226.30303720	J=3/2-3/2, F=3/2-1/2	0.0049
226.31454000	J=3/2-3/2, F=3/2-3/2	0.0116
226.33249860	J=3/2-3/2, F=3/2-5/2	0.0053
226.34192980	J=3/2-3/2, F=5/2-3/2	0.0055
226.35987100	J=3/2-3/2, F=5/2-5/2	0.0282
226.61657140	J=3/2-1/2, F=1/2-3/2	0.0063
226.63219010	J=3/2-1/2, F=3/2-3/2	0.0498
226.65955840	J=3/2-1/2, F=5/2-3/2	0.1660
226.66369280	J=3/2-1/2, F=1/2-1/2	0.0495
226.67931140	J=3/2-1/2, F=3/2-1/2	0.0616
226.87419080	J=5/2-3/2, F=5/2-3/2	0.1685
226.87478130	J=5/2-3/2, F=7/2-5/2	0.2669
226.87589600	J=5/2-3/2, F=3/2-1/2	0.1002
226.88742020	J=5/2-3/2, F=3/2-3/2	0.0319
226.89212800	J=5/2-3/2, F=5/2-5/2	0.0317
226.90535740	J=5/2-3/2, F=3/2-5/2	0.0013

Table B.1

Hyperfine structure lines of CN(2-1) (Muller et al., 2005).

Rest frequency (GHz)	HCN Transition	Relative intensity
88.63393600	J=1-0, F=0-1	0.1111
88.63041600	J=1-0, F=1-1	0.3333
88.63184700	J=1-0, F=2-1	0.5556
177.25967700	J=2-1,F=2-2	0.0833
177.25992300	J=2-1,F=1-0	0.1111
177.26111000	J=2-1,F=2-1	0.2500
177.26122300	J=2-1,F=3-2	0.4667
177.26201220	J=2-1,F=1-2	0.0056
177.26344500	J=2-1,F=1-1	0.0833

Table B.2

Hyperfine structure lines of HCN(1-0) and HCN(2-1) (Muller et al., 2005).

APPENDIX C

Observation details for sources lacking emission and absorption lines

---

Table C.1 shows details of the observations for which no $\geq 3\sigma$ detections of emission or absorption were made with either the CO(1-0), CN-A or CN-B lines.

	MACSJ0242.5-2132	Abell 3112	Abell 496	RXCJ0132.6-0804
Observation date	2018 Jan 12	2018 Jan 11	2018 Jan 13	2018 Jan 16
Integration time (s)	1300	1300	6800	2500
CO(1-0) vel. resolution (km s^{-1})	3.3	2.7	2.6	2.9
Frequency resolution (kHz)	977	977	977	977
Angular resolution (arcsec)	0.48	0.54	0.48	0.62
PWV (mm)	6.5	6.6	2.2	4.3
FoV (arcsec)	67.9	62.9	60.2	67.5
ALMA configuration	C43-5	C43-5	C43-5	C43-5
Maximum spacing (m)	1400	1400	1400	1400
CO(1-0) noise per channel (mJy)	1.87	1.10	0.55	1.80
115 GHz cont. flux density (mJy)	39.6	30.4*	59.0	38.6

	Abell 2415	Abell 3581	RXCJ1356.0-3421
Observation date	2018 Jan 23	2018 Sep 11	2018 Sep 11
Integration time (s)	5400	1700	1200
CO(1-0) vel. resolution (km s^{-1})	2.7	2.6	3.1
Frequency resolution (kHz)	977	977	977
Angular resolution (arcsec)	0.57	0.92	0.91
PWV (mm)	1.76	0.72	0.7
FoV (arcsec)	61.9	59.5	63.4
ALMA configuration	C43-5	C43-4	C43-4
Maximum spacing (m)	1400	784	784
CO(1-0) noise per channel (mJy)	0.35	0.85	1.32
115 GHz cont. flux density (mJy)	27.2	59.1	25.9

Table C.1

A summary of the ALMA observations in which no absorption or emission lines were detected, all of which were taken using ALMA band 3. *The continuum source of Abell 3112 is extended to the North West, with a flux density peaking at 12.9 mJy.

C.1 Residuals of Absorption and Emission Line Fits

Fig. C.1, C.2 and C.3 show the residuals for the spectra shown in Fig. 5.2, 5.3 and 5.4, calculated using the Gaussian best fits for the emission and absorption lines which are given in Tab. 5.5.

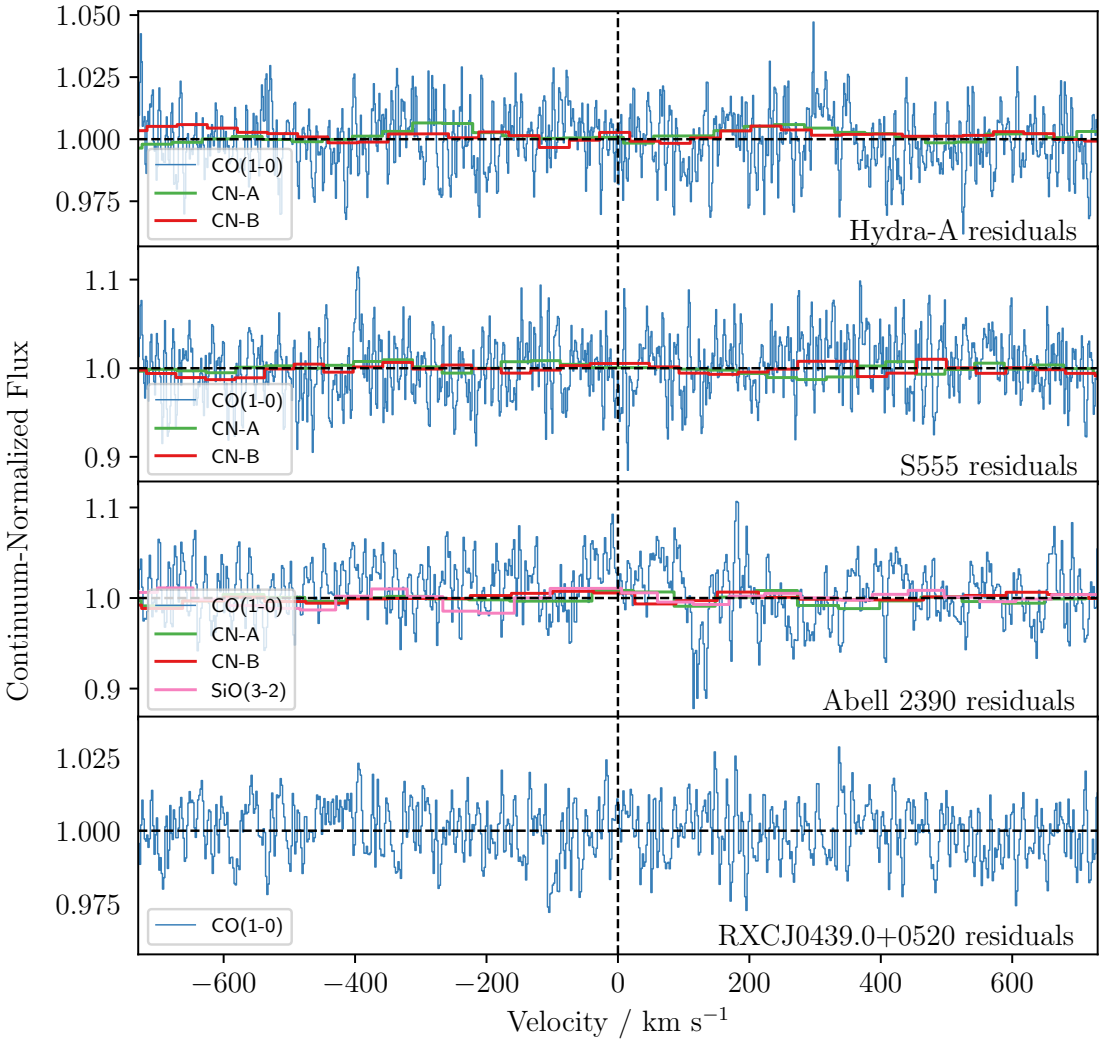

Figure C.1

Fig. C.1 and C.2 are the residuals for the spectra shown in Fig. 5.2 and 5.3 and their Gaussian best fits as given in Table 5.5. These are the sources which have CO and/or CN emission along the line-of-sight to their bright continuum sources. The only residual plot which reveals detail not encapsulated by the Gaussian best fit is the CO(1-0) spectrum of Abell 2390. This is due to the saw tooth shape of the absorption (see Fig. 5.2).

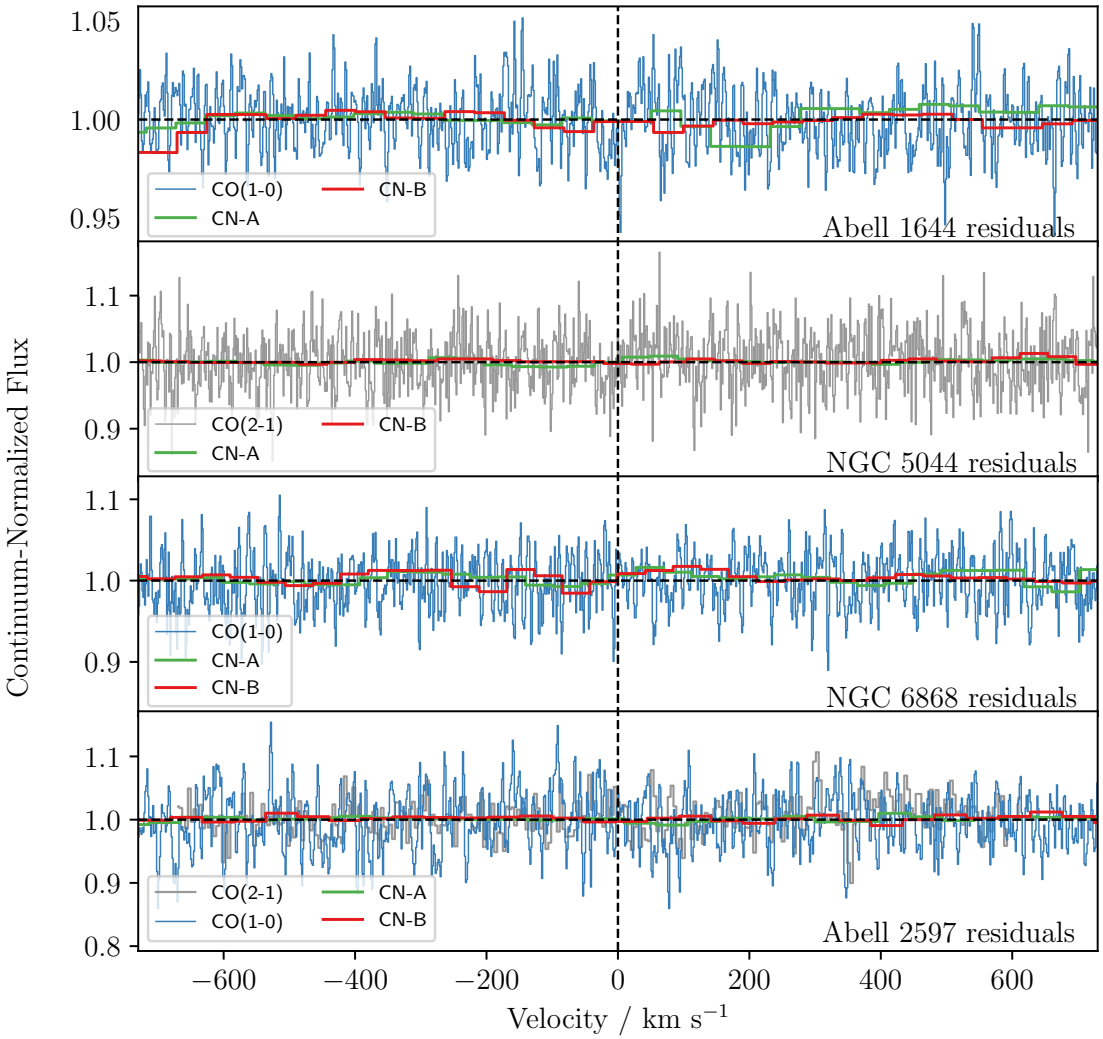

Figure C.2

Residuals for the spectra shown in Fig. 5.2 and their Gaussian best fits as given in Table 5.5. Continued from Fig. C.1.

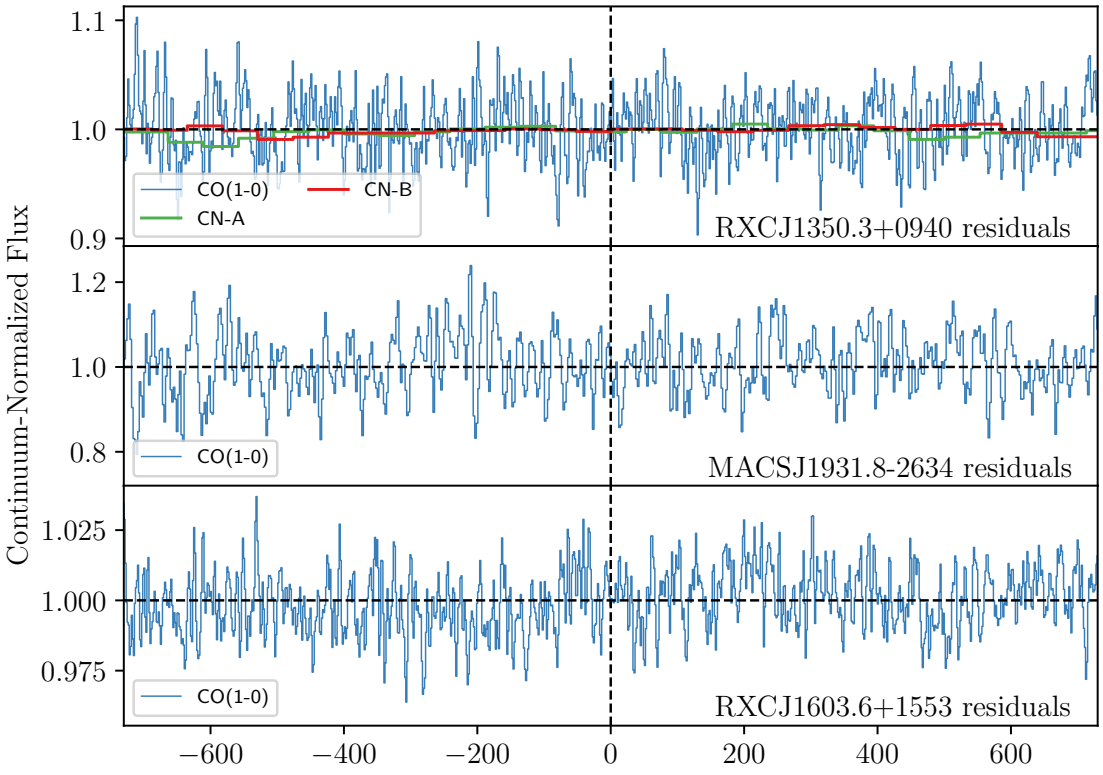

Figure C.3

Residuals for spectra shown in Fig. 5.4, calculated with their best fits as given in Table 5.5. These are the sources which have CO and/or CN emission, but not absorption.

Bibliography

Abazajian K. N., et al., 2009, ApJs, 182, 543

Abdollahi S., et al., 2020, ApJs, 247, 33

Algaba J.-C., et al., 2015, Journal of Korean Astronomical Society, 48, 237

Allen S., Ettori S., Fabian A., 2001, MNRAS, 324, 877

Allen S. W., Schmidt R. W., Ebeling H., Fabian A. C., van Speybroeck L., 2004, MNRAS, 353, 457

Allen S. W., Rapetti D. A., Schmidt R. W., Ebeling H., Morris R. G., Fabian A. C., 2008, MNRAS, 383, 879

Allison J. R., et al., 2020, MNRAS, 494, 3627

Ando R., Kohno K., Tamura Y., Izumi T., Umehata H., Nagai H., 2016, Publications of the Astronomical Society of Japan, 68, 6

Antonucci R. R. J., Miller J. S., 1985, ApJ, 297, 621

Baars J. W. M., Genzel R., Pauliny-Toth I. I. K., Witzel A., 1977, A&A, 500, 135

Baek J., Chung A., Kim J., Taehyun J., 2020, The Bulletin of The Korean Astronomical Society, 45, 30

Ballesteros-Paredes J., Hartmann L. W., Vazquez-Semadeni E., Heitsch F., Zamora-Aviles M. A., 2011, MNRAS, 411, 65

Bauer F. E., Fabian A. C., Sanders J. S., Allen S. W., Johnstone R. M., 2005, MNRAS, 359, 1481

Bianchi S., Maiolino R., Risaliti G., 2012, Advances in Astronomy, 2012, 782030

Bird J., Martini P., Kaiser C., 2008, ApJ, 676, 147

Blandford R., Meier D., Readhead A., 2019, Annual Review of Astronomy and Astrophysics, 57, 467

Boger G. I., Sternberg A., 2005, ApJ, 632, 302

Bohringer H., et al., 2002, ApJ, 566, 93

Böhringer H., et al., 2004, A&A, 425, 367

Bolatto A. D., Leroy A., Israel F. P., Jackson J. M., 2003, ApJ, 595, 167

Bolatto A. D., Wolfire M., Leroy A. K., 2013, Annual Review of Astronomy and Astrophysics, 51, 207

Bondi H., 1952, MNRAS, 112, 195

Bower R. G., Benson A. J., Malbon R., Helly J. C., Frenk C. S., Baugh C. M., Cole S., Lacey C. G., 2006, MNRAS, 370, 645

Braine J., Combes F., 1992, A&A, 264, 433

Brown T., Wilson C., 2019, arXiv e-prints, p. arXiv:1905.06950

Buote D. A., Brighenti F., Mathews W. G., 2004, ApJl, 607, L91

Canning R. E. A., et al., 2013, MNRAS, 435, 1108

Cheale R. A., et al., 2019, MNRAS, 484, 2757

Chira R. A., Ibáñez-Mejía J. C., Mac Low M. M., Henning T., 2019, A&A, 630, A97

Churazov E., Brüggen M., Kaiser C. R., Böhringer H., Forman W., 2001, ApJ, 554, 261

Cole S., Lacey C. G., Baugh C. M., Frenk C. S., 2000, MNRAS, 319, 168

Combes F., 2008, Astrophys. Space Sci., 313, 321

Combes F., et al., 2013, A&A, 558, A124

Combes Gupta, N. Jozsa, G. I. G. Momjian, E. 2019, A&A, 623, A133

Crawford C. S., Allen S. W., Ebeling H., Edge A. C., Fabian A. C., 1999, MNRAS, 306, 857

Croton D. J., et al., 2006, MNRAS, 365, 11

David L. P., et al., 2011, ApJ, 728, 162

David L. P., et al., 2014, ApJ, 792, 94

Davis T. A., 2014, MNRAS, 445, 2378

Donahue M., de Messières G. E., O'Connell R. W., Voit G. M., Hoffer A., McNamara B. R., Nulsen P. E. J., 2011, ApJ, 732, 40

Downes D., Wilson T. L., Bieging J., Wink J., 1980, A&As, 40, 379

Draine B. T., Lee H. M., 1984, ApJ, 285, 89

Dutson K. L., White R. J., Edge A. C., Hinton J. A., Hogan M. T., 2013, MNRAS, 429, 2069

Dutson K. L., Edge A. C., Hinton J. A., Hogan M. T., Gurwell M. A., Alston W. N., 2014, MNRAS, 442, 2048

Dwarakanath K. S., Owen F. N., van Gorkom J. H., 1995, ApJl, 442, L1

ESO.org 2021

Ebeling H., Voges W., Bohringer H., Edge A. C., Huchra J. P., Briel U. G., 1996, MNRAS, 281, 799

Ebeling H., Edge A. C., Bohringer H., Allen S. W., Crawford C. S., Fabian A. C., Voges W., Huchra J. P., 1998, MNRAS, 301, 881

Ebeling H., Edge A. C., Allen S. W., Crawford C. S., Fabian A. C., Huchra J. P., 2000, MNRAS, 318, 333

Eckart A., Cameron M., Genzel R., Jackson J. M., Rothermel H., Stutzki J., Rydbeck G., Wiklind T., 1990, ApJ, 365, 522

Edge A. C., 1989

Edge A. C., 2001, MNRAS, 328, 762

Edge D. O., Shakeshaft J. R., McAdam W. B., Baldwin J. E., Archer S., 1959, MNRAS, 68, 37

Edge A. C., Ivison R. J., Smail I., Blain A. W., Kneib J.-P., 1999, MNRAS, 306, 599

Edge A. C., Wilman R. J., Johnstone R. M., Crawford C. S., Fabian A. C., Allen S. W., 2002, MNRAS, 337, 49

Edge A. C., et al., 2010, A&A, 518, L47

Egami E., Rieke G. H., Fadda D., Hines D. C., 2006, ApJ Letters, 652, L21

Ehlert S., et al., 2011, MNRAS, 411, 1641

Fabian A. C., 1994, Annual Review of Astronomy and Astrophysics, 32, 277

Fanaroff B. L., Riley J. M., 1974, MNRAS, 167, 31P

Ferrarese L., Merritt D., 2000, ApJ, 539, L9

Fogarty K., et al., 2019, arXiv e-prints, p. arXiv:1905.01377

García-Burillo S., et al., 2014, A&A, 567, A125

Gaspari M., Melioli C., Brighenti F., D'Ercole A., 2011, MNRAS, 411, 349

Gaspari M., Ruszkowski M., Oh S. P., 2013, MNRAS, 432, 3401

Gaspari M., Brighenti F., Temi P., 2015, A&A, 579, A62

Gaspari M., Temi P., Brighenti F., 2017, MNRAS, 466, 677

Gaspari M., et al., 2018, Astrophys. J., 854, 167

Gastaldello F., et al., 2013, Astrophys. J., 770, 56

Geréb K., Maccagni, F. M. Morganti, R. Oosterloo, T. A. 2015, A&A, 575, A44

Gerin M., Liszt H., Neufeld D., Godard B., Sonnentrucker P., Pety J., Roueff E., 2019, A&A, 622, A26

Ginard D., et al., 2012, A&A, 543, A27

Glenn J., Hunter T. R., 2001, ApJs, 135, 177

Godard B., Falgarone E., Gerin M., Hily-Blant P., de Luca M., 2010, A&A, 520, A20

Gong Y., et al., 2016, A&A, 588, A104

Graham A. W., Colless M. M., Busarello G., Zaggia S., Longo G., 1998, AAPS, 133, 325

Greaves J. S., Nyman L. A., 1996, A&A, 305, 950

Green T. S., et al., 2016, MNRAS, 461, 560

Green T. S., et al., 2017, MNRAS, 465, 4872

Gültekin K., et al., 2009, ApJ, 698, 198

Hacar A., Bosman A. D., van Dishoeck E. F., 2019, arXiv e-prints, p. arXiv:1910.13754

Hamer S. L., 2012

Hamer S., et al., 2013, MNRAS, 437, 862

Hamer S. L., et al., 2014, MNRAS, 437, 862

Hamer S. L., et al., 2016, MNRAS, 460, 1758

Hansen L., Jorgensen H. E., Norgaard-Nielsen H. U., 1995, A&A, 297, 13

Harada N., Nishimura Y., Watanabe Y., Yamamoto S., Aikawa Y., Sakai N., Shimonishi T., 2019, ApJ, 871, 238

Hardcastle M. J., Croston J. H., 2020, New Astronomy Reviews, 88, 101539

Harris C. R., et al., 2020, Nature, 585, 357

Haynes M. P., Hogg D. E., Maddalena R. J., Roberts M. S., van Zee L., 1998, The Astronomical Journal, 115, 62

Heckman T. M., Best P. N., 2014, Annual Review of Astronomy and Astrophysics, 52, 589

Heidt J., Wagner S. J., 1996, A&A, 305, 42

Henkel C., Wilson T. L., Walmsley C. M., Pauls T., 1983, A&A, 127, 388

Hernández Vera M., Lique F., Dumouchel F., Hily-Blant P., Faure A., 2017, MNRAS, 468, 1084

Herrera-Camus R., et al., 2020, A&A, 633, L4

Hlavacek-Larrondo J., Fabian A. C., Edge A. C., Hogan M. T., 2012, MNRAS, 424, 224

Hogan M., 2014b

Hogan M. T., 2014a, PhD thesis, Durham University

Hogan M. T., et al., 2015a, MNRAS, 453, 1201

Hogan M. T., et al., 2015b, MNRAS, 453, 1223

Hudson D. S., Mittal R., Reiprich T. H., Nulsen P. E. J., Andernach H., Sarazin C. L., 2010, A&A, 513, A37

Hunter J. D., 2007, Comput. Sci. Eng., 9, 90

Iben Jr. I., 1975, ApJ, 196, 525

Israel F. P., van Dishoeck E. F., Baas F., Koornneef J., Black J. H., de Graauw T., 1990, A&A, 227, 342

Iwasawa K., Allen S. W., Fabian A. C., Edge A. C., Ettori S., 1999, MNRAS, 306, 467

Jaffe W., 1990, A&A, 240, 254

Jaffe W., Bremer M. N., van der Werf P. P., 2001, MNRAS, 324, 443

Jaffe W., Bremer M. N., Baker K., 2005, MNRAS, 360, 748

Johnson R. E., Markevitch M., Wegner G. A., Jones C., Forman W. R., 2010, ApJ, 710, 1776

Johnstone R. M., Fabian A. C., Taylor G. B., 1998, MNRAS, 298, 854

Johnstone R. M., Fabian A. C., Morris R. G., Taylor G. B., 2005, MNRAS, 356, 237

Jones E., Oliphant T., Peterson P., 2011, SciPy Open Source Scientific Tools for Python, www.scipy.org

Juráňová A., et al., 2018, arXiv e-prints,

Kameno S., et al., 2020, arXiv e-prints, p. arXiv:2004.09369

Kashlinsky A., 1982, MNRAS, 200, 585

King A., Pounds K., 2015, Ann. Rev. Astron. Astrophys., 53, 115

King A. R., Pringle J. E., 2007, MNRAS, 377, L25

King A. R., Pringle J. E., Hofmann J. A., 2008, MNRAS, 385, 1621

Kobayashi C., Nakasato N., 2011, ApJ, 729, 16

Kormendy J., Ho L. C., 2013, ARAA, 51, 511

Kravtsov A. V., Borgani S., 2012, ARAA, 50, 353

LaMassa S. M., et al., 2015, ApJ, 800, 144

Larson R. B., 1981, MNRAS, 194, 809

Le Borgne J.-F., Mathez G., Mellier Y., Pello R., Sanahuja B., Soucail G., 1991, A&As, 88, 133

Lim J., Leon S., Combes F., Dinh-V-Trung 2000, ApJ Letters, 545, L93

Lin H. W., McDonald M., Benson B., Miller E., 2015, ApJ, 802, 34

Liszt H., Lucas R., 2001, A&A, 370, 576

Loomis R. A., Cleeves L. I., Öberg K. I., Guzman V. V., Andrews S. M., 2015, ApJ, 809, L25

Lucas R., Liszt H., 1994, A&A, 282, L5

Lucas R., Liszt H., 1996, A&A, 307, 237

Magorrian J., et al., 1998, ApJ, 115, 2285

Mangum J. G., Shirley Y. L., 2015, Publications of the Astronomical Society of the Pacific, 127, 266

Márquez I., Masegosa J., González-Martin O., Hernández-Garcia L., Pović M., Netzer H., Cazzoli S., del Olmo A., 2017, Frontiers in Astronomy and Space Sciences, 4, 34

Massaro E., Giommi P., Leto C., Marchegiani P., Maselli A., Perri M., Piranomonte S., Sclavi S., 2009, A&A, 495, 691

McCoy M., et al., 2017, ApJ, 851, 76

McDonald M., et al., 2013, ApJ, 774, 23

McDonald M., Gaspari M., McNamara B. R., Tremblay G. R., 2018, ApJ, 858, 45

McKee C. F., Ostriker E. C., 2007, Annual Review of Astronomy and Astrophysics, 45, 565

McLure R. J., Dunlop J. S., 2002, MNRAS, 331, 795

McMullin J. P., Waters B., Schiebel D., Young W., Golap K., 2007, in Shaw R. A., Hill F., Bell D. J., eds, Astronomical Society of the Pacific Conference Series Vol. 376, Astronomical Data Analysis Software and Systems XVI. p. 127

McNamara B. R., Nulsen P. E. J., 2012, New J. Phys., 14, 055023

McNamara B. R., et al., 2000, ApJl, 534, L135

McNamara B. R., Russell H. R., Nulsen P. E. J., Hogan M. T., Fabian A. C., Pulido F., Edge A. C., 2016, ApJ, 830, 79

Meijerink Spaans, M. Israel, F. P. 2007, A&A, 461, 793

Mittal R., Whelan J. T., Combes F., 2015, MNRAS, 450, 2564

Morganti R., Oosterloo T. A., Emonts B. H. C., van der Hulst J. M., Tadhunter C. N., 2003, ApJl, 593, L69

Morganti R., Peck A. B., Oosterloo T. A., van Moorsel G., Capetti A., Fanti R., Parma P., de Ruiter H. R., 2009, A&A, 505, 559

Muller S., Guelin M., 2008, Astron. Astrophys., 491, 739

Muller H. S. P., Schloder F., Stutzki J., Winnewisserr G., 2005, Journal of Molecular Structure, 742, 215

Muller S., et al., 2011, A&A, 535, A103

Muller S., et al., 2013, A&A, 551, A109

Murphy T., et al., 2010, MNRAS, 402, 2403

Nagai H., et al., 2019, arXiv e-prints, p. arXiv:1905.06017

Narayan R., Yi I., 1994, ApJl, 428, L13

Nawaz M. A., Bicknell G. V., Wagner A. Y., Sutherland R. S., McNamara B. R., 2016, MNRAS, 458, 802

Nulsen P. E. J., McNamara B. R., Wise M. W., David L. P., 2005, ApJ, 628, 629

O'Dea C. P., Baum S. A., Maloney P. R., Tacconi L. J., Sparks W. B., 1994, ApJ, 422, 467

Olivares V., et al., 2019, arXiv e-prints,

Oosterloo T. A., Morganti R., Tzioumis A., Reynolds J., King E., McCulloch P., Tsvetanov Z., 2000, The Astronomical Journal, 119, 2085

Oosterloo T., Raymond Oonk J. B., Morganti R., Combes F., Dasyra K., Salomé P., Vlahakis N., Tadhunter C., 2017, A&A, 608, A38

Paglione T. A. D., et al., 2001, ApJs, 135, 183

Papadopoulos P. P., Seaquist E. R., Scoville N. Z., 1996, ApJ, 465, 173

Parma P., Murgia M., de Ruiter H. R., Fanti R., Mack K. H., Govoni F., 2007, A&A, 470, 875

Peng Y., Vogel S. N., Carlstrom J. E., 1995, ApJ, 455, 223

Perotto L., et al., 2020, A&A, 637, A71

Peterson J. R., Fabian A. C., 2006, Physics Reports, 427, 1

Pizzolato F., Soker N., 2005, ApJ, 632, 821

Pizzolato F., Soker N., 2010, MNRAS, 408, 961

Pratt G. W., et al., 2010, A&A, 511, A85

Proga D., Begelman M. C., 2003, Astrophys. J., 592, 767

Qi C., Öberg K. I., Wilner D. J., 2013, ApJ, 765, 34

Rafferty D. A., McNamara B. R., Nulsen P. E. J., Wise M. W., 2006, ApJ, 652, 216

Rafferty D. A., McNamara B. R., Nulsen P. E. J., 2008, ApJ, 687, 899

Readhead A. C. S., Lawrence C. R., Myers S. T., Sargent W. L. W., Hardebeck H. E., Moffet A. T., 1989, ApJ, 346, 566

Remillard R. A., McClintock J. E., 2006, Annual Review of Astronomy and Astrophysics, 44, 49

Richards J. L., et al., 2011, ApJ Supplement Series, 194, 29

Rioja M., Dodson R., 2011, ApJ, 141, 114

Riquelme Bronfman, L. Mauersberger, R. Finger, R. Henkel, C. Wilson, T. L. Cortés-Zuleta, P. 2018, A&A, 610, A43

Robertson B., Hernquist L., Cox T. J., Di Matteo T., Hopkins P. F., Martini P., Springel V., 2006, ApJ, 641, 90

Robitaille T., Bressert E., 2012, APLpy: Astronomical Plotting Library in Python, Astrophysics Source Code Library (ascl:1208.017)

Rodriguez-Fernandez Combes, F. Martin-Pintado, J. Wilson, T. L. Apponi, A. 2006, A&A, 455, 963

Rodríguez-Fernández N. J., Tafalla M., Gueth F., Bachiller R., 2010, A&A, 516, A98

Roman-Duval J., Jackson J. M., Heyer M., Rathborne J., Simon R., 2010, ApJ, 723, 492

Rose T., et al., 2019, MNRAS, 485, 229

Ruffa I., et al., 2019, MNRAS, 484, 4239

Russell H. R., McNamara B. R., Edge A. C., Hogan M. T., Main R. A., Vantyghem A. N., 2013, MNRAS, 432, 530

Russell H. R., et al., 2019, MNRAS, 490, 3025

Saikia D. J., Jamrozy M., 2009, Bulletin of the Astronomical Society of India, 37, 63

Salomé P., Combes F., 2003, A&A, 412, 657

Salomé P., Combes F., Revaz Y., Downes D., Edge A. C., Fabian A. C., 2011, Astron. Astrophys., 531, A85

Sander B., Hensler G., 2019, MNRAS, 490, L52

Savage B. D., Sembach K. R., 1991, ApJ, 379, 245

Schmidt M., 1963, Nature, 197, 1040

Schneider M. D., Frenk C. S., Cole S., 2012, Journal of Cosmology and Astroparticle Physics, 2012, 030

Schwope A., et al., 2000, Astronomische Nachrichten, 321, 1

Serra P., et al., 2012, MNRAS, 422, 1835

Seyfert C. K., 1943, ApJ, 97, 28

Singh R., et al., 2013, A&A, 558, A43

Sliwa K., Wilson C. D., Matsushita S., Peck A. B., Petitpas G. R., Saito T., Yun M., 2017, ApJ, 840, 8

Sofia U. J., Lauroesch J. T., Meyer D. M., Cartledge S. I. B., 2004, ApJ, 605, 272

Sokolovsky K. V., et al., 2017, MNRAS, 464, 274

Solomon P. M., Rivolo A. R., Barrett J., Yahil A., 1987, ApJ, 319, 730

Somboonpanyakul T., McDonald M., Lin H. W., Stalder B., Stark A., 2018, ApJ, 863, 122

Stahler S. W., Palla F., 2004, The Formation of Stars

Steidel C. C., Erb D. K., Shapley A. E., Pettini M., Reddy N., Bogosavljević M., Rudie G. C., Rakic O., 2010, ApJ, 717, 289

Tadhunter C., 2008, New Astronomy Reviews, 52, 227

Taniguchi Y., Ohyama Y., Sanders D. B., 1999, ApJ, 522, 214

Taylor G. B., 1996, ApJ, 470, 394

Taylor G. B., Perley R. A., Inoue M., Kato T., Tabara H., Aizu K., 1990, ApJ, 360, 41

Temi P., Amblard A., Gitti M., Brighenti F., Gaspari M., Mathews W. G., David L., 2018a, ApJ, 858, 17

Temi P., Amblard A., Gitti M., Brighenti F., Gaspari M., Mathews W. G., David L., 2018b, The Astrophysical Journal, 858, 17

The Astropy Collaboration et al., 2013, A&A, 558, A33

The Astropy Collaboration et al., 2018, AJ, 156, 123

Thompson A. R., Moran J. M., Swenson George W. J., 2017, Interferometry and Synthesis in Radio Astronomy, 3rd Edition, doi:10.1007/978-3-319-44431-4.

Tremblay G. R., et al., 2012, MNRAS, 424, 1042

Tremblay G. R., et al., 2016, Nature, 534, 218

Tremblay G. R., et al., 2018, ApJ, 865, 13

Urry C. M., Padovani P., 1995, Publications of the Astronomical Society of the Pacific, 107, 803

Van Rossum G., Drake F. L., 2009, Python 3 Reference Manual. CreateSpace, Scotts Valley, CA

Vantyghem A. N., et al., 2017, ApJ, 848, 101

Vazquez-Semadeni E., Gomez G. C., Jappsen A. K., Ballesteros-Paredes J., Gonzalez R. F., Klessen R. S., 2007, ApJ, 657, 870

Vermeulen R. C., Ogle P. M., Tran H. D., Browne I. W. A., Cohen M. H., Readhead A. C. S., Taylor G. B., Goodrich R. W., 1995, ApJ, 452, L5

Véron-Cetty M.-P., Woltjer L., Staveley-Smith L., Ekers R. D., 2000, A&A, 362, 426

Virtanen P., et al., 2020, Nature Methods, 17, 261

Wagner A. Y., Bicknell G. V., Umemura M., 2012, ApJ, 757, 136

Wiklind T., Combes F., 1996a, A&A, 315, 86

Wiklind T., Combes F., 1996b, Nature, 379, 139

Wiklind T., Combes F., 1997a, A&A, 324, 51

Wiklind T., Combes F., 1997b, A&A, 328, 48

Wiklind T., Combes F., Kanekar N., 2018, ApJ, 864, 73

Wilson T. L., 1999, Reports on Progress in Physics, 62, 143

Wilson C. D., 2018, MNRAS, 477, 2926

Wise M. W., McNamara B. R., Nulsen P. E. J., Houck J. C., David L. P., 2007, Astrophys. J., 659, 1153

Zhang Z.-Y., Romano D., Ivison R. J., Papadopoulos P. P., Matteucci F., 2018, Nature, 558, 260

van Gorkom J. H., Knapp G. R., Ekers R. D., Ekers D. D., Laing R. A., Polk K. S., 1989, The Astronomical Journal, 97, 708

van der Walt S., Colbert S. C., Varoquaux G., 2011, Comput. Sci. Eng., 13, 22